SUPERPOSITIONS OF LIGHT FIELDS CARRYING ORBITAL ANGULAR MOMENTUM

By

Angela Dudley

A thesis submitted in fulfilment of the academic requirements for the PhD degree of Science in the School of Chemistry and Physics, University of KwaZulu-Natal, Durban.

Supervisor:
Prof. Andrew Forbes

January 2012

Abstract

The work presented in this thesis is centred on the generation of superimposed optical fields which each carry orbital angular momentum (OAM) and the development of OAM measurement techniques. Optical fields which carry OAM have found applications ranging from optical tweezing to quantum cryptography. Due to the fact that they offer a potentially infinite-dimensional state space, much interest has been generated in the measurement of OAM in optical fields, in order for higher-dimensional quantum information processing to be realised. In this study we generate superpositions of higher-order Bessel beams and show that even though we can create a field which carries no overall OAM, we can still witness an angular rotation in the intensity profile of the beam. We also develop two new OAM measurement techniques: (1) a robust odd-even-OAM interferometer and (2) a method to measure the OAM density of an optical field by means of a single spatial light modulator (SLM).

In the first chapter we give an overview of the literature regarding optical OAM, followed by the derivation of the Helmholtz wave equation from Maxwell's equations. We illustrate that helically-phased beams, having a phase factor of $\exp(il\theta)$, possess a well-defined OAM. Definitions for the fundamental Gaussian mode, as well as two OAM-carrying modes: Laguerre-Gaussian (LG) and Bessel-Gaussian (BG) modes are also given. Since a majority of this thesis involves generating superimposed OAM fields as well as the measurement of OAM, chapter 2 contains detailed discussions on the optical components used to generate and measure OAM. In section 2.9 we present one of our contributions to the field of OAM-measurement, which involves a stable Dove-prism embedded Mach-Zehnder interferometer, capable of sorting 41 OAM states into odd and even ports with a contrast ranging from 92% to 61%.

We implement the Dove prism embedded Mach-Zehnder interferometer to mimic an amplitude damping channel for OAM states in chapter 3. Our device is useful in modelling a 'lossy' environment for OAM states. In chapter 4 we develop a new technique for the generation of superimposed Bessel beams through the use of a single digital hologram and theoretically and experimentally show that even though the superimposed Bessel beams can be constructed to produce no overall OAM, a rotation in the beam's intensity profile is still present, as the field propagates. This rotation is due to the differing longitudinal wave-vectors present in the field and we make quantitative, experimental measurements of the angular rotation rates, which are in very good agreement with our theoretical predictions. We also show that the far-field of these superimposed Bessel beams, exhibit no rotation in their intensity profile and we offer a

theoretical explanation for this occurrence. In chapter 5, we adapt our technique for generating superimposed Bessel beams to create non-diffracting speckle fields, which are known to possess optical vortices, and show that by controlling the standard deviation of the phase distribution within the digital hologram, we are able to control the evolution of the non-diffracting speckle field into a non-diffracting zero-order Bessel beam. Our final chapter contains a novel technique for the measurement of the OAM density of optical fields, by implementing two optical components: an SLM and a lens.

Declaration 1

The experimental work described in this thesis was carried out at the Council for Scientific and Industrial Research, National Laser Center, while registered with the School of Physics, University of KwaZulu-Natal, Durban, Westville, from August 2009 to January 2012, under the supervision of Professor Andrew Forbes.

These studies represent original work by the author and have not otherwise been submitted in any form for any degree or diploma to any tertiary institution. Where use has been made of the work of others it is duly acknowledged in the text.

Signed:_____

On this_____day of_____2012

As the candidate's supervisor I have approved this dissertation for submission.

_____

Prof Andrew Forbes

On this_____day of_____2012

Declaration 2 - Plagiarism

I, ……. declare that

1. The research reported in this thesis, except where otherwise indicated, is my original research.

2. This thesis has not been submitted for any degree or examination at any other university.

3. This thesis does not contain other persons' data, pictures, graphs or other information, unless specifically acknowledged as being sourced from other persons.

4. This thesis does not contain other persons' writing, unless specifically acknowledged as being sourced from other researchers. Where other written sources have been quoted, then:
   a. Their words have been re-written but the general information attributed to them has been referenced
   b. Where their exact words have been used, then their writing has been placed in italics and inside quotation marks, and referenced.

5. This thesis does not contain text, graphics or tables copied and pasted from the Internet, unless specifically acknowledged, and the source being detailed in the thesis and in the References sections.

Signed: ……

Declaration 3 – Publications

Peer-Reviewed Journal Papers:

[1]. R. Vasilyeu, **A. Dudley**, N. Khilo, and A. Forbes, "Generating superpositions of higher-order Bessel beams," Opt. Express **17**(26), 23389-23395 (2009).

[2]. **A. Dudley**, M. Nock, T. Konrad, F. S. Roux, and A. Forbes, "Amplitude damping of Laguerre-Gaussian modes," Opt. Express **18**(22), 22789-22795 (2010).

[3]. M. Lavery, **A. Dudley**, A. Forbes, J. Courtial, and M. Padgett, "Robust interferometer for the routing of light beams carrying orbital angular momentum," New J. of Phys. **13**(9), 093014 (2011).

[4]. I. Litvin, **A. Dudley**, and A. Forbes, "Poynting vector and orbital angular momentum density of superpositions of Bessel beams," Opt. Express **19**(18), 16760-16771 (2011).

[5]. **A. Dudley**, R. Vasilyeu, V. Belyi , N. Khilo, P. Ropot, and A. Forbes, "Controlling the evolution of nondiffracting speckle by complex amplitude modulation on a phase-only spatial light modulator," Opt. Commun. **285**(1), 5-12 (2012).

[6]. R. Rop, **A. Dudley**, C. López-Mariscal, and A. Forbes, "Measuring the rotation rates of superpositions of higher-order Bessel beams," J. Mod. Opt. **59**(3), 259-267 (2012).

[7]. **A. Dudley**, I. Litvin, and A. Forbes, "Quantitative measurement of the orbital angular momentum density of light," App. Opt. **51**(7), 823-833 (2012).

[8]. **A. Dudley** and A. Forbes, "From stationary annular rings to rotating Bessel beams," J. Opt. Soc. Am. A **29**(4), 567-573 (2012).

[9]. I. Litvin, **A. Dudley**, F. S. Roux, and A. Forbes, "Azimuthal decomposition with digital holograms," Opt. Express **20**(10), 10996-11004 (2012).

International Conference Papers:

[1]. **A. Dudley**, R. Vasilyeu, A. Forbes, N. Khilo, P. Ropot, V. Belyi, and N. Kazak, "Superpositions of higher-order Bessel beams and nondiffracting speckle fields," Proc. SPIE **7430**, 74300A (2009). doi: 10.1117/12.826884.

[2]. R. Vasilyeu, **A. Dudley**, N. Khilo, and A. Forbes, "Generating superpositions of higher-order bessel beams," OSA Frontiers in Optics, paper FThB6 (2009).

[3]. **A. Dudley,** M. Nock, T. Konrad, and A. Forbes, "Amplitude damping channel for orbital angular momentum," International Conference on Orbital Angular Momentum, paper P10 (2010).

[4]. **A. Dudley**, M. Nock, T. Konrad, F. S. Roux, and A. Forbes, "Mimicking an amplitude damping channel for Laguerre Gaussian modes," OSA Frontiers in Optics, paper JWA58 (2010).

[5]. **A. Dudley**, I. A. Litvin, and A. Forbes, "Measuring the orbital angular momentum density for a superposition of Bessel beams," OSA Frontiers in Optics, paper FThG7 (2011).

National Conference Papers:

[1]. **A. Dudley**, R. Vasilyeu, V. Belyi, N. Khilo, P. Ropot, and A. Forbes, "Superpositions of higher order Bessel beams and nondiffracting speckle fields," 55th South African Institute of Physics conference (2009).

[2]. **A. Dudley**, R. Vasilyeu, V. Belyi, N. Khilo, P. Ropot, and A. Forbes, "Experimental generation and application of the superposition of higher-order Bessel beams," 55th South African Institute of Physics conference (2009).

[3]. **A. Dudley**, M. Nock, T. Konrad, F. S. Roux, and A. Forbes, "Amplitude damping of vortex modes," 56th South African Institute of Physics conference (2010).

[4]. **A. Dudley**, R. Vasilyeu, V. Belyi, N. Khilo, P. Ropot, and A. Forbes, "Affects of binary and continuous phase modulations on the structure of Bessel beams," 56th South African Institute of Physics conference (2010).

[5]. R. Rop, **A. Dudley**, Y. Ismail, and A. Forbes, "Investigating the rotation rates of superimposed Bessel beams," 56th South African Institute of Physics conference (2010).

[6]. **A. Dudley**, M. Lavery, A. Forbes, and M. Padgett, "Stable interferometer for orbital angular momentum sorting," 57th South African Institute of Physics conference (2011).

Signed: ……

Table of Contents

List of Figures

tilting in the direction of the applied electric field, thus changing the refractive index of the liquid crystal pixel and consequently the phase of the incident wave.

Fig. 2.3.4. Photograph of the SLM, illustrating the diffraction orders due to the pixelation of the device. An intensity profile of the field, reflected from the liquid crystal display, is shown as an insert.

Fig. 2.3.5. (a) The computer-generated hologram addressed to the SLM so as to produce the NLC logo (f). (b) – (e) the grating which is placed over (a) so as to separate the first diffraction order from the zero diffraction order, illustrated in (g) – (j). The red arrow marks the undiffracted Gaussian spot.

Fig. 2.4.1. *Top row*: A series of computer-generated holograms, with increasing l (from left to right), with accompanying experimentally recorded vortex modes (*bottom row*). For the recording of the experimentally produced modes (*bottom row*) a blazed grating was used (this will be discussed in section 2.4.2).

Fig. 2.4.2 *Top row*: illustrates the mode (c) that is produced when a Gaussian beam (a) illuminates a spiral hologram (b). Adding a grating to the spiral hologram, as in the insert of (e), the undiffracted and diffracted components separate, as in the insert of (f).

Fig. 2.4.1.1. *Top row*: A mode produced by a displaced spiral hologram accompanied with a cross-sectional intensity profile (taken across the white dotted line). *Middle row*: Experimentally recorded (*top*) and theoretically calculated (*bottom*) intensity profiles for holograms displaced at a distance of 0.0 mm, 0.04 mm and 0.08 mm. *Bottom row*: Plot of the percentage of vortex mode present in the superposition, as a function of the displacement distance. The green curve is the theoretical result and the red dots are the measured data.

Fig. 2.4.2.1. *Left:* A blazed grating. *Right*: A cross-sectional profile of the blazed grating (taken across the red dotted line on the left).

Fig. 2.4.2.2. A series of blazed spiral holograms for l = -3 to 3.

with each row). The red ring denotes the ring-slit. *Column 4*: The corresponding experimentally recorded field at the Fourier plane.

Fig. 5.3.2. *Column 1*: Ring-slit holograms, where the phase modulation within the ring-slit is described by a continuous normal distribution (the frequency of the phase modulation increases with each row, (a) and (c) 10 pixels; (e) and (g) 50 pixels; (i) and (k) 100 pixels). The red ring denotes the ring-slit. *Column 2*: The corresponding experimentally recorded field in the Fourier plane. *Column 3*: Ring-slit holograms, where the phase modulation within the ring-slit is described by a binary normal distribution (the frequency of the phase modulation increases with each row). The red ring denotes the ring-slit. *Column 4*: The corresponding experimentally recorded field in the Fourier plane.

Fig. 5.3.3. Graph of the standard deviation for each of the four distributions as a function of the frequency of the phase modulation (or correlation radius).

Fig. 5.3.4. Simulated images for the non-diffracting speckle field, for each of the four corresponding distributions. *Row 1*: continuous uniform. *Row 2*: binary uniform. *Row 3*: continuous normal. *Row 4*: binary normal. The standard deviation increases from left to right. The values for the standard deviation are given in the bottom right corner of each image.

Fig. 6.2.1. (a) A schematic of the generation of the optical field and the decomposition of its OAM spectrum. (b) The Gaussian beam used to illuminate the hologram, (c), for the generation of the optical field, (d), defined by $u(r,\theta,z)$. The hologram, having a transmission function of $t(r,\theta)$, in (e) together with the lens L_2 performs the decomposition (Eq. (6.2.10)), producing the inner-product, P, represented in (f) and mathematically defined by $u(\rho,\varphi,z)$. (SLM: spatial light modulator and O: objective – used to magnify the optical field (d)).

Fig. 6.3.1. A schematic of the experimental setup for measuring the OAM density as a function of the radial position, R. L: Lens (f_1 = 25 mm; f_2 = 150 mm; f_3 = 200 mm and f_4 = 200 mm); M: Mirror; LCD: Liquid Crystal Display; O: Objective; PM: Pop-up Mirror; CCD: CCD Camera. The objective, O_2, was placed at the Fourier plane of lens, L_4. The corresponding optical fields and holograms appear at the appropriate planes.

Fig. 6.3.2. The initial optical field was divided radially into individual ring-slits. The phase within the annular ring was varied azimuthally for various values of l. The rest of the LCD was

programmed with a checkerboard pattern so as to restrict the transmission function to the ring alone. The ten rings have the following radii: $r_1 = 600$ µm, $r_2 = 880$ µm, $r_3 = 1160$ µm, $r_4 = 1440$ µm, $r_5 = 1720$ µm, $r_6 = 2000$ µm, $r_7 = 2280$ µm, $r_8 = 2560$ µm, $r_9 = 2840$ µm and $r_{10} = 3120$ µm. The black and white images in rows 2 and 4 are grey-scale experimental images of the first optical field that we tested.

Fig. 6.4.1. *First column*: Holograms and the corresponding experimentally produced fields in the Fourier plane (*second column*) accompanied with theoretically calculated fields (*third column*). The white dots in (c) denoted the radial positions of each of the ten ring-slits used as the match-filters.

Fig. 6.4.2. The measured OAM spectrum of the field given in Fig. 6.4.1 (b), as a function of the radial ring (or radial position), given by numbers 1 to 10, for azimuthal phase values of $m = -4$ to 4. The height of each bar represents the measured coefficients $|a_m|^2$.

Fig. 6.4.3. (a) A density plot of the OAM density for the field given in Fig. 6.4.1 (b). Red denotes negative OAM and blue denotes positive. Light to dark blue denotes an increase in positive OAM and light to dark red denotes an increase in negative OAM. (b), (c) and (e) the OAM density for the fields in Fig. 6.4.1.(b), (e) and (h), respectively. The blue curve denotes the theoretical OAM density and the red points the experimentally measured OAM density. Inserts for density plots of the OAM density for (c) and (e) are given as inserts, (d) and (f), respectively.

Fig. 6.4.4. (a) The hologram used to generate the experimental field in (b). The theoretically calculated field is given in (c). A magnification of the ring-slit is given as an insert in (a). (d) The theoretical (blue curve) and experimentally measured (red points) OAM density. (e) A density plot of the OAM density. Red denotes negative OAM and blue denotes positive. Light to dark blue denotes an increase in positive OAM and light to dark red denotes an increase in negative OAM.

Fig. 6.4.5. (a) The hologram used to generate the experimental field given in (b) of which the theoretical field is represented in (c). A magnification of the ring-slit is given as an insert in (a). (d) The theoretical (blue curve) and experimentally measured (red points) OAM density. (e) A density plot of the OAM density. Red denotes negative OAM and blue denotes positive. Light

List of Symbols

θ: azimuthal angle

l: azimuthal mode index

m: azimuthal mode index

n: azimuthal mode index

p: radial mode index

Δm: charge of fork hologram

n: diffraction order

θ_B: blazed angle

$\hbar$: Plank's constant

$\vec{E}$: electric field

$\vec{B}$: magnetic field

ε_0: permittivity of free space

μ_0: permeability of free space

c: speed of light

z: propagation axis

k: wave-number

k_z: longitudinal wave-number

k_r: radial wave-number

ω_0: beam waist

z_R: Rayleigh range

u: complex-valued amplitude

A: complex-valued amplitude

I: intensity

J_l: Bessel function of order l

α: cone angle

φ: angle on complex plane

$\mathbf{A}$: vector on complex plane

ϕ: phase modulation

t: transmission function

$\Delta\varphi$: phase difference

β: relative angle between Dove prisms

A, B: output ports

$|\psi\rangle$: initial quantum state

ρ_S: final quantum state

M_0, M_1: Krauss operators

P: probability

γ_1: weighting of Gaussian mode

γ_2: weighting of vortex mode

Acknowledgements

I wish to express my sincere gratitude and appreciation to everyone who assisted and supported me throughout the course of this work. I would like to make special mention of the following people:

My supervisor, Prof. Andrew Forbes, for all the time and effort he spent in assisting me in my work. Thank you for being an inspirational mentor and for motivating me to pursue relevant research. During the course of my PhD, you have taught me to be a more methodical experimental researcher; an improved scientific writer; a better presenter of my work to a varied audience; as well as encouraging me to form networks with other researchers in my field.

I am very grateful to the CSIR National Laser Centre for allowing me the opportunity to conduct this research and for sourcing funding for me to visit laboratories overseas and gain invaluable experience.

This work has led me to work with many interesting researchers. At the CSIR National Laser Centre, I would like to thank Dr F. S. Roux for always assisting and guiding me with theoretical problems that I encountered. To Prof. Thomas Konrad, my co-supervisor, and Michael Nock, at the University of KwaZulu-Natal, thank you for all your input and fruitful discussions regarding the OAM amplitude damping channel. As well as a special thank you to Prof. Konrad for proofreading my thesis. To our collaborators in Minsk, Ruslan Vasilyeu, Prof. Vladimir Belyi, Prof. Nikolai Khilo and Dr Piotr Ropot, thank you for all your time and effort in making our joint work a success. I am very grateful to Prof. Miles Padgett for providing me the opportunity to spend some time with his group at the University of Glasgow and to Martin Lavery for our successful work on the robust interferometer.

To my fellow colleagues, Melanie, Darryl and Yaseera, thank you for all your help in the laboratory and for making the journey through my PhD less daunting and more entertaining.

I am so grateful to my family for their support and for encouraging me to further my studies. To my parents for teaching me to work diligently and with integrity. Finally, my husband, Jonathan, thank you for always taking an interest in my research and for providing endless support while I pursue my goals.

CHAPTER ONE

Orbital Angular Momentum of Light

1.1. Overview

The behaviour of a light beam is governed by Maxwell's equations, which form the foundation for the derivation of the Helmholtz wave equation [1]. Maxwell's formulation of electromagnetic theory also illustrates that an optical field can have an induced polarization, due to the field's electric flux density. The polarization of an optical field is associated with the field's spin angular momentum (SAM) and was predicted by Poynting, who introduced the analogy between circular polarization (a component of SAM) and a rotating object [2]. The first experimental demonstration of a circularly-polarized light beam transferring SAM to a quarter-wave plate, was performed by Beth in 1936 [3]. The orbital component of optical angular momentum, not associated with the polarization of an optical field but rather with its wavefront, was only discovered nearly 60 years later by Allen *et al*. They showed that Laguerre-Gaussian (LG) laser modes, having an azimuthal phase dependence, possess a well-defined orbital angular momentum (OAM) [4]. LG beams contain a phase singularity, around which the phase (or wavefront) of the field increases azimuthally, $\exp(il\theta)$, thus forming an optical vortex. Here l indicates the azimuthal mode index (or topological charge of the optical vortex) and θ is the azimuthal angle. The intensity profile of a LG beam appears as a 'ring' or 'donut', because the intensity vanishes at the point of the singularity (where the phase or wavefront is undefined), resulting in a dark core in the centre of the beam.

The discovery made by Allen *et al.* was not the first study into helically-phased beams and in fact they had been investigated for quite some time. Prior to 1992, no correlation to the beam's orbital angular momentum was made, but what was of interest to most, was that these helically-phased beams required a phase singularity (or optical vortex) to propagate as a dark core along the axis of the beam. Since the centre of the optical vortex possesses zero intensity, it makes sense that no one noted any angular momentum while studying only the phase singularity. If they had studied the light surrounding the singularity, they would have noted that it possesses OAM.

Investigations into singularities present in electromagnetic fields started in the 1970s with Nye and Berry. They first discovered that sound waves scattered off a rough surface produced intensity nulls around which the phase varied from 0 to 2π [5]. Later Nye and Berry discovered that phase singularities could also be produced by interfering multiple light beams [6]. Currently it is known that optical fields can be produced to contain multiple singularities, whose trajectories can form complex 3D shapes. Even though many investigations had been made into the formation and dynamics of optical vortices none noted that these optical vortices give rise to an angular momentum within the optical field (independent of the photon spin, associated with circular polarization).

Since the discovery that LG beams carry OAM of $l\hbar$ per photon [4, 7], numerous techniques for generating helically-phased beams have been realized. One of the earlier methods involved a diffractive optical element consisting of a diffraction grating with a fork dislocation [8]. When a fundamental Gaussian mode is centred on the fork dislocation, a helically-phased beam is produced as the output. Recently this diffractive optic has been encoded onto the liquid crystal display of a spatial light modulator (SLM) [9]. Although this method was available at the time of Allen *et al.*'s work, they made use of a telescope consisting of cylindrical lenses which transforms Hermite-Gaussian modes to LG modes [7]. Another approach which seems quite intuitive, is to pass a plane wave through an optical component which has a helical profile, so as to impart a helical structure into the phase profile of the beam. An optical element which is capable of such a transformation is a spiral phase plate (SPP) [10]. All of these methods will be discussed in chapter 2.

Helically-phased beams in the form of LG modes have opened up many new research areas in the field of optical angular momentum. Just as Beth was able to witness the transfer of SAM to a suspended quarter-wave plate, so a similar observation with the transfer of OAM to matter should also be noted. In a similar fashion to the quarter-wave plate, which is used to generate circularly polarized light, one would expect to witness a transfer of OAM to the cylindrical lens mode converter, however this has proved too technically challenging. Alternatively, the transfer of OAM to matter was demonstrated with the use of an optical tweezer, which involved a micrometer-sized graphite particle illuminated by a tightly focused LG beam [11]. Since this demonstration, the field of optical trapping and tweezing has expanded from investigating how a trapped birefringent particle changes the SAM of a beam, but leaves the OAM component unchanged [12] to changing the sign of the angular momentum in order to develop optically driven micro-machines [13].

Helically-phased modes, which possess OAM at the single photon level, have offered a quantum optical system with a multi-dimensional Hilbert space for the investigations of quantum entanglement. Quantum entanglement, which is realized through the use of parametric down conversion, involves measuring a parameter of one of the down converted photons providing information about the parameter of its entangled photon pair, even though the two photons are spatially separated. This is not only a natural consequence of conservation of momentum or energy, but also a demonstration of the Einstein, Podolosky, Rosen (EPR) paradox [14]. If one were to measure the position of the two entangled photons there would be strong quantum correlations between the measurements as the two photons are created at the same lateral position. If one wanted to measure the momentum of each photon, there too would be strong correlations between the measurements due to the conservation of momentum during the down conversion process. However, if the decision to measure either the position or momentum is made at the last minute, this requires that the other entangled photon has a well-defined position and momentum, which violates the uncertainty principle and validates the nonlocality of quantum mechanics. This has been demonstrated experimentally with position and momentum [15] and time and energy [16] and recently OAM [17]. Here it was shown that strong correlations are present in the OAM states of entangled photon pairs due to the conservation of momentum during the down conversion process. However, to demonstrate the EPR paradox they also showed strong correlations with a complementary basis: a superposition of LG and Gaussian modes.

Since these fields offer an infinite-dimensional state space they provide a larger bandwidth for quantum cryptography [18-20] leading to many publications being dedicated to the measurement of OAM in order for higher-dimensional quantum information processing to be a success. Just as the fork dislocation, when illuminated with a fundamental Gaussian mode, will produce a helically-phased beam, so the process also works in reverse: a helically-phased beam illuminating a fork dislocation will produce a Gaussian mode, which when coupled into a single mode fibre allows for detection [17]. Adaptations to the fork dislocation have been made so as to produce 2D detection grids [21, 22]. A recent measurement technique has involved transforming the azimuthal position in an input beam to a transverse position in the output beam which is then focused to a lateral position [23]. A device which maintains the helical structure of the beam is a Dove prism embedded Mach-Zehnder interferometer [24 -26]. By setting the angle between the two Dove prisms appropriately all the odd values of l will constructively

interfere at one output port, while all the even l values appear at other output. Some of these measurement techniques will be discussed in detail in chapter 2.

In this chapter, Maxwell's equations will be given, leading to the derivation of the paraxial approximation of the Helmholtz wave equation (section 1.2.). The paraxial approximation of the Helmholtz wave equation will be used as the basis for investigating phase-structured electromagnetic waves (section 1.3.). Once the link between optical wavefront and OAM has been made, particular solutions of the paraxial approximation of the Helmholtz wave equation will be discussed. We will first discuss Gaussian beams (section 1.4.) as this is the output of the laser system used in this work. They have a flat wavefront, corresponding to an OAM value of $l = 0$, and are often used as the initial beam in most optical setups for generating beams which carry OAM. Two other modes which will be discussed are LG (section 1.5.) and Bessel beams (section 1.6.), as they each carry an OAM of $l\hbar$ per photon and are the two modes implemented in this thesis. Other beams which have an azimuthal angular dependence of $\exp(il\theta)$ do exist, such as Mathieu and Airy beams, but as we have not applied them in this work, they will not be considered here.

1.2. Maxwell's equations and the paraxial approximation of the Helmholtz wave equation

The derivation of the paraxial Helmholtz wave equation begins with Maxwell's equations in a vacuum, defined as

$$\nabla \cdot \vec{E} = 0, \tag{1.2.1}$$

$$\nabla \cdot \vec{B} = 0, \tag{1.2.2}$$

$$\nabla \times \vec{E} = -\frac{\partial \vec{B}}{\partial t}, \tag{1.2.3}$$

$$\nabla \times \vec{B} = \varepsilon_0 \mu_0 \frac{\partial \vec{E}}{\partial t}. \tag{1.2.4}$$

ε_0 and μ_0 are the permittivity and the permeability of free space, respectively and are related to the speed of light in a vacuum, c, as follows $c = 1/\sqrt{\mu_0 \varepsilon_0}$.

The wave equation is obtained by taking the curl of Faraday's law of induction (Eq. (1.2.3)) and making use of the vector identity $\nabla\times\left(\nabla\times\vec{E}\right)=\nabla(\nabla\cdot\vec{E})-\nabla^2\vec{E}$,

$$\nabla\times\left(\nabla\times\vec{E}\right)=-\frac{\partial\left(\nabla\times\vec{B}\right)}{\partial t}\Rightarrow\nabla\left(\nabla\cdot\vec{E}\right)-\nabla^2\vec{E}=-\frac{\partial\left(\nabla\times\vec{B}\right)}{\partial t}. \tag{1.2.5}$$

Substituting Eqs (1.2.1) and (1.2.4) into the above equation, yields the wave equation

$$-\nabla^2\vec{E}=-\frac{\partial\left(\varepsilon_0\mu_0\dfrac{\partial\vec{E}}{\partial t}\right)}{\partial t}\Rightarrow\nabla^2\vec{E}=\varepsilon_0\mu_0\frac{\partial^2\vec{E}}{\partial t^2} \tag{1.2.6}$$

$$\nabla^2\vec{E}-\frac{1}{c^2}\frac{\partial^2\vec{E}}{\partial t^2}=0. \tag{1.2.7}$$

The Helmholtz wave equation, which is the time-independent form of the wave equation (Eq. (1.2.7)), is obtained by performing separation of variables on the electric field, so as to remove the time-dependent component. The electric field (or wave function) $\vec{E}(x,y,z,t)$, can be separated into spatial ($A(x,y,z)$) and time ($T(t)$) domains

$$E(x,y,z,t)=A(x,y,z)T(t). \tag{1.2.8}$$

Substituting Eq. (1.2.8) into Eq. (1.2.7) results in

$$\begin{aligned}\nabla^2\left(A(x,y,z)T(t)\right)-\frac{1}{c^2}\frac{\partial^2\left(A(x,y,z)T(t)\right)}{\partial t^2}&=T(t)\nabla^2A(x,y,z)-\frac{A(x,y,z)}{c^2}\frac{\partial^2T(t)}{\partial t^2}=0\\ T(t)\nabla^2A(x,y,z)=\frac{A(x,y,z)}{c^2}\frac{\partial^2T(t)}{\partial t^2}&\Rightarrow\frac{\nabla^2A(x,y,z)}{A(x,y,z)}=\frac{1}{c^2T(t)}\frac{\partial^2T(t)}{\partial t^2}\end{aligned} \tag{1.2.9}$$

$$\frac{\nabla^2A(x,y,z)}{A(x,y,z)}=\frac{1}{c^2T(t)}\frac{\partial^2T(t)}{\partial t^2}. \tag{1.2.10}$$

In order for the above equation to hold true, both sides, left and right, need to be equal to the same constant, $-k^2$ (chosen only for convenience in the resulting solution)

$$\frac{\nabla^2A(x,y,z)}{A(x,y,z)}=-k^2 \tag{1.2.11}$$

and

$$\frac{1}{c^2 T(t)}\frac{\partial^2 T(t)}{\partial t^2} = -k^2. \tag{1.2.12}$$

Rearranging Eq. (1.2.11) results in

$$\nabla^2 A(x, y, z) + k^2 A(x, y, z) = \left(\nabla^2 + k^2\right) A(x, y, z) = 0, \tag{1.2.13}$$

which is the Helmholtz wave equation, where k is the wave-vector and is defined as $k = \omega/c$ or $k = 2\pi/\lambda$.

Within the paraxial approximation, the complex magnitude of the electric field becomes

$$E(x, y, z) = u(x, y, z)\exp(ikz), \tag{1.2.14}$$

where u is the complex-valued amplitude which modulates the sinusoidal plane, $\exp(ikz)$, and z is the axis of propagation. Substituting the above form for the electric field (Eq. (1.2.14)) into the Helmholtz wave equation (Eq. 1.2.13)), yields

$$\nabla^2\left(u(x, y, z)\exp(ikz)\right) + k^2 u(x, y, z)\exp(ikz) = 0$$

$$\exp(ikz)\left(\frac{\partial^2 u(x, y, z)}{\partial x^2} + \frac{\partial^2 u(x, y, z)}{\partial y^2}\right) + \frac{\partial^2 u(x, y, z)\exp(ikz)}{\partial z^2} + k^2 u(x, y, z)\exp(ikz) = 0$$

$$\exp(ikz)\left(\frac{\partial^2}{\partial x^2} + \frac{\partial^2}{\partial y^2}\right)u(x, y, z) + \exp(ikz)\left(\frac{\partial^2}{\partial z^2} + 2ik\frac{\partial}{\partial z} - k^2\right)u(x, y, z) + k^2 u(x, y, z)\exp(ikz) = 0$$

$$\left(\frac{\partial^2}{\partial x^2} + \frac{\partial^2}{\partial y^2}\right)u(x, y, z) + \left(\frac{\partial^2}{\partial z^2} + 2ik\frac{\partial}{\partial z} - k^2\right)u(x, y, z) + k^2 u(x, y, z) = 0$$

$$\left(\frac{\partial^2}{\partial x^2} + \frac{\partial^2}{\partial y^2} + \frac{\partial^2}{\partial z^2}\right)u(x, y, z) + 2ik\frac{\partial u(x, y, z)}{\partial z} = 0. \tag{1.2.15}$$

Equation (1.2.15) is the Helmholtz equation, without the paraxial approximation. To approximate the above equation in the paraxial regime, the following condition which defines the paraxial approximation is implemented

$$\left|\frac{\partial^2 u(x,y,z)}{\partial z^2}\right| << k\left|\frac{\partial u(x,y,z)}{\partial z}\right|. \tag{1.2.16}$$

The paraxial approximation, described mathematically above, states that the longitudinal variation in the amplitude, $u(x,y,z)$, is small in comparison to the wavelength of the beam ($k = 2\pi/\lambda$). Or that the rate of change of the field in the z direction is small compared to the transverse direction. Therefore the third term in Eq. (1.2.15) is neglected, resulting in

$$\left(\frac{\partial^2}{\partial x^2}+\frac{\partial^2}{\partial y^2}\right)u(x,y,z)+2ik\frac{\partial u(x,y,z)}{\partial z}=0, \tag{1.2.17}$$

which is termed the paraxial approximation of the Helmholtz wave equation.

The paraxial approximation is used to describe laser beam propagation as the divergence angle of the beam is considered to be small. There exist many solutions to the paraxial Helmholtz wave equation (Eq. (1.2.17)), whose amplitude distribution, $u(x,y,z)$, is described by either a Gaussian, LG, Bessel, Airy (all having cylindrical symmetry) or Mathieu (having elliptic-cylindrical symmetry) functions. However, we will not discuss all of these solutions; instead we will focus on the solutions which have been implemented in this thesis, namely: Gaussian (section 1.4), Laguerre-Gaussian (section 1.5) and Bessel solutions (section 1.6).

1.3. Azimuthal phase dependent beams and their orbital angular momentum

Since this thesis is dedicated to individual fields carrying OAM and superpositions of these fields, we will (for the benefit of the reader) illustrate that light, having an amplitude distribution of the form $u(r,\varphi,z) = u_0(r,z)\exp(il\theta)$, will possess OAM. Determining the total angular momentum density for an optical field has been implemented previously in many publications [27-35]. In this derivation, we proceed in a similar fashion, by first calculating the Poynting vector for the beam to illustrate that the OAM density is proportional to l, the azimuthal mode index.

In order to obtain the Poynting vector, we will start with a vector potential in the Lorentz gauge. Since we are not concerned with SAM, we will consider only linearly polarized light and in

particular, we will consider the vector potential to be linearly polarized along the $\hat{x}$ direction [34]

$$\vec{A}(x, y, z) = u(x, y, z)\exp(i(kz - \omega t))\hat{x}. \tag{1.3.1}$$

From the vector potential, the components of the electric and magnetic fields in terms of the complex amplitude distribution, *u*, can be obtained

$$\vec{B}(x, y, z) = \nabla \times \vec{A}(x, y, z) = ik\exp(i(kz - \omega t))\left(u(x, y, z)\hat{y} + \frac{i}{k}\frac{\partial u(x, y, z)}{\partial y}\hat{z}\right) \tag{1.3.2}$$

and

$$\vec{E}(x, y, z) = \frac{ic^2}{\omega}\nabla \times \vec{B}(x, y, z) = i\omega\exp(i(kz - \omega t))\left(u(x, y, z)\hat{x} + \frac{i}{k}\frac{\partial u(x, y, z)}{\partial x}\hat{z}\right). \tag{1.3.3}$$

The derivatives of the field in the *z* direction have been neglected, as we are considering the paraxial limit.

The time-average Poynting vector, which gives the directional energy flux density, is determined as

$$\vec{S} = \left\langle \vec{S}_{real} \right\rangle = \varepsilon_0 c^2 \left\langle \vec{E}_{real} \times \vec{B}_{real} \right\rangle, \tag{1.3.4}$$

where the real components of the electric and magnetic fields are found to be

$$\vec{E}_{real} = \tfrac{1}{2}(\vec{E} + \vec{E}^*) \tag{1.3.5}$$

and

$$\vec{B}_{real} = \tfrac{1}{2}(\vec{B} + \vec{B}^*), \tag{1.3.6}$$

respectively. By substituting Eqs (1.3.2), (1.3.3), (1.3.5) and (1.3.6) into the equation for the time-averaged Poynting vector (Eq. (1.3.4)), the following result is obtained

$$\vec{S} = \varepsilon_0 c^2 \left\langle \vec{E}_{real} \times \vec{B}_{real} \right\rangle = \frac{\varepsilon_0 c^2}{4} \left(\vec{E} \times \vec{B}^* + \vec{E}^* \times \vec{B} \right) \tag{1.3.7}$$

$$\vec{S} = \frac{\varepsilon_0 \omega c^2}{4} \left(i\left(u \nabla u^* - u^* \nabla u \right) + 2k|u|^2 \hat{z} \right) \tag{1.3.8}$$

The gradient in the above expression only applies in the transverse directions, *x* and *y*.

The result for the Poynting vector, as described in Eq. (1.3.8), is now applied to a field (described in cylindrical coordinates) having an amplitude distribution of $u(r,\theta,z) = u_0(r,z)\exp(il\theta)$, resulting in each component of the Poynting vector being expressed as

$$S_r = 0, \tag{1.3.9}$$

$$S_\theta = \frac{l\omega\varepsilon_0 u_0^2}{2r}, \tag{1.3.10}$$

$$S_z = k\varepsilon_0 \omega u_0^2. \tag{1.3.11}$$

Here the radial component of the Poynting vector vanishes for the nondiffracting case, but is non-zero for a more general diffracting field. By implementing the following expression for the total angular momentum density

$$L_z = \frac{1}{c^2} \left(r \times S \right)_z, \tag{1.3.12}$$

and substituting in the components for the Poynting vector, as given in Eqs (1.3.9) to (1.3.11), we obtain the total angular momentum density to be

$$L_z = \frac{l\omega\varepsilon_0 u_0^2}{2c^2}. \tag{1.3.13}$$

Since, by definition the field has no SAM, the only angular momentum present in the field is OAM. From Eq. (1.3.13), we see that the OAM density of the beam is well-defined and

proportional to the integer l, which arises from the azimuthal phase dependence, $\exp(il\theta)$, of the amplitude distribution.

1.4. Gaussian beams

The first solution to the paraxial Helmholtz wave equation, that we will consider, is the Gaussian beam. This is the fundamental mode that we will use in the laboratory to generate beams having an azimuthal phase dependence in their amplitude distribution. The complete expression for the amplitude of the Gaussian beam is

$$u(r,z) = \frac{\omega_0}{\omega(z)} \exp\left(\frac{-r^2}{\omega^2(z)}\right) \exp\left(-ik\frac{r^2}{2R(z)} - i\Phi(z)\right), \tag{1.4.1}$$

where ω_0 is the minimum beam radius and the expressions for the radius of curvature, $R(z)$, beam radius, $\omega(z)$, and Gouy phase $\Phi(z)$ are given as

$$R(z) = z\left(1 + \frac{z_R^2}{z^2}\right), \tag{1.4.2}$$

$$\omega^2(z) = \omega_0^2\left(1 + \frac{z^2}{z_R^2}\right), \tag{1.4.3}$$

and

$$\Phi(z) = \tan^{-1}\left(\frac{z_R}{z}\right). \tag{1.4.4}$$

$z_R = \frac{\pi\omega_0^2}{\lambda}$ is termed the Rayleigh range and gives a measure as to how quickly a beam will diverge. If z_R is short, the beam will diverge quickly and if it is long, the beam will diverge slowly.

The optical intensity can be found by making use of the following relationship $I(r,z) = |u(r,z)|^2$,

$$I(r,z)=\left(\frac{\omega_0}{\omega(z)}\right)^2\exp\left(\frac{-2r^2}{\omega^2(z)}\right). \tag{1.4.5}$$

The intensity has a Gaussian distribution, with the peak occurring at r = 0 and decreasing monotonically with an increase in r, evident in Fig. 1.4.1 (a).

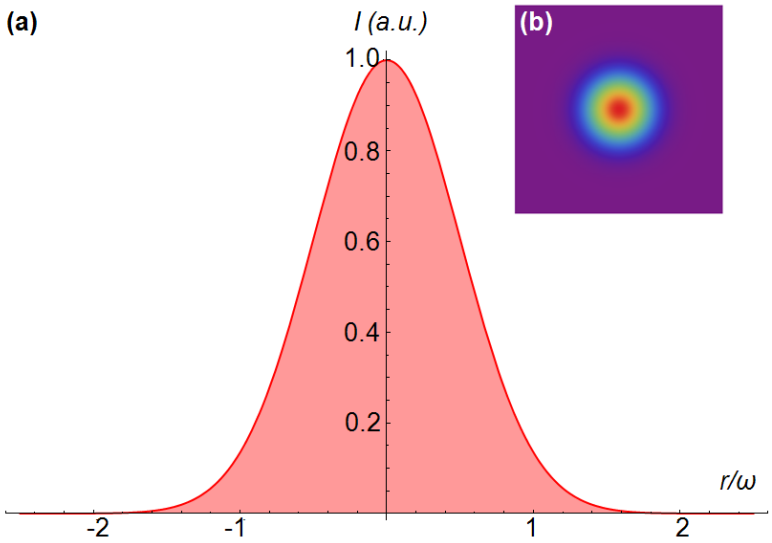

Fig. 1.4.1. (a) Cross-sectional profile and (b) transverse profile of the intensity of a Gaussian beam.

1.5. Laguerre-Gaussian beams

The previously discussed Gaussian mode is not the only solution to the paraxial approximation of the Helmholtz wave equation and in fact there exist many other solutions, such as the Laguerre-Gaussian (LG) mode, whose amplitude distribution is

$$u_{l,p}(r,\theta,z)=\frac{1}{\omega(z)}\sqrt{\frac{2p!}{\pi(|l|+p)!}}\left(\frac{\sqrt{2}r}{\omega(z)}\right)^{|l|}\exp\left(\frac{-r^2}{\omega(z)}\right)L_p^{|l|}\left(\frac{2r^2}{\omega^2(z)}\right)\exp\left(\frac{ikr^2}{2R(z)}\right)\exp(il\theta)\exp(-i\Phi(p,l,z)), \tag{1.5.1}$$

where $\Phi(p,l,z)$ is the Gouy phase for the LG mode and is given by

$$\Phi(p,l,z) = (2p + l + 1)\arctan\left(\frac{z}{z_R}\right). \tag{1.5.2}$$

The other parameters, such as $R(z)$ and $\omega(z)$, are defined as for the Gaussian beam, in Eqs (1.4.2) and (1.4.3), respectively. The LG modes are appropriately given their name as the expression is a mixture of a Laguerre polynomial and Gaussian parameters. A LG mode is described by the indices, l and p. If the indices are set to zero, $l = p = 0$, then the mode simplifies to a Gaussian mode.

A series of transverse intensity profiles for various values of l and p is depicted in Fig. 1.5.1. When $l \neq 0$ the intensity profile is described by a central null, whose radius increases with increasing $|l|$ and the radial index, p, denotes the number of concentric rings, given by $p + 1$. The cross-sectional intensity profile for two LG modes having the following indices $p = 0$, $l = 1$ and $p = 0$, $l = 2$ are given in Figs 1.5.2. and 1.5.3, respectively, to illustrate that the radius of the annular ring increases with $|l|$.

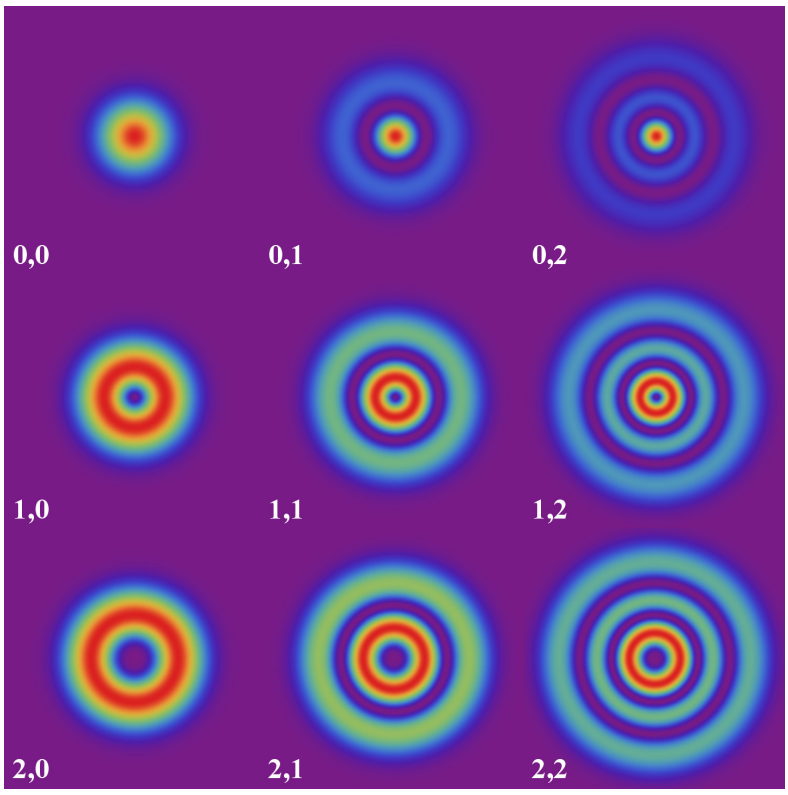

Fig. 1.5.1. Transverse intensity profiles of $LG_{l,p}$ modes. The corresponding indices, l and p, are given as inserts.

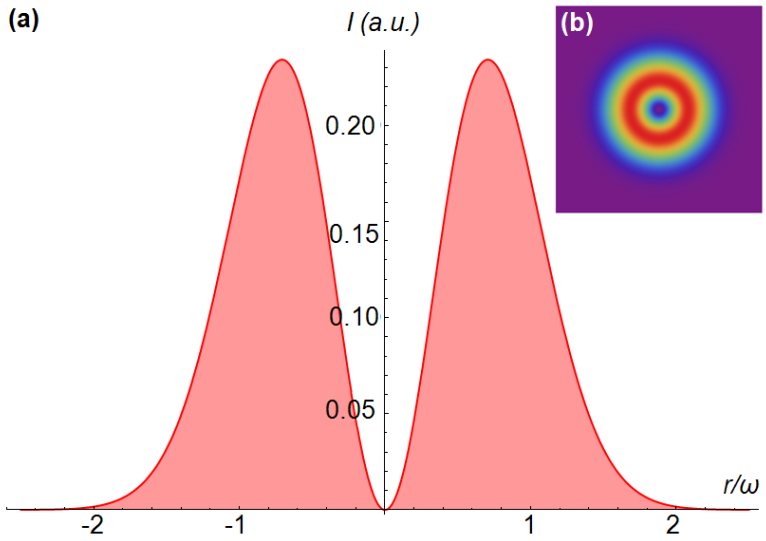

Fig. 1.5.2. (a) Cross-sectional profile and (b) transverse profile of the intensity of a $LG_{1,0}$ beam.

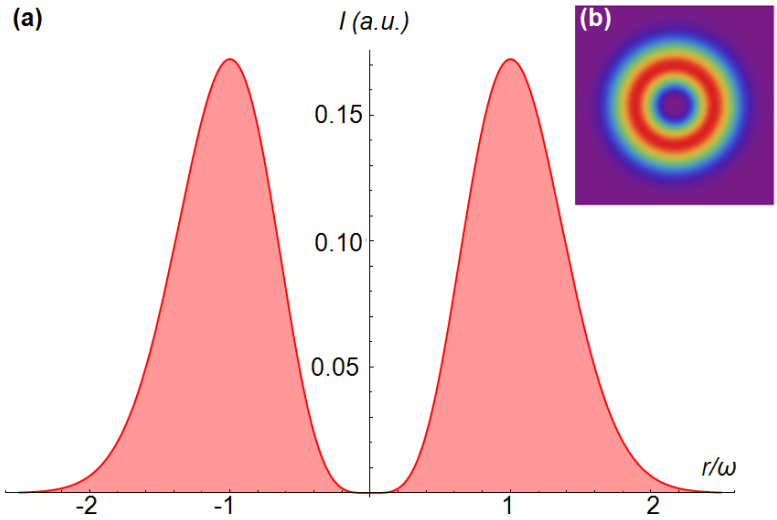

Fig. 1.5.3. (a) Cross-sectional profile and (b) transverse profile of the intensity of a $LG_{2,0}$ beam.

In this work, we choose to alter only the phase component of our initial Gaussian beam with a spatial light modulator (this technique will be discussed in detail in chapter 2), and so we are unable to generate true LG modes, such as that described in Eq. (1.5.1), and instead we generate an approximation, mathematically described as

$$u(r,\theta) = u_0(r)\exp(il\theta). \tag{1.5.3}$$

u is the amplitude distribution of the approximated LG mode, often termed an optical vortex; u_0 is the initial Gaussian amplitude distribution and $\exp(il\theta)$ is the azimuthally-varying phase factor, which gives rise to the OAM carried in the optical vortex.

When the mode index $l = 0$, no azimuthally-varying phase is imparted to the initial Gaussian beam, u_0, resulting in the beam remaining in its initial Gaussian state, having a spherical wavefront. As $|l|$ increases so the azimuthally-varying phase factor, $\exp(il\theta)$, converts the spherical wavefront, of the Gaussian beam, into a helical wavefront, where the number of spirals in the wavefront is given by $|l|$. The sign of l denotes the handedness of the spiral. A clockwise rotation can be assigned to a positive l and an anticlockwise rotation to a negative l.

The first row, in Fig. 1.5.4, contains a surface plot of the wavefront of different vortex modes. This too can be viewed as the phase profile, $\exp(il\theta)$, imparted to the initial Gaussian beam. A wavefront maps out a surface of points, in the wave, all possessing the same phase. The values for $|l|$ increase from left to right and are given as inserts in the first row. At the centre of each phase profile, it is evident that the phase is undefined. This manifests as a null in the intensity of the mode, which is evident in the middle row. The intensity profiles, given in the middle row, are calculated by implementing Eq. (1.5.3). Corresponding 3D plots of the wavefronts, for each mode, are given in the bottom row, illustrating that the mode index $|l|$ assigns the number of spirals in the wavefront and the sign of l its handedness.

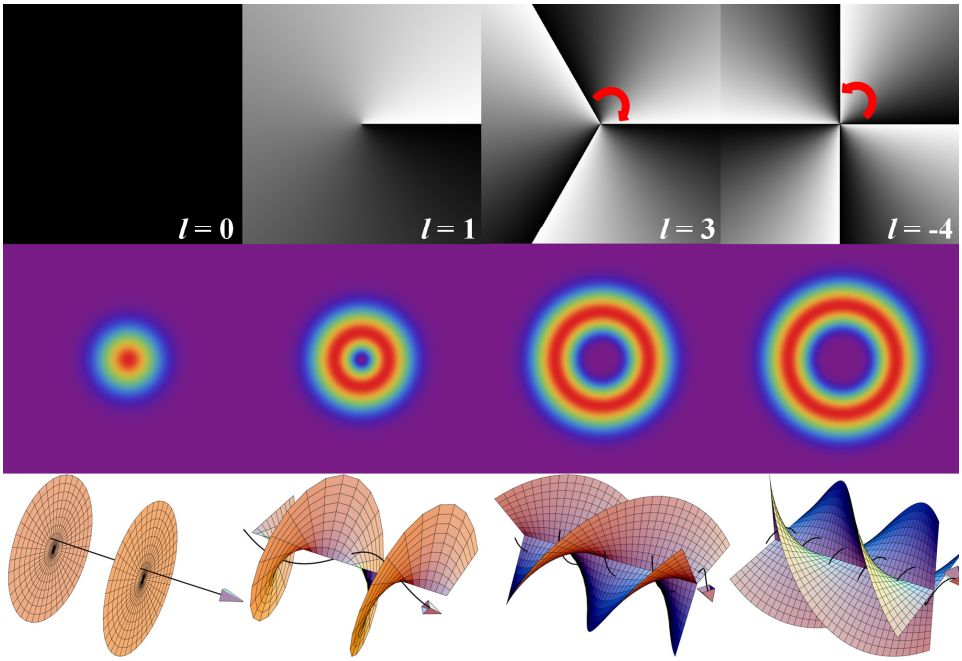

Fig. 1.5.4. *Top row*: Phase profiles for various vortex modes. The red arrow denotes the rotation in the phase profile. *Middle row*: Corresponding transverse intensity profiles for the various vortex modes. *Bottom row*: Corresponding wavefronts for the various vortex modes, courtesy of [36].

1.6. Bessel beams

Another solution to the Helmholtz wave equation, which we are interested in, for their non-diffracting nature and ability to carry OAM, are Bessel beams. It was Durnin [37] who first discovered a set of solutions for the free-space Helmholtz equation which are propagation-invariant and are mathematically described by Bessel functions. Mathematically, these solutions consist of an infinite number of concentric rings, existing over an infinite area, resulting in the beam carrying an infinite amount of power. Since this is not physically possible, the Bessel beam that is generated in the laboratory is an approximation – a Bessel-Gauss beam, whose field is described as

$$u[r,\theta,z] = A\frac{\omega_0}{\omega(z)}\exp\left[i\left(k-\frac{k_r^2}{2k}\right)z - i\Phi(z) + il\theta\right]J_l\left(k_r r/(iz/z_R)\right)\times\exp\left[\left(\frac{-1}{\omega^2(z)}+\frac{ik}{2R(z)}\right)\left(r^2+\frac{k_r^2 z^2}{k^2}\right)\right]. \tag{1.6.1}$$

A is an amplitude factor, J_l is the l^{th}-order Bessel function, k_r is the radial wave-vector and ω_0 is the initial beam waist. The parameters $\omega(z)$, z_R, $R(z)$ and $\Phi(z)$ have the same definition as for those presented in section 1.4. When the propagation distance, z, is zero, the field simplifies to a Bessel function enveloped by a Gaussian beam

$$u(r,\theta,0) = AJ_l(k_r r)\exp\left[-\left(\frac{r}{\omega_0}\right)^2 + il\theta\right]. \tag{1.6.2}$$

Both the zero-order and higher-order Bessel beams propagate over an extended distance in a diffraction free manner. To illustrate the visual distinction between a zero-order and a higher-order Bessel beam, an example of their cross-sectional and transverse intensity profiles appear in Figs 1.6.1 and 1.6.2, respectively.

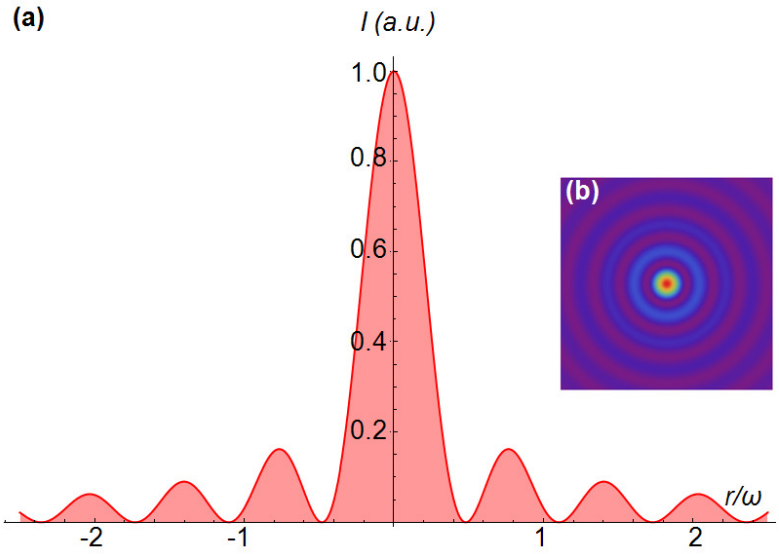

Fig. 1.6.1. (a) Cross-sectional profile and (b) transverse profile of the intensity of a zero-order Bessel beam.

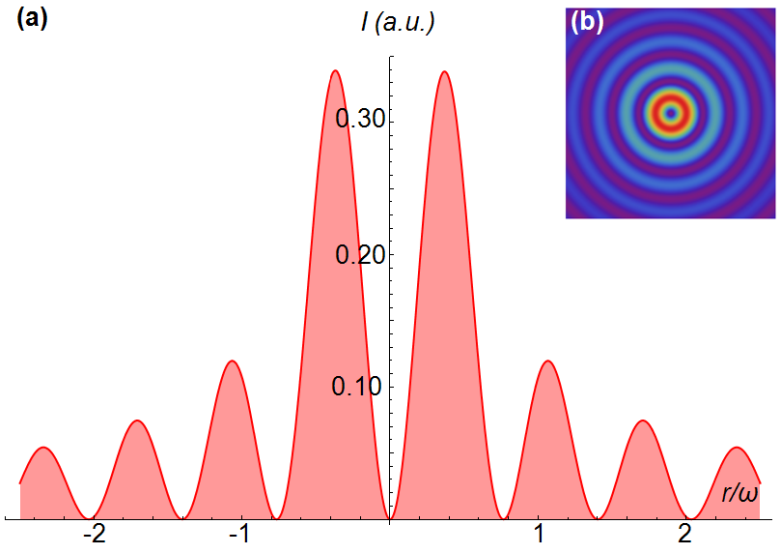

Fig. 1.6.2. (a) Cross-sectional profile and (b) transverse profile of the intensity of a higher-order ($l = 3$) Bessel beam.

The original method for generating zero-order Bessel beams was introduced by Durnin [38], when he illuminated a ring-slit aperture in the back focal plane of a lens with a plane wave. Since then, refractive optical elements, such as axicons [39-41] and diffractive optical elements such as computer generated holograms [42-47], have been used to generate both zero and higher-order Bessel beams. In chapter 3 we will illustrate how we generate superpositions of higher-order Bessel beams.

Another interesting property of these beams, apart from being non-diffracting, is they are self-reconstructing [48, 49], meaning they are able to reconstruct after encountering an obstacle. The light rays, forming a Bessel beam, propagate on a cone, so placing an obstacle in the path of the beam will cause some of the light to be obstructed but the light rays that are not blocked, will reconstruct to reform the Bessel beam.

1.7. Conclusion

We started the chapter with a literature review of optical OAM (section 1.1), followed by implementing Maxwell's equations to derive the paraxial approximation of the Helmholtz wave equation (section 1.2.). Since beams carrying a phase factor of $\exp(il\theta)$ are of particular importance in this thesis, due to the fact that they possess a well-defined OAM, it was shown in section 1.3 that this phase factor gives rise to OAM in the beam. Some solutions to the

Helmholtz wave equation, which are implemented in this thesis, such as Gaussian beams (section 1.4), LG beams (section 1.5) and Bessel beams (section 1.6) were defined.

1.8. References

[1]. J. C. Maxwell, "A treatise on electricity and magnetism," (Oxford: Clarendon Press) Art. 793 (1891).

[2]. J. H. Poynting, "The wave motion of a revolving shaft, and a suggestion as to the angular momentum in a beam of circularly polarized light," Proc. Roy. Soc. London A **82**(557), 560-567 (1909).

[3]. R. A. Beth, "Mechanical detection and measurement of the angular momentum of light," Phys. Rev **50**(2), 115-125 (1936).

[4]. L. Allen, M. W. Beijersbergen, R. J. C. Spreeuw, and J. P. Woerdman, "Orbital angular momentum of light and the transformation of Laguerre-Gaussian laser modes," Phys. Rev. A **45**(11), 8185-8189 (1992).

[5]. J. F. Nye and M. Berry, "Dislocations in wave trains," Proc. R. Soc. Lond. A **336**(1605), 165-190 (1974).

[6]. M. Berry, J. Nye, and F. Wright, "The elliptic umbilic diffraction catastrophe," Phil. Trans. R. Soc. Lond. **291**(1382), 453-484 (1979).

[7]. M. W. Beijersbergen, L. Allen, H. E. L. O. Van der Veen, and J. P. Woerdman, "Astigmatic laser mode converters and the transfer of orbital angular momentum," Opt. Commun. **96**(1-3), 123-132 (1993).

[8]. V. Yu Bazhenov, M. V. Vasnetsov, and M. S. Soskin, "Laser beams with screw dislocations in their wavefronts," JETP Lett. **52**(8), 429-431 (1990).

[9]. J. E. Curtis, B. A. Koss, and D. G. Grier, "Dynamic holographic optical tweezers," Opt. Commun. **207**(1-6), 169-175 (2002).

[10]. M. W. Beijersbergen, R. P. C. Coerwinkel, M. Kristensen, and J. P. Woerdman, "Helical-wave-front laser-beams produced with a spiral phaseplate," Opt. Commun. **112**(5-6), 321-327 (1994).

[11]. H. He, M. E. J. Friese, N. R. Heckenberg, and H. Rubinsztein-Dunlop, "Direct observation of transfer of angular momentum to absorptive particles from a laser beam with a phase singularity," Phys. Rev. Lett. **75**(5), 826-829 (1995).

[12]. M. Friese, T. Nieminen, N. R. Heckenberg, and H. Rubinsztein-Dunlop,
"Optical alignment and spinning of laser-trapped microscopic particles," Nature **394**, 348-350 (1998).

[13]. M. Friese, H. Rubinsztein-Dunlop, J. Gold, P. Hagberg, and D. Hanstorp, "Optically driven micromachine elements," Appl. Phys. Lett. **78**(4), 547-549 (2001).

[14]. A. Einstein, B. Podolsky, and N. Rosen, "Can quantum-mechanical description of physical reality be considered complete?" Phys. Rev. **47**(10), 777-780 (1935).

[15]. J. Howell, R. Bennink, S. Bentley, and R. Boyd, "Realization of the Einstein–Podolsky–Rosen paradox using momentum- and position entangled photons from spontaneous parametric down conversion," Phys. Rev. Lett. **92**(21), 210403 (2004).

[16]. P. G. Kwiat, A. Steinberg, and R. Chiao, "High-visibility interference in a Bell-inequality experiment for energy and time," Phys. Rev. A **47**(4), R2472-R2475 (1993).

[17]. A. Mair, A. Vaziri, G. Weihs, and A. Zeilinger, "Entanglement of the orbital angular momentum states of photons," Nature **412**, 313-316 (2001).

[18]. A. Vaziri, G. Weihs, and A. Zeilinger, "Experimental two-photon three-dimensional quantum entanglement," Phys. Rev. Lett. **89**(24), 240401 (2002).

[19]. J. T. Barreiro, T.-C. Wei, and P. G. Kwiat, "Beating the channel capacity limit for linear photonic superdense coding," Nature Phys. **4**, 282-286 (2008).

[20]. J. Leach, B. Jack, J. Romero, A. K. Jha, A. M. Yao, S. Franke-Arnold, D. Ireland, R. W. Boyd, S. M. Barnett, and M. J. Padgett, "Quantum correlations in optical angle-orbital angular momentum variables," Science **329**(5992), 662-665 (2010).

[21]. G. Gibson, J. Courtial, M. J. Padgett, M. Vasnetsov, V. Pas'ko, S. M. Barnett and S. Franke-Arnold, "Free-space information transfer using light beams carrying orbital angular momentum," Opt. Express **12**(22), 5448-5456 (2004).

[22]. S. N. Khonina, V. V. Kotlyar, R. V. Skidanov, V. A. Soifer, P. Laakkonen, and J. Turunen, "Gauss–Laguerre modes with different indices in prescribed diffraction orders of a diffractive phase element," Opt. Commun. **175**(4-6), 301-308 (2000).

[23]. G. C. G. Berkhout, M. P. J. Lavery, J. Courtial, M. W. Beijersbergen, and M. J. Padgett, "Efficient sorting of orbital angular momentum states of light," Phys. Rev. Lett. **105**(15), 153601 (2010).

[24]. J. Leach, M. J. Padgett, S. M. Barnett, S. Franke-Arnold, and J. Courtial, "Measuring the orbital angular momentum of a single photon," Phys. Rev. Lett. **88**(25), 257901 (2002).

[25]. M. Lavery, A. Dudley, A. Forbes, J. Courtial and M. Padgett, "Robust interferometer for the routing of light beams carrying orbital angular momentum," New J. of Phys. **13**(9), 093014 (2011).

[26]. C. Gao, X. Qi, Y. Liu, J. Xin, and L. Wang, "Sorting and detecting orbital angular momentum states by using a Dove prism embedded Mach–Zehnder interferometer and amplitude gratings," Opt. Commun. **284**(1), 48-51 (2011).

[27]. H. I. Sztul and R. R. Alfano, "The Poynting vector and angular momentum of Airy beams," Opt. Express **16**(13), 9411-9416 (2008).

[28]. K. Volke-Sepulveda, V. Garcés-Chávez, S. Chávez-Cerda, J. Arlt, and K. Dholakia, "Orbital angular momentum of high-order Bessel light beams," J. Opt. B Quantum Semiclassical Opt. **4**(2), S82-S89 (2002).

[29]. M. J. Padgett and L. Allen, "The Poynting vector in Laguerre-Gaussian laser modes," Opt. Commun. **121**(1-3), 36-40 (1995).

[30]. L. Allen and M. J. Padgett, "The Poynting vector in Laguerre-Gaussian beams and the interpretation of their angular momentum density," Opt. Commun. **184**(1-4), 67-71 (2000).

[31]. R. Zambrini and S. M. Barnett, "Angular momentum of multimode and polarization patterns," Opt. Express **15**(23), 15214-15227 (2007).

[32]. A. T. O'Neil, I. MacVicar, L. Allen, and M. J. Padgett, "Intrinsic and extrinsic nature of the orbital angular momentum of a light beam," Phys. Rev. Lett. **88**(5), 053601 (2002).

[33]. M. V. Berry, "Paraxial beams of spinning light," Proc. SPIE **3487**, 6-11 (1998). doi: 10.1117/12.317704.

[34]. L. W. Davis, "Theory of electromagnetic beams," Phys. Rev. A **19**(3), 1177-1179 (2003).

[35]. L. Allen, M. J. Padgett, and M. Babiker, "The orbital angular momentum of light," Prog. in Opt. **39**, 291-372 (1999).

[36]. Downloaded from Optics Group at Glasgow University: www.physics.gla.ac.uk/Optics/play/photonOAM/morePictures/

[37]. J. Durnin, "Exact solutions for nondiffracting beams. I. The scalar theory," J. Opt. Soc. Am. A **4**(4), 651-654 (1987).

[38]. J. Durnin, J. J. Miceli, Jr., and J. H. Eberly, "Diffraction-free beams," Phys. Rev. Lett. **58**(15), 1499-1501 (1987).

[39]. R. M. Herman, and T. A. Wiggins, "Production and uses of diffractionless beams," J. Opt. Soc. Am. A **8**(6), 932-942 (1991).

[40]. J. Arlt, and K. Dholakia, "Generation of high-order Bessel beams by use of an axicon," Opt. Commun. **177**(1-6), 297-301 (2000).

[41]. J. H. McLeod, "The axicon: a new type of optical element," J. Opt. Soc. Am. **44**(8), 592-597 (1954).

[42]. J. Turunen, A. Vasara, and A. T. Friberg, "Holographic generation of diffraction-free beams," Appl. Opt. **27**(19), 3959-3962 (1988).

[43]. A. Vasara, J. Turunen, and A. T. Friberg, "Realization of general nondiffracting beams with computer-generated holograms," J. Opt. Soc. Am. A **6**(11), 1748-1754 (1989).

[44]. J. A. Davis, E. Carcole, and D. M. Cottrell, "Nondiffracting interference patterns generated with programmable spatial light modulators," Appl. Opt. **35**(4), 599-602 (1996).

[45]. J. A. Davis, E. Carcole, and D. M. Cottrell, "Intensity and phase measurements of nondiffracting beams generated with a magneto-optic spatial light modulator," Appl. Opt. **35**(4), 593-598 (1996).

[46]. C. Paterson, and R. Smith, "Higher-order Bessel waves produced by axicon-type computer-generated holograms," Opt. Commun. **124**(1-2), 121-130 (1996).

[47]. D. McGloin, G. C. Spalding, H. Melville, W. Sibbett, and K. Dholakia, "Three-dimensional arrays of optical bottles," Opt. Commun. **225**(4-6), 215-222 (2003).

[48]. R.P. MacDonald, S.A. Boothroyd, T. Okamoto, J. Chrostowski, and B. A Syrett, "Interboard optical data distribution by Bessel beam shadowing," Opt. Commun. **122**(4-6), 169-177 (1996).

[49]. Z. Bouchal, J. Wagner, and M. Chlup, "Self-reconstruction of a distorted nondiffracting beam," Opt. Commun. **151**(4-6), 207-211 (1998).

CHAPTER TWO

Components to Manipulate Orbital Angular Momentum

2.1. Introduction

Since the discovery that photons in helically-phased light beams have a quantized OAM [1, 2], researchers have developed techniques to efficiently generate light beams which carry OAM, be it either a true LG mode or an optical vortex. The generation of such modes has advanced from cylindrical lens mode converters [1] to spiral phase plates (SPP) [3] and the widely-used fork hologram [4]. The fork holograms, previously only generated in the form of computer generated holograms, printed on transparent-film, are now reproduced with a liquid crystal device: a spatial light modulator (SLM) [5].

Apart from being able to generate beams which carry OAM, there is also a great need to be able to measure the amount of OAM present in an optical field. The need for measurement techniques has arisen as a means for higher-dimensional quantum information processing, for example quantum cryptography [6 – 8], to be a success. Currently, many techniques exist in the area of measuring OAM, ranging from computer-generated holograms [9-12] to interferometers [13-15]. The fork hologram, which when illuminated with the output mode from a laser, or single-mode fiber, produces the required OAM state in the first-diffraction order. This can also be used in reverse to couple light of a particular OAM state into a single-mode fibre [9]. However, taking advantage of the large state-space offered by OAM requires that at any given time one must test for all possible states, and in the case of the fork hologram, one can only test for the OAM state that is encoded in the fork hologram. Attempts to develop more complicated holograms which test multiple states have been made [10, 11], however their efficiency is inversely proportional to the number of states being tested. Recently it has been shown that two SLMs in conjunction with a lens can be used to convert the OAM state of light to a specific lateral position [12]. Even though this approach proved effective for the separation of eleven OAM states, it is limited in that the resulting spots slightly overlap. Other techniques have involved de-multiplexing free-space OAM beams [16], as well as investigating the diffraction patterns of beams carrying OAM [17]. In all of the previously mentioned measurement

techniques, the OAM mode is altered during the measurement procedure. An alternative setup which does not alter the OAM state during the measurement procedure, is a Mach-Zehnder interferometer with two Dove prisms in each arm [13], which sorts odd and even OAM states into two separate ports.

All of the above mentioned techniques to generate optical OAM will be discussed in this chapter. We will first look at how holograms, and in particular digital holograms, are used to generate, as well as detect, vortex modes. Due to the fact that one can easily compute the digital hologram one wishes to create, this is the only technique that we implement in this work. The other two methods for generating vortex modes, SPPs and cylindrical lens mode converters, although not executed experimentally in this work, will be outlined in sections 2.6 and 2.7, respectively. The only other technique for measuring OAM modes that will be discussed in this chapter is the Dove-prism embedded Mach-Zehnder interferometer. The concept behind this device will be outlined in section 2.8. This interferometer is known to be very unstable and in section 2.9, we present a new arrangement for a robust "odd-even OAM sorter" [14]. In the following chapter, chapter 3, we will implement the Dove-prism embedded Mach-Zehnder interferometer to mimic an amplitude damping channel for OAM modes [18].

2.2. Digital holography

Before discussing the technique of digital holography, it makes sense to first introduce the principle behind conventional holography. A schematic illustrating the process behind conventional holography is given in Fig. 2.2.1. Conventional holography involves creating a hologram by illuminating an object with a laser beam [19]. The interference pattern that is obtained between the object beam and the reference beam is recorded onto photographic film and is termed a hologram. By reversing the process and illuminating the hologram (or interference pattern) with the initial reference beam (at the same angle of incidence as when producing the hologram), the object beam is reconstructed.

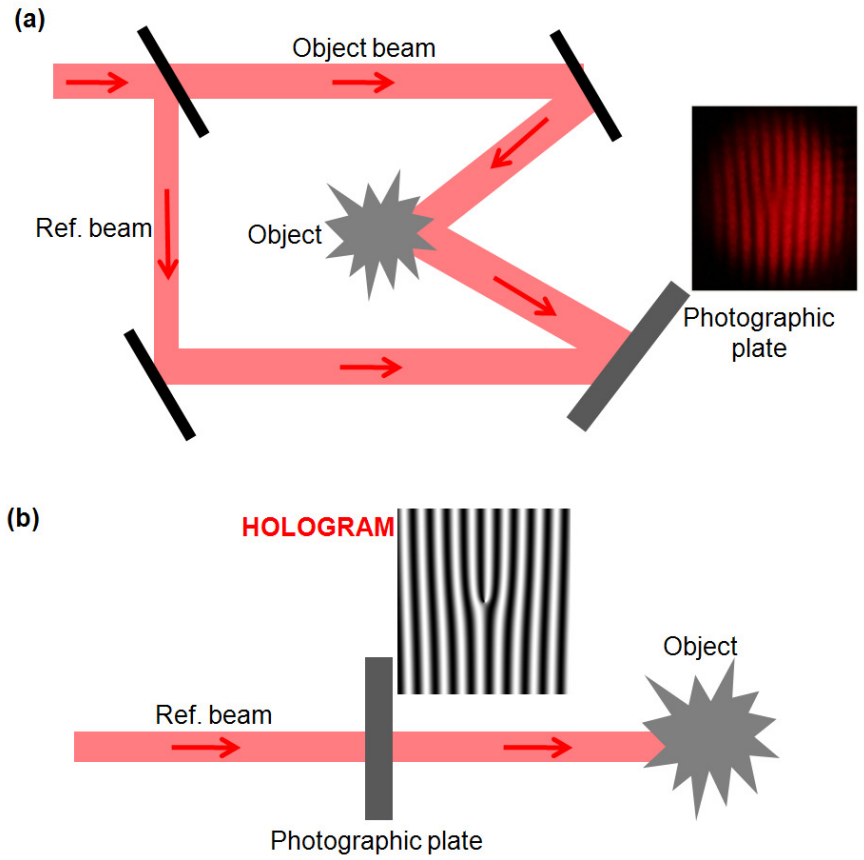

Fig. 2.2.1. Schematic illustrating the principle behind how (a) a hologram is constructed and (b) then used to form the desired object beam.

In the case of digital holography one does not need the object beam to physically exist. If the interference pattern between the reference beam and the object we wish to reconstruct can be mathematically formulated, the interference pattern can be computed and is often referred to as a computer-generated hologram. The computer-generated hologram can then be printed onto photographic film, thus resorting back to the early holography techniques. However, with the innovation of liquid crystal devices, these computer-generated holograms can be implemented digitally. The advantage in this technology is that no physical printing of the hologram is required. Instead a calculated hologram is electronically addressed to a liquid-crystal display (much like displaying an image on a computer screen), which allows a single liquid crystal display to be re-used for many different holograms, resulting in no re-alignment of the optical setup when a hologram is changed.

2.3. Spatial light modulators

A device which implements liquid crystal technology for the construction of digital holograms is a spatial light modulator (SLM). It is suitably given its name because it modulates the phase (and in some cases the amplitude) of an incident beam. The SLM that we utilize in this work is a HoloEye PLUTO VIS SLM. It is a phase-only device and we use it to alter only the phase structure of our reference beam. This device can also be used to perform amplitude modulation, which will be discussed in chapter 4.

A photograph of one of our SLMs appears in Fig. 2.3.1. It consists of a liquid crystal display which is programmed and addressed by a circuit board via a flex-cable. Mathematically, a grey-scale interference pattern between our reference beam and the object beam that we wish to reconstruct is computed and programmed onto the SLM, where we are able to modulate the phase of our reference beam. The phase of the reference beam is altered according to the shade of grey present at each pixel of the computer-generated hologram.

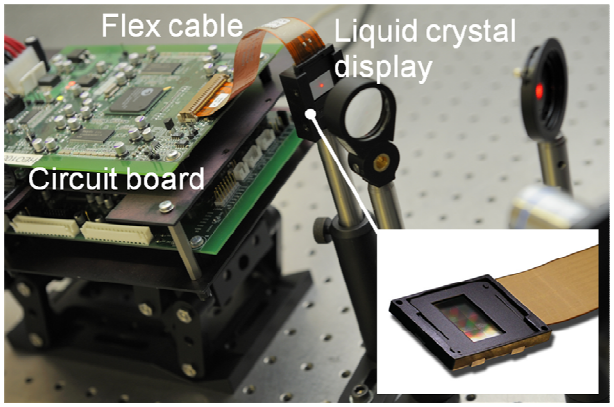

Fig. 2.3.1. Photograph of a HoloEye SLM, marking the circuit board, flex-cable and liquid crystal display (of which an enlarged view is contained as an insert in the bottom right corner).

The liquid crystal display is the crucial component of the SLM and (in our case) it consists of 1920×1080 pixels each having a dimension of 8 μm. The mechanism of the display is based on electrically controlled birefringence. Each pixel is addressed by two electrodes and the molecules making up the pixels are aligned parallel to the electrodes, as in Fig. 2.3.2. When the electrodes are applied with an electric field, the molecules are forced to tilt in the direction of the electric field.

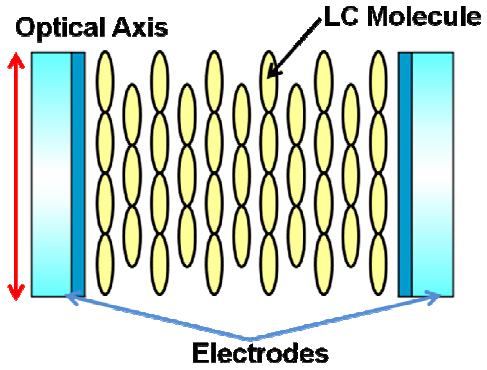

Fig. 2.3.2. Representation of an individual pixel in the liquid crystal display.

The grey-scale holograms are represented with 256 grey levels and the voltages across each pixel are adjusted appropriately according to the shade of grey present at each pixel in the hologram. This is depicted in Fig. 2.3.3, where black, representing no phase modulation, requires no voltage to be addressed to the electrodes. Increasing the phase modulation (or grey-level) involves increasing the voltage applied across the pixels. When no voltage is applied across the pixel, the molecules remain aligned parallel to the electrodes. As the voltage increases the molecules tilt further away from their initial orientation.

The incident light needs to be linearly polarized, parallel to the axis of the liquid crystal molecules (i.e. vertically polarized). When the molecules tilt in the direction of the applied electric field, the refractive index seen by the light changes accordingly and consequently so does its phase, evident from the following relationship

$$\delta = \frac{2\pi}{\lambda} dn. \tag{2.3.1}$$

δ represents the phase-shift experienced by the beam; λ is the wavelength of the incident beam; d is the optical path length in the liquid crystal pixel and n is the refractive index of the liquid crystal pixel, which is proportional to the voltage applied across the electrodes.

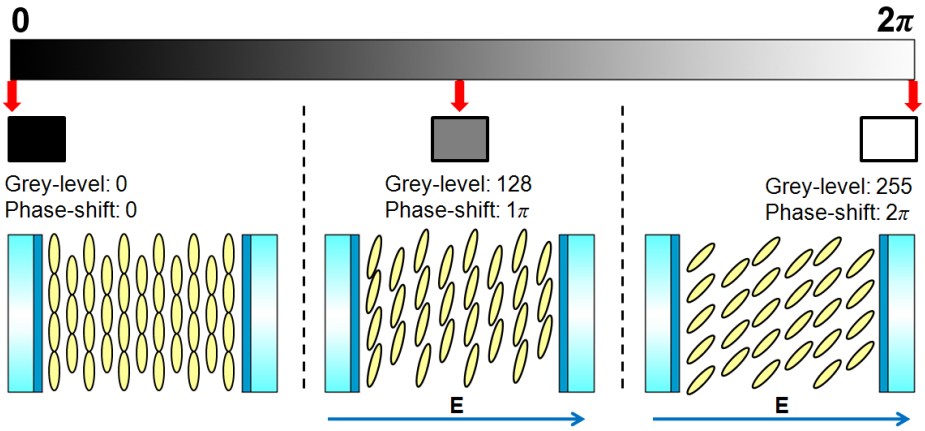

Fig. 2.3.3. A schematic, illustrating that the grey value present in the hologram is translated into an electric field applied across an array of liquid crystal molecules. This results in the molecules tilting in the direction of the applied electric field, thus changing the refractive index of the liquid crystal pixel and consequently the phase of the incident wave.

From Eq. (2.3.1) it is evident that the phase modulation is dependent on the wavelength of the incident light. For example, if one requires a grey-level of 128 to represent a 1π phase shift, then the voltage required to produce this phase shift for a wavelength of 633 nm will differ from that required for 534 nm. It is for this reason that the user needs to adapt the electro-optical response of the SLM when switching between different laser sources. The calibration procedure for optimizing the SLM at a particular wavelength is outlined in appendix A1.

Although SLMs are extremely versatile, they are not free of efficiency problems. The major concern is that not all of the incident light is diffracted to produce the desired object beam. This is due to (1) the structure of the liquid crystal display and (2) the diffraction efficiency of the device.

The liquid crystal display consists of a 2D array of pixels, where the spacing between the pixels cause the device to operate as a 2D grating, resulting in the light being diffracted into many orders. Figure 2.3.4 contains a photograph of the SLM, while it is not addressed with a computer-generated hologram, illustrating how the grid structure of the pixels produces many diffraction orders. This is also evident in the intensity profile of the field reflected from the SLM (contained as an insert in Fig. 2.3.4). The other orders, surrounding the bright central spot are additional diffraction spots from the 2D grating structure. When the incoming light is incident on a non-pixel (i.e. a space between pixels) the light is lost and not reflected. This is referred to as the ‘fill factor’, which means that a certain portion of the area of the liquid crystal

display is covered by pixels while the remaining area by non pixels. This also contributes to the efficiency problems.

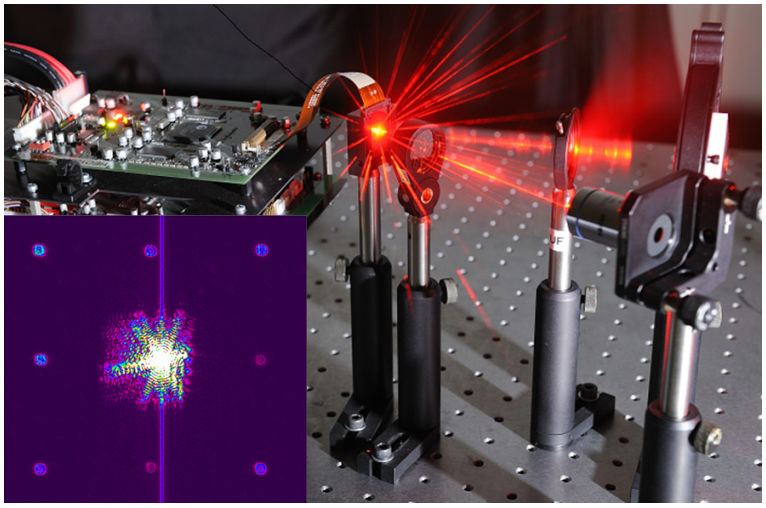

Fig. 2.3.4. Photograph of the SLM, illustrating the diffraction orders due to the pixelation of the device. An intensity profile of the field, reflected from the liquid crystal display, is shown as an insert.

The second issue is that the liquid crystal device is unable to diffract the entire incident beam into the required object beam. These devices are known to have a less than perfect diffraction efficiency, and in the case of the HoloEye SLM, it has a diffraction efficiency of 80%. This means that 80% of the incident beam will be diffracted into the required object mode, while the remaining 20% will consist of the undiffracted incident beam. The field reflected from the liquid crystal display will consist of a superposition of diffracted object beam and undiffracted reference beam, which will give rise to a reduction in the quality of the required mode. To overcome this issue, a grating is placed on top of the computer-generated hologram so as to separate the diffracted object beam (the first order) from undiffracted reference beam (the zero order).

To illustrate this, first ignore all the other orders which are introduced due to the pixelation of the display and consider only the centre on-axis order. Figure 2.3.5 contains an example where a computer-generated hologram is used to generate our institute's logo (NLC), when it is illuminated by a Gaussian beam. When the display contains only the computer-generated hologram, a Gaussian spot appears in the centre of the object beam. This is the portion of the incident reference Gaussian beam which has not been diffracted. To separate the diffracted and

undiffracted components a grating is placed over the computer-generated hologram. This is illustrated in columns 2 to 5 of Fig. 2.3.5. By decreasing the grating spacing, the diffracted and undiffracted components are separated farther apart. It is the diffracted component (the NLC logo) that moves farther away from the undiffracted stationary Gaussian component.

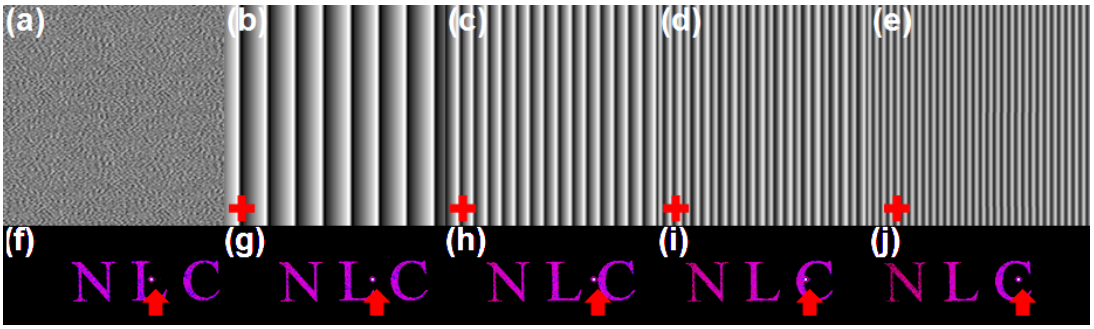

Fig. 2.3.5. (a) The computer-generated hologram addressed to the SLM so as to produce the NLC logo (f). (b) – (e) the grating which is placed over (a) so as to separate the first diffraction order from the zero diffraction order, illustrated in (g) – (j). The red arrow marks the undiffracted Gaussian spot.

Since a basic understanding of how a SLM works has been given we will move onto the computer-generated holograms that are produced, so as to realize vortex modes in the laboratory. The two types of holograms that will be discussed are termed spiral and fork holograms and the choice for their names will become evident in sections 2.4 and 2.5.

2.4. Spiral holograms

The mode which we are interested in creating is a vortex mode, whose amplitude distribution is mathematically described by Eq. (1.5.3). Therefore since we use a Gaussian beam as our initial reference beam, we need only generate a hologram which represents the following transmission function

$$t(\theta) = \exp(il\theta). \tag{2.4.1}$$

A variety of spiral holograms are given in Fig. 2.4.1, accompanied with experimentally produced vortex modes. As the number of times that the phase in the spiral hologram varies from 0 (black) to 2π (white), so the topological charge carried by the vortex mode increases.

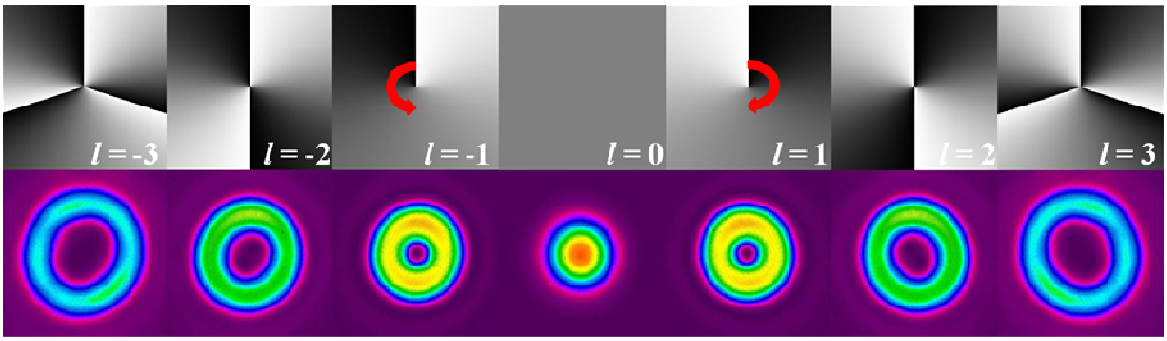

Fig. 2.4.1. *Top row*: A series of computer-generated holograms, with increasing *l* (from left to right), with accompanying experimentally recorded vortex modes (*bottom row*). For the recording of the experimentally produced modes (*bottom row*) a blazed grating was used (this will be discussed in section 2.4.2).

However, as with most computer-generated holograms, if a grating has not been introduced the vortex mode produced will consist of a mixture of the undiffracted Gaussian beam and the diffracted vortex mode. This results in *l* individual vortices (or singularities) each of a topological charge of one, existing in the final mode. This effect is illustrated in Fig. 2.4.2 (c). To overcome this problem, a grating is added to the hologram so as to spatially separate the undiffracted and diffracted components. In particular a blazed grating is used, which is discussed in section 2.4.2.

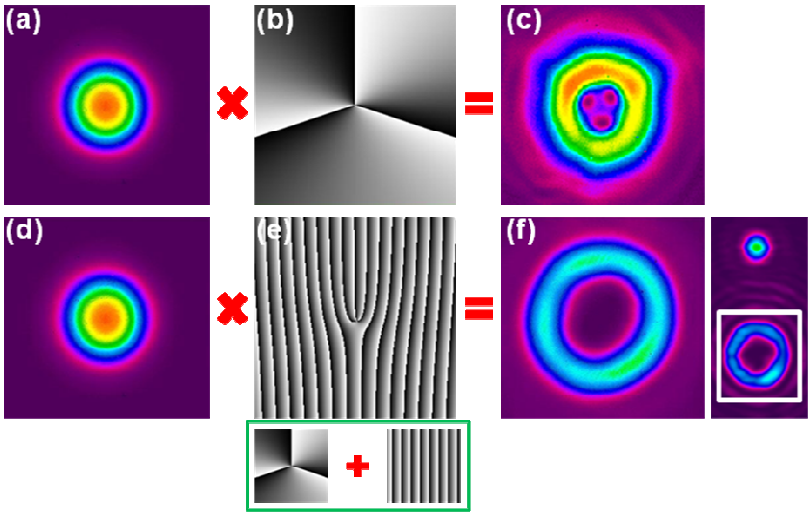

Fig. 2.4.2 *Top row*: illustrates the mode (c) that is produced when a Gaussian beam (a) illuminates a spiral hologram (b). Adding a grating to the spiral hologram, as in the insert of (e), the undiffracted and diffracted components separate, as in the insert of (f).

2.4.1. Off-axis spiral holograms

The spiral hologram, as given in Eq. (2.4.1), will only form the required vortex mode as long as the reference Gaussian mode illuminates the centre of the hologram. In other words, the propagation axis of the Gaussian beam needs to be collinear with the singularity in the spiral hologram. Any displacement of the initial Gaussian beam off of the singularity in the hologram produces a superposition of a Gaussian and a vortex mode. This has been noted in Ref. [20].

By measuring the ratio between the maximum and minimum intensities in the annular ring (illustrated in Fig. 2.4.1.1), the percentages of Gaussian and vortex modes present in the field can be determined. Figure 2.4.1.1 contains a theoretically plotted intensity profile for a mode produced by a displaced spiral hologram, where $l = 1$, as well as the cross-sectional intensity profile. The ratio of I_1 to I_2 gives the ratio of Gaussian to vortex mode present in the field. The next two rows contain experimentally recorded and theoretically calculated intensity profiles for spiral holograms displaced by a distance of 0 mm, 0.04 mm and 0.08 mm. The graph in the bottom row contains a plot of the vortex percentage present in the superposition, as a function of the displacement of the singularity in the hologram. The red points are measured results and the green curve is the theoretical calculation, illustrating very good agreement.

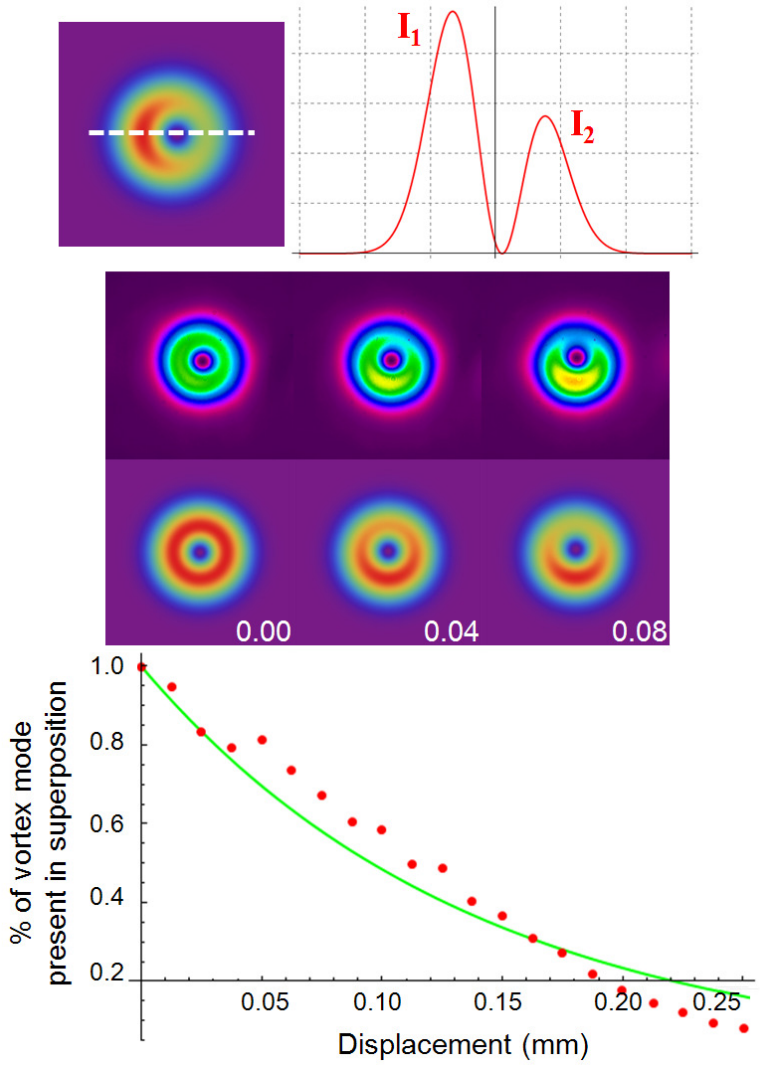

Fig. 2.4.1.1. *Top row*: A mode produced by a displaced spiral hologram accompanied with a cross-sectional intensity profile (taken across the white dotted line). *Middle row*: Experimentally recorded (*top*) and theoretically calculated (*bottom*) intensity profiles for holograms displaced at a distance of 0.0 mm, 0.04 mm and 0.08 mm. *Bottom row*: Plot of the percentage of vortex mode present in the superposition, as a function of the displacement distance. The green curve is the theoretical result and the red dots are the measured data.

2.4.2. Blazed spiral holograms

A blazed grating, unlike a standard grating which consists of a series of sinusoidal grooves, is constructed in such a way that the grooves have a triangular profile [21] (refer to Fig. 2.4.2.1). Unlike sinusoidal gratings, which produce a diffraction pattern whose intensity profile is

described by a Gaussian function around the first diffraction order, a blazed grating transfers most of the incident light solely to the first diffraction order. The efficiency for the blazed grating to transmit the light into the first diffraction order is dependent on the blaze angle θ_B (given in Fig. 2.4.2.1).

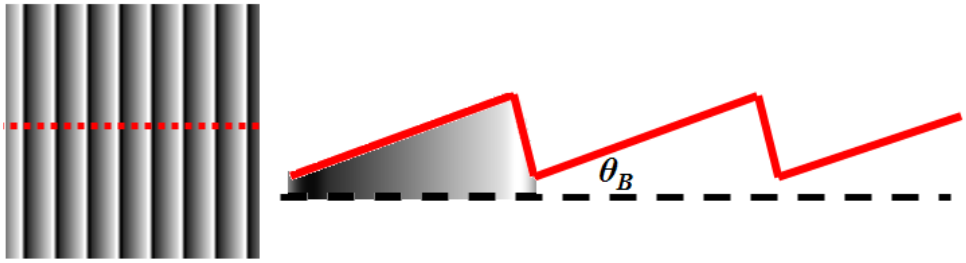

Fig. 2.4.2.1. *Left*: A blazed grating. *Right*: A cross-sectional profile of the blazed grating (taken across the red dotted line on the left).

The expression for a spiral hologram (Eq. 2.4.2) superimposed with a blazed grating is given as [22]

$$t(r,\theta) = \mathrm{mod}\left(l\theta - \frac{2\pi}{\Lambda} r\cos\theta, \quad 2\pi \right), \tag{2.4.2.1}$$

where Λ is the grating spacing. Examples of holograms (computed with the use of Eq. (2.4.2.1)) are given in Fig. 2.4.2.2, for a set grating spacing of Λ = 23 pixels. As the value of l increases so the number of dislocations (or fork prongs) increases. The sign of l denotes whether the prongs point up (positive) or down (negative).

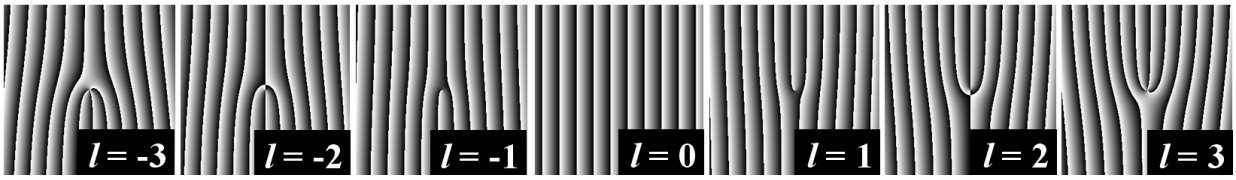

Fig. 2.4.2.2. A series of blazed spiral holograms for l = -3 to 3.

There is a limit to the dimension of the grating spacing, Λ, which can be written to the SLM. If it is too small, then unwanted dislocations may appear in the hologram, as in the case of Fig. 2.4.2.3 (b) - (d). This will result in unwanted singularities (or vortices) appearing in the desired mode, where the number of additional vortices is related to the number of unwanted

dislocations. An example of this is given as an insert in Fig. 2.4.2.3 (d). These interference patterns (b) – (d) that are formed are termed Moiré patterns [23].

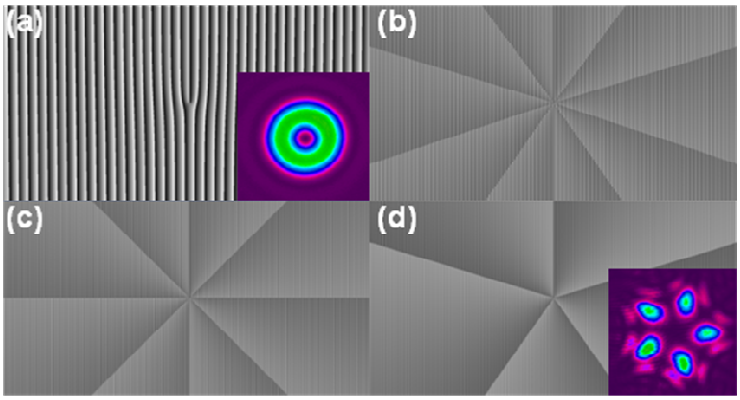

Fig. 2.4.2.3 Blazed spiral holograms having the following grating spacings (a) 50 pixels; (b) 9 pixels; (c) 7 pixels; and (d) 4 pixels. An insert of the required vortex mode produced by hologram (a) is given. The mode produced by hologram (d) is also given as an insert.

To detect an OAM mode of charge l, a blazed spiral hologram can be used when it is assigned the complex conjugate of the mode of interest (i.e. $(\exp(il\theta))^* = \exp(-il\theta)$). For example, if one requires to detect photons having an OAM of $l = 2$, then a blazed spiral hologram of $\Delta m = -2$ is encoded onto the SLM and a single mode fibre is placed at the first diffraction order to couple in the Gaussian mode.

Figure 2.4.2.4 contains a photograph of the experimental setup, which we used to detect incoming vortex modes with the use of a blazed spiral hologram. SLM 1 was used to generate the vortex mode (the hologram is depicted alongside SLM 1), which was then imaged with a 4f system to the plane of SLM 2. A 4f lens system was used, as opposed to a 2f system (which merely images the amplitude), as we wanted to image both the amplitude and phase. The hologram encoded onto SLM 2 is the complex conjugate of that which was programmed onto SLM 1 and appears next to SLM 2. After SLM 2, we monitor the two diffraction orders, $n = 0$ and $n = 1$, and noted that a Gaussian mode was produced in the 0^{th} diffraction order, resulting in light being coupled into the single mode fibre. A vortex mode was produced in the first diffraction order, resulting in minimal light (due to a misalignment in the system) being coupled into the single mode fibre.

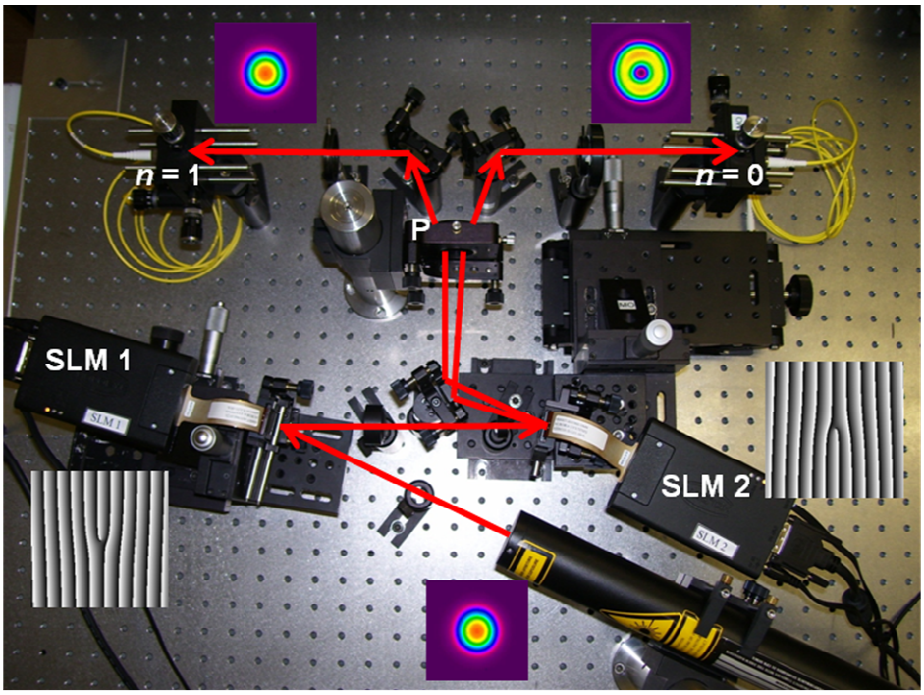

Fig. 2.4.2.4. A photograph, with accompanying labels, illustrating the detection of a $l = 1$ vortex mode. The red arrows mark the direction of the beam, as well as the two diffraction orders after SLM 2. The prism (P) speeds up the diffraction of the two orders.

2.5. Fork holograms

The next form of hologram that is used to generate vortex modes is a fork hologram. It is very similar to the blazed spiral hologram, in its appearance, however instead of producing a single vortex mode in the first diffraction order, vortex modes are produced in all the other diffraction orders.

The transmission function for a fork hologram, as with all computer-generated holograms, is produced by determining the interference pattern between a reference beam, in this case a plane wave, and an optical vortex, resulting in the following transmittance function [24]

$$t(r,\theta) = \exp\left(i \cos\left(l\theta - \frac{2\pi}{\Lambda} r \cos\theta \right) \right), \tag{2.5.1}$$

where Λ is the grating spacing. Examples of holograms (computed using Eq. (2.5.1)) are given in Fig. 2.5.1, for a set grating spacing of $\Lambda = 21$ pixels. As the value of l increases so the

number of fork prongs increases and the sign of l denotes whether the prongs point up (positive) or down (negative), just as in the case of the blazed spiral holograms.

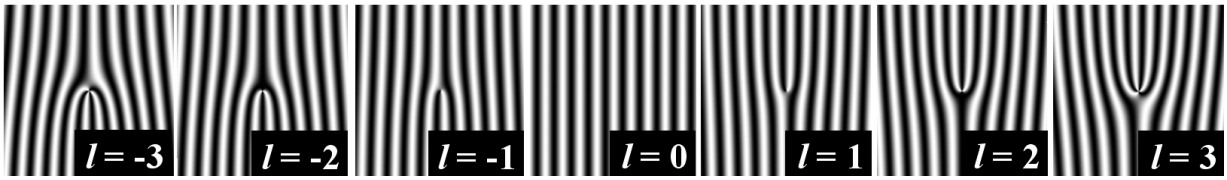

Fig. 2.5.1. A series of fork holograms for l = -3 to 3.

The grating used in the fork hologram is a sinusoidal grating and a cross-section of the grating is given in Fig. 2.5.2.

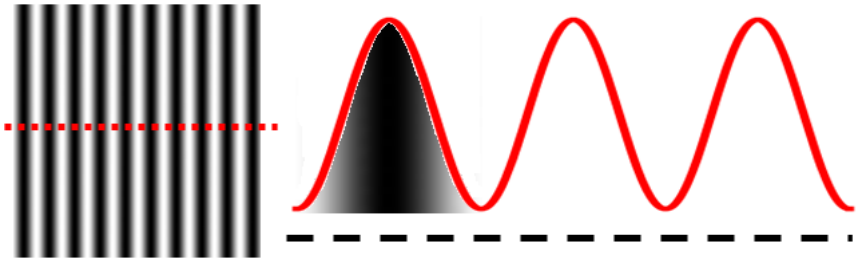

Fig. 2.5.2. *Left*: A sinusoidal grating. *Right*: A cross-sectional profile of the sinusoidal grating (taken across the red dotted line on the left).

In using the fork hologram, which has a sinusoidal grating, to generate vortex modes, $-n$ to n diffraction orders are produced. The topological charge of the vortex at each diffraction order is dependent on the diffraction order, n, and the charge of the fork hologram, Δm, as follows [9]

$$l = n\Delta m. \tag{2.5.2}$$

A particular scenario is given in Fig. 2.5.3, when a Gaussian beam (having a topological charge of l = 0) illuminates the centre of the fork hologram, Δm = 1, and the topological charges of the vortices at each diffraction order is given by Eq. (2.5.2), i.e. l_{-2} = -2, l_{-1} = -1, l_0 = 0, l_1 = 1and l_2 = 2. Diffraction orders on either side of n = -2 and n = 2, do exist, but have been omitted for simplicity. As in the case of the blazed spiral hologram, the incident beam needs to be centred on the singularity in the fork hologram in order for a pure vortex mode to be produced.

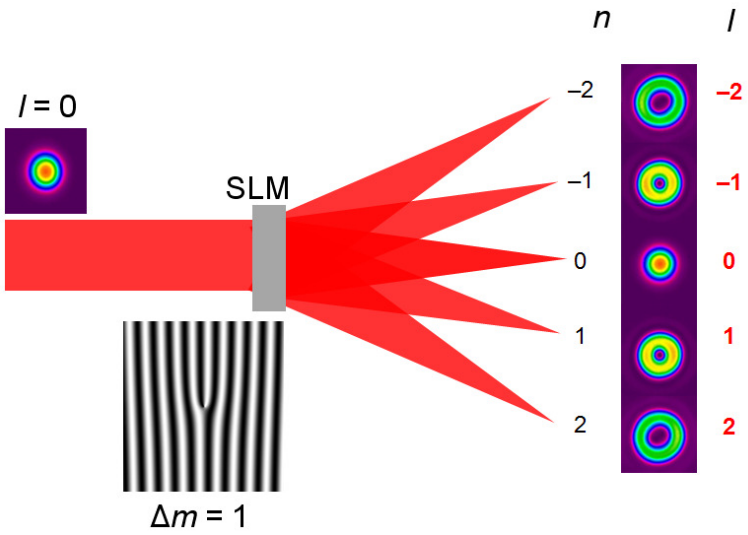

Fig. 2.5.3. A schematic illustrating the diffraction orders that are produced when a Gaussian beam, $l = 0$, illuminates a fork hologram, having a charge of $\Delta m = 1$.

As well as being used for the generation of vortex beams, the fork hologram can also be used in reverse to measure topological charges of vortex beams.

In Ref [9], it is stated that: "*Reversing this process, a photon with angular momentum Δmħ before the grating can be detected by the mono-mode fibre detector placed in the first diffraction order*". This means that an incident vortex mode, having a charge equal to the charge of the "fork" hologram, will produce a Gaussian beam in the first diffraction order. The corresponding charge of the vortex mode present at each of the n^{th} diffraction orders is determined as follows

$$l_n = n\Delta m + l_i, \tag{2.5.3}$$

where l_n denotes the charge in the n^{th} diffraction order and l_i is the initial charge in the beam, incident on the fork hologram.

An example is given in Fig. 2.5.4. If a vortex mode having a charge of $l_i = 2$, illuminates a fork hologram having a charge of $\Delta m = -2$, then a Gaussian beam will form in the first diffraction order. Intuitively, this makes sense as we are multiplying the vortex mode $u_0\exp(il\theta)$ by its complex conjugate, $\exp(-il\theta)$, and so the Gaussian component, u_0, is produced. A single-mode fibre, which couples in only the Gaussian mode, is placed at the first diffraction order so as to

detect single photons possessing an OAM of $-\Delta m$ (in this case an OAM value of $2\hbar$). The disadvantage to this technique is that only the photons possessing an OAM of $-\Delta m$ are detected.

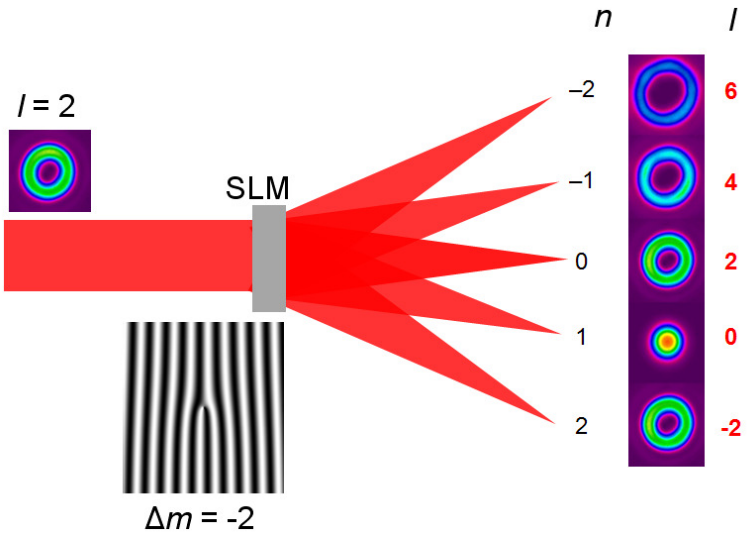

Fig. 2.5.4. A schematic illustrating how a fork hologram can be used to detect a vortex mode of charge $-\Delta m$.

2.6. Spiral phase plates

A spiral phase plate (SPP) [3], also referred to as a vortex lens, is constructed from a piece of transparent material (such as fused silica) which has a gradually increasing, spiralling thickness. This imposes a vortex structure on the incident beam by linearly varying the optical path length and thus inducing a phase shift in the beam. An example of a SPP is given in Fig. 2.6.1.

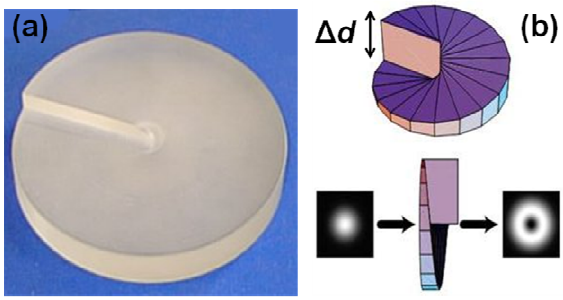

Fig. 2.6.1. (a) A photograph of a SPP courtesy of [25]. (b) Schematic of the mechanism of a SPP courtesy of [26].

When etching or micro-machining the spiral surface into the transparent material, the pitch (given as Δd in Fig. 2.6.1) is related to the wavelength, λ, the desired charge, Δm and the refractive indices of the material, n_m, and its surroundings, n_s, [27]

$$\Delta d = \frac{\Delta m \lambda}{\mu}\left(n_m - n_s\right). \tag{2.6.1}$$

μ is termed the pitch multiplicity and is given by the number of pitch edges (or dislocations) in the SPP.

The number of spirals etched into the SPP can be increased, similar to the spiral hologram. However, the spiral surface needs to be 'smooth' in order for the SPP to be efficient at diffracting the light, so increasing the number of spirals will decrease the diffraction efficiency. Another disadvantage of SPPs is that each one is applicable to one wavelength and one topological charge. The charge, Δm, offered by the SPP can be changed to $-\Delta m$, by flipping the SPP.

2.7. Cylindrical lens mode converters

The next method that we will mention is that of cylindrical lenses which are used to convert Hermite-Gaussian (HG) modes into LG modes and was first used by Allen *et al.* [2]. Our discussion of cylindrical lenses will not be very detailed, as this technique is not used in this work and HG modes are not discussed in this thesis.

A cylindrical lens mode converter, also termed an astigmatic mode converter, is based on cylindrical lenses which convert HG modes of all orders to corresponding LG modes. In order for this to be realized, two steps need to take place. Firstly, the HG mode needs to be rotated by 45° so that it forms a diagonal HG (DHG) mode, which is a superposition of two HG modes. The mathematical representation of this, for the first-order case, is

$$DHG_{10} = \frac{1}{\sqrt{2}}\left(HG_{10} + HG_{01}\right). \tag{2.7.1}$$

The second step involves introducing a relative phase shift of 90° between the two HG modes as this will represent a LG mode

$$LG_{10} = \frac{1}{\sqrt{2}}\left(HG_{10} + iHG_{01}\right). \qquad (2.7.2)$$

In order for the two HG modes to be out of phase by 90°, a pair of cylindrical lenses is used to alter the Gouy phase of the HG modes depending on their mode indices, thus introducing a relative phase shift between them.

The Gouy phase of the HG mode is altered by changing the Rayleigh range of the mode, without changing the position of the beam waist. By placing a lens into the HG mode, which has a Rayleigh range of z_A, the focal length is selected such that the Rayleigh range changes to z_B, while leaving the position of the beam waist unaltered. Aligning the lens in the x direction will result in the Rayleigh range in the y - z plane being affected; resulting in the Rayleigh ranges, z_{Bx} and z_{By}, no longer being equal. This differing in the Rayleigh ranges, in the $x - y$ and $y - z$ planes, means that the HG_{10} and HG_{01} mode pair will be out of phase. The mode is then elliptical, or astigmatic. A second cylindrical lens is introduced and aligned along the same axis so that the Rayleigh ranges, z_{Bx} and z_{By}, are once again equal.

2.8. Dove prism embedded Mach-Zehnder interferometer

The next device that we will discuss is a Mach-Zehnder interferometer, with a Dove prism inserted in each of its arms, which is used to sort odd and even vortex modes [13]. A Mach-Zehnder interferometer can be aligned appropriately so that constructive and destructive interference occurs simultaneously in the two output ports. In the case of the 'odd-even OAM sorter', depicted in Fig. 2.8.1, which is based on the Mach-Zehnder interferometer, a Dove prism, which flips the transverse cross-section of a transmitted beam [28] (illustrated in Fig. 2.8.1 (a)), is placed in each arm of the interferometer.

Rotating the cross-sectional phase profile of the transmitted vortex beam, introduces a relative phase difference between the two arms of the interferometer. The phase difference, $\Delta\varphi$, is proportional to the state, l, of the transmitted vortex beam and the relative angle, β, between the two Dove prisms and is defined as $\Delta\varphi = 2l\beta$. When the two Dove prisms are rotated with respect to each other by an angle of 90º, the transmitted vortex beam is rotated by an angle of 180º and the relative phase difference between the two arms of the interferometer is $\Delta\varphi = l\pi$. By appropriately adjusting the path length of the interferometer, constructive interference will occur

in one of the two output ports for even *l*-valued states and in the opposite port for odd *l*-valued states.

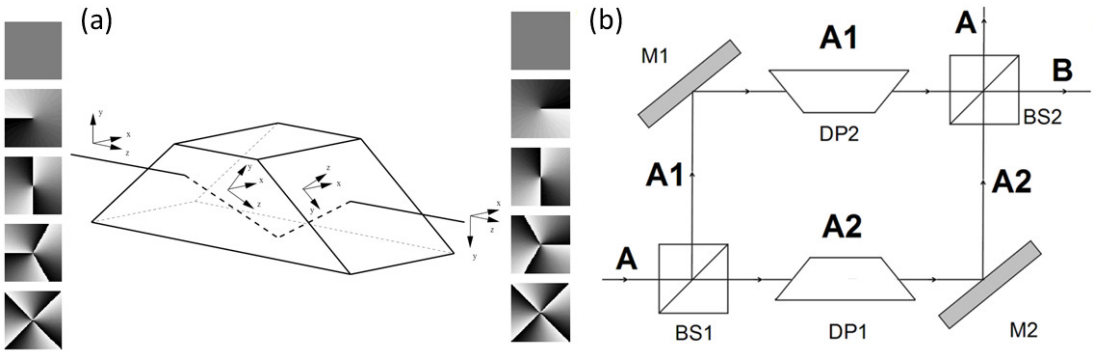

Fig. 2.8.1. (a) The effect a single Dove prism has on the phase profile of a beam. (b) Schematic of the 'odd-even OAM sorter' (BS: beam-splitter, M: mirror, DP: Dove prism).

The additional phase acquired by the beam (exiting in port A) from each of the optical components, in propagating through the arms, A1 and A2, is given by

$$\varphi_{A1\to A} = \underbrace{\pi}_{BS1} + \underbrace{\pi}_{M1} + \underbrace{2l\beta}_{DP2} + \underbrace{\frac{2\pi}{\lambda}t}_{BS2} + \frac{2\pi}{\lambda}d_1 \tag{2.8.1}$$

and

$$\varphi_{A2\to A} = \underbrace{\frac{2\pi}{\lambda}t}_{BS1} + \underbrace{\pi}_{M2} + \underbrace{\pi}_{BS2} + \frac{2\pi}{\lambda}d_2, \tag{2.8.2}$$

respectively. d_1 and d_2 are the path lengths of the two arms, A1 and A2, respectively and t is the optical path length of the beam-splitter. For the beam exiting in port B, the additional phase incurred by the optical components is given by

$$\varphi_{A1\to B} = \underbrace{\pi}_{BS1} + \underbrace{\pi}_{M1} + \underbrace{2l\beta}_{DP2} + \underbrace{\frac{2\pi}{\lambda}t + \frac{2\pi}{\lambda}t}_{BS2} + \frac{2\pi}{\lambda}d_1 \tag{2.8.3}$$

and

$$\varphi_{A2\to B} = \underbrace{\frac{2\pi}{\lambda}}_{BS1} t + \underbrace{\pi}_{M2} + \underbrace{\frac{2\pi}{\lambda}}_{BS2} t + \frac{2\pi}{\lambda} d_2 . \tag{2.8.4}$$

Since the two arms of the interferometer are equal, $d_1 = d_2$, the phase difference in output port A is determined as

$$\Delta\varphi_A = 2l\beta \tag{2.8.5}$$

and that in port B as

$$\Delta\varphi_B = \pi + 2l\beta \tag{2.8.6}$$

The additional phase shift of π, in Eq. (2.8.6), is due to the reflection in the first beam-splitter.

In the case where the relative angle, β, between the two Dove prisms is set to 90°, the phase difference in each output port reduces to the following

$$\Delta\varphi_A = 2l\frac{\pi}{2} = l\pi \tag{2.8.7}$$

$$\Delta\varphi_B = \pi + 2l\frac{\pi}{2} = (l+1)\pi. \tag{2.8.8}$$

From the above equations it is evident that when l is even, constructive interference occurs in port A and destructive interference occurs in port B and vice versa for the case of l being odd. Therefore this device has been termed an 'odd-even OAM sorter'. Examples of vortex modes being sorted into odd (A) and even ports (B) is given in Fig. 2.8.2.

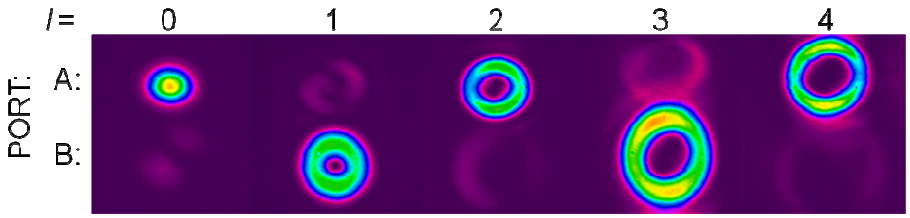

Fig. 2.8.2. Experimental results of the interferometer sorting various vortex modes. The even vortex modes (l = 0, 2 and 4) exit in port A and odd vortex modes exit in port B.

In the following section we adapt this device to produce a robust version of the 'odd-even OAM sorter'

2.9. Robust Dove prism embedded Mach-Zehnder interferometer

2.9.1. Introduction

The implementation of the 'odd-even OAM sorter' has been reported in numerous publications, some of which include introducing a binary amplitude grating to further detect OAM states [29], developing an amplitude damping channel for OAM [18] and developing a linear optical CNOT gate for OAM [30]. The implementation of such an interferometer to sort odd and even *l*-states, especially in the case of developing a cascade of *N*-1interferometers to measure *N l*-states, can prove technically challenging. To date, the only attempt to make such a device more stable has involved incorporating a Sagnac interferometer [31, 32], as opposed to a Mach-Zehnder interferometer, which is known to be phase-stable. Such an approach does, however, require additional polarization optics to further sort the OAM states. Even though many publications have been dedicated to the implementation of the Dove prism embedded Mach-Zehnder interferometer, none, to the best of our knowledge, have attempted to make the device more stable.

In this section we develop a robust Dove prism embedded Mach-Zehnder interferometer (requiring no internal degrees of freedom) capable of sorting odd and even OAM states of light [14]. We demonstrate its efficiency by sorting a maximum of forty-one OAM states (l = -20 to l = 20), producing a contrast between constructive and destructive interference which ranges over the tested OAM states from 92% to 61%. The development of a robust interferometer has implications in quantum cryptography and high density information transfer.

2.9.2. Concept

The main point to remember is that by appropriately adjusting the path length of the interferometer and setting the relative angle between the two Dove prisms to 90º, constructive interference will occur in one of the two output ports for even *l*-valued states and in the opposite

port for odd l-valued states. The relative phase difference between the two arms of the interferometer is $\Delta\varphi = l\pi$. In this section we will discuss the principle behind our improved, robust interferometer.

In setting up each optical component of the 'odd-even OAM sorter', many degrees of freedom play a role in ensuring the correct outcome. The alignment of the beam-splitters, Dove prisms and mirrors within the interferometer, as well as the path length, need to be adjusted. In this work, we make use of a prism (illustrated in Fig. 2.9.2.1 (a) and (b)), similar to a Dove prism, in that it rotates the transverse cross-section of a transmitted beam, but its entry and exit faces are perpendicular to the optical axis. This construction of a phase-rotating prism having parallel sides, first noted in Ref. [33], allows one to easily mount it on either side of a beam-splitter. Introducing right-angled prisms, as opposed to mirrors, we are able to glue all the optical components into a single compact housing, depicted in the photograph in Fig 2.9.2.1 (c). By leaving the second right-angled prism free-standing, the optical path length of the interferometer can be finely adjusted.

In studying Fig. 2.9.2.1 (a), it is evident that a displacement of the incoming beam in the y-direction will have no effect on the functioning of the Dove prism, provided the optical axis of incoming beam is perpendicular to the optic axis of the Dove prism. Rotating the orientation of the Dove prism, as given in Fig. 2.9.2.1 (a), by 90º, so as to produce that in Fig. 2.9.2.1 (b), the Dove prism is insensitive to a displacement of the incident beam in the x-direction. The fact that the 'odd-even OAM sorter' requires that the two Dove prisms be rotated with respect to each other by an angle of 90º, aids the alignment of the interferometer. One of the paths will be insensitive to a horizontal displacement of the transmitted beam, while the other is insensitive to a vertical displacement of the transmitted beam. The only constraint is that perfect overlap of the two paths in the two exiting ports, A and B, be achieved, which is easily possible by adjusting the position and tilt of the incoming beam with the use of two mirrors.

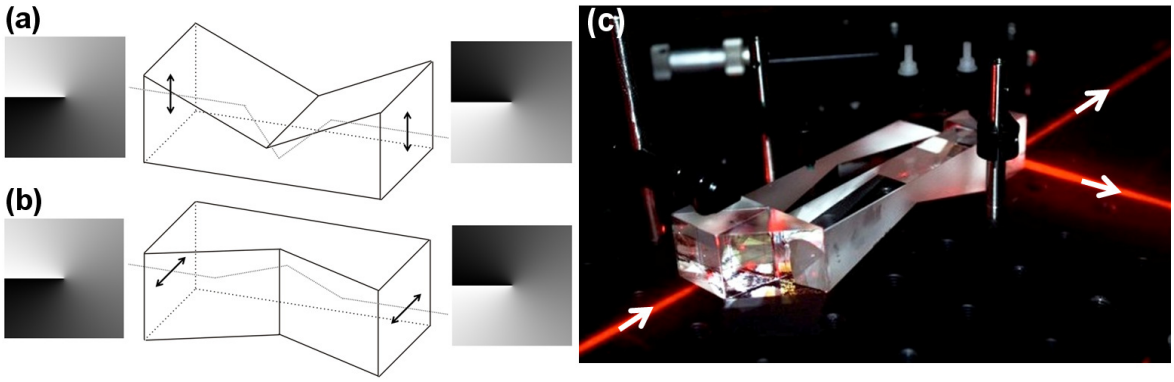

Fig. 2.9.2.1 (a) and (b) The phase-rotating prism, illustrating how its orientation can make it either insensitive to a vertical or horizontal displacement, respectively. (c) A photograph of the robust 'odd-even OAM sorter'. The white arrows denote the direction of the beam.

2.9.3. Experimental methodology and results

A photograph of the device that was developed appears in Fig. 2.9.2.1 (c) and a schematic, labelling each of the components is presented in Fig. 2.9.3.1.

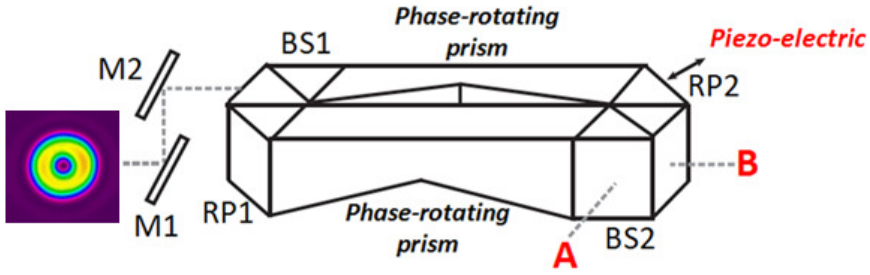

Fig. 2.9.3.1. Schematic of the robust 'odd-even OAM sorter' (M: mirror, BS: beam-splitter, RP: right-angled prism, A: output port A, B: output port B).

The various vortex modes (l = -20 to 20) that we wished to sort with our interferometer, were prepared by illuminating blazed, l-charged spiral holograms, encoded on a Hamamtsu SLM, with a HeNe laser ($\lambda \sim 633$ nm). Two mirrors, M1 and M2 (in Fig. 2.9.3.1), were placed in front of the interferometer, so as to steer the incoming vortex mode through the interferometer. The optical components of the interferometer (two beam-splitters, two Dove prisms and a right-angled prism) were all glued together and clamped onto a flat stage. A piezoelectric mount was attached to the second right-angled prism, RP2, so that accurate selection of the interferometer path length could be obtained. The sorting of odd and even l-valued vortex modes into the

output ports A and B, respectively, was obtained by accurately overlapping the near- and far-field planes of the two fields exiting in each output port through the use of a mere four degrees of freedom: the two mirrors positioned before the interferometer, M1 and M2, as well as correctly setting the path length of the interferometer.

To test the effectiveness of the interferometer in separating odd and even l-valued vortex modes, the intensity of the interference pattern in one of the output ports was monitored with a photodiode, while the path length of the interferometer oscillated back and forth between constructive and destructive interference by the use of a piezoelectric mount and a function generator. The fringe contrast, $(v_{max} - v_{min})/(v_{max} + v_{min})$, where v_{max} and v_{min} are the maximum and minimum voltages from the photodiode, was calculated for various incoming vortex modes and is depicted graphically in Fig. 2.9.3.2 (a). Some of the odd and even vortex modes existing in their appropriate ports are given in Fig. 2.9.3.2 (b).

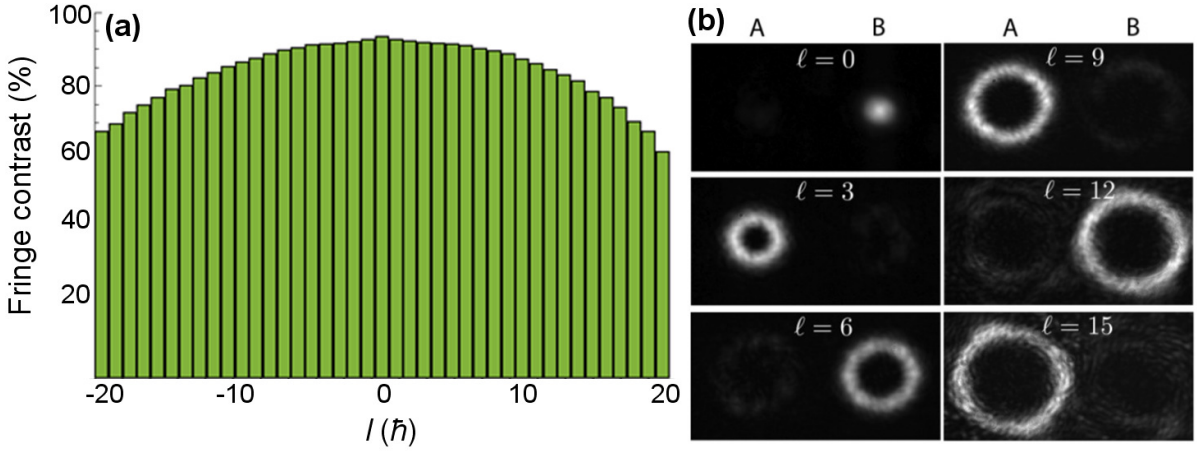

Fig. 2.9.3.2. (a). The measured fringe contrast as a function of l. (b) Some experimental results of the interferometer sorting various vortex modes. The even vortex modes (l = 0, 6 and 12) exit in port B and odd vortex modes (l = 3, 9 and 15) exit in port A.

Since the SLMs are not free of aberrations, they do pose a limitation on the purity of the vortex mode that is created. Even though the flattest of our SLMs was used and careful alignment of the optics was undertaken, the aberrations present, lead to a degradation in the performance of the interferometer, especially at high l-valued vortex modes. When an aberration is added to a beam carrying OAM, the beam becomes a superposition of different l-valued modes. At the lowest integer value of l, l = 0, the fringe contrast is at a maximum (at 92.2%), illustrating that constructive and destructive interference for the case of a low l-valued OAM state is notably

distinctive. As the magnitude of l increases, so the contrast decreases, illustrating that constructive and destructive interference for higher $|l|$-valued OAM states becomes less obvious. Across twenty-one OAM states (from l = -10 to l = 10) the contrast drops from 92.2% to 85.3%, indicating that our setup is extremely robust at sorting OAM states. Special mention should be made that no adjustment of the four degrees of freedom (external to the interferometer) needed to be made during the course of collecting the measurements in Fig. 2.9.3.2. Previously to obtain such results, one would have to adjust all the degrees of freedom for each optical component within the interferometer, whereas our setup has reduced the interferometer to having no degrees of freedom. Since we are able to produce high contrast over twenty-one OAM states (from l = -10 to l = 10) we suggest this setup to be suitable in quantum optics experiments such as quantum cryptography.

It should, however, be noted that due to the fact that the Dove prism can invert the polarization of a passing beam the 'odd-even-sorting' nature of the interferometer no longer works for an incoming polarization that is neither horizontal nor vertical. We tested this by rotating the polarization of the incident beam from horizontal to linear with the use of a half-wave plate and noticed that the interference fringes in ports A and B disappeared.

2.10. Conclusion

In this chapter we have introduced experimental techniques which are used to either generate or measure fields carrying OAM. We discussed how digital holography can be used to implement a computer generated hologram (which can be used to either create or measure an optical OAM field) through the use of SLMs. In sections 2.4 and 2.5 we explained how the spiral and fork holograms, respectively can be used to generate optical vortices as well as how the fork hologram is used to detect OAM, by producing a Gaussian beam in the desired diffraction order which is then coupled into a single mode fibre. We also examined two other optical components which can be used to manipulate OAM: SPPs (2.6), which impart a helical structure to the transmitted beam, thus increasing or decreasing its OAM appropriately, and cylindrical lens (2.7). The last device that we discussed is a Dove-prism embedded Mach-Zehnder interferometer which is used to sort odd and even OAM modes.

We presented our experimentally developed, robust 'odd-even OAM sorting' interferometer, which has no degrees of freedom and instead the alignment is simply restricted to only four degrees of freedom via two mirrors external to the interferometer, and correct setting of the path

length [14]. We showed that this device is capable of separating twenty-one OAM states of light, having a contrast higher than 85.3%, sufficient in the detection of single photons for quantum information processing. The construction of a less technically-demanding interferometer will prove useful in the cascading of interferometers and the insertion into other sorting methods [12] for the detection of an increased OAM state-space. The ability to efficiently measure a large number of OAM states has applications in quantum cryptography [6-8] and quantum computation [34].

2.11. References

[1]. M. W. Beijersbergen, L. Allen, H. E. L. O. Van der Veen, and J. P. Woerdman, "Astigmatic laser mode converters and the transfer of orbital angular momentum," Opt. Commun. **96**(1-3), 123-132 (1993).

[2]. L. Allen, M. W. Beijersbergen, R. J. C. Spreeuw, and J. P. Woerdman, "Orbital angular momentum of light and the transformation of Laguerre-Gaussian laser modes," Phys. Rev. A **45**(11), 8185-8189 (1992).

[3]. M. W. Beijersbergen, R. P. C. Coerwinkel, M. Kristensen, and J. P. Woerdman, "Helical-wave-front laser-beams produced with a spiral phaseplate," Opt. Commun. **112**(5-6), 321-327 (1994).

[4]. V. Yu Bazhenov, M. V. Vasnetsov, and M. S. Soskin, "Laser beams with screw dislocations in their wavefronts," JETP Lett. **52**(8), 429-431 (1990).

[5]. J. E. Curtis, B. A. Koss, and D. G. Grier, "Dynamic holographic optical tweezers," Opt. Commun. **207**(1-6), 169-175 (2002).

[6]. A. Vaziri, G. Weihs, and A. Zeilinger, "Experimental two-photon three-dimensional quantum entanglement," Phys. Rev. Lett. **89**(24), 240401 (2002).

[7]. J. T. Barreiro, T.-C. Wei, and P. G. Kwiat, "Beating the channel capacity limit for linear photonic superdense coding," Nature Phys. **4**, 282-286 (2008).

[8]. J. Leach, B. Jack, J. Romero, A. K. Jha, A. M. Yao, S. Franke-Arnold, D. Ireland, R. W. Boyd, S. M. Barnett, and M. J. Padgett, "Quantum correlations in optical angle-orbital angular momentum variables," Science **329**(5992), 662-665 (2010).

[9]. A. Mair, A. Vaziri, G. Weihs, and A. Zeilinger, "Entanglement of the orbital angular momentum states of photons," Nature **412**, 313-316 (2001).

[10]. G. Gibson, J. Courtial, M. J. Padgett, M. Vasnetsov, V. Pas'ko, S. M. Barnett and S. Franke-Arnold, "Free-space information transfer using light beams carrying orbital angular momentum," Opt. Express **12**(22), 5448-5456 (2004).

[11]. S. N. Khonina, V. V. Kotlyar, R. V. Skidanov, V. A. Soifer, P. Laakkonen, and J. Turunen, "Gauss–Laguerre modes with different indices in prescribed diffraction orders of a diffractive phase element," Opt. Commun. **175**(4-6), 301-308 (2000).

[12]. G. C. G. Berkhout, M. P. J. Lavery, J. Courtial, M. W. Beijersbergen, and M. J. Padgett, "Efficient Sorting of Orbital Angular Momentum States of Light," Phys. Rev. Lett. **105**(15), 153601 (2010).

[13]. J. Leach, M. J. Padgett, S. M. Barnett, S. Franke-Arnold, and J. Courtial, "Measuring the orbital angular momentum of a single photon," Phys. Rev. Lett. **88**(25), 257901 (2002).

[14]. M. Lavery, A. Dudley, A. Forbes, J. Courtial and M. Padgett, "Robust interferometer for the routing of light beams carrying orbital angular momentum," New J. of Phys. **13**(9), 093014 (2011).

[15]. C. Gao, X. Qi, Y. Liu, J. Xin, and L. Wang, "Sorting and detecting orbital angular momentum states by using a Dove prism embedded Mach–Zehnder interferometer and amplitude gratings," Opt. Commun. **284**(1), 48-51 (2011).

[16]. A. Gatto, M. Tacca, P. Martelli, P. Boffi and M. Martinelli, "Free-space orbital angular momentum division multiplexing with Bessel beams," J. Opt. **13**, 064018 (2011).

[17]. J. M. Hickmann, E. J. S. Fonseca, W. C. Soares, and S. Chavez-Cerda, "Angular momentum," Phys. Rev. Lett. **105**(5), 053904 (2010).

[18]. A. Dudley, M. Nock, T. Konrad, F. S. Roux, and A. Forbes, "Amplitude damping of Laguerre-Gaussian modes," Opt. Express **18**(22), 22789-22795 (2010).

[19]. P. Hariharan, "Basics of Holography," Cambridge University Press, Cambridge, (2002).

[20]. A. Vaziri, G. Weihs and A. Zeilinger, "Superpositions of the orbital angular momentum for applications in quantum experiments," J. Opt. B: Quantum Semiclass. Opt. **4**, S47-S51 (2002).

[21]. C. Palmer, "Diffraction grating handbook," 6th edition, Newport Corporation (2005).

[22]. J. Arlt "Applications of the Laguerre–Gaussian beams and Bessel beams to both non-linear optics and atom optics," *PhD Thesis,* School of Physics and Astronomy, University of St Andrews (1999).

[23]. A. K. Jain, M. Figueiredo, and J. Zerubia "Energy minimization methods in computer vision and pattern recognition," p. 198, Springer (2001).

[24]. C. S. Guo, X. Liu, X. Y. Ren, H. T. Wang, "Optimal annular computer-generated holograms for the generation of optical vortices," J. opt. Soc. Am. **22**(2), 385-390 (2005).

[25]. http://www.physics.umd.edu/courses/Phys726/The_Quantum_Vortex.htm

[26]. http://www.st-andrews.ac.uk/~www_pa/Scots_Guide/MMWave/QO/components/spir.html

[27]. G. A. Swartzlander, "The optical vortex lens," Optics & Photonics News **17**(11), 39-43 (2006).

[28]. M. Born and E. Wolf, *Principles of Optics* (Pergamon Press, Oxford, 1980), 6th ed.

[29]. C. Gao, X. Qi, Y. Liu, J. Xin, and L. Wang, "Sorting and detecting orbital angular momentum states by using a Dove prism embedded Mach–Zehnder interferometer and amplitude gratings," Opt. Commun. **284**(1), 48-51 (2011).

[30]. L. Deng, H. Wang, and K. Wang, "Quantum CNOT gates with orbital angular momentum and polarization of single-photon quantum logic," J. Opt. Soc. Am. B **24**(9), 2517-2520 (2007).

[31]. S. Slussarenko, V. D'Ambrosio, B. Piccirillo, L. Marrucci, and E. Santamato, "The polarizing sagnac interferometer: a tool for light orbital angular momentum sorting and spin-orbit photon processing," Opt. Express **18**(26), 27205-27216 (2010).

[32]. C.C. Leary, L.A. Baumgardner, and M.G. Raymer, "Stable mode sorting by two-dimensional parity of photonic transverse spatial states," Opt. Express **17**(4), 2435-2452 (2009).

[33]. J. Leach, J. Courtial, K. Skeldon, S. M. Barnett, S. Franke-Arnold, and M. J. Padgett, "Interferometric methods to measure orbital and spin, or the total angular momentum of a single photon," Phys. Rev. Lett. **92**(1), 013601 (2004).

[34]. M. A. Nielsen and I. L. Chuang, "Quantum Computation and Quantum Information," Cambridge University Press, Cambridge, (2000).

CHAPTER THREE

Amplitude Damping Channel for Orbital Angular Momentum

3.1. Introduction

We implement the Dove prism embedded Mach-Zehnder interferometer to mimic an amplitude damping channel for vortex modes [1]. The principle behind amplitude damping will be presented in section 3.2.1. followed by the concept as to how the Dove prism embedded Mach-Zehnder interferometer can be used to form an amplitude damping channel for vortex modes in section 3.2.2. We test our channel on a vortex mode, having an azimuthal index of $l = 1$, and demonstrate that it decays to a Gaussian mode in good agreement with the theoretical model in section 3.2.3. The reason behind developing this channel is since we are able to characterize the action of such a channel on OAM states, we propose using it to investigate the dynamics of entanglement.

3.2. Amplitude damping of orbital angular momentum states

Storing and processing information in the OAM states of photons offers high storage and increased computation capacity per photon and since many of the tasks in quantum information processing depend upon entanglement, the evolution of entanglement needs to be examined [2]. Studies into how the entanglement of OAM states decoheres through a turbulent medium are currently being pursued [3]. The amplitude damping channel that we present here is important for studying how entanglement will decay through a 'lossy' system.

3.2.1. Amplitude damping

Before presenting the channel that we have developed to perform amplitude damping, it makes sense to first discuss the process of amplitude damping. Amplitude damping is a quantum

operation which describes energy dissipation from excited systems, such as atoms or spin systems, to an environment [4]. Furthermore, it can also comprise the dissipation of momentum (angular momentum, OAM or any other measurable quantity) due to an interaction with the environment. The action of amplitude damping results in the ground state, $|0\rangle$, being left invariant, while the excited state, $|1\rangle$, remains either invariant or decays to the ground state, by losing a quantum of energy to the environment. The amplitude damping channel, representing the state change for a two-level system, can be defined by the following transformation

$$\rho_s = |\psi\rangle\langle\psi| \rightarrow M_0|\psi\rangle\langle\psi|M_0^* + M_1|\psi\rangle\langle\psi|M_1^*, \tag{3.2.1.1}$$

where the Kraus operators are [4]

$$M_0 = \begin{pmatrix} 1 & 0 \\ 0 & \sqrt{1-P} \end{pmatrix} \tag{3.2.1.2}$$

and

$$M_1 = \begin{pmatrix} 0 & \sqrt{P} \\ 0 & 0 \end{pmatrix}. \tag{3.2.1.3}$$

P is the probability that the excited state decays to the ground state. Since the amplitude damping is given for a two-level system, we will consider the initial state of the system (in terms of OAM) to be represented as follows

$$|\psi\rangle = \gamma_1|l=0\rangle + \gamma_2|l=1\rangle, \tag{3.2.1.4}$$

which is an arbitrary superposition of the states $|l=0\rangle$ (the ground state) and $|l=1\rangle$ (the excited state). $|\gamma_1|^2 + |\gamma_2|^2 = 1$, while $|l=0\rangle$ and $|l=1\rangle$ represent vortex modes of charges l = 0 and l =1 respectively.

By substituting the Kraus operators (Eqs (3.2.1.2) and (3.2.1.3)), along with the initial state (Eq. (3.2.1.4)), into Eq. (3.2.1.1), the final state of the system, ρ_s, can be found

$$\rho_s = |\psi\rangle\langle\psi| \rightarrow \underbrace{M_0|\psi\rangle\langle\psi|M_0^*}_{Term1} + \underbrace{M_1|\psi\rangle\langle\psi|M_1^*}_{Term2}$$

$$Term1 = \begin{pmatrix} 1 & 0 \\ 0 & \sqrt{1-P} \end{pmatrix}\left[\begin{pmatrix} \gamma_1 \\ 0 \end{pmatrix} + \begin{pmatrix} 0 \\ \gamma_2 \end{pmatrix}\right]\left[\begin{pmatrix} \gamma_1^* & 0 \end{pmatrix} + \begin{pmatrix} 0 & \gamma_2^* \end{pmatrix}\right]\begin{pmatrix} 1 & 0 \\ 0 & \sqrt{1-P} \end{pmatrix}$$

$$Term1 = \begin{pmatrix} \gamma_1\gamma_1^* & \gamma_1\gamma_2^*\sqrt{1-P} \\ \gamma_1^*\gamma_2\sqrt{1-P} & \gamma_2\gamma_2^*(1-P) \end{pmatrix}$$

$$Term2 = \begin{pmatrix} 0 & \sqrt{P} \\ 0 & 0 \end{pmatrix}\left[\begin{pmatrix} \gamma_1 \\ 0 \end{pmatrix} + \begin{pmatrix} 0 \\ \gamma_2 \end{pmatrix}\right]\left[\begin{pmatrix} \gamma_1^* & 0 \end{pmatrix} + \begin{pmatrix} 0 & \gamma_2^* \end{pmatrix}\right]\begin{pmatrix} 0 & \sqrt{P} \\ 0 & 0 \end{pmatrix}$$

$$Term2 = \begin{pmatrix} \gamma_2\gamma_2^* P & 0 \\ 0 & 0 \end{pmatrix}$$

$$\rho_s = |\psi\rangle\langle\psi| \rightarrow \begin{pmatrix} \gamma_1\gamma_1^* & \gamma_1\gamma_2^*\sqrt{1-P} \\ \gamma_1^*\gamma_2\sqrt{1-P} & \gamma_2\gamma_2^*(1-P) \end{pmatrix} + \begin{pmatrix} \gamma_2\gamma_2^* P & 0 \\ 0 & 0 \end{pmatrix}$$

$$\rho_s = \begin{pmatrix} \gamma_1^2 + \gamma_2^2 p & \gamma_1\gamma_2^*\sqrt{1-P} \\ \gamma_1^*\gamma_2\sqrt{1-P} & \gamma_2^2(1-P) \end{pmatrix}. \qquad (3.2.1.5)$$

Coupling the system appropriately to an environment with two orthogonal states $|K=0\rangle_E$ and $|K=1\rangle_E$, the unitary time evolution operator, U_{SE}, of the system, S, and the environment, E, produces the following transformation of the amplitude damping channel and can be described mathematically as

$$|l=0\rangle_S|K=0\rangle_E \overset{U_{SE}}{\rightarrow} |l=0\rangle_S|K=0\rangle_E \qquad (3.2.1.6)$$

$$|l=1\rangle_S|K=0\rangle_E \overset{U_{SE}}{\rightarrow} \sqrt{P}|l=0\rangle_S|K=1\rangle_E + \sqrt{1-P}|l=1\rangle_S|K=0\rangle_E. \qquad (3.2.1.7)$$

Here K represents an element in the environment, such as a path along which the photon propagates. If $|l=1\rangle$ represents the excitation of the system and $|K=1\rangle$ the excitation of the environment, then consequently $|l=0\rangle$ and $|K=0\rangle$ represent the ground state of the system and the environment respectively. Equations (3.2.1.6) and (3.2.1.7) illustrate that the probability that the excited state remains unchanged or that it decays to the ground state is given by 1 - P and P, respectively and hence the amplitude of the excited state has been 'damped'.

In the next step we need to verify that the transformations defined in Eqs (3.2.1.6) and (3.2.1.7) result in the final state presented in Eq. (3.2.1.5). Firstly, the state of the system and the environment is determined as

$$\rho_{SE} = U_{SE}\left(\left|\psi\right\rangle_S \left|K=0\right\rangle_E \;\; {}_S\left\langle\psi\right|_E \left\langle K=0\right|\right)U_{SE}^T$$

$$\begin{aligned}\rho_{SE} = &\left(\gamma_1\left|l=0\right\rangle_S \left|K=0\right\rangle_E + \gamma_2\left(\sqrt{P}\left|l=0\right\rangle_S \left|K=1\right\rangle_E + \sqrt{1-P}\left|l=1\right\rangle_S \left|K=0\right\rangle_E\right)\right)\times \\ &\left({\gamma_1}^* {}_S\left\langle l=0\right|_E \left\langle K=0\right| + {\gamma_2}^*\left(\sqrt{P}\,{}_S\left\langle l=0\right|_E \left\langle K=1\right| + \sqrt{1-P}\,{}_S\left\langle l=1\right|_E \left\langle K=0\right|\right)\right).\end{aligned} \tag{3.2.1.8}$$

In order to determine the state of only the system, ρ_s, the environment is traced out

$$\rho_S = Tr_E\left[\rho_{SE}\right] = \sum_{K=0}^{1} {}_E\left\langle K\left|\rho_{SE}\right|K\right\rangle_E \tag{3.2.1.9}$$

and by substituting in Eq. (3.2.1.8) and taking into account that $\left|K=0\right\rangle_E$ and $\left|K=1\right\rangle_E$ are an orthonormal basis, the state of the system can be simplified to

$$\rho_S = \begin{pmatrix} {\gamma_1}^2 + {\gamma_2}^2 P & \gamma_1{\gamma_2}^*\sqrt{1-P} \\ {\gamma_1}^*\gamma_2\sqrt{1-P} & {\gamma_2}^2(1-P) \end{pmatrix}, \tag{3.2.1.10}$$

which is Eq. (3.2.1.5).

Therefore, we need a channel that is going to perform the transforms defined in Eqs (3.2.1.6) and (3.2.1.7). By setting *K*, an element of the environment, to a path in the optical system, the overall action of the channel on the state (given in Eq. (3.2.1.4)) can be denoted as

$$\gamma_1\left|l=0\right\rangle^A + \gamma_2\left|l=1\right\rangle^A \rightarrow \gamma_1\left|l=0\right\rangle^A + \gamma_2\left(\sqrt{1-P}\left|l=1\right\rangle^A + \sqrt{P}\left|l=0\right\rangle^B\right), \tag{3.2.1.11}$$

where A and B are paths in the optical setup.

The system which performs the transformation given in Eq. (3.2.1.11) is discussed in the following section.

3.2.2. Concept

Figure 3.2.2.1 contains the schematic of the optical system, which performs the action of amplitude damping on the state given in Eq. (3.2.1.4) and is mathematically described in Eq. (3.2.1.11).

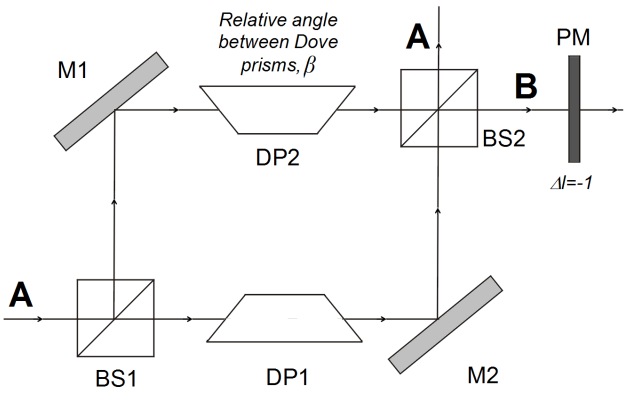

Fig. 3.2.2.1. Schematic of the OAM amplitude damping channel. (BS: beam-splitter, M: mirror, DP: Dove prism, PM: phase mask). The labels A and B denote the optical path and are associated as the ground state of the environment $|K=0\rangle$ and the excited state of the environment $|K=1\rangle$, respectively.

Our channel is based on the 'odd-even OAM sorter' presented in section 2.8, where we showed that the relative phase difference, $\Delta\varphi$, is proportional to the charge l of the incoming vortex mode and the relative angle β, between the two Dove prisms: $\Delta\varphi = 2l\beta$. The relative angle, β, between the two Dove prisms can be varied resulting in the vortex mode exiting solely in port A or port B, or in a weighted superposition of both ports A and B. This allows us to control how much of the initial vortex mode will exit into the two environments, A (the ground state of the environment) and B (the excited state of the environment). By introducing a hologram, which decreases the azimuthal mode index by 1, in port B, the 'excited' vortex mode ($l = 1$) will decay to an 'unexcited' Gaussian mode, thus performing the action of amplitude damping. To illustrate that our channel, presented in Fig. 3.2.2.1, performs the required transformation given in Eq. 3.2.1.11, we pass each of the states ($|l=0\rangle$ and $|l=1\rangle$) through our channel.

- CASE 1: Incoming Gaussian mode ($l = 0$)

When a Gaussian mode ($l = 0$) enters the device, the relative phase shift is $\Delta\varphi = 2l\beta = 0$, independent of the relative angle, β, between the two Dove prisms. Therefore there will always be constructive interference in port A and destructive interference in port B, for the Gaussian mode. The transformation for this case can be written mathematically as

$$\left|l=0\right\rangle^{A} \rightarrow \left|l=0\right\rangle^{A}. \tag{3.2.2.1}$$

- CASE 2: Incoming vortex mode ($l = 1$)

For a vortex mode having a charge of $l = 1$ there is a non-vanishing relative phase shift of $\Delta\varphi = 2l\beta = 2\beta$. This phase shift leads to partially constructive and destructive interference in both ports A and B, dependent on the relative angle, β, between the two Dove prisms. Only the state $l = 1$ can exit in port B and the hologram in this port maps this to a Gaussian ($l = 0$) state. The amplitudes of the fields emerging from the second beam-splitter in ports A and B are described as

$$U^{A}{}_{afterBS2} = \frac{1}{\sqrt{2}}\left(\underbrace{U^{A}{}_{beforeBS2}}_{reflected\ @\ BS2} + \underbrace{U^{B}{}_{beforeBS2}}_{transmitted\ @\ BS2}\right) = \frac{U_0}{2}\left(e^{i(\theta+2\beta)} + e^{i\theta}\right) = U_0 e^{i\theta} e^{i\beta}\cos\beta \tag{3.2.2.2}$$

and

$$U^{B}{}_{afterBS2} = \frac{1}{\sqrt{2}}\left(\underbrace{U^{A}{}_{beforeBS2}}_{transmitted\ @\ BS2} + \underbrace{-U^{B}{}_{beforeBS2}}_{reflected\ @\ BS2}\right) = \frac{U_0}{2}\left(e^{i(\theta+2\beta)} - e^{i\theta}\right) = U_0 e^{i\theta} e^{i\beta} i\sin\beta, \tag{3.2.2.3}$$

where U denotes the amplitude of the field. Only one of the reflected fields incurs a π phase shift due to the manner in which the beamsplitters are constructed.

It is then evident that the amplitude in port A, for an input vortex mode of $l = 1$, is proportional to $\cos\beta$ and consequently the power

$$P_A \propto \cos^2\beta. \tag{3.2.2.4}$$

The amplitude in port B, for an input vortex mode of $l = 1$, is proportional to $\sin\beta$ and its power

$$P_B \propto \sin^2 \beta. \qquad (3.2.2.5)$$

The state emerging from ports A and B, for an incoming vortex mode ($l = 1$), can be written in a general form as

$$|l=1\rangle^A \rightarrow \cos\beta|l=1\rangle^A + \sin\beta|l=0\rangle^B = \sqrt{1-P}|l=1\rangle^A + \sqrt{P}|l=0\rangle^B, \qquad (3.2.2.6)$$

where $\sqrt{1-P} = \cos\beta$ and $\sqrt{P} = \sin\beta$.

Including the result from case 1 above the general transformation of the device is given as

$$\gamma_1|l=0\rangle^A + \gamma_2|l=1\rangle^A \rightarrow \gamma_1|l=0\rangle^A + \gamma_2\left(\cos\beta|l=1\rangle^A + \sin\beta|l=0\rangle^B\right), \qquad (3.2.2.7)$$

which is a form of the required amplitude damping transformation described in Eq. (3.2.1.11)

3.2.3. Experimental methodology and results

A photograph of the experimental setup to test the concept of our amplitude damping channel appears in Fig. 3.2.3.1. The interferometer used here is the one described in section 2.8, as opposed to our new robust interferometer in section 2.9, as we needed the Dove prisms to be free-standing so that we could rotate them and set the relative angle, β.

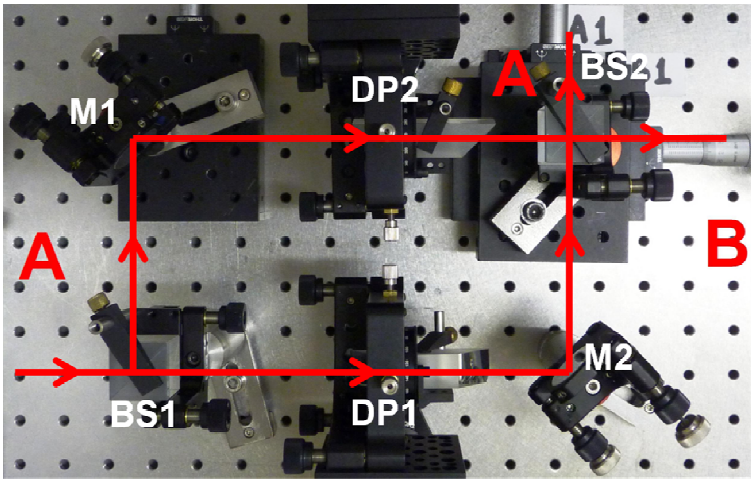

Fig. 3.2.3.1. Photograph of the interferometer used in the OAM amplitude damping channel. (BS: beam-splitter, M: mirror, DP: Dove prism). The labels A and B denote the optical path.

A HeNe laser operating at a wavelength of 633 nm was directed onto a SLM (HoloEye PLUTO VIS SLM with 1920×1080 pixels of pitch 8 μm and calibrated for a 2π phase shift at λ =632.8 nm), where a blazed spiral hologram was used to initialise the vortex mode, before entering the interferometer. The two exiting ports of the interferometer, A and B, were monitored with a CCD camera, while the relative angle, β, between the two Dove prisms was varied.

The relative angle between the Dove prisms was set to $\beta = 90°$, so as to check the interferometer functioned correctly [5] (i.e. even modes exist in port A and odd modes in port B). The results are given in Fig. 2.8.2. When a Gaussian mode enters the interferometer, it only exits in port A (Fig. 3.2.3.2). The results presented in Fig. 3.2.3.2 are instructive when considering the errors in the system due to imperfect alignment and environmental fluctuations. We should expect 100% transmission in port A, and no transmission in port B, however the variance in the data is given as 0.88 ± 0.06 and 0.15 ± 0.08 for ports A and B, respectively.

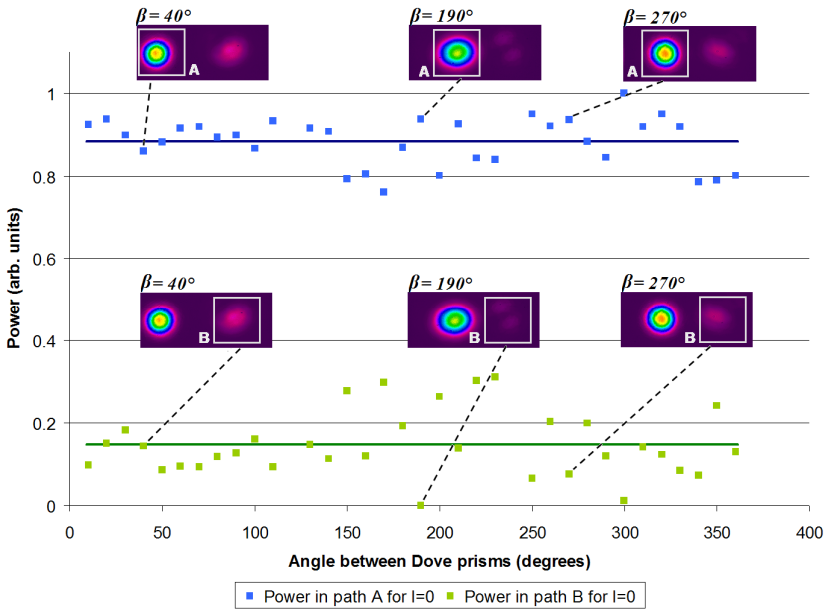

Fig. 3.2.3.2. Plot of the power of the beam in port A (light blue points) and port B (light green points) for various values of β. The dark blue line (dark green line) is the mean of all the measured powers in port A (port B).

To test the amplitude damping channel concept, the incoming mode was then set to a vortex mode (of $l = 1$) and the angle between the two Dove prisms varied from 0^o to 360^o, in increments of 10°. The data is shown in Fig. 3.2.3.3 for port A and Fig. 3.2.3.4 for port B. In performing these measurements, for each rotation of the Dove prism, constructive and destructive interference was first achieved in port A and B, respectively, for the case of an incoming Gaussian beam, so as to ensure the interferometer is correctly aligned before passing through the vortex mode. From Fig. 3.2.3.3 it is evident that when the relative angle between the two Dove prisms is an even multiple of 90^o, maximum transmission of the vortex mode occurs, which is in agreement with the 'odd-even OAM sorting' nature of the device. At an even multiple of 90^o, the reverse occurs in port B (Fig. 3.2.3.4), where minimum transmission of the vortex mode occurs. At odd multiples of 90°, minimum transmission of the vortex mode occurs in port A and maximum transmission in port B. As the angle increases from 0^o to 90^o (and any multiple of these angles) the transmission of the vortex mode in port A decreases, but consequently increases in port B.

Our theoretical model, given in Eq. (3.2.2.7), restricts the probability that the vortex exists in ports A and B by $\cos^2\beta$ and $\sin^2\beta$, respectively. This is evident in Figs 3.2.3.3 and 3.2.3.4, where

our measured data are in very good agreement with the predicted model. The errors given in the measurements in Figs 3.2.3.3 and 3.2.3.4 are the standard deviations of the measurements in Fig. 3.2.3.2, for ports A (0.06) and B (0.08).

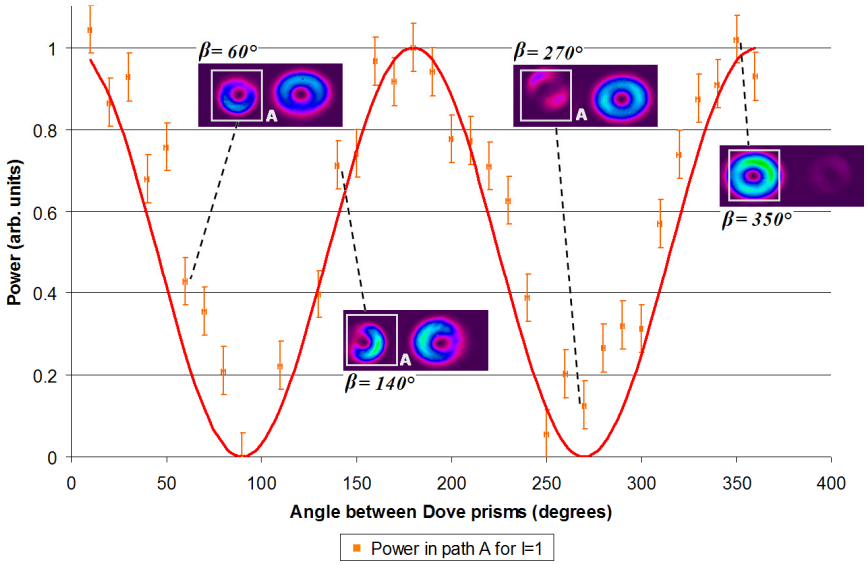

Fig. 3.2.3.3. Plot of the power of the beam recorded in port A (orange) for various values of β. The results follow the trend of that given in Eq. (3.2.2.4), $P_A \sim \cos^2\beta$. (red).

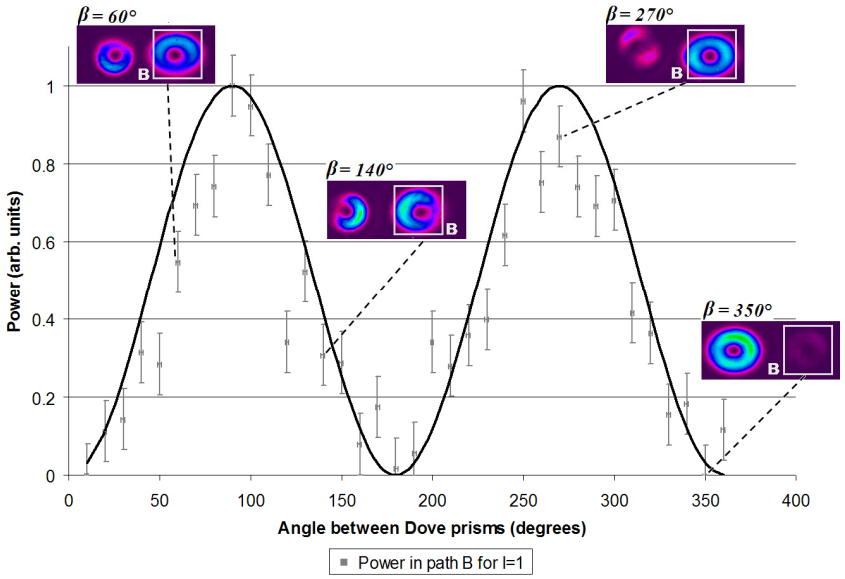

Fig. 3.2.3.4. Plot of the power of the beam recorded in port B (grey) for various values of β. The results follow the trend of that given in Eq. (3.2.2.5), $P_B \sim \sin^2\beta$. (black).

3.3. Conclusion

In this section we have presented an optical system, comprising an interferometer with Dove prisms in both arms, that acts as an amplitude damping channel for a two-level OAM system, and have verified its action experimentally using the vortex mode (l = 1) and a Gaussian mode [1]. This device is significant in that amplitude damping is a fundamental tool in classifying the behaviour of many quantum systems that incur the loss of energy. It can be used to describe the evolution of an atom that spontaneously emits a photon as well as how the state of a photon evolves in an optical system due to scattering and attenuation. The interferometer portion of this device can also be used for the classical superposition of vortex modes [6]. As well as to separate an incoming vortex mode into two different ports, where one has control over the weighting of the vortex mode assigned to each port. The advantage of this particular concept is that in entanglement decay experiments, this device can also be used to predict analytically the entanglement decay in OAM states when passing through such a channel. The concurrence of the entanglement will be measured both before and after the channel with standard state tomography techniques, thus allowing for a quantitative comparison of theory and experiment in the decoherence of entanglement due to interactions with a noisy environment.

3.4. References

[1]. A. Dudley, M. Nock, T. Konrad, F. S. Roux, and A. Forbes, "Amplitude damping of Laguerre-Gaussian modes," Opt. Express **18**(22), 22789-22795 (2010).

[2]. T. Konrad, F. De Melo, M. Tiersch, C. Kasztelan, A. Arag and A. Buchleitner, "Evolution equation for quantum entanglement," Nature Phys. **4**, 99-102 (2007).

[3]. B. Pors, C. H. Monken, E. R. Eliel, and J. P. Woerdman, "Transport of orbital-angular-momentum entanglement through a turbulent atmosphere," Opt. Express **19**(7), 6671-6683 (2011).

[4]. M. A. Nielsen and I. L. Chuang, "Quantum Computation and Quantum Information," Cambridge University Press, Cambridge, (2000).

[5]. J. Leach, M. J. Padgett, S. M. Barnett, S. Franke-Arnold, and J. Courtial, "Measuring the orbital angular momentum of a single photon," Phys. Rev. Lett. **88**(25), 257901 (2002).

[6]. A. Vaziri, G. Weihs, and A. Zeilinger, "Superpositions of the orbital angular momentum for application in quantum experiments," J. Opt. B: Quantum Semiclass. Opt. **4**, S47-S51 (2002).

CHAPTER FOUR

Superpositions of Higher-Order Bessel Beams

4.1. Introduction

Laguerre-Gaussian beams are not the only optical field which carry OAM. Any optical field which has a helical phase structure, such as higher-order Bessel beams, also carry OAM. In section 1.6, it was shown that zero-order Bessel beams have a bright central maximum, while the higher-orders have a dark central core (or vortex). Both of these forms of Bessel beams propagate in a diffraction-free manner. Durnin [1] first illustrated that a zero-order Bessel beam can be generated by illuminating a ring-slit aperture, placed in the back focal plane of a lens, with a plane wave. Other techniques, to generate both zero and higher-order Bessel beams, include axicons [2-4] and computer generated holograms [5-10]. Another approach creates a superposition of higher-order Bessel beams by illuminating an axicon with a superposition of LG modes [11].

In this chapter we extend Durnin's ring-slit experiment to produce superpositions of higher-order Bessel beams, by introducing multiple azimuthal phase components at various radial distances within the physical ring-slit aperture [12]. This concept is illustrated in Fig. 4.1.1, where two azimuthal phase factors, $\exp(il\theta)$ and $\exp(im\theta)$, programmed at different radial positions, produces a superposition of an l^{th} order and m^{th} order Bessel beam. We illustrate how the physical ring-slit aperture and hologram can be replaced by a single hologram [13].

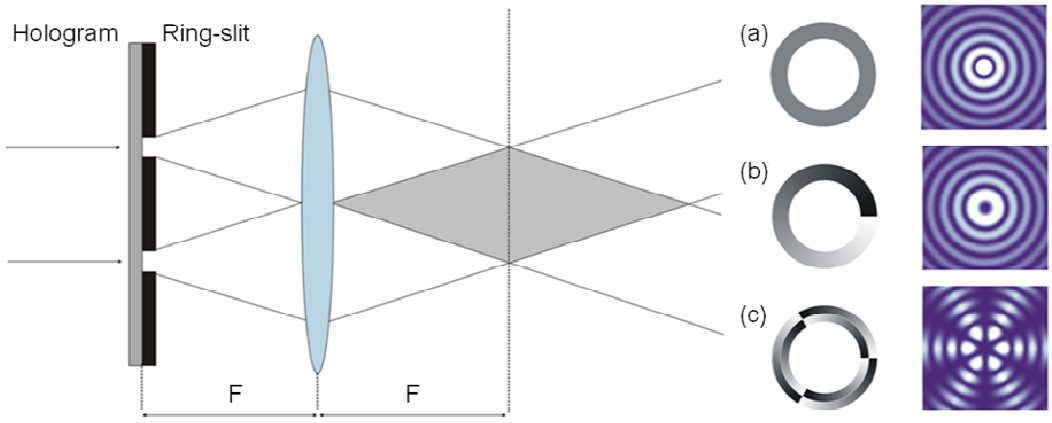

Fig. 4.1.1. An adaptation of Durnin's ring slit experiment [1]. (b) and (c): Illuminating the physical ring-slit aperture, with a beam whose angular spectrum carries an azimuthally varying phase, generates higher-order, and superpositions of higher-order, Bessel beams.

Theoretical studies into the rotation of superimposed Bessel beams have been made [12, 14], however the experimental determination of their rotation rates has not yet, to the best of our knowledge, been investigated. In this chapter we also experimentally measure the rotation rates of superpositions of higher-order Bessel beams [13]. We show that by varying the parameters of the ring-slit hologram (in terms of the width and the azimuthal order, l), we can control the rotation rates of the intensity profile. Therefore, it is an ideal tool for the controlled rotation of trapped particles [11]. The theoretical description for superimposed Bessel beams, along with its angular rotation, is presented in section 4.2. We also investigate, both theoretically and experimentally, the field produced at the ring-slit aperture and investigate its transition to the far-field (i.e. the field consisting of superimposed higher-order Bessel beams). We show that due to the fact that the longitudinal wave-vectors all propagate in the same direction (and do not overlap one another) in the near-field, no rotation is evident in the intensity profile. The area of the field which experiences the rotation increases as the field propagates to the far-field because the wave-vectors start to overlap one another to a greater degree.

4.2. Theory

In this work we implement Durnin's ring-slit aperture experiment [1] and encode a digital ring-slit hologram onto a SLM and illuminate it with an expanded Gaussian beam. We divide the ring-slit aperture into two ring-slits and encode each with an azimuthally varying phase. A schematic of the setup is given in Fig. 4.2.1, where the regions of interest, propagating after the

ring-slit aperture, are planes P_1 (the near-field), the region P_2 (the transition region from near- to far-field) and region P_3 (the far-field).

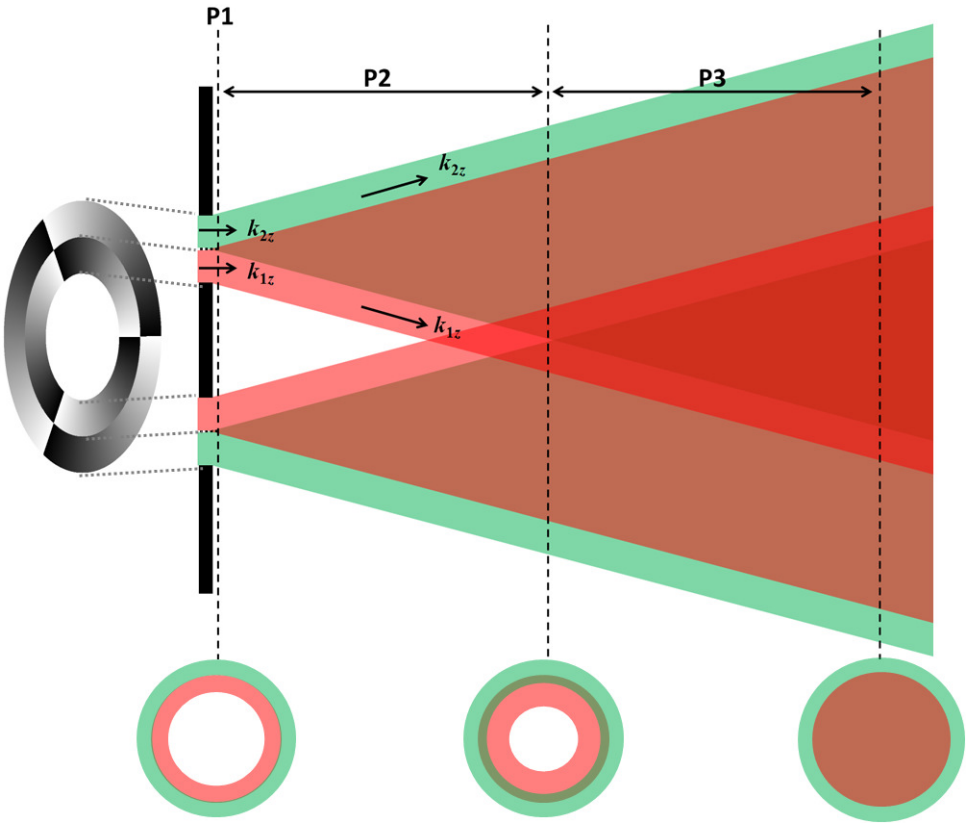

Fig. 4.2.1. A schematic of the generation of the annular field, propagating from near- (P_1) to far-field (P_3). The green (red) rays denote the rays originating from the outer (inner) ring-slit. The three rings (at the bottom of the schematic) aid the illustration, as to how the annular fields overlap and become completely indistinguishable as the propagation from the aperture increases.

The ring-slit aperture has the following transmission function

$$t(r,\theta)=\begin{cases}\exp(il\theta) & R_1-\dfrac{\Delta}{2}\le r\le R_1+\dfrac{\Delta}{2}\\ \exp(-il\theta) & R_2-\dfrac{\Delta}{2}<r\le R_2+\dfrac{\Delta}{2},\\ 0 & elsewhere\end{cases} \tag{4.2.1}$$

and apart from being illustrated in Fig. 4.2.1, is also represented in Fig. 4.2.2. R_1 and R_2 are the radii of each of the two ring-slits, respectively and Δ is the width of each ring-slit (here we have

chosen the widths of the two ring-slits to be equal). θ is the azimuthal angle and l is the azimuthal mode index.

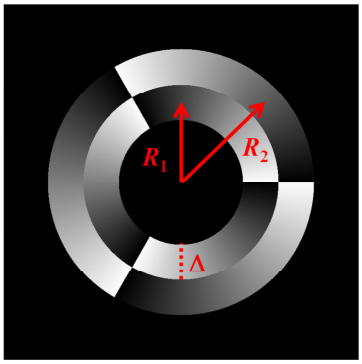

Fig 4.2.2. The transmission function described in Eq. (4.2.1) for an azimuthal mode index of l = 3.

Since the field illuminating the ring-slit aperture is an expanded Gaussian beam and the ring-slits are extremely thin (of the order of micro-meters), the field produced at the ring-slit aperture (i.e. at the plane P_1 where $z = z_0$), is represented as

$$A(r,\theta,z_0)=\begin{cases}\exp(il\theta)\exp(ik_{1z}z_0) & R_1-\dfrac{\Delta}{2}\le r\le R_1+\dfrac{\Delta}{2}\\ \exp(-il\theta)\exp(ik_{2z}z_0) & R_2-\dfrac{\Delta}{2}< r\le R_2+\dfrac{\Delta}{2}\\ 0 & elsewhere\end{cases}. \tag{4.2.2}$$

k_{1z} and k_{2z} are the longitudinal wave-numbers, defined as $k_{1z} = k\cos\alpha_1$ and $k_{2z} = k\cos\alpha_2$, where $k = 2\pi/\lambda$ and α is the opening angle of the cone on which the wave-vectors (produced by each ring-slit) propagate.

A simple annular field, containing no azimuthally-varying phase factors, may be expressed as

$$A(r)=\exp\left(\left(\frac{-(r-R_0)}{\Delta/2}\right)^n\right), \tag{4.2.3}$$

and is depicted graphically in Fig. 4.2.3. R_0 denotes the radius of the ring-slit; Δ is the width of the ring-slit; and n assigns the steepness (or gradient) of the edges of the ring-slit.

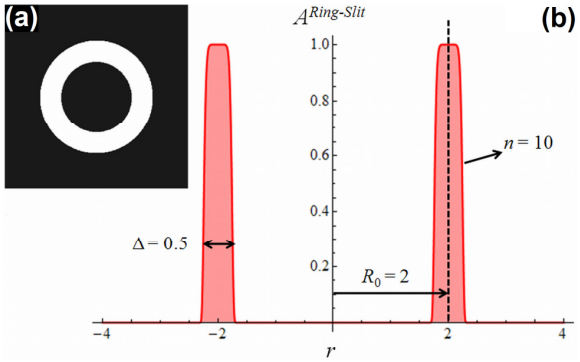

Fig. 4.2.3. (a) A density plot and (b) a cross-sectional plot of the ring-slit aperture described in Eq. (4.2.3) for the following parameters: ring-slit radius, R_0 = 2, ring-slit width, Δ = 0.5 and gradient, n = 10 (the units are arbitrary).

The ring-slit aperture that we are considering consists of two ring-slits of differing radii, and by taking into account that the optical field is a linear system, the two annular fields are additive, resulting in the overall ring-slit field, which in the near-field (P_1), has been written as

$$A(r,\theta,z_0) = A_1(r)\exp(il\theta)\exp(ik_{1z}z_0) + A_2(r)\exp(-il\theta)\exp(ik_{2z}z_0)$$
$$= \exp\left(\left(\frac{-(r-R_1)}{\Delta/2}\right)^n\right)\exp(il\theta)\exp(ik_{1z}z_0) + \exp\left(\left(\frac{-(r-R_2)}{\Delta/2}\right)^n\right)\exp(-il\theta)\exp(ik_{2z}z_0). \quad (4.2.4)$$

Since the two ring-slits are arbitrarily thin and close to one another, we can assume their radii to be equivalent, i.e. $R_1 \approx R_2 \approx R_0$, resulting in the field simplifying to

$$A(r,\theta,z_0) = \exp\left(\left(\frac{-(r-R_0)}{\Delta/2}\right)^n\right)\left(\exp(il\theta)\exp(ik_{1z}z_0) + \exp(-il\theta)\exp(ik_{2z}z_0)\right). \quad (4.2.5)$$

The intensity of the ring-slit field is determined as

$$I(r,\theta,z_0) = 4\cos^2\left(\frac{k_{1z}z_0 - k_{2z}z_0 + 2l\theta}{2}\right)\left(\cosh\left(\frac{2(r-R_0)}{\Delta}\right) - \sinh\left(\frac{2(r-R_0)}{\Delta}\right)\right)^{2n}. \quad (4.2.6)$$

The intensity profile for the ring-slit field, given above in Eq. (4.2.6), illustrates that it is modulated in the azimuthal co-ordinate, θ, by the function $\cos^2(l\theta)$. Therefore, the number of intensity maxima and minima, arranged on the circumference of the ring-slit, is twice the azimuthal mode index, l.

The angular rotation, experienced by the intensity profile, as the ring-slit field propagates in the near-field (P_1) along the z-axis, is then given by

$$\frac{d\theta}{dz_0} = \frac{k_{2z} - k_{1z}}{2l}. \tag{4.2.7}$$

During the propagation of the ring-slit field, the longitudinal wave-vectors, k_{1z} and k_{2z}, both propagate in the same direction, parallel to the z-axis, which is illustrated in Fig. 4.2.1. This results in no angular rotation existing, as the ring-slit field propagates,

$$\frac{d\theta}{dz_0} = 0. \tag{4.2.8}$$

In determining the field in the region P_2, the region in which the field transitions from near- to far-field, the Fresnel diffraction integral of the field at the ring-slit aperture (Eq. (4.2.4)) can be calculated to be

$$A(r,\theta,z) = \frac{e^{ikz}}{i\lambda z}\int_0^{2\pi}\int_{R_1-\frac{\Delta}{2}}^{R_2+\frac{\Delta}{2}} A(r,\theta_1,z_0)\exp\left(i\frac{k}{2z}({r_1}^2 + r^2 - 2rr_1\cos(\theta_1-\theta)\right) r_1 dr_1 d\theta_1, \tag{4.2.9}$$

and is known to produce the Bessel-Gauss[15, 16] and Bessel functions. Each of the two ring-slits (the inner having an azimuthal mode index of l and the outer, $-l$) will contribute to a Bessel Gauss beam and the resulting superposition of the field in region P_2 can be described as

$$A(r,\theta,z) = A_{BG\,1}(r,\theta,z) + A_{BG\,2}(r,v,z) =$$
$$\left(\frac{1}{\sqrt{1+\left(\frac{z}{z_r}\right)^2}}\right)\left(\begin{array}{l}\exp\left[i\left(kz - \frac{{k_{1r}}^2 z}{2k} - \Phi(z)\right) - \left(\frac{1}{\omega^2(z)} - \frac{ik}{2R(z)}\right)\left(r^2 + \left(\frac{k_{1r}z}{k}\right)^2\right) + ik_{1z}z + il\theta\right] J_l\left(\frac{k_{1r}r}{1+i(z/z_r)}\right) + \\ \exp\left[i\left(kz - \frac{{k_{2r}}^2 z}{2k} - \Phi(z)\right) - \left(\frac{1}{\omega^2(z)} - \frac{ik}{2R(z)}\right)\left(r^2 + \left(\frac{k_{2r}z}{k}\right)^2\right) + ik_{2z}z - il\theta\right] J_{-l}\left(\frac{k_{2r}r}{1+i(z/z_r)}\right)\end{array}\right). \tag{4.2.10}$$

The functions $\omega(z)$, $R(z)$ and $\Phi(z)$ denote the beam size, radius of curvature and Gouy phase, respectively and take on the standard Gaussian beam propagation form. J_l is the l^{th} order Bessel function and k_r denotes the transverse wave-number, associated with each of the two Bessel beams, namely 1 and 2, and is determined as follows: $k_r = k\sin\alpha$.

Similarly the intensity in the region of P_2 can be determined by combining the relationship $I = AA^*$ with the angular rotation, which results in

$$\frac{d\theta}{dz} = \frac{k_{2z} - k_{1z}}{2l}. \tag{4.2.11}$$

The wave-vectors in this region do not point in the same direction resulting in a non-zero rotation rate. However the only section of the field which experiences this angular rotation is the section which consists of the contributions from both ring-slits, which visually means: the sections which consist of both green and red rays. As the field propagates further towards the far-field (P_3), the overlap in the field, which consists of both ring-slit contributions, increases, resulting in the angular rotation becoming more evident.

To determine the far-field of the ring-slit aperture (P_3), whose transmission function $t(r,\theta)$ is given in Eq. (4.2.1), the Kirchoff-Huygens diffraction integral is used:

$$A(r,\theta,z) = \frac{-i}{\lambda z}\int_0^{2\pi}\int_{R_1-\frac{\Delta}{2}}^{R_2+\frac{\Delta}{2}} t(r,\theta_1)\exp\left[i\frac{k}{2f}\left(1-\frac{z}{f}\right)r_1^2\right]\exp\left[-i\frac{krr_1}{f}\cos(\theta_1-\theta)\right]r_1 dr_1 d\theta_1. \tag{4.2.12}$$

The contribution resulting from the inner and the outer ring-slits produces the following superposition, which describes the far-field of the ring-slit aperture [12]

$$A_l(r,\theta,z) = \frac{-ik}{f}\int_{R_1-\frac{\Delta}{2}}^{R_1+\frac{\Delta}{2}} i^l \exp(il\theta)J_l\left(\frac{krr_1}{f}\right)\exp\left[-\frac{r_1^2}{\omega^2}+\frac{ikr_1^2}{2f}\left(1-\frac{z}{f}\right)\right]r_1 dr_1 \tag{4.2.13}$$

$$A_{-l}(r,\theta,z) = \frac{-ik}{f}\int_{R_2-\frac{\Delta}{2}}^{R_2+\frac{\Delta}{2}} i^{-l} \exp(-il\theta)J_{-l}\left(\frac{krr_1}{f}\right)\exp\left[-\frac{r_1^2}{\omega^2}+\frac{ikr_1^2}{2f}\left(1-\frac{z}{f}\right)\right]r_1 dr_1 \tag{4.2.14}$$

$$A(r,\theta,z) = J_l(k_{1r}r)\exp(il\theta)\exp(ik_{1z}z) + J_{-l}(k_{2r}r)\exp(-il\theta)\exp(ik_{2z}z), \tag{4.2.15}$$

where the following approximation

$$k_r = k \sin\alpha = k \sin\frac{R}{f} \approx \frac{kR}{f} \tag{4.2.16}$$

has been used. The intensity of the superimposed Bessel field is determined as

$$I(r,\theta,z) \propto J_l^2(k_{1r}r) + J_{-l}^2(k_{2r}r) + 2J_l(k_{1r}r)J_{-l}(k_{2r}r)\cos\left(k_{1z}z - k_{2z}z + 2l\theta\right). \tag{4.2.17}$$

Since the annular rings generating the superimposed Bessel beams are arbitrarily thin and close to one another, we can assume the transverse wave-numbers to be equivalent (i.e. $k_{1r} \sim k_{2r} = k_r$), resulting in $J_l(k_{1r}r) \sim J_l(k_{2r}r) = J_l(k_r r)$. By implementing the Bessel function identity, $J_{-l}(k_{2r}r) = (-1)^l J_l(k_{2r}r)$, the intensity in Eq. (4.2.17) can be simplified to produce

$$I(r,\theta,z) \propto 2J_l^2(k_r r)\left((-1)^l + 1 + 2(-1)^l \cos(k_{1z}z - k_{2z}z + 2l\theta)\right). \tag{4.2.18}$$

The intensity profile for the superimposed Bessel beams, given above in Eq. (4.2.18), illustrates that it is modulated in the azimuthal co-ordinate, θ, by the function $\cos^2(l\theta)$. Therefore, the number of intensity maxima is twice the order l of the two Bessel beams, resulting in a superposition of a l^{th} order Bessel beam, with its mirror image, producing an intensity pattern having $2|l|$ intensity maxima, or petals, arranged on the circumference of the set of Bessel rings. This intensity profile experiences an angular rotation, as the field propagates along the z-axis. The rotation angle is

$$\theta = \frac{(k_{2z} - k_{1z})z}{2l} \tag{4.2.19}$$

and the rotation rate is given by

$$\frac{d\theta}{dz} = \frac{k_{2z} - k_{1z}}{2l}. \tag{4.2.20}$$

Since the longitudinal wave-vectors all propagate in different directions in the far-field and the field contributions from the two ring-slits completely overlap (evident in Fig. 4.2.1), the angular rotation is non-zero and the near-diffraction-limited beam at P_3 experiences the rotation.

4.3. Generating superpositions of higher-order Bessel beams with a physical ring-slit aperture and a hologram

In this section we will outline how we make use of a physical ring-slit aperture and a SLM to generate superpositions of higher-order Bessel beams. In section 4.4, we will then show how our technique can be reproduced into a simpler single hologram.

The setup to generate superpositions of higher-order Bessel beams is given as a schematic in Fig. 4.1.1 above. A detailed diagram of our experimental setup is given in Fig. 4.3.1. A HeNe laser ($\lambda \sim 633$ nm) was expanded through a 15 × telescope before illuminating a physical ring-slit aperture ($R = 3$ mm and $\Delta = 150$ μm). The ring field produced at the plane of the ring-slit aperture was relay imaged to the plane of the liquid crystal display with a 0.75 × telescope. A Holoeye HEO1080P SLM with 1920 × 1080 pixels of pitch 8 μm and calibrated for a 2π phase shift at ~ 633 nm was used to impart the azimuthal phase variation to the ring field. The field produced in the Fourier plane after lens, L5, was magnified with a 10 × objective and detected on a CCD camera (Spiricon, USB L130). The objective and CCD camera were both positioned on a translation stage in order to investigate the propagation of the resulting field. An interferometer, denoted by the red overlay, was introduced in the experimental setup so as to interfere a plane wave with the superposition field to reveal the fork interference patterns [17]. The beam size of the Gaussian beam was large in comparison to the Bessel field in the Fourier plane so the wavefront of the Gaussian field can be assumed to be flat, similar to a plane wave.

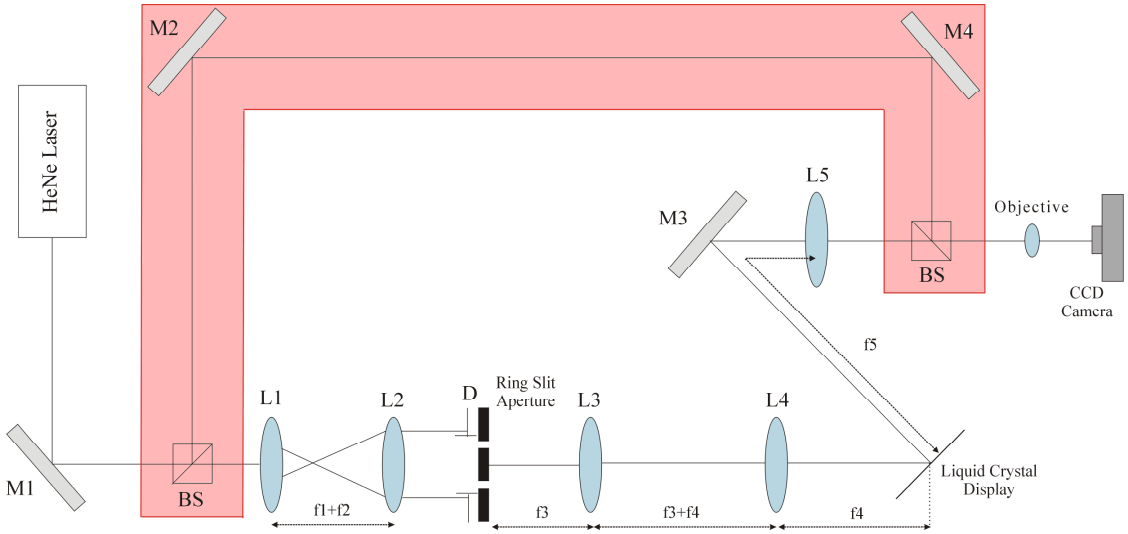

Fig. 4.3.1. The experimental setup for generating a superposition of higher-order Bessel beams, by using a physical ring-slit aperture and a hologram. The interferometer used to interfere the field produced at the Fourier plane with a plane wave is denoted in the red overlay. (M: mirror; BS: beam-splitter; L: lens and D: diaphragm). (f_1 = 10 mm, f_2 = 150 mm, f_3=100 mm, f_4=75mm and f_5 = 200 mm).

In this system the alignment of the ring field onto the hologram programmed on the SLM, was critical. The liquid crystal display was placed on a standard micro-meter translation stage, so as to carefully position it in the centre of the ring field. It should also be pointed out that this approach was not optimized for energy transmission; the loss through the ring-slit aperture was very high. Results for this experimental setup are given in the next section.

4.3.1. Results

The results obtained with the setup described in Fig. 4.3.1 appear in Fig. 4.3.1.1.

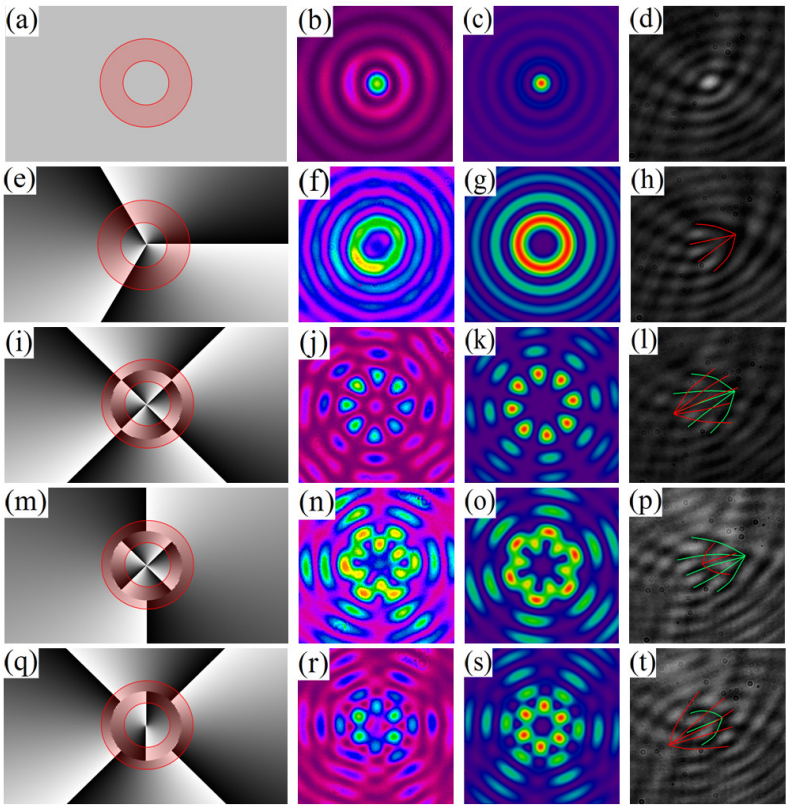

Fig. 4.3.1.1. *First column*: Holograms applied to the SLM. *Second column*: The observed intensity pattern observed in the Fourier plane. *Third column*: The theoretical prediction of the superposition field. *Fourth column*: The interference pattern of the superposition field and a plane wave. Data is shown for (a) – (d): A_0, (e) – (h): A_3, (i) – (l): $A_{4,-4}$, (m) – (p): $A_{2,-4}$, and (q) – (t): $A_{4,-2}$. The ring field is shown as a red overlay on the hologram.

When the ring field illuminates a hologram which has no azimuthally varying phase, Fig. 4.3.1.1 (a), it produces the well known zero-order Bessel beam. In conducting the experiment, a blazed grating was added to the holograms (appearing in the first column of Fig. 4.3.1.1), we have neglected to include them here as we want to highlight the azimuthal components. In the case of a single azimuthal component ((e)) a higher-order Bessel beam is produced ((f)). The fields are interfered with a plane wave to reveal the vortex nature of the fields. In the case that a third-order Bessel beam interferes with a plane wave, three dislocations are noted in the fork interference pattern ((h)). By increasing the number of azimuthal components ((i), (m) and (q)), the field in the Fourier plane becomes more complex ((j), (n) and (r)), however, the theoretical predications ((k), (o) and (s)) are in very good agreement with the measured field. When the two azimuthal phases are equal, but of opposite handedness (i), a petal pattern is produced (j), as described in Eq. (4.2.18). Due to the azimuthally varying phase which is imparted to the ring

field, the resulting fields possess vortices. The orientation of these vortices is not very intuitive and has recently been investigated [18]. For the superposition of two higher-order Bessel beams, the interference patterns contain two overlapping forks. The number of dislocations or spaces between the fork prongs conveys the order of the Bessel fields involved in the superposition and the direction of the fork prongs communicates the sign of the Bessel beams.

Even though we have illustrated the concept with only two Bessel beams, it is possible to extend this to any number of azimuthal components. The result in Fig. 4.3.1.2 is for a three-component superposition, where the azimuthal indices are as follows -3, 0 and 3 (labeled from the outer ring to the inner ring). Good agreement between experimentally recorded and theoretically predicted fields is obtained.

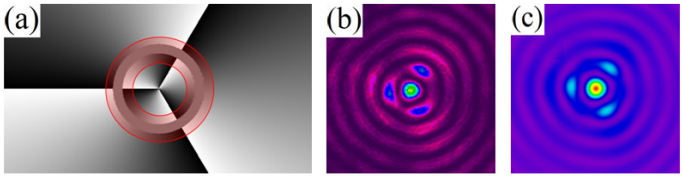

Fig. 4.3.1.2. (a) Hologram applied to the liquid crystal display. The red overlay denotes the section of the hologram which was illuminated by the ring field. (b) The experimental beam cross-section of the field produced at the Fourier plane and the theoretically calculated field (c).

The propagation of the fields generated with this technique was also investigated and experimental images of the intensity profile, recorded at intervals along its propagation, appear in Fig. 4.3.1.3. In studying the experimental images contained in Fig. 4.3.1.3, it is evident that the intensity profile containing the highest amount of energy occurs half way along the field's propagation. This occurs at the focal length of the Fourier transforming lens. It is also evident that the field is quasi-non-diffracting as it maintains its intensity profile for a set portion of its propagation. The non-diffracting nature of certain fields has been investigated in great detail [19-27] and can be explained by the fact that the fields are derived from the annular structure of the ring-slit aperture and the azimuthal phase is only an additional degree of freedom. The field also appears to rotate as it propagates, evident in the images contained in Fig. 4.3.1.3.

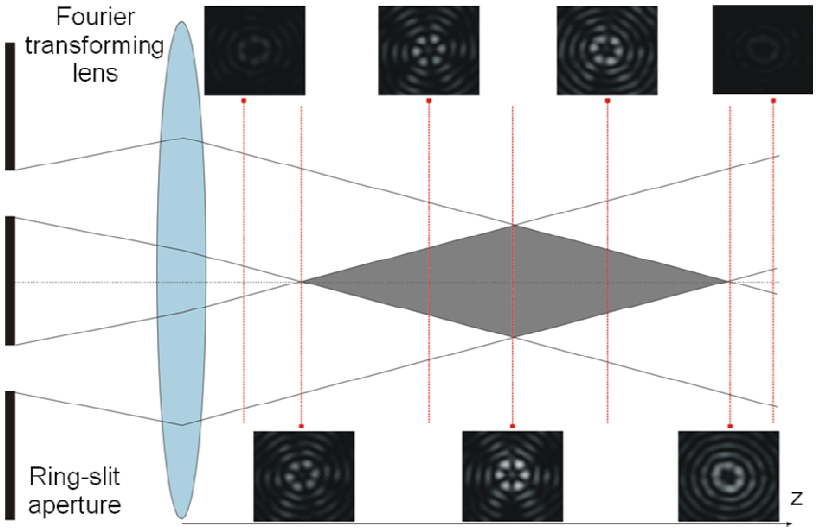

Fig. 4.3.1.3. Images of the intensity profile of the experimentally produced field $A_{3,-3}$ captured at intervals along its propagation. The grey area denotes the region in which the Bessel field exists.

4.4. Generating superpositions of higher-order Bessel beams with a single hologram

In this section we will introduce a technique that has allowed us to remove the physical ring-slit in our previous setup (Fig. 4.3.1) and instead make use of a single hologram to produce the superposition fields in Fig. 4.3.1.1. The technique involves addressing alternating sets of pixels on the liquid crystal display with phase values that are out of phase by π, resulting in the light reflected from the LCD being scattered from its initial propagation axis [28]. By being able to control the amplitude that is transmitted along the propagation axis, we were able to operate our phase-only SLM in both amplitude and phase mode. We are therefore able to encode Durnin's ring-slit [1] into a single hologram, as well as have control over the phase within the ring-slits. This technique which involves addressing alternating sets of pixels with phase values that are out of phase by π, so as to produce a checkerboard pattern, is discussed in section 4.4.1. after which the experimental realization is presented in section 4.4.2.

4.4.1. Checkerboard approach

Ideally if we wanted to encode the ring-slit aperture onto the SLM, we would need a SLM that is capable of controlling both phase and the amplitude. A hologram, such as that in Fig. 4.4.1.1 (a), if encoded on a phase and amplitude SLM, would transmit light within the ring-slit and not transmit light in the surrounding black areas.

Even though we do not have a phase and amplitude SLM, we can still use our phase-only SLM by addressing the sections, in which we do not want to transmit any light, with a checkerboard pattern. An example of such a hologram is given in Fig. 4.4.1.1 (b) accompanied with a zoomed-in section of the checkerboard pattern.

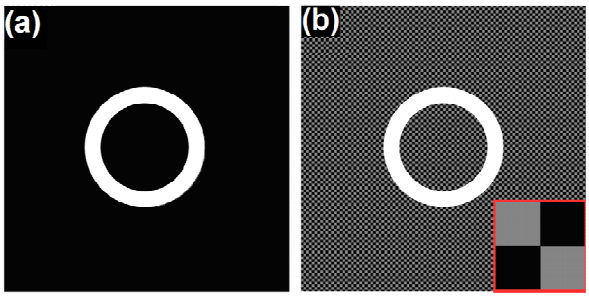

Fig. 4.4.1.1. In order to reproduce Durnin's ring-slit experiment [1] either (a) the light can be suitably apertured by a physical ring-slit aperture; or (b) complex amplitude modulation can be used on a phase-only SLM to execute both the amplitude and phase transformations in one step. The inset in (b) shows the checkerboard pattern used to modulate the amplitude.

To understand why a pattern consisting of alternating sets of pixels, that are assigned phase values that are out of phase by π, can be used to mimic an amplitude mask, the schematic in Fig. 4.4.1.2 needs to be introduced. This figure represents phase values on a complex plane. In the checkerboard pattern the weighting of each of the phase values, 0 and π, is uniform (or equal), which in the complex plane approach translates to each vector (A_1 and A_2) having the same amplitude, but pointing in opposite directions along the x-axis. This leads to the resultant, A_3, having no amplitude (or DC component) and is positioned at the origin of the complex plane. The fact that the resultant has no amplitude means that the average amplitude of the field at the checkerboard hologram is zero. This results in a zero in the intensity on the propagation axis in the Fourier plane, with the light shifted away from the origin due to the high spatial frequency of the checkerboard, as illustrated in Fig. 4.4.1.2 (c). When the SLM is addressed with a single

uniform grey-level (Fig. 4.4.1.2 (d)), the resultant vector in the complex plane, A_3, has an amplitude, lying along the positive x-axis, meaning the average amplitude at this phase-mask is non-zero, giving rise to an on-axis intensity in the Fourier plane, evident in Fig. 4.4.1.2 (e). Experimentally, through 'trial-and-error', it was found that the checkerboard pattern diffracted the on-axis intensity the best, when each checker was assigned to an area of 5 × 5 pixels on the SLM.

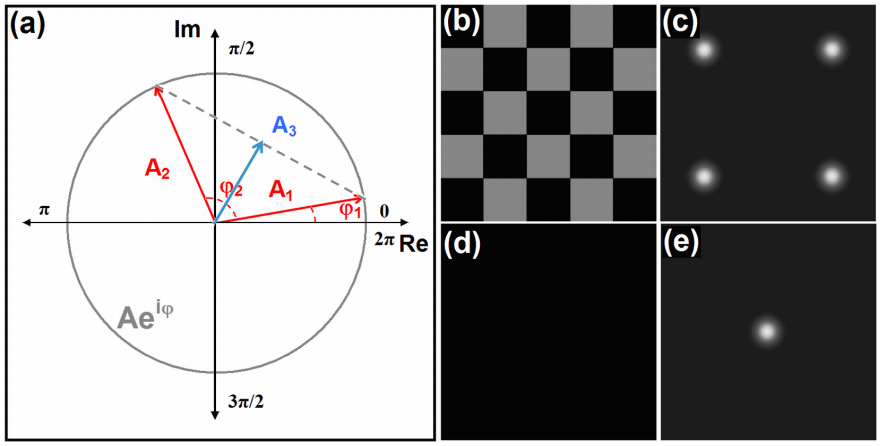

Fig. 4.4.1.2. (a) The complex plane representation; the angles, φ_1 and φ_2, for each vector, A_1 and A_2, represents a phase value in the hologram. The resultant amplitude, A_3, is denoted by the blue vector. (b) The checkerboard hologram and (c) the corresponding Fourier plane, illustrating that the light is distributed off of its propagation axis. (d) A plain black hologram. (e) The Fourier transform of the hologram in (d) illustrating an on-axis intensity component.

4.4.2. Experimental methodology

The experimental setup for implementing the single ring-slit hologram is very similar to that described in section 4.3, but with the physical ring-slit aperture removed as well as the imaging optics associated with it. The setup that we implement is depicted in Fig. 4.4.2.1 and entails a He-Ne laser being expanded through a 6 × telescope and directed onto the liquid crystal display of a SLM. Due to the dynamic programming of SLMs, the azimuthal phase within each of the ring-slits can easily be varied. Some of the ring-slit holograms that are encoded onto the SLM appear in the top row of Fig. 4.4.3.1. A blazed grating was added to these holograms, so as to separate the undiffracted and diffracted components reflected from the SLM. The Fourier transform of the field at the ring-slit hologram was obtained with the use of lens L_3. The field was then magnified with a 10 × objective and captured on a CCD camera. The objective and

CCD camera were positioned on a translation stage on an optical rail in order to investigate the propagation of the resulting field.

Apart from positioning a 10 × objective and a CCD camera at the Fourier plane, P_3, of lens L_3, to record the non-diffracting superimposed Bessel beam, a second lens, L_4, was placed a focal length away from the Fourier plane of lens, L_3, to relay the field at LCD_1 to plane P_1. This allowed us to investigate the structure of the ring-slit field (evident at P_1) which produces a petal structure in the far-field (illustrated at P_3). The propagation of the ring-slit field, relayed to plane, P_1, was investigated by positioning a CCD camera on a rail and recording the field from plane P_1 to plane P_2 (a distance of two focal lengths from lens, L_4).

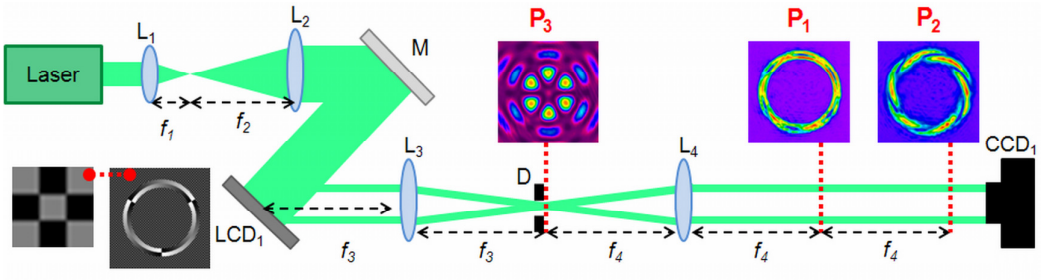

Fig. 4.4.2.1. A schematic of the experimental setup for investigating the field formed by a ring-slit hologram, as well as the propagation and Fourier transform of such a field. L: Lens (f_1 = 25 mm; f_2 = 75 mm; f_3 = 100 mm and f_4 = 100 mm); M: Mirror; LCD: Liquid Crystal Display; D: Diaphragm; CCD: CCD Camera. The planes of interest are marked P_1, P_2 and P_3. P_3 is the Fourier plane of the ring-slit hologram; P_1 is the relayed-field (in both phase and amplitude) at the ring-slit hologram; and P_2 occurs a distance of $2f$ after L_4.

4.4.3. Results

All the digital ring-slit holograms, used in the experiment (depicted in Fig. 4.4.2.1), are given in the first row of Fig. 4.4.3.1. The first ring-slit hologram, Fig. 4.4.3.1 (1a), consists of a single ring-slit containing an azimuthal phase of l = +3 and has the following dimensions (in pixels): R_1 = 180, Δ = 20. The next five ring-slit holograms, Fig. 4.4.3.1 (1b) – (1f), all consist of two ring-slits, having oppositely varying azimuthal phases, varying in azimuthal order from l_{inner} = +1 to +5 (l_{outer} = -1 to -5), respectively. The ring-slit holograms in Figs 4.4.3.1 (1b) – (1f) each have the following dimensions (in pixels): R_1 = 180, R_2 = 190, Δ = 10**.** The last two ring-slit holograms (Fig. 4.4.3.1 (1g) and (1h)) are divided into three and four ring-slits, respectively, having the following azimuthal orders: l_{inner} = -3, l_{middle} = 2, l_{outer} = 1, and l_{inner} = -2, $l_{middle1}$ = -1,

$l_{middle2} = 2$, $l_{outer} = 1$. The dimensions (in pixels) of the ring-slits in Fig. 4.4.3.1 (1g) and (1h) are: $R_1 = 180$, $R_2 = 190$, $R_3 = 200$, $\Delta = 10$ and $R_1 = 168$, $R_2 = 176$, $R_3 = 184$, $R_4 = 192$, $\Delta = 8$.

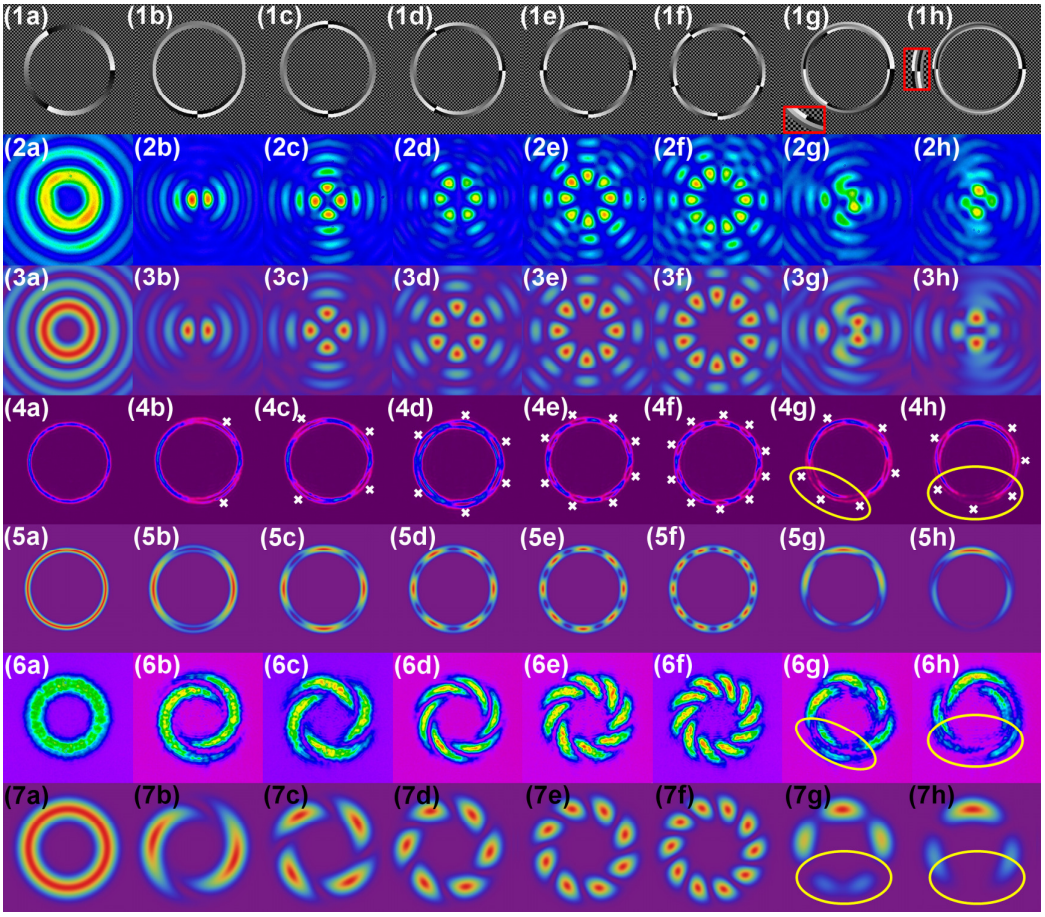

Fig. 4.4.3.1. *First row*: The ring-slit holograms addressed to LCD_1. A zoomed-in section of three and four ring-slits are depicted as inserts ((1g) and (1h)). *Second and third rows*: The experimentally produced and theoretically calculated fields produced in the Fourier plane (i.e. plane P_3), respectively. *Fourth and fifth rows*: The experimental and theoretical fields, respectively, produced at plane P_1. The white "X" marks the singularities. *Sixth and seventh rows*: The experimental and theoretical fields, respectively, produced at plane P_2.

The far-fields of the ring-slit holograms, presented in the first row of Fig. 4.4.3.1, are shown in the second row of Fig. 4.4.3.1, accompanied with their theoretical predictions in the third row (calculated with the use of Eq. (4.2.15)). For a single ring-slit, containing an azimuthal index of $l = +3$, the field produced in the Fourier plane, P_3, is a third order Bessel beam. In the case that the ring-slit hologram consists of two ring-slits, where the orders of the two azimuthal phases are of equal but opposite handedness, a petal structure is produced, where the number of petals

is denoted by $2|l|$, as expected from theory [8]. It is interesting, to note from previous investigations [4, 8], that even though these fields have a global OAM of zero, their cross-sectional intensity distribution rotates as the petal field propagates, due to the differing radial wave-vectors. Their rotation rate, which is dependent on the differing radial wave-vectors and the azimuthal index, l, is given in Eq. (4.2.20). The fields produced in the Fourier plane, P_3, for the ring-slit holograms, contained in Figs 4.4.3.1 (1g) and (1h) are given in Figs 4.4.3.1 (2g) and (2h), respectively. These two ring-slit holograms consist of three and four ring-slits, respectively, and produce a non-symmetric superposition of higher-order Bessel beams. Even though it is difficult to intuitively predict how the field will manifest in the Fourier plane for these two cases, our experimentally recorded fields (Figs 4.4.3.1 (2g) and (2h)) are in very good agreement with the theoretically calculated fields (Figs 4.4.3.1 (3g) and (3h)). These two fields are calculated by extending the amplitude distribution, given in Eq. (4.2.15), to represent a superposition of three and four Bessel beams, respectively.

The intensity profiles of the superimposed non-diffracting fields were captured at discrete distances along their propagation (one example is given in Fig. 4.4.3.2). In Fig. 4.4.3.2 the petal structure appears at the beginning of its propagation with low intensity, reaching a maximum mid-way through, and then decreasing again as the conical waves separate out again back to an annular ring structure. It is also evident from this figure that the intensity appears to rotate about the propagation axis. From such images the angular position of a selected petal was calculated and plotted as a function of the propagation distance (one example is given in Fig 4.4.3.3). The rotation rate of the intensity profile as it propagates was then determined from the slope of the straight line which best fits the measured angular positions, as a function of the propagation distance. The slope of the linear fit, in Fig. 4.4.3.3, was calculated to be 9.6 rad/m, which is within 13% of the theoretically calculated result of 11.1 rad/m.

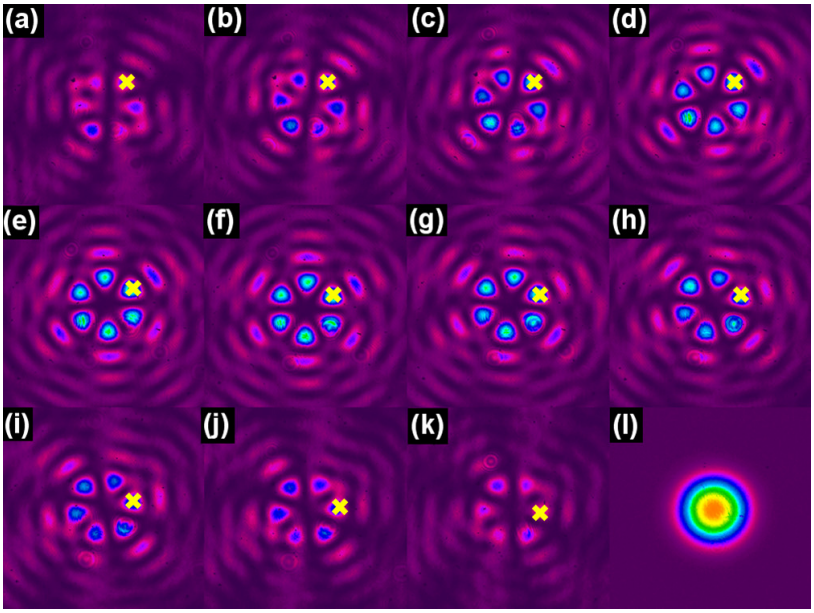

Fig. 4.4.3.2. (a) - (k) Images of the intensity profiles of the experimentally produced field, for $|l|$ = 3, captured at intervals along its propagation. The yellow 'X' denotes a selected petal. Monitoring its change in position illustrates a rotation in the field as it propagates. (l) The initial Gaussian beam which illuminated the SLM.

The error between the experimentally measured and theoretically calculated rotation rates was attributed to the technique we implemented to calculate the angular position of the petal. Since the coordinate for the centroid of the petal was obtained by manually selecting this pixel in the CCD image, error analysis in the angular positions needed to be performed. The standard deviation in the angular position was obtained by assuming that the manually selected coordinate lies within a one-sixth range of the petal's diameter from the true centroid,

$$\theta_\sigma = \arctan\left(\frac{\sigma}{R}\right) = \arctan\left(\frac{D}{18R}\right). \qquad (4.4.3.1)$$

D is the diameter of the petal and R is the distance from the propagation axis to the centroid of the petal. In Fig. 4.4.3.1 it is evident that the radius, R, increases with the Bessel beam order $|l|$, which results in the standard deviation of the petal position, which is scaled as a function of R, to be scaled as a function of $|l|$.

Figure 4.4.3.3 below contains the measured angular positions as a function of the propagation distance, for the case when the azimuthal order was $|l|$ = 3 and the difference between the two

radial wave-vectors was $\Delta k \sim 66\ m^{-1}$.The standard deviation in the angular position is 80 mrad and the error in the propagation distance is 1mm; as this is the smallest increment on the optical rail on which the detection system was mounted.

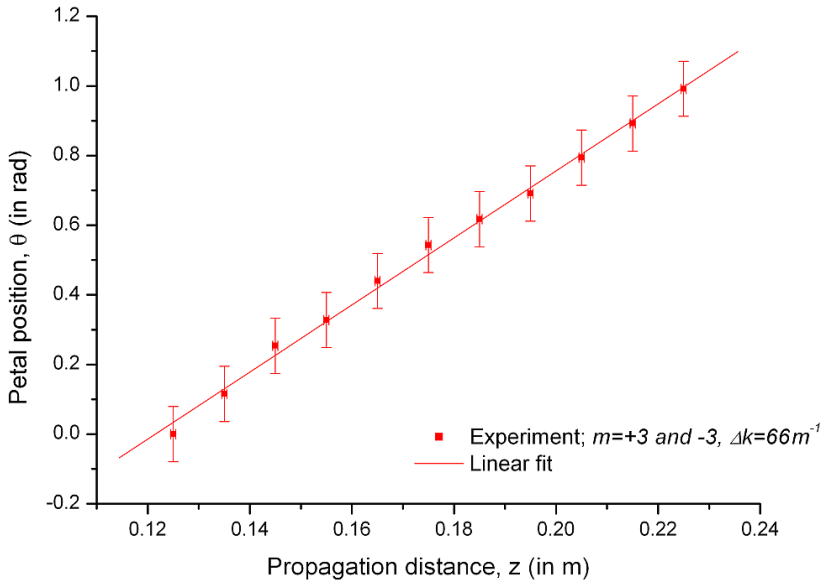

Fig. 4.4.3.3. Graph of the angular position of a selected petal as a function of the propagation axis z. ($|l| = 3$ and $\Delta k = 66\ m^{-1}$)

Similar graphs, as that presented in Fig. 4.4.3.3, were obtained for various values of $|l|$ and Δk, from which the rotation rates were calculated from the slopes of their linear fits. Figures 4.4.3.4 and 3.4.3.5 contain plots of the measured rotation rates as a function of the azimuthal order, $|l|$, and the difference between the two radial wave-vectors, Δk, respectively. The theoretical predictions, taken from Eq. (4.2.20), are given as dashed lines. Figure 4.4.3.4 is a plot of the measured rotation rate, for six different sets of radial wave-vectors, plotted as a function of the azimuthal order $|l|$, illustrating that as the magnitude of $|l|$ increases, so there is a hyperbolic decrease in the rotation rate. The rotation rates were also plotted as a function of the difference between the two radial wave-vectors, for various azimuthal orders, $|l|$, and are depicted in Fig. 4.4.3.5. By increasing the distance between the two radial wave-vectors (achieved by increasing the width of the inner and outer ring-slits in the holograms), the rotation rate of the petals are increased, evident in Fig. 4.4.3.4. There is very good agreement in our measured rotation rates and the theoretical model (dashed curves).

Since the rotation rates are dependent on the angular position of the petal, the standard deviation was determined by the standard deviation in the slope of the graph of the petal position, as a function of the propagation distance, by the following relationship

$$\theta = slope \times z \rightarrow slope_{\sigma} = \frac{\theta_{\sigma} - nz_{\sigma}}{z} = \frac{\theta_{\sigma}}{z}. \qquad (4.4.3.2)$$

θ_{σ} is the standard deviation in the angular position of the petal given by Eq. (4.4.3.1) and z is the median of the propagation intervals at which the field is captured. The standard deviation for the rotation rate (Eq. (4.4.3.2)), for the case when $|l| = 3$, was found to be ~ 0.5 rad/m. Since the radius of each ring-slit could be accurately measured to within a single pixel, the absolute error for the difference between the two wave-vectors, and hence the error in the x axis, was calculated to be ~ 6 m^{-1}.

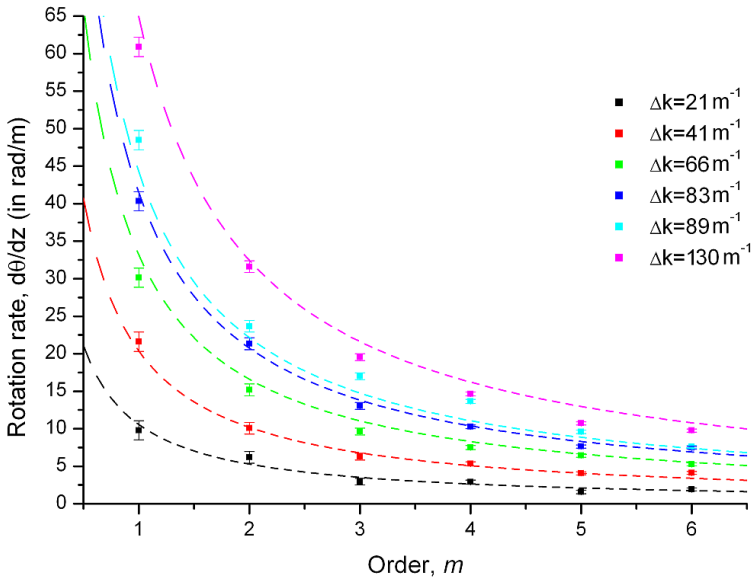

Fig. 4.4.3.4. Graphs of the rotation rates, for various differences between the two radial wave-vectors, as a function of the azimuthal order, $|l|$.

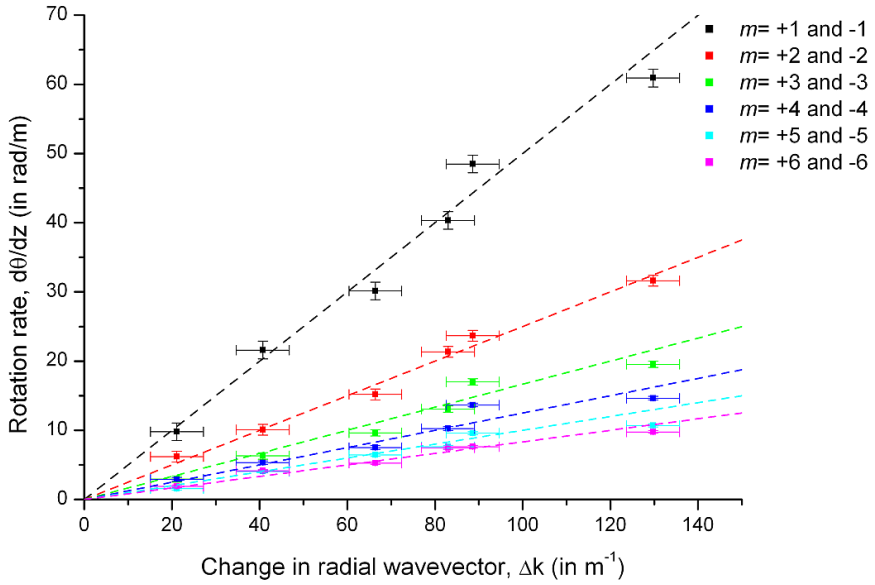

Fig. 4.4.3.5. Graphs of the rotation rates, for various azimuthal orders $|l|$, as a function of the difference, Δk, between the two radial wave-vectors.

In all of the measurements given so far (Figs 4.4.3.3, 4.4.3.4 and 4.4.3.5), the azimuthal phase within the outer ring-slit varied from black to white in a clockwise direction and that in the inner ring-slit in an anticlockwise direction. By inverting the handedness of the two ring-slits, the field will rotate with the same rate, but in the opposite direction. An example of this is given in the video slides of Fig. 4.4.3.6.

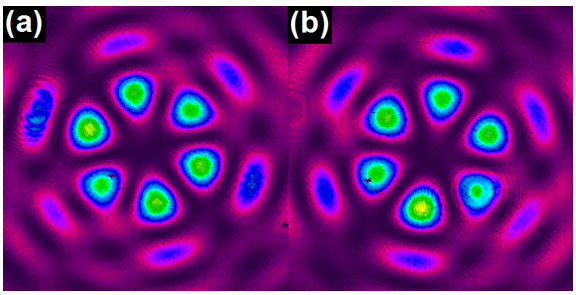

Fig. 4.4.3.6. Video clips containing experimental images, captured at intervals along the beam's propagation, for fields generated from holograms having the following parameters (a) $l_{inner} = +3$; $l_{outer} = -3$ and (b) $l_{inner} = -3$; $l_{outer} = +3$. In the electronic version of this thesis the videos may be viewed at the following links: (a) Media1 and (b) Media2.

The optical field produced at the plane of the ring-slit hologram (i.e. at the plane of LCD_1) was relayed to plane P_1, where all the other diffraction orders had been removed (at plane P_3)

through the use of the diaphragm, D, and experimental images are shown in the fourth row of Fig. 4.4.3.1. It is interesting to note that when the ring-slit is addressed with a single azimuthally varying phase, no singularities appear in the ring-slit field. However, by introducing a second ring-slit (having a different radial wave-vector) singularities appear in the ring-slit field, where the number of singularities is denoted by $2|l|$ (the same for the number of petals). The experimental fields (Fig. 4.4.3.1 (4a) – (4f)), produced at plane P_1, are in good agreement with those predicted theoretically, using Eq. (4.2.10) (with $n = 2$) and depicted in the fifth row of Fig. 4.4.3.1 (Fig. 4.4.3.1 (5a) – (5f)). By increasing the number of ring-slits to either three or four, it becomes very difficult to individually locate each of the singularities in the field as some of them start to overlap. This is evident, experimentally, within the yellow rings in Figs 4.4.3.1 (4g) and (4h) and theoretically in Figs 4.4.3.1 (5g) and (5h). Since it is difficult to locate the singularities in the "singularity"-field, when the number of ring-slits is increased, we suggest using interferometric techniques to aid the categorizing of the singularities [17].

It is well-known that the intensity of the petal field is dependent on the function $\cos^2(l\theta)$, evident in Eq. (4.2.18). This cosine behaviour, as a function of the azimuthal angle, of the intensity profile is also present in the near-field. This is evident in Fig. 4.4.3.7 where the intensity profile, as a function of the angular position in the field, is plotted for the case of $l_{inner} = +3$ and $l_{outer} = -3$. It agrees well with the intensity profile plotted for the theoretically predicted field, given in Eq. (4.2.10), illustrating that the intensity maxima of the near- and far-field both depend on the function $\cos^2(l\theta)$.

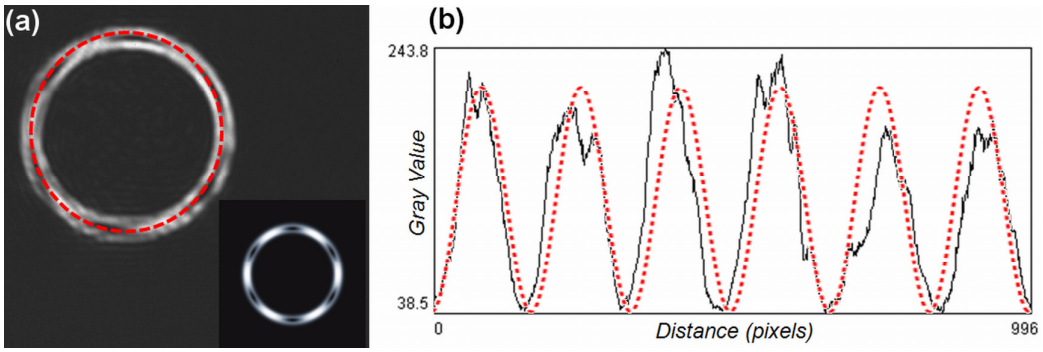

Fig. 4.4.3.7. (a) The experimentally recorded field at plane P_1 for a ring-slit consisting of the following azimuthal phases: $l_{inner} = +3$ and $l_{outer} = -3$. The theoretical prediction is given as an insert. The red, dashed ring marks the line for which the intensity profile is plotted (b). (b) The solid black curve is the experimental intensity profile and the red dashed curve is the theoretical intensity profile, $\cos^2(l\theta)$.

Propagating the field a distance of one focal length from plane P_1 to plane P_2, we see that the annular structure containing singularities transforms into spirals. The experimental fields produced at plane P_2 for each of the eight ring-slit holograms are given in the sixth row of Fig. 4.4.3.1 and accompanied with theoretical predictions in the seventh row. In the case of a single ring-slit, having a non-zero azimuthal mode index, the field appears as a diverging version of the field at P_1. For the five holograms, each consisting of two ring-slits, having opposite azimuthal orders, there are $2|l|$ spokes, evident in Figs 4.4.3.1 (6b) – (6f). Introducing more ring-slits into the hologram results in the spokes merging, making it difficult to resolve individual spokes (evident within the yellow rings in Figs 4.4.3.1 (6g), (6h), (7g) and (7h)).

The propagation of the field at plane P_1 to the field at P_2 was recorded and selected experimental images of the field at intervals along its propagation are given in Fig. 4.4.3.8. It is interesting to note that even though a rotation in the intensity profile for the petal field (in the vicinity of plane P_3, i.e. the far-field) exists as the petal field propagates, no rotation in the fields at P_1 propagating to P_2 exists as the field propagates. This is in accordance with the theoretical prediction given in Eqs (4.2.8) and (4.2.11), where the rotation rate for such a field is determined to be non-existent, but becomes more evident the closer the field propagates to the far-field.

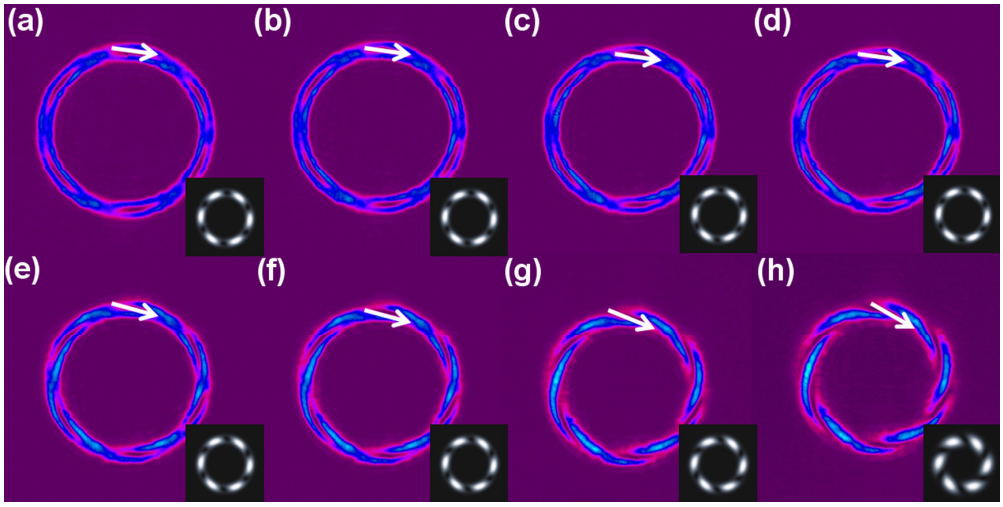

Fig. 4.4.3.8. Experimental intensity profiles of the field captured at evenly spaced intervals from plane P_1 to plane P_2. The distances from plane P_1 are given as (a) 0 mm, (b) 10 mm, (c) 20 mm, (d) 30 mm, (e) 40 mm, (f) 50 mm (g) 60 mm and (h) 70 mm. The white arrows illustrate the movement of a selected singularity. Inserts are given for the theoretical predictions.

Switching the handedness of the azimuthal phases in the two ring-slits, is known to cause the petal field, produced in the Fourier plane, P_3, to rotate in the opposite direction [13]. Even though the spiral field, produced at plane P_2, does not rotate as it propagates, swapping the handedness of the azimuthal phases (within the two ring-slits), results in the direction of the spokes to switch from clockwise to anti-clockwise (and vice versa). This is evident in the last column of Fig. 4.4.3.9 and is in good agreement with the theoretical prediction.

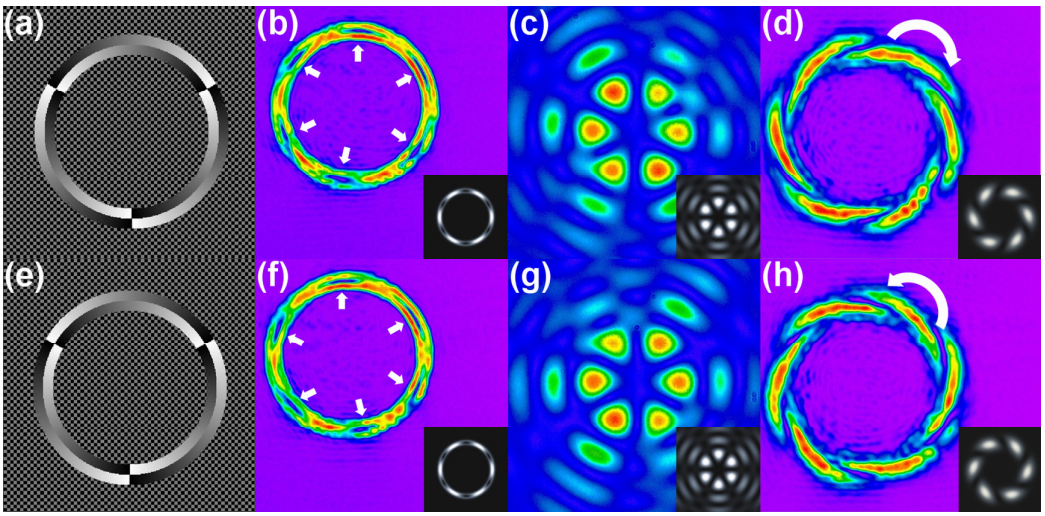

Fig. 4.4.3.9 *First column*: The ring-slit hologram applied to LCD_1. *Second column*: The corresponding optical fields for the ring-slits. The white arrows mark the locations of the singularities. *Third column*: The Fourier transform of the ring-slit hologram. *Fourth column*: The corresponding field, produced at plane P_2. The white arrow marks the handedness of the spokes. Theoretical predictions are accompanied as inserts.

4.5. Conclusion

We have presented two techniques to experimentally realize the superposition of higher-order Bessel beams [12, 13]. Our first technique involved a physical ring-slit aperture and an azimuthally varying hologram [12], whereas our second technique was a simplified version, involving only one hologram [13]. Both techniques produced fields which agreed very well with the theoretical prediction. The existence of higher-order vortices were revealed by interfering the field with a plane wave. These fields have aided the understanding of certain resonator modes [29].

In this chapter we have also illustrated that we are able to control the rotation rates of superimposed Bessel beams, by varying the parameters in the ring-slit hologram, namely the azimuthal order $|l|$ and the difference, Δk, between the two radial wave-vectors [13]. The different radial wave-vectors lead to different longitudinal wave-vectors which produce the self-imaging phenomenon and the rotation is then a manifestation of the continuous change of the intensity pattern. Our experimentally measured rotation rates are in very good agreement with those predicted theoretically. This technique is an ideal tool for the controlled rotation of trapped particles in optical trapping experiments.

We also showed that a ring-slit field transforms from an annular structure (embedded with singularities) to a spiral structure, consisting of spokes situated around a ring, which shows no rotation in its intensity profile [30]. Since Bessel beams, and especially superpositions of Bessel beams, are widely used in optical tweezing, understanding the structure of the field at planes other than the Fourier plane is necessary. The ring-slit field, embedded with singularities, can be used to trap low-index particles at set distances on the circumference of a circle.

4.6. References

[1]. J. Durnin, J.J. Miceli, and J.H. Eberly, "Diffraction-free beams," Phys. Rev. Lett. **58**(15), 1499-1501 (1987).

[2]. R.M. Herman and T.A. Wiggins, "Production and uses of diffractionless beams," J. Opt. Soc. Am. A **8**(6), 932-942 (1991).

[3]. J. Arlt and K. Dholakia, "Generation of high-order Bessel beams by use of an axicon," Opt. Commun. **177**(1-6), 297-301 (2000).

[4]. J.H. McLeod, "The axicon: a new type of optical element," J. Opt. Soc. Am. **44**(8), 592-597 (1954).

[5]. J. Turunen, A. Vasara, and A.T. Friberg, "Holographic generation of diffraction-free beams," Appl. Opt. **27**(19), 3959-3962 (1988).

[6]. A. Vasara, J. Turunen and A.T. Friberg, "Realization of general nondiffracting beams with computer-generated holograms," J. Opt. Soc. Am. A **6**(11), 1748-1754 (1989).

[7]. J.A. Davis, E. Carcole, and D.M. Cottrell, "Nondiffracting interference patterns generated with programmable spatial light modulators," Appl. Opt. **35**(4), 599-602 (1996).

[8]. J.A. Davis, E. Carcole, and D.M. Cottrell, "Intensity and phase measurements of nondiffracting beams generated with a magneto-optic spatial light modulator," Appl. Opt. **35**(4), 593-598 (1996).

[9]. C. Paterson and R. Smith, "Higher-order Bessel waves produced by axicon-type computer-generated holograms," Opt. Commun. **124**(1-2), 121-130 (1996).

[10]. D. McGloin, G.C. Spalding, H. Melville, W. Sibbett, and K. Dholakia, "Three-dimensional arrays of optical bottles," Opt. Commun. **225**(4-6), 215-222 (2003).

[11]. D. McGloin, V. Garces-Chavez, and K. Dholakia, "Interfering Bessel beams for optical micro-manipulation, " Opt. Lett. **28**(8), 657-659 (2003).

[12]. R. Vasilyeu, A. Dudley, N. Khilo, and A. Forbes, "Generating superpositions of higher-order Bessel beams," Opt. Express **17**(26), 23389-23395 (2009).

[13]. R. Rop, A. Dudley, C. López-Mariscal, and A. Forbes, "Measuring the rotation rates of superpositions of higher-order Bessel beams," J. Mod. Opt. **59**(3), 259-267 (2012).

[14]. V.V. Kotlyar, S.N. Khonina, R.V. Skidanov, and V.A. Soifer, "Rotation of laser beams with zero of the orbital angular momentum," Opt. Commun. **274**(1), 8-14 (2007).

[15]. R. H. Jordan and D. G. Hall, "Free-space azimuthal paraxial wave equation: the azimuthal Bessel Gauss beam solution" Opt. Lett. **19**(7), 427-429 (1994).

[16]. F. Gori, G. Guattari, and C. Padovani, "Bessel-Gauss beams," Opt. Commun. **64**(6), 491-495 (1987).

[17]. T.A. King, W. Hogervorst, N.S. Kazak, N.A. Khilo, and A.A. Ryzhevich, "Formation of higher-order Bessel light beams in biaxial crystals," Opt. Commun. **187**(4-6), 407-414 (2001).

[18]. T. Ando, N. Matsumoto, Y. Ohtake, Y. Takiguchi, and T. Inoue, "Structure of optical singularities in coaxial superpositions of Laguerre–Gaussian modes," J. Opt. Soc. Am. A **27**(12), 2602-2612 (2010).

[19]. J. C. Gutiérrez-Vega, M. D. Iturbe-Castillo, and S.Chávez-Cerda, "Alternative formulation for invariant optical fields: Mathieu beams," Opt. Lett. **25**(20), 1493-1495 (2000).

[20]. J. C. Gutiérrez-Vega, M. D. Iturbe-Castillo, E. Tepichin, G. Ramírez, R. M. Rodríguez-Dagnino, and S. Chávez-Cerda, "New Member in the Family of Propagation Invariant Optical Fields: Mathieu beams," Opt. and Phot. News **11**(12), 35-36 (2000).

[21]. S. Chávez-Cerda, M.J. Padgett, I. Allison, G.H.C. New, Julio C. Gutiérrez-Vega, A.T. O'Neil, I. MacVicar, and J. Courtial, "Holographic generation and orbital angular momentum of high-order Mathieu beams," J. Opt. B: Quantum Semiclass. Opt. **4**, S52-S57 (2002).

[22]. J. C. Gutiérrez-Vega, Rodolfo Rodríguez-Masegosa, and S. Chávez-Cerda , "Focusing evolution of Generalized Propagation Invariant Optical Fields ," J. Opt. A: Pure Appl. Opt. **5**, 276-282 (2003).

[23]. M. A. Bandres, J. C. Gutiérrez-Vega, and S. Chávez-Cerda, "Parabolic nondiffracting optical wavefields," Opt. Lett. **29**(1), 44-46, (2004).

[24]. C. López-Mariscal, J. C. Gutiérrez-Vega, and S. Chávez-Cerda, "Production of high--order Bessel beams with a Mach--Zehnder interferometer," Appl. Opt. **43**(26), 5060-5063 (2004).

[25]. C. López-Mariscal, M. A. Bandrés, S. Chávez-Cerda, and J. C. Gutiérrez-Vega, "Observation of Parabolic nondiffracting wave fields," Opt. Express **13**(7), 2364-2369 (2005).

[26]. C. López-Mariscal and J. C. Gutiérrez-Vega , "The generation of nondiffracting beams using unexpensive computer-generated holograms," Am. J. Phys **75**(1), 36-42 (2007)

[27]. J. C. Gutiérrez-Vega and C. López-Mariscal, "Nondiffracting vortex beams with continuous orbital angular momentum order dependence," J. Opt. A: Pure Appl. Opt. **10**(1), 015009, (2008).

[28]. D.W.K. Wong, and G. Chen, "Redistribution of the zero order by the use of a phase checkerboard pattern in computer generated holograms,"Appl. Optics **47**(4), 602-610 (2008).

[29]. D. Naidoo, K. Aït-Ameur, M. Brunel and A. Forbes, "Intra-cavity generation of superpositions of Laguerre–Gaussian Beams," Appl. Phys B. doi: 10.1007/s00340-011-4775-x

[30]. A. Dudley and A. Forbes, "From stationary annular rings to rotating Bessel beams," J. Opt. Soc. Am. A **29**(4), 567-573 (2012).

CHAPTER FIVE

Non-diffracting Speckle Fields

5.1. Introduction

Any field that has an annular spatial spectrum falls into the family of non-diffracting fields. Their ability to maintain their intensity profile during propagation has interested many researchers, resulting in many publications being dedicated to their formation, some of which are mentioned in section 4.1.

In this chapter, we turn our attention to random non-diffracting fields (also termed non-diffracting speckle fields). The first attempt to create a non-diffracting speckle field involved illuminating a weakly scattering diffuser (produced by spraying finishing mist on a flat glass plate) with a thin ring field [1]. Simpler and more efficient methods of generating non-diffracting speckle fields have been realized with the use of a single SLM [2]. This is a computational approach, equivalent to the experimental setup of Ref. [1], where the computer-generated hologram applied to the SLM is the Fourier transform of a ring-slit containing a random binary pattern.

Even though investigations into generating non-diffracting speckle fields have been made, none, to the best of our knowledge, show agreement between a theoretically calculated speckle field and an experimentally measured field. The major reason for this is that illuminating a diffuser with a ring field (as described in Ref. [1]) makes it virtually impossible to mathematically formulate the transmission function within the ring-slit in order to compute a theoretical prediction. We make use of a single SLM and implement the checkerboard pattern which allows us to operate our phase-only SLM in both phase and amplitude mode. This allows us to define the transmission function of the ring-slit and so a theoretical calculation of the resulting speckle can be made.

In this chapter we will outline the experimental setup used to generate non-diffracting speckle and illustrate the benefit of the checkerboard pattern [3]. Since speckle plagues many optical

systems, an understanding of speckle formation is imperative for the development of tools for its removal [4, 5]. Speckle is also proving useful in metrological techniques [6-10] and non-diffracting speckle is of particular interest in the non-destructive testing of materials [11], all of which benefit from a knowledge of speckle formation. Current investigations considered the effect the dimensions and the geometry of the ring-slit have on the longitudinal correlation [12] and the clustering (or snake-like patterns) of the speckles [13, 14], respectively. The structure of the random hologram or diffuser also has an influence on the formation of speckle clustering [14, 15]. In section 5.3, we make further investigations into the formation of speckle by studying the effect binary and continuous phase modulations within the ring-slit, for both the uniform and normal distribution, have on the structure of the speckle [3]. Our experimental results are accompanied by a theoretical explanation to validate what we experimentally witness.

5.2. Experimental methodology

The experimental setup used to generate non-diffracting speckle fields is very similar to that presented in Fig. 4.4.2, for the generation of non-diffracting Bessel beams, and is presented below in Fig. 5.2.1. A HeNe laser was expanded through a 6 × telescope before illuminating a ring-slit hologram, encoded with a random phase modulation. In our previous attempts, a physical ring-slit aperture was imaged onto the SLM and the phase modulation within the ring field would be modified. However, with this approach, in the case of non-diffracting speckle fields, one cannot define the transmission function of the ring field and this is why we implemented the checkerboard pattern, so as to reproduce the entire transmission function onto a single hologram. The dynamic addressing of SLMs allows the radius and width of the ring-slit, the frequency of the phase modulation, the number of grey-levels used to represent the phase modulation, and the distribution used to describe the phase modulation to be varied appropriately. The plane at the SLM (P1) was relay imaged with a 1 × telescope to plane P2 (denoted in Fig. 5.2.1). A physical ring-slit, contained within the red border in Fig. 5.2.1, was placed at P2 when needed, to allow for comparison between the results obtained with the ring-slit hologram and the physical ring-slit in conjunction with the random hologram. The field at plane P2 was Fourier transformed, with the use of lens L5, before being magnified by a 10 × objective and detected on a CCD camera. The non-diffracting nature of the produced speckle field is illustrated in Fig. 5.2.1 (i) - (ii), illustrating that the intensity profile of the field remains invariant as the field propagates.

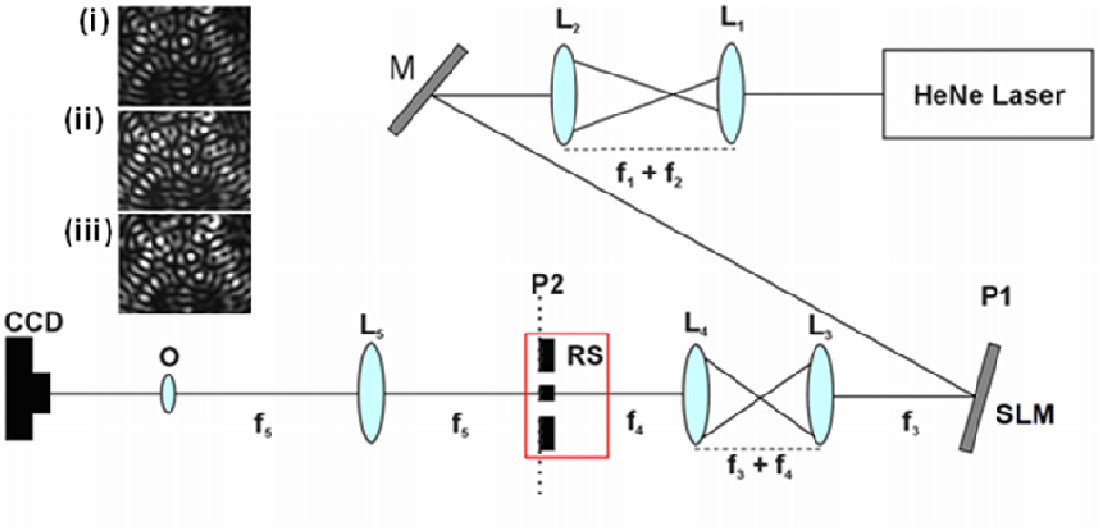

Fig. 5.2.1. The experimental design for generating non-diffracting speckle. The physical ring-slit (RS) which can be introduced into the optical setup when needed is denoted inside the red border. (L: lens (f_1 = 25 mm; f_2 = 150 mm; f_3 = 50 mm; f_4 = 50 mm; f_5 = 200 mm); M: mirror; SLM: spatial light modulator; O: objective; CCD: CCD camera). (i) – (iii) The intensity profile of the non-diffracting speckle field recorded at intervals along its propagation.

Figure 5.2.2 contains the results obtained with the physical ring-slit and a random hologram (column 2) and the hologram which incorporates the checkerboard pattern (column 4). These results were first obtained by illuminating the SLM when it was addressed by the holograms given in column 3 of Fig. 5.2.2. The SLM was then addressed with the same random holograms as those in column 3, but with the checkerboard pattern removed (i.e. those in column 1), and the field at the SLM was then imaged onto a physical ring-slit (R = 3 mm and Δ = 150 μm). The alignment of the physical ring-slit was adjusted until the field in the Fourier plane resembled that which was obtained with the checkerboard pattern. Both methods produced identical results (evident in comparing columns 2 and 4), illustrating that this technique is extremely effective in mimicking an amplitude mask. By being able to encode the transmission function into a single hologram and with the dynamic addressing of SLMs, the parameters which describe the ring-slit, such as radius, width and phase modulation can all be easily adjusted.

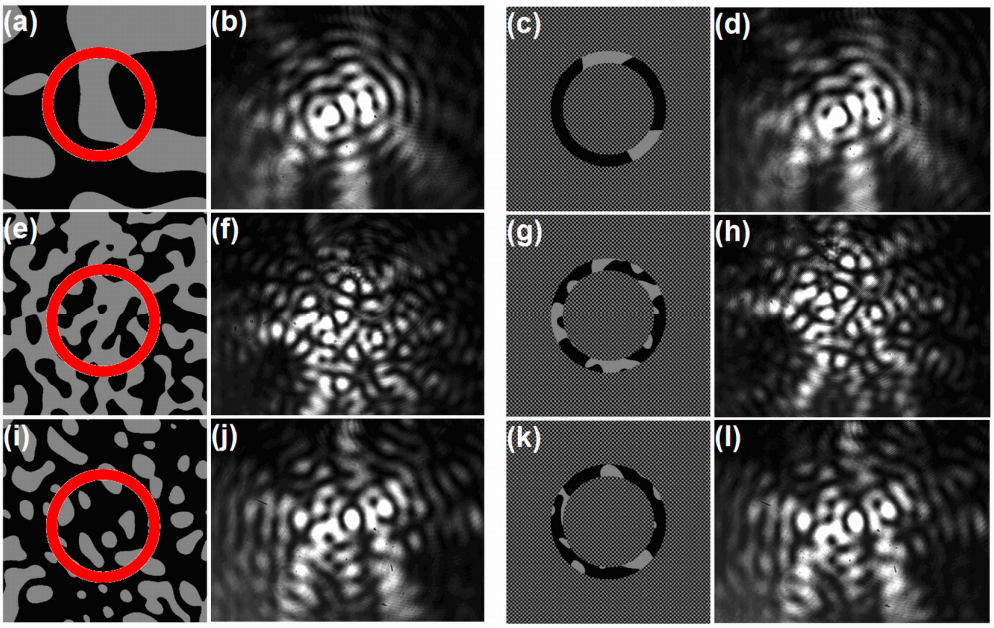

Fig. 5.2.2. *Column 1*: Random holograms which were illuminated with a ring field, denoted in red. *Column 2*: The corresponding experimentally measured Fourier transform. *Column 3*: The same random holograms as those in column 1, but with the checkerboard encoded. *Column 4*: The experimentally measured Fourier transform of column 3.

Since the phase modulation within the ring-slit can be mathematically defined, we can compute a theoretical prediction for the resulting speckle field. An example is given in Fig. 5.2.3, illustrating that the experimentally produced non-diffracting speckle field is in very good agreement with the theoretical prediction. This approach, for the first time, allows for quantitative studies in the dynamics of speckle formation, and is implemented with a single device – a SLM.

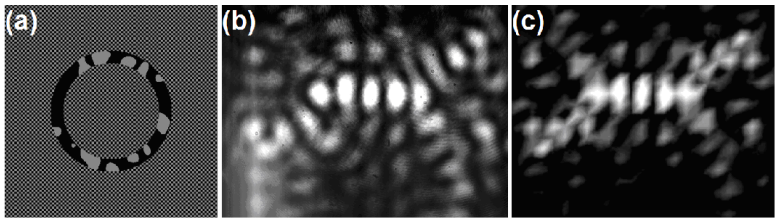

Fig. 5.2.3. (a) The ring-slit hologram applied to the SLM. (b) The corresponding experimentally produced field in the Fourier plane and (c) the theoretically calculated field at the Fourier plane.

5.3. Results and discussion

In our experimental investigations we test four different forms of phase modulation within the ring-slit, described by the following distributions: (i) continuous uniform, (ii) binary uniform, (iii) continuous normal and (iv) binary normal.

- (i) and (ii): continuous uniform and binary uniform distributions

In the case where the phase modulation is described by a continuous uniform distribution, the phase values exist in the range $\{0, 2\pi\}$, and the phase modulation is defined as

$$\phi(x, y) = 2\pi \times U(x, y), \tag{5.3.1}$$

where $U(x,y)$ is a uniform random number in the range $\{0,1\}$.

For the case that the phase modulation within the ring-slit is described by a binary uniform distribution, there is an equal probability that the phase values will be assigned either a value of 0 or π, which is mathematically described as

$$\phi(x, y) = \begin{cases} 0, & U(x, y) \le 0.5 \\ \pi, & U(x, y) > 0.5 \end{cases}. \tag{5.3.2}$$

Figure 5.3.1 contains the ring-slit holograms and the corresponding fields in the Fourier plane for the continuous uniform and binary uniform distributions. The frequency of the phase modulation within the ring-slit increases for each row (i.e. the phase modulation becomes more complicated). The amplitude mask has been removed in Fig 5.3.1, so as to highlight the phase-modulation within the ring-slit.

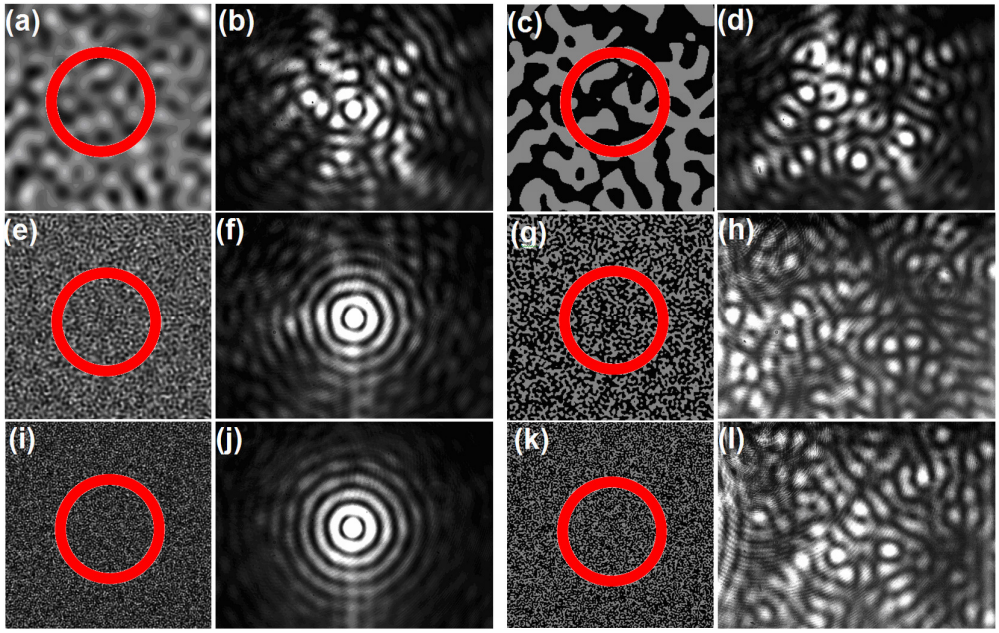

Fig. 5.3.1. *Column 1*: Ring-slit holograms, where the phase modulation within the ring-slit is described by a continuous uniform distribution (the frequency of the phase modulation increases with each row, (a) and (c) 10 pixels; (e) and (g) 50 pixels; (i) and (k) 100 pixels). The red ring denotes the ring-slit. *Column 2*: The corresponding experimentally recorded field at the Fourier plane. *Column 3*: Ring-slit holograms, where the phase modulation within the ring-slit is described by a binary uniform distribution (the frequency of the phase modulation increases with each row). The red ring denotes the ring-slit. *Column 4*: The corresponding experimentally recorded field at the Fourier plane.

In column 2 of Fig 5.3.1, it is evident that the zero-order Bessel beam starts to reconstruct as the frequency of the phase modulation increases. However, this is not the case with the binary uniform distribution and instead as the frequency of the phase modulation increases, so the speckle becomes more chaotic (evident in column 4).

To understand why different distributions produce different forms of non-diffracting speckle, the complex plane approach (first introduced in section 4.4.1) can be used. The amplitude modulation (introduced in section 4.4.1) is just a specific form of phase modulation where the two vectors, A_1 and A_2, are weighted and positioned on the complex plane in such a way that they produce a resultant having zero amplitude, thus completely suppressing the on-axis intensity in the Fourier plane.

In the case of the continuous uniform phase modulation the vectors on the complex plane, A_1 to A_{256}, all have the same amplitude and emanate from the origin of the complex plane from 0 to 2π. This produces a resultant, having the same amplitude as each of the 256 vectors, and pointing along the negative *x*-axis (i.e. $\varphi = \pi$). The average amplitude of the field at the plane of these holograms, is non-zero and due to the ring-slit geometry restricting this phase modulation, a zero-order Bessel beam manifests in the Fourier plane, evident in the three images in column 2 of Fig 5.3.1. In order to verify if the DC-offset experiences an increase or a decrease with an increase in the frequency of the phase modulation, we analysed the standard deviation within the ring-slit and this will be presented later for all four distributions.

For the binary uniform case, there is an equal probability that either a value of 0 or π will be selected to represent the phase modulation within the ring-slit and so the two vectors on the complex plane each have the same amplitude, but point in opposite directions ($\varphi_1 = 0$, $\varphi_2 = \pi$). The amplitude of the resultant is zero, so the DC component of the field at the ring-slit is zero, resulting in no zero-order Bessel beam forming in the Fourier plane. However, as the frequency of the phase modulation increases, the 'noise' around the DC-component increases and the nondiffracting speckle becomes more chaotic, evident in column 4 of Fig. 5.3.1.

- <u>(iii) and (iv): continuous normal and binary normal distributions</u>

When the phase values, within the ring-slit, are described by a normal distribution, having a mean of zero and a standard deviation of 1, the phase values are defined as

$$\phi(x, y) = 2\pi \times N(x, y), \tag{5.3.3}$$

where $N(x,y)$ is a normal random number. The probability density function for our continuous normal distribution is

$$f(x) = \frac{1}{\sqrt{2\pi\sigma^2}} \exp\left(\frac{-(x-\mu)^2}{2\sigma^2}\right), \tag{5.3.4}$$

where μ and σ are the mean and standard deviation, respectively.

The last case that we consider is the binary normal case. Here phase values within the ring-slit are assigned a value of either 0 or π, where the probability of selecting either value is bounded by a Gaussian envelope,

$$\phi(x,y) = \begin{cases} 0, & N(x,y) \le 0.5 \\ \pi, & N(x,y) > 0.5 \end{cases}. \tag{5.3.5}$$

The results obtained with these two distributions appear below in Fig. 5.3.2. The holograms containing phase modulations described by a continuous normal distribution and a binary normal distribution are given in column 1 and 3 of Fig. 5.3.2. The non-diffracting speckle fields produced by the holograms (described in columns 1 and 3) are shown in columns 2 and 4, respectively. It is evident that in the case of both distributions, the non-diffracting speckle starts to evolve into a zero-order Bessel beam as the frequency of the phase modulation increases.

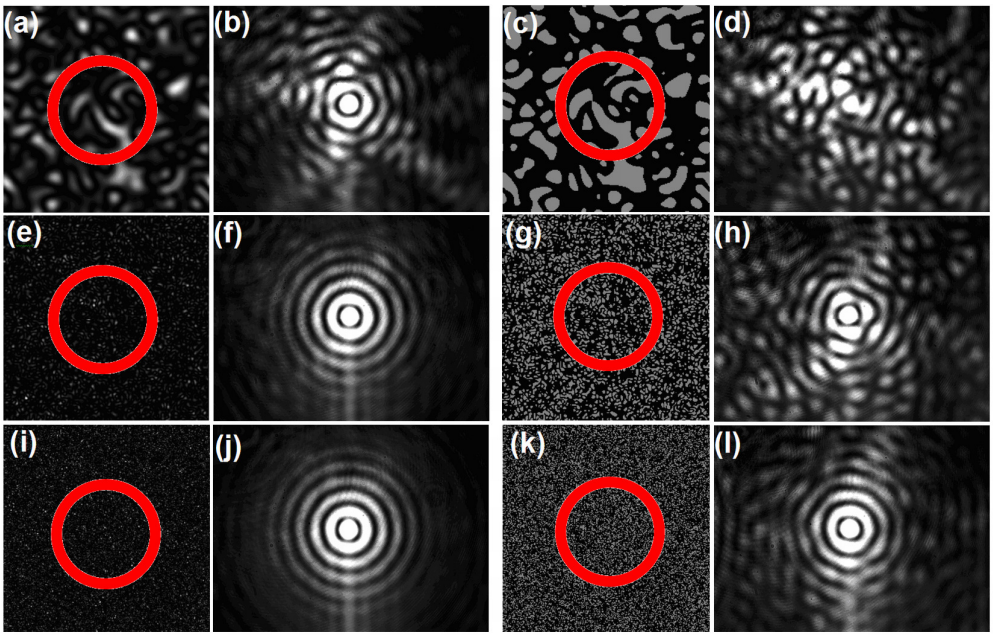

Fig. 5.3.2. *Column 1*: Ring-slit holograms, where the phase modulation within the ring-slit is described by a continuous normal distribution (the frequency of the phase modulation increases with each row, (a) and (c) 10 pixels; (e) and (g) 50 pixels; (i) and (k) 100 pixels). The red ring denotes the ring-slit. *Column 2*: The corresponding experimentally recorded field in the Fourier plane. *Column 3*: Ring-slit holograms, where the phase modulation within the ring-slit is described by a binary normal distribution (the frequency of the phase modulation increases with

each row). The red ring denotes the ring-slit. *Column 4*: The corresponding experimentally recorded field in the Fourier plane.

Once again the effects noted in Fig. 5.3.2 can be explained by visualizing a complex plane to represent the phase values in the hologram. For the continuous normal distribution, the vectors on the complex plane are weighted by a normal distribution. This results in the resultant vector having a non-zero amplitude and consequently an average amplitude of the field exists at the ring-slit producing a zero-order Bessel beam in the Fourier plane. This is evident experimentally in column 2 of Fig. 5.3.2.

When the phase modulation is described by a binary normal distribution a similar effect is noted (column 4 of Fig. 5.3.2). This is due to the fact that the probability of selecting either a phase value of 0 or a phase value of π, is bounded by a normal distribution; giving rise to the amplitudes of the two vectors in the complex plane being unequal . The resultant vector therefore has a non-zero amplitude and so a mean amplitude exists within the ring-slit giving rise to a zero-order Bessel beam in the Fourier plane.

For all of the above four cases, the transition of the speckle field, as the frequency modulation increases, can be understood by investigating the effect the standard deviation of the distribution has on the complex plane analogy. A graph illustrating how the standard deviation for each of the four distributions varies as a function of the frequency of the phase modulation is given in Fig. 5.3.3. The *x*-axis represents an increase in the correlation radius of the phase modulation within the ring-slit. The correlation radius is defined as the distance over which a 2π phase shift occurs in the phase modulation. Therefore a small correlation radius indicates that the frequency of the phase modulation is high, while a large correlation radius means the frequency of the phase modulation is low. The *y*-axis denotes the standard deviation of the distribution.

For the case of the continuous uniform distribution, the standard deviation for the continuous uniform distribution decreases as the frequency of the phase modulation decreases. In terms of the complex plane, this means that the range in which the 256 vectors exist on the complex plane becomes smaller. If all 256 vectors on the complex plane are restricted to a segment which has a small opening angle, then the amplitude of the resultant vector will increase, resulting in the zero-order Bessel beam becoming more predominant in the Fourier plane, as illustrated in column 2 of Fig. 5.3.1.

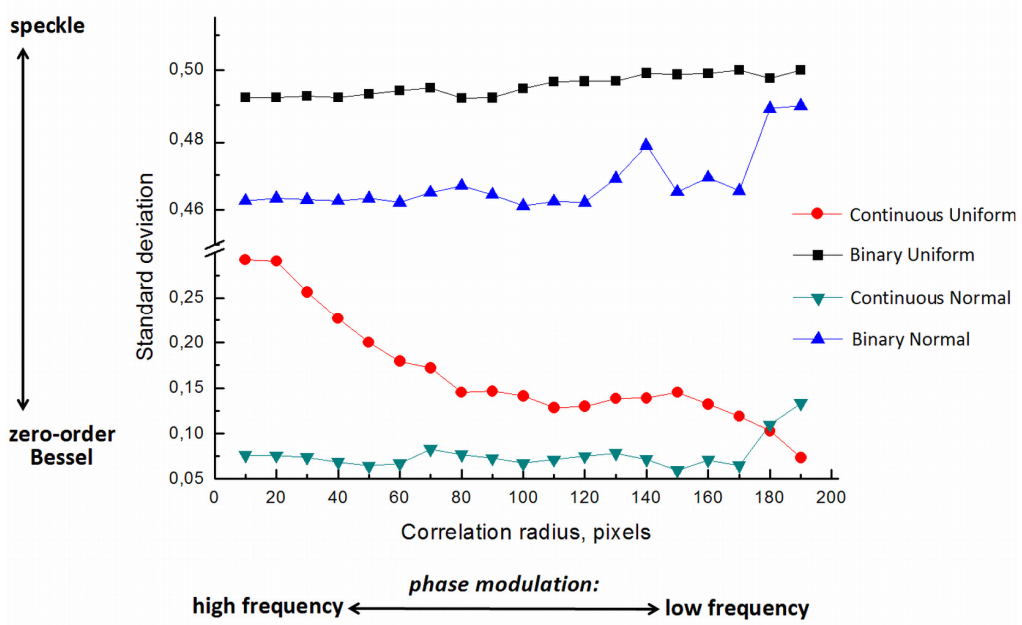

Fig. 5.3.3. Graph of the standard deviation for each of the four distributions as a function of the frequency of the phase modulation (or correlation radius).

From Fig. 5.3.3, it is evident that the standard deviation for the uniform binary distribution does not vary as the frequency of the phase modulation increases. This would then explain why the amplitude of the two vectors in the complex plane remains unchanged as the frequency of the phase modulation increases. This results in no change occurring in the DC-offset and consequently no zero-order Bessel beam forms in the Fourier plane, evident in column 4 of Fig. 5.3.1.

In the continuous normal distribution, an increase in the frequency of the phase modulation has no effect on the standard deviation (evident in Fig. 5.3.3). Instead the standard deviation remains fairly constant. This results in no fluctuations in the average amplitude of the field within the ring-slit taking place. In this case, as the frequency of the phase modulation increases not much change is noted in the intensity of the zero-order Bessel beam in the Fourier plane, as is the case in column 2 of Fig. 5.3.2.

From fig. 5.3.3, one can see that as the frequency of the phase modulation increases, the standard deviation decreases ever so slightly, resulting in a slight increase in the amplitude of the resultant vector. Consequently, the zero-order Bessel beam starts to appear as the frequency of the phase modulation increases.

In conclusion, we see that by engineering the frequency of the phase modulation, there is not much of a transition from non-diffracting speckle to a zero-order Bessel beam. Only one of the distributions (the binary normal distribution) shows a transition from chaotic speckle to a zero-order Bessel beam. This is also evident in comparing Figs 5.3.1 and 5.3.2, where the binary normal distribution (column 4, Fig. 5.3.2) displays the development from fully-developed speckle to a zero-order Bessel beam. The two continuous cases on the other hand, do not seem to start off as chaotic speckle; instead we see Bessel-like clusters. The binary uniform distribution is the polar opposite. Increasing the frequency of the phase modulation does not result in the field attaining a quasi-zero-order Bessel beam state and instead the field develops into more chaotic speckle (evident in Fig. 5.3.3 and in the intensity profiles in column 4 of Fig. 5.3.1). By decreasing the standard deviation of all four distributions, this restricts the two vectors to a smaller area on the complex plane and so the zero-order Bessel beam becomes more predominated in the Fourier plane. Some simulated results are given in Fig. 5.3.4 (row 1: continuous uniform, row 2: binary uniform, row 3: continuous normal, and row 4: binary normal). By varying the standard deviation, one can control where in the 'speckle to zero-order Bessel beam' spectrum the field can exist.

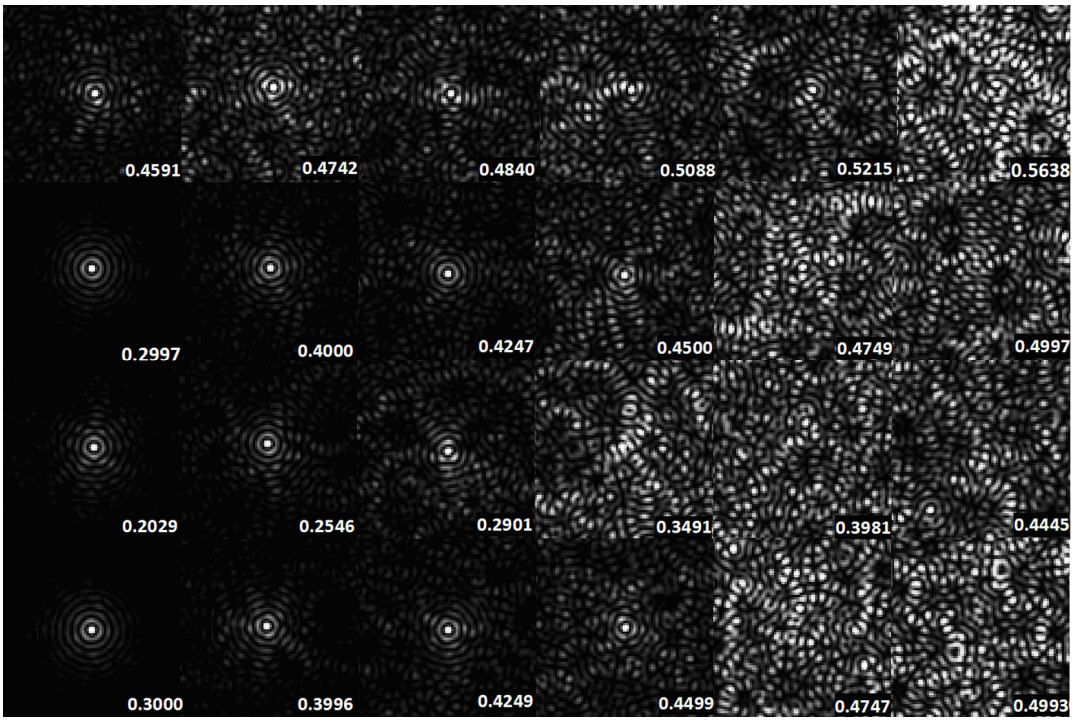

Fig. 5.3.4. Simulated images for the non-diffracting speckle field, for each of the four corresponding distributions. *Row 1*: continuous uniform. *Row 2*: binary uniform. *Row 3*:

continuous normal. *Row 4*: binary normal. The standard deviation increases from left to right. The values for the standard deviation are given in the bottom right corner of each image.

5.4. Conclusion

Modulating the amplitude in the ring-slit holograms, allows us to obtain good agreement between our experimentally produced non-diffracting speckle fields and theoretical predictions. We investigated the effect that binary and continuous phase modulations for two different distributions, (uniform and normal), have on the structure of the speckle field [3]. We discovered that we can control the evolution of the fully-developed non-diffracting speckle into a zero-order Bessel beam by adjusting the standard deviation of the distribution, which can be explained by analysing the DC component of the Fourier series. Having a 'dial' to select between either a zero-order Bessel beam, fully-developed non-diffracting speckle, or any mixture in-between, one can develop fields that are 'tailor-made' for specific functions. For example in the case of the non-destructive testing of materials, fields can be designed so as to optimise the assessment of materials and solutions. Non-diffracting fields are also widely used in optical tweezers. By being able to switch between a zero-order Bessel beam and non-diffracting speckle, one can randomly disperse particles, accumulated in the column of the Bessel beam, in a predetermined area of a cell or sample.

5.5. References

[1]. J. Turunen, A. Vasara, and A. T. Friberg, "Propagation invariance and self-imaging in variable-coherence optics," J. Opt. Soc. Am. A **8**(2), 282-289 (1991).

[2]. D. Cottrell, J. Craven, and J. Davis, "Nondiffracting random intensity patterns," Opt. Lett. **32(3)**, 298-300 (2007).

[3]. A. Dudley, R. Vasilyeu, V. Belyi , N. Khilo, P. Ropot, and A. Forbes, "Controlling the evolution of nondiffracting speckle by complex amplitude modulation on a phase-only spatial light modulator," Opt. Commun. **285**(1), 5-12 (2012).

[4]. R. K. Tyson, "Principles of adaptive optics," Academic, (1991).

[5]. M. C. Roggemann and B. Welsh, "Imaging through turbulence," CRC, Boca Raton, FL, (1996).

[6]. E. Kolenovic, W. Osten, and W. Juptner, "Influence of phase singularities on the interferometric measurement of out-of-plane displacements," Proc. SPIE **3744**, 174 (1999). doi: 10.1117/12.357710.

[7]. W. Wang, T. Yokozeki, R. Ishijima, M. Takeda, and S. Hanson, "Optical vortex metrology based on the core structures of phase singularities in Laguerre-Gauss transform of a speckle pattern," Opt. Express **14**(22), 10195-10206 (2006).

[8]. F. Chiang, "Super-resolution digital speckle photography for micro/nano measurements," Optics and Lasers in Engineering **47**(2), 274-279 (2009).

[9].P. Picart, J. Pascal, and J. Breteau, "Systematic errors of phase-shifting speckle interferometry," Appl. Opt. **40**(13), 2107-2116 (2001).

[10]. P. Jacquot, "Speckle interferometry: A review of the principal methods in use for experimental mechanics applications," Strain **44**, 57-69 (2008).

[11]. P. Jacquot and M. Fournier, "Interferometry in speckle light", Springer, Berlin, (2000).

[12]. M. Ibrahim, J. Uozumi, and T. Asakura, "Longitudinal correlation properties of speckles produced by ring-slit illumination," Opt. Rev. **5**(3), 129-137 (1998).

[13]. K. Uno, J. Uozumi, and T. Asakura, "Speckle clustering in diffraction patterns of random objects under ring-slit illumination," Opt. Commun. **114**(3-4), 203-210 (1995).

[14]. M. Ibrahim, J. Uozumi and T. Asakura, "On the generation of clustered speckles due to ring-slit illumination," Optik **106**, 33-41 (1997).

[15]. V. Belyi, N. Kazak, N. Khilo, and P. Ropot, "Vortex structure of elongated speckles," Proc. SPIE **6729**, 67290C (2007). doi: 10.1117/12.751866

CHAPTER SIX

Measuring the Orbital Angular Momentum Density of an Optical Field

6.1. Introduction

In chapter 2, various methods of measuring OAM are mentioned, however, even though these techniques are efficient at sorting modes (and even in some cases single photons) carrying OAM, they do not allow one to obtain a quantitative measurement for the OAM density. They merely measure the global OAM – the average value across the entire field. Some publications, however, have demonstrated the transfer of local OAM to trapped particles [1-3] and shown that the rotation rates of a particle trapped at different radial positions is proportional to r^{-3} [1], or that a particle trapped at different radial positions in an optical field (produced by interfering two vortex beams with unequal charges) rotate in opposite directions [3]. Attempts to make quantitative measurements of the OAM carried in an optical field have been made by measuring these rotation rates [4, 5]. This is not only an indirect measurement, but also a difficult experiment to conduct. These measurements only show that the rotation rates increase linearly with laser power [4] and that the rotation rates of low-index particles are not affected by beam imperfections [5]. An even more complicated method involves using the Doppler shift of a rotating detector [6, 7].

In this chapter we investigate theoretically (in section 6.2) the OAM density for superpositions of higher-order Bessel beams from first principles, by calculating the Poynting vector of the field, from which we can deduce both the linear and angular momentum components [8, 9]. We then use the Fresnel diffraction integral to form an experimental expression for the OAM density, from which we can make a direct comparison between theory and experiment. In section 6.3, we develop a simple method for measuring the OAM density in optical fields, using only a SLM and a Fourier transforming lens. Since there is interest in the superposition of OAM carrying fields, at both the classical [10-12] and quantum levels [13], we test the approach on superimposed non-diffracting higher-order Bessel beams. We obtain quantitative measurements

for the OAM density as a function of the radial position, for both symmetric and non-symmetric superpositions. We obtain good agreement with the theoretical prediction which is presented in section 6.4. The results indicate that the magnitude and direction of the OAM in the optical field is dependent on the location within the field's spatial distribution. In other words, different parts of the field carry different amounts of OAM. Being able to determine the OAM distribution is significant in optical trapping and tweezing.

6.2. Theory

In obtaining the theoretical result for the OAM density for a coherent superposition of two Bessel beams, we follow the same procedure as that presented in section 1.3. The same steps taken in formulating Eqs (1.3.1) to (1.3.13) (although it contains the case for a single field, possessing the phase factor $\exp(il\theta)$) are applied here.

This problem, of formulating the Poynting vector, has been tackled previously by others [4, 14 - 19]. We first take the general result for the Poynting vector, presented in Eq. (1.3.8), which we will then apply to our specific problem of coherent superpositions of non-diffracting Bessel beams.

- CASE 1: Symmetric superposition

The form for a symmetric superposition of two Bessel beams having differing cone angles and opposite azimuthal phases is

$$u^I(r,\theta,z) = A_0[J_l(q_1 r)\exp(i\Delta kz)\exp(il\theta) + \alpha_0 J_{-l}(q_2 r)\exp(-i\Delta kz)\exp(-il\theta)], \qquad (6.2.1)$$

where J_l is the Bessel function of order l. A_0 is the energy contained within the first Bessel beam, J_l,

$$A_0 = \sqrt{\int_{ring1} \exp(-2(r/\omega)^2) r dr} \qquad (6.2.2)$$

and the energy contained within the second Bessel beam, J_{-l}, is denoted as $\alpha_0 A_0$, where

$$\alpha_0 = \sqrt{\int_{ring\,2} \exp(-2(r/\omega)^2) r dr \Big/ \int_{ring\,1} \exp(-2(r/\omega)^2) r dr} \tag{6.2.3}$$

with *ring*1 and *ring*2 denoting the bounds of the inner and outer radii for the inner and outer rings, respectively and ω the radius of the Gaussian beam illuminating the ring-slit. The cone angles, γ_1 and γ_2, differ as a result of the generation process (outlined in chapter 4). As a result of the differing cone angles, both the radial and longitudinal wave numbers differ for the two beams. The radial wave numbers become $q_i = k\sin\gamma_i$, while the longitudinal wave numbers, given by $k_i = k\cos\gamma_i$ differ from the central z-dependent wave number (k) by $\pm\Delta k$. The subscripts i refer to the first (second) beam in the superposition. Each of the components of the Poynting vector, (S_r, S_θ and S_z) for the field given in Eq. (6.2.1) can be determined by substituting the amplitude of the field (Eq. (6.2.1)) into Eq. (1.3.8)

$$S_r = -\frac{A_0^2 \alpha_0 \varepsilon_0 \omega c^2}{2}\left[\left(q_2 J_{-l-1}(q_2 r) J_l(q_1 r) + q_1 J_{-l}(q_2 r) J_{l+1}(q_1 r)\right)\sin\left(2[l\theta + \Delta k z]\right)\right] \tag{6.2.4}$$

$$S_\theta = \frac{A_0^2 l \varepsilon_0 \omega c^2}{2r}\left(J_l^2(q_1 r) - \alpha_0^2 J_{-l}^2(q_2 r)\right) \tag{6.2.5}$$

$$S_z = \frac{A_0^2 \varepsilon_0 \omega c^2 k}{2}\left(J_l^2(q_1 r) + \alpha_0^2 J_{-l}^2(q_2 r) + 2\alpha_0 J_l(q_1 r) J_{-l}(q_2 r)\cos\left(2[l\theta + \Delta k z]\right)\right). \tag{6.2.6}$$

The total OAM density (along the direction of propagation, z) is defined as

$$L_z = \frac{1}{c^2}\left(r \times S\right)_z. \tag{6.2.7}$$

Here, the units of S are the conventional W/m^2 and the OAM density (L_z) is consequently expressed as the angular momentum per unit volume, or Ns/m^2. By substituting in each component of the Poynting vector (given in Eqs (6.2.4) to (6.2.6)) into the expression for the total OAM density (Eq. (6.2.7)) and taking only the z-component, the OAM density for the field described in Eq. (6.1.1) is

$$L_z(r) = \frac{l \varepsilon_0 \omega A_0^2}{2}\left(J_l^2(q_1 r) + \alpha_0^2 J_{-l}^2(q_2 r)\right). \tag{6.2.8}$$

An illustration which describes the experimental measurement is given in Fig. 6.2.1 (a). The figure is divided into two parts: (1) the generation of the optical field for which we wish to measure the OAM density and (2) the measurement of the OAM density, which is achieved by performing the inner-product.

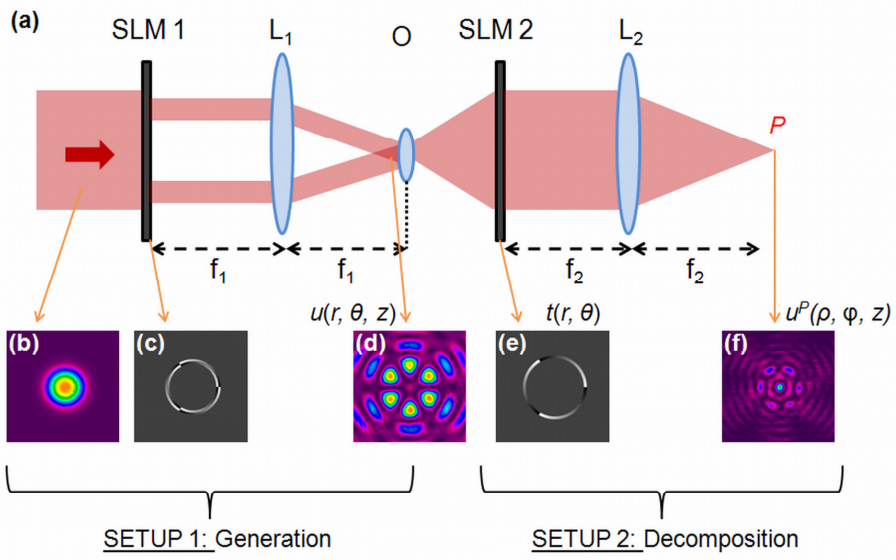

Fig. 6.2.1. (a) A schematic of the generation of the optical field and the decomposition of its OAM spectrum. (b) The Gaussian beam used to illuminate the hologram, (c), for the generation of the optical field, (d), defined by $u^I(r,\theta,z)$. The hologram, having a transmission function of $t(r,\theta)$, in (e) together with the lens L_2 performs the decomposition, producing the inner-product, P, represented in (f) and mathematically defined by $u^P(\rho,\varphi,z)$. (SLM: spatial light modulator and O: objective – used to magnify the optical field (d)).

The optical field, $u^I(r,\theta\, z)$ is directed onto the match-filter $t(r,\theta)$, where the Fourier transform is taken so as to form an experimental measurement. The match-filter is a function of r, allowing one to select a specific radial position within the optical field, $u^I(r,\theta\, z)$. The azimuthal phase within the match-filter can also be varied, resulting in different azimuthal weightings at different radial positions in the optical field being measured. It is not only restricted to our case of superimposed Bessel beams, but can be implemented with any OAM-carrying optical field.

First we need to relate a measurable quantity (such as the intensity of the inner-product) to the OAM spectrum, so as to form an experimental expression for Eq. (6.2.8), the OAM density. We first start by defining the field of the inner-product, by making use of the Fresnel diffraction

integral, so as to propagate the initial field, $u^l(r,\theta,z)$, multiplied by the match-filter, $t(r,\theta)$, to the plane of the inner-product, P

$$u^P(\rho,\phi,z)=\frac{\exp(i2kf)}{i\lambda f}\int_0^{\infty}\int_0^{2\pi} t(r,\theta)u(r,\theta,z)\exp\left(-i\frac{k}{f}r\rho\cos(\theta-\phi)\right)rdrd\theta. \tag{6.2.9}$$

f is the focal length of the lens used in the modal decomposition.

The field is evaluated at the origin, $\rho = 0$, so as to return the desired inner-product between the field $u^l(r,\theta,z)$ and the match filter $t(r,\theta)$. We also only need to consider the cases when the azimuthal mode of the match-filter is either l or $-l$ (i.e. n = l and $-l$), because the weighting of the azimuthal mode, a_n, will be non-zero when the match-filter possesses an azimuthal mode of the complex conjugate of one of the azimuthal modes present in the initial field, $u^l(r,\theta,z)$.

By substituting the initial field, Eq. (6.2.1) into Eq. (6.2.9), and considering only the signal at the origin, $u^P(0,\varphi,z)$, for both cases of $m = l$ and $m = -l$, we find that

$$u_l^P(\rho=0,z)=\frac{\exp(i2kf)}{i\lambda f}2\pi A_0\int_{R_1}^{R_2} J_l(q_1 r)\exp(i\Delta kz)rdr \tag{6.2.10}$$

and

$$u_{-l}^P(\rho=0,z)=\frac{\exp(i2kf)}{i\lambda f}2\pi A_0\alpha_0\int_{R_1}^{R_2} J_{-l}(q_2 r)\exp(-i\Delta kz)rdr, \tag{6.2.11}$$

where R_1 and R_2 are the inner and outer radii of the ring-slit used in the match-filter.

The ring-slit in the match-filter is thin, resulting in Eqs (6.2.9) and (6.2.10) being simplified by noting that the ring-slit may be assumed to be at a single radial position, $R \approx R_1 \approx R_2$, of width $2\Delta R$ (where R is the radius of the ring-slit)

$$u_l^P(\rho=0,z)=\frac{\exp(i2kf)}{i\lambda f}2\pi A_0\, 2\Delta R\cdot RJ_l(q_1 R)\exp(i\Delta kz) \tag{6.2.12}$$

and

$$u_{-l}^{P}(\rho=0,z)=\frac{\exp(i2kf)}{i\lambda f}2\pi A_0\alpha_0 2\Delta R\cdot RJ_{-l}(q_2R)\exp(-i\Delta kz). \tag{6.2.13}$$

Since the intensity of an optical field is defined as $I_l = \varepsilon_0 c(u_l\, u_l^*)$, the measured intensity at the origin of the inner-product, $I(0)$, and the theoretical Bessel function can be related as

$$\frac{I_l(0)}{\varepsilon_0 c}\left(\frac{f\lambda}{4\pi\Delta R\cdot RA_0}\right)^2 = J_l^2(q_1R) \tag{6.2.14}$$

and

$$\frac{I_{-l}(0)}{\varepsilon_0 c}\left(\frac{f\lambda}{4\pi\Delta R\cdot RA_0}\right)^2 = \alpha_0^2 J_{-l}^2(q_2R), \tag{6.2.15}$$

for the two cases, where the azimuthal mode index of the match-filter is either l or $-l$, respectively. Substituting these two equations (Eqs (6.2.14) and (6.2.15)) into the theoretical result for the OAM density (Eq. (6.2.8)), the following experimental form for the OAM density is obtained

$$L_z(R)=\frac{l\omega}{2c\eta}\left(\frac{\lambda f}{S_{Ring}}\right)^2\left(I_l(0)-I_{-l}(0)\right). \tag{6.2.16}$$

η is a factor for the optical efficiency of the experimental setup and S_{Ring} is the area ($4\pi\Delta R.R$) of the match-filter's ring-slit and is a function of its radius, R.

We will now generalize the expressions for the theoretical (Eq. (6.2.8)) and experimental (Eq. (6.2.16)) OAM densities, for a generalized symmetric superposition of Bessel beams, described as

$$u^{I}(r,\theta,z)=A_0\sum_{l=-N}^{N}\alpha_l J_l(q_l r)\exp(i\Delta k_l z)\exp(il\theta)+\alpha_{-l}J_{-l}(q_{-l}r)\exp(-i\Delta k_{-l}z)\exp(-il\theta). \tag{6.2.17}$$

where α_l and α_{-l} denote the energy contained in each of the ring-slits, with respect to the energy contained in the first ring-slit. Since the θ-component of the Poynting vector, S_θ, is a linear operator (this proof is included in Appendix A2), the generalized experimental and theoretical OAM density is obtained by extending the results given in Eqs (6.2.8) and (6.2.16)

$$L_z(r) = \frac{\varepsilon_0 \omega A_0^2}{2} \sum_{l=-N}^{N} l\alpha_l^2 J_l^2(q_l r) - l\alpha_{-l}^2 J_{-l}^2(q_{-l} r) \tag{6.2.18}$$

and

$$L_z(r) = \frac{\omega}{2c\eta}\left(\frac{\lambda f}{S_{Ring}}\right)^2 \sum_{l=-N}^{N} l\left(I_l(0) - I_{-l}(0)\right), \tag{6.2.19}$$

respectively.

- CASE 2: Non-symmetric superposition

The amplitude for a non-symmetric superposition of two Bessel beams, is defined as

$$u^I(r,\theta,z) = A_0\left(J_l(q_1 r)\exp(i\Delta kz)\exp(il\theta) + \alpha_0 J_m(q_2 r)\exp(-i\Delta kz)\exp(im\theta)\right), \tag{6.2.20}$$

where the azimuthal indices are of different orders, $l \neq m$. By following the same procedure for determining the Poynting vector and consequently the OAM density, as described in the symmetric case, the theoretical OAM density is

$$L_z(r,\theta,z) = \frac{\varepsilon_0 \omega A_0^2}{2}\left(lJ_l^2(q_1 r) + m\alpha_0^2 J_m^2(q_2 r) + (l+m)\alpha_0 \cos\left((l-m)\theta + 2\Delta kz\right)J_l(q_1 r)J_m(q_2 r)\right). \tag{6.2.21}$$

Unlike the symmetric case (Eq. (6.2.8)) this form for the OAM density is a function of the azimuthal angle, θ, in the plane of the inner-product and is evaluated by summing over the OAM density values for a range of angles varying from 0 to 2π. It is also a function of Δkz, however since this only produces a constant phase-shift (i.e. a rotation in the intensity profile of the optical field), it is neglected.

The on-axis intensity in the inner-product plane is related to the Bessel function by following the same steps outlined in Eqs (6.2.9) to (6.2.15) and remembering that the match-filter must be set to both l and m, resulting in

$$\frac{I_l(0)}{\varepsilon_0 c}\left(\frac{f\lambda}{4\pi\Delta R \cdot RA_0}\right)^2 = J_l^2(q_1 R) \tag{6.2.22}$$

and

$$\frac{I_m(0)}{\varepsilon_0 c}\left(\frac{f\lambda}{4\pi\Delta R \cdot RA_0}\right)^2 = \alpha_0^2 J_m^2(q_2 R). \tag{6.2.23}$$

Substituting Eqs (6.2.22) and (6.2.23) into Eq. (6.2.21) produces the expression for the experimental measurement of the OAM density

$$L_z(R,\theta,z) = \frac{\omega}{2c\eta}\left(\frac{\lambda f}{S_{Ring}}\right)^2 \left(lI_l(0) + mI_m(0) + (l+m)\cos\left((l-m)\theta + 2\Delta kz\right)\sqrt{I_l(0)}\sqrt{I_m(0)}\right). \tag{6.2.24}$$

No measurement for the angle θ can be made, as there exists only one measurement for the on-axis intensity in the inner-product plane. Instead the experimental equation for the OAM density is integrated over θ, resulting in the average OAM density

$$\overline{L_z(R)} = \frac{\omega}{2c\eta}\left(\frac{\lambda f}{S_{Ring}}\right)^2 \left(lI_l(0) + mI_m(0)\right), \tag{6.2.25}$$

where the term Δkz can be neglected. As this result has no angular dependence, the measurement does not pertain to a specific radial direction, but instead is an average measurement across the field.

The amplitude distribution of the non-symmetric superposition can be generalised in the following form

$$u^I(r,\theta,z) = A_0 \sum_{l=-N}^{N} \sum_{m=-N}^{N} \alpha_l J_l(q_l r)\exp(i\Delta k_l z)\exp(il\theta) + \alpha_m J_m(q_m r)\exp(i\Delta k_m z)\exp(im\theta). \tag{6.2.26}$$

Since the θ-component of the Poynting vector, S_θ, is a linear operator, the theoretical and experimental results for the OAM density is determined by extending the simple form in Eqs (6.2.21) and (6.2.25). However, the equations become very cumbersome and have been neglected. In verifying our results for a generalized non-symmetric superposition, the OAM density is calculated by substituting the amplitude distribution (Eq. (6.2.26)) into Eq. (6.2.8) to determine the Poynting vector for calculating the theoretical OAM density.

We conduct the experiment on six different optical fields, which will appear in section 6.4. The first three fields consist of a superposition of two Bessel beams, of orders l = 3 and -3, where the energy in the two Bessel beams are (1) equal; (2) the l = -3 order Bessel beam is heavily weighted; and (3) the l = +3 order Bessel beam is heavily weighted. The theoretical and experimental OAM densities are calculated using Eqs (6.2.8) and (6.2.16). We also measure the OAM density for a non-symmetric superposition of two Bessel beams, l = 3 and m = -4, using Eqs (6.2.21) and (6.2.26). The fifth optical field is a superposition of three Bessel beams and even though the OAM density is not explicitly given in this thesis, it is easily calculated by substituting the amplitude of the optical field into Eqs (1.3.8) and (6.2.7). Similarly, we use Eqs (1.3.8) and (6.2.7) to measure the OAM density of the last optical field, a non-symmetric superposition of four Bessel beams.

6.3. Experimental methodology

The experimental setup for measuring the OAM density for symmetric and non-symmetric superpositions of Bessel beams is denoted in Fig. 6.3.1. A HeNe laser (λ ~ 633 nm) was expanded through a 6 × telescope and directed onto the liquid crystal display (LCD) of a SLM, labelled LCD_1 so as to generate the six optical fields for which we wish to measure the OAM density. The fields were generated using the holograms presented in section 4.4.

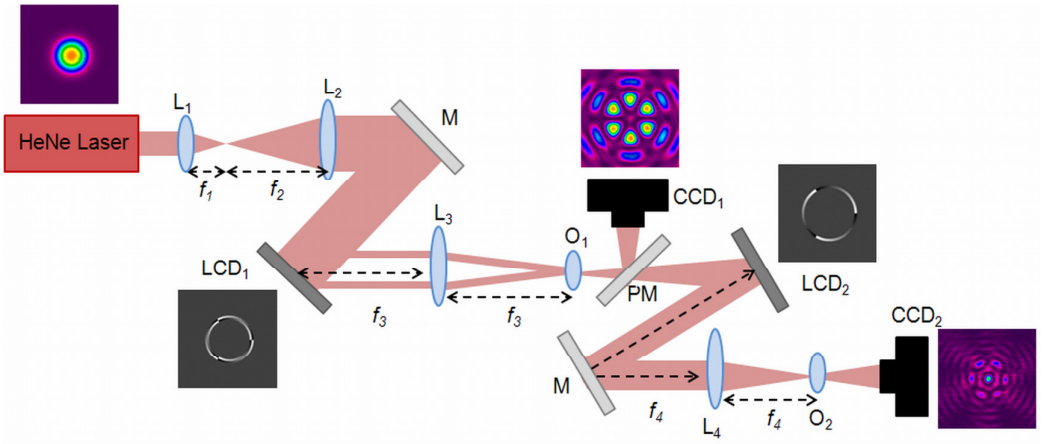

Fig. 6.3.1. A schematic of the experimental setup for measuring the OAM density as a function of the radial position, *R*. L: Lens (f_1 = 25 mm; f_2 = 150 mm; f_3 = 200 mm and f_4 = 200 mm); M: Mirror; LCD: Liquid Crystal Display; O: Objective; PM: Pop-up Mirror; CCD: CCD Camera. The objective, O_2, was placed at the Fourier plane of lens, L_4. The corresponding optical fields and holograms appear at the appropriate planes.

Some of the ring-slit holograms, programmed onto LCD_1, for the creation of superimposed Bessel beams can be found in the next section, section 6.4. The area surrounding the ring-slit, where we do not want to transmit any light, is encoded with a checkerboard pattern so as to mimic an amplitude mask. This checkerboard technique was explained in section 4.4.1. The resulting images of our non-diffracting superposition field, formed at the focal plane of L_3, was magnified with a 10× objective, O_1, and directed to the LCD of the second SLM, LCD_2. A pop-up mirror, PM_1, was used to direct the field at the plane of LCD_2 so as to be recorded on CCD_1. This allowed us to quantitatively measure the radial positions within the initial optical field.

The modal decomposition was achieved by executing an inner product of the incoming field with the match filter and a Fourier transforming lens, L_4. Since the match-filter was programmed digitally the phase factor, $\exp(-im\theta)$, was easily varied for various m values, and for particular radial (r) positions. The coefficient a_m, at set radial positions, was found by assigning the match-filter to a narrow ring-slit having a radius, R, and a width of 20 pixels. This allows us to find the local OAM density rather than the global OAM density.

The image presented in Fig. 6.3.2, illustrates the concept of the match-filter: the experimental field (second and fourth row of Fig. 6.3.2) was subdivided into 10 ring-slits. In this work, the match-filters consist of ring-slits having ten different radii (r_1 = 75; r_2= 110; r_3 = 145; r_4 = 180; r_5 = 215; r_6 = 250; r_7 = 285; r_8 = 320; r_9 = 355 and r_{10} = 390 (given in pixels), each consisting of

a width of 20 pixels). The azimuthal phase within each ring-slit was varied according to the complex conjugate of the azimuthal modes present in the initial amplitude distribution. The dynamical aspect of SLMs allows us to radially locate where in the optical field we wish to make a measurement of the OAM density. Due to the fact that LCD_2 was orientated as the mirror image of LCD_1 in our experimental setup, the complex conjugate of the azimuthal mode index, m, on LCD_1 is equivalent to m on LCD_2. If the experimental setup were orientated differently, such that the two SLMs have the same orientation, the complex conjugate of the azimuthal mode index, m, on LCD_1 is then equivalent to $-m$ on LCD_2. The OAM density for a particular radial position can then be obtained by measuring the on-axis intensity of the inner-product on CCD_2.

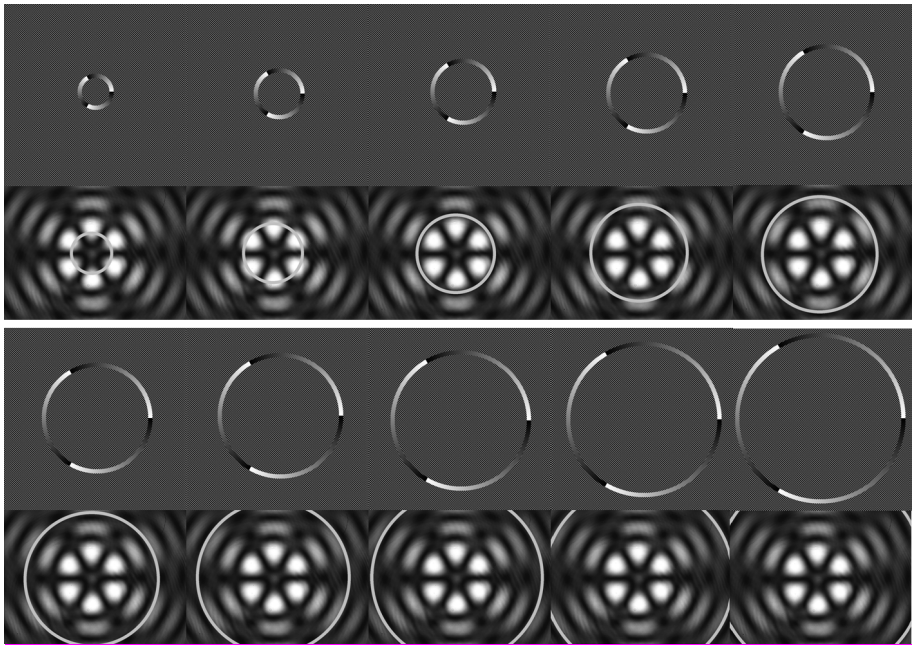

Fig. 6.3.2. The initial optical field was divided radially into individual ring-slits. The phase within the annular ring was varied azimuthally for various values of l. The rest of the LCD was programmed with a checkerboard pattern so as to restrict the transmission function to the ring alone. The ten rings have the following radii: $r_1 = 600$ µm, $r_2 = 880$ µm, $r_3 = 1160$ µm, $r_4 = 1440$ µm, $r_5 = 1720$ µm, $r_6 = 2000$ µm, $r_7 = 2280$ µm, $r_8 = 2560$ µm, $r_9 = 2840$ µm and $r_{10} = 3120$ µm. The black and white images in rows 2 and 4 are grey-scale experimental images of the first optical field that we tested.

In the next section we will present our results for the six optical fields that we tested using our OAM density measurement setup, described in Fig. 6.3.1.

6.4. Results and discussion

- Optical field #s 1, 2 and 3 - symmetric superposition of two Bessel beams

The holograms for the first test of our OAM measurement technique, described in section 6.4, are given in the first column of Fig. 6.4.1. They consist of a ring-slit separated into two ring-slits, each possessing an azimuthal phase of equal order but opposite handedness, (i.e. $l_{inner} = 3$ and $l_{outer} = -3$). The widths of the two ring-slits differ in Figs 6.4.1 (d) and (g). This allowed us to adjust the energy present in each of the two Bessel beams and subsequently set the values of A_0 and α_0 in Eq. (6.2.11). The ring-slit dimensions are: (a) $r_1 = 173$, $r_2 = 188$, Δr_1, $\Delta r_2 = 15$; (d) $r_1 = 173$, $r_2 = 188$, $\Delta r_1 = 7$, $\Delta r_2 = 23$; (g) $r_1 = 173$, $r_2 = 188$, $\Delta r_1 = 23$, $\Delta r_2 = 7$ (all given in pixels). When the orders, $|l|$, of the two azimuthal phases are of equal order, but of opposite handedness, a petal structure is produced, where the number of petals is denoted by $2|l|$ as expected from theory [20]. This is evident in Fig. 6.4.1 (b) and (c).

In the other two cases (Fig. 6.4.1 (d) and (g)) the two ring-slits cover slightly different areas, producing Bessel beams containing differing energies. The $l = -3$ order Bessel beams is heavily weighted by increasing the area of the outer ring-slit (evident in Fig. 6.4.3 (d)), resulting in a smearing of the petals as the $l = -3$ order Bessel beam is favoured in the optical field (evident in Fig. 6.4.1 (e) and (f)). In Fig. 6.4.1 (g) the $l = 3$ order Bessel beam is heavily weighted by increasing the area of the inner ring-slit, resulting in a similar smearing of the petals.

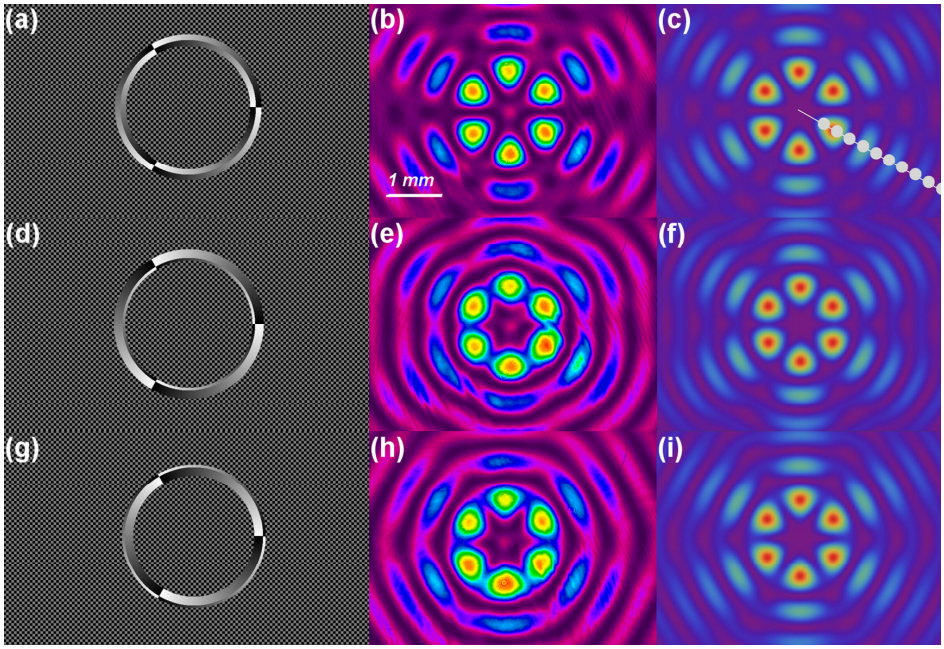

Fig. 6.4.1. *First column*: Holograms and the corresponding experimentally produced fields in the Fourier plane (*second column*) accompanied with theoretically calculated fields (*third column*). The white dots in (c) denoted the radial positions of each of the ten ring-slits used as the match-filters.

The OAM spectrum of the first optical field, given in the first row of Fig. 6.4.1, was obtained by measuring the intensity at the origin of the inner-product field, at plane P, with a CCD camera, CCD_2, for each of the ten match-filters whose azimuthal phase varied from l = -4 to 4. This measured OAM spectrum is shown in Fig. 6.4.2, illustrating that the only components of the OAM spectrum, that are present in the field, are l = -3 and 3, which are the complex conjugates of the azimuthal modes present in the initial amplitude distribution.

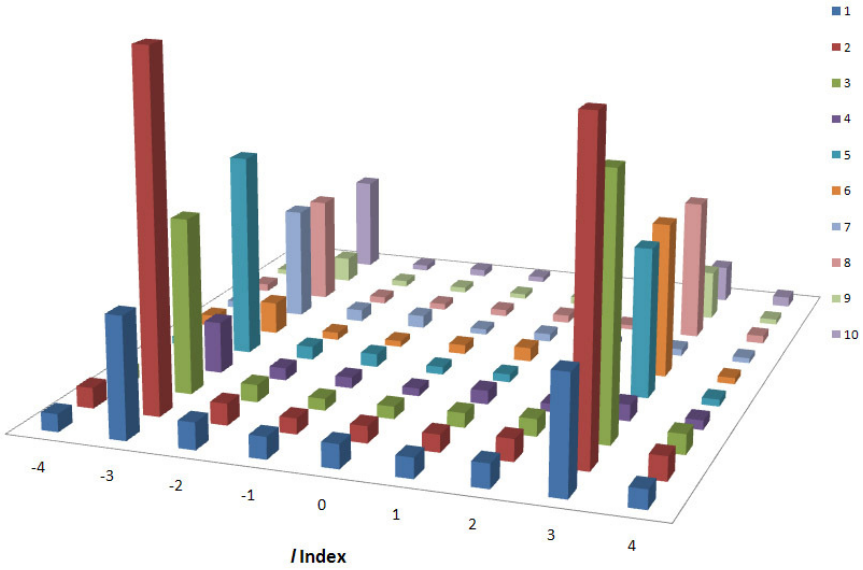

Fig. 6.4.2. The measured OAM spectrum of the field given in Fig. 6.4.1 (b), as a function of the radial ring (or radial position), given by numbers 1 to 10, for azimuthal phase values of $m = -4$ to 4. The height of each bar represents the measured coefficients $|a_m|^2$.

The OAM density for each of the fields, denoted experimentally in the second column of Fig. 6.4.1, was determined by measuring the intensity at the origin of the inner-product field at the Fourier plane of L_4 for each of the match-filters and substituted into Eq. (6.2.16) or (6.2.25). Figure 6.4.3 contains the measured OAM densities as a function of the radial position for the first three optical fields.

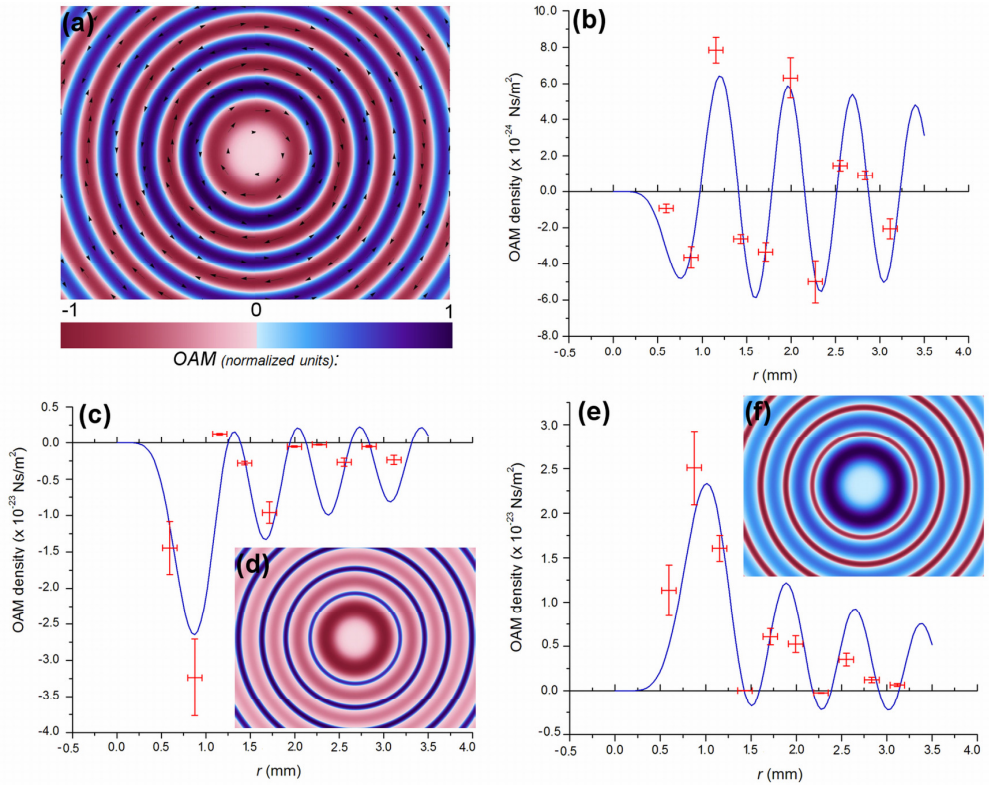

Fig. 6.4.3. (a) A density plot of the OAM density for the field given in Fig. 6.4.1 (b). Red denotes negative OAM and blue denotes positive. Light to dark blue denotes an increase in positive OAM and light to dark red denotes an increase in negative OAM. (b), (c) and (e) the OAM density for the fields in Fig. 6.4.1.(b), (e) and (h), respectively. The blue curve denotes the theoretical OAM density and the red points the experimentally measured OAM density. Inserts for density plots of the OAM density for (c) and (e) are given as inserts, (d) and (f), respectively.

Since the incoming optical field in Fig. 6.4.1 (b), consists of an equal weighting of $l_{\text{inner}} = 3$ and $l_{\text{outer}} = -3$ order Bessel beams, the OAM density represented as a density plot in the x - y plane consists of evenly-sized concentric rings of positive and negative OAM. Figure 6.4.3.(b), which contains the radial cross-sectional profile of the OAM density, also depicts this behaviour, as the OAM density oscillates evenly around a value of zero. In the next two cases, where $l_{\text{inner}} = -3$ (+3) is heavily weighted, the OAM is predominantly negative (positive) and is evident in Fig. 6.4.3 (d) ((f)). The cross-sectional profile of the OAM density exists predominantly in the negative (positive) quadrant of the graph, evident in Fig. 6.4.3 (c) ((e)).

The error analysis for these measurements first involved calculating a theoretical error band for the OAM density, by determining the minimum and maximum values when the inner and outer radii of the ring-slit in the match-filters were displaced by half the width of the ring-slit (i.e. 10 pixels). Since this error is miniscule, the error bands lie on top of one another and are not evident in the graphs. Displacing the ring-slit in the match-filter by half of its width, the experimental absolute x-error is 80 μm (10 pixels × 8um). In experimentally measuring the on-axis intensity of the inner-product, we pin-pointed the errors to be dependent on three factors: (1) human error in reading the on-axis intensity of the inner-product on CCD_2; (2) the positioning of CCD_2 in the Fourier plane of L_4; and (3) an adjustment of the ring-slit (by half of its width) in the match-filter on LCD_2. For the first factor, a 10 pixel diameter aperture on the CCD camera was positioned around the on-axis intensity on CCD_2 and the percentage error for the total energy when the aperture was moved 7 pixels off of its centre, was determined and included into the experimental error for the OAM density. The second factor entailed measuring the percentage error for the on-axis intensity when CCD_2 was positioned 1 mm before and 1 mm after the Fourier plane of L_4. The last error measurement required the percentage error in the measured intensity, due to an increase or decrease (by half the width) of the radius of ring-slit on LCD_2, to be determined. All of these factors were included into all the measurements for the OAM density.

- Optical field # 4 - non-symmetric superposition of two Bessel beams

Figure 6.4.4 (a) contains the hologram, which consists of two ring-slits having azimuthal phases $l_{inner} = 3$ and $l_{outer} = -4$, used to generate the fourth optical field presented in Fig. 6.4.4 (b). The dimensions of the ring-slits are: $r_1 = 173$, $r_2 = 188$, Δr_1, $\Delta r_2 = 15$ (all given in pixels). The field obtained at the Fourier plane (Fig. 6.4.4 (b)) is in good agreement with the theoretically calculated field (Fig. 6.4.4 (c)) and consists of a petal structure, where the number of petals is given by $|l_{inner}|+| l_{outer}|$, (i.e. 7 petals). For this non-symmetric superposition, described mathematically by Eq. (6.2.20), the field has a global OAM of $-1\hbar$ ($3\hbar + -4\hbar$), resulting in the OAM density being mostly negative radially across the field, evident in both Figs 6.4.4 (d) and (e). Since the OAM density is not symmetric and consequently not uniform in all radial directions, the OAM density plotted in Fig. 6.4.4 (d) is not for a particular angular point, but instead an average over all angular points, given by Eq. (6.2.25).

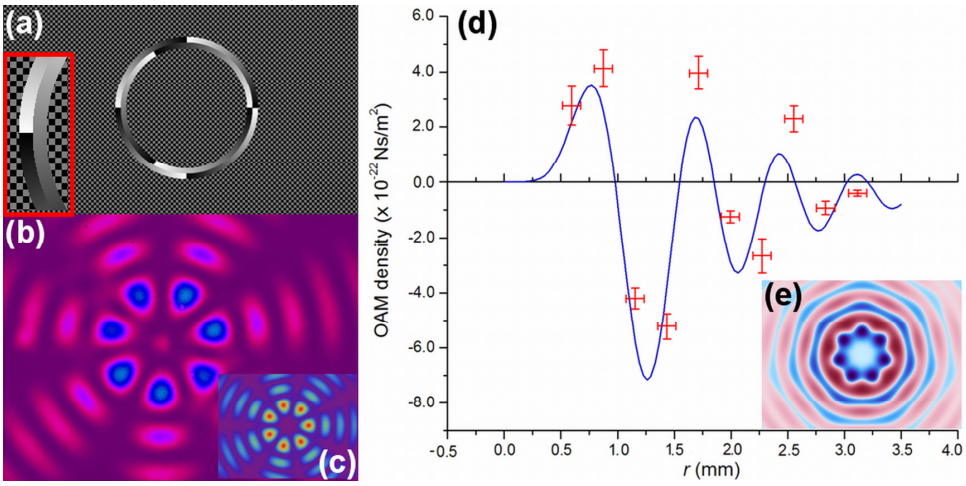

Fig. 6.4.4. (a) The hologram used to generate the experimental field in (b). The theoretically calculated field is given in (c). A magnification of the ring-slit is given as an insert in (a). (d) The theoretical (blue curve) and experimentally measured (red points) OAM density. (e) A density plot of the OAM density. Red denotes negative OAM and blue denotes positive. Light to dark blue denotes an increase in positive OAM and light to dark red denotes an increase in negative OAM.

- Optical field # 5 - non-symmetric superposition of three Bessel beams

The fifth field was generated by encoding $LCD_1$with the hologram presented in Fig. 6.4.5 (a). This hologram is divided into three ring-slits, having the following azimuthal phase variations: l_{inner} = -3, l_{middle} = 2, l_{outer} = 1, thus producing a non-symmetric superposition of three Bessel beams in the Fourier plane. The dimensions of the ring-slits in Fig. 6.4.5 (a) are: r_1 = 170, r_2 = 180, r_3 = 190, Δr_1, Δr_2, Δr_3 = 10 (all given in pixels). Although one cannot intuitively predict how the field will manifest in the Fourier plane, our experimental field (Fig. 6.4.5 (b)) is in very good agreement with the theoretically calculated field (Fig. 6.4.5 (c)). Here the global OAM is zero, as the three ring-slits are equally weighted and the azimuthal mode indices of each of the ring-slits sums to zero. Therefore the OAM density exists equally in both the negative and positive quadrants (evident in Fig. 6.4.5 (d)). Since the OAM density is not uniform in all radial directions of the optical field (evident in Fig. 6.4.5 (e)), the OAM density plotted in Fig. 6.4.5 (d) is an average over all angular points.

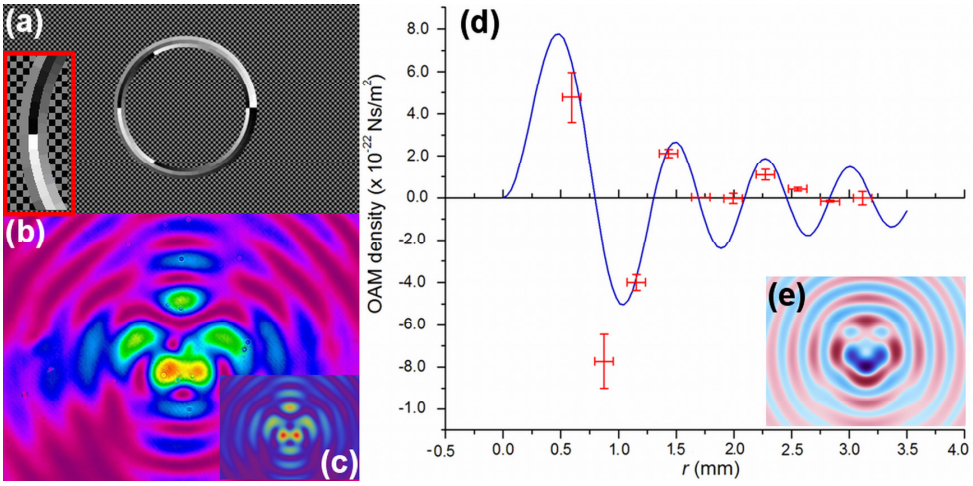

Fig. 6.4.5. (a) The hologram used to generate the experimental field given in (b) of which the theoretical field is represented in (c). A magnification of the ring-slit is given as an insert in (a). (d) The theoretical (blue curve) and experimentally measured (red points) OAM density. (e) A density plot of the OAM density. Red denotes negative OAM and blue denotes positive. Light to dark blue denotes an increase in positive OAM and light to dark red denotes an increase in negative OAM.

- Optical field # 6 - non-symmetric superposition of four Bessel beams

The ring-slits for that last hologram (Fig. 6.4.6 (a)) have the following azimuthal mode indices: $l_{inner} = -2$, $l_{middle1} = -1$, $l_{middle2} = 2$, $l_{outer} = 1$, and the physical dimensions (in pixels) are: $r_1 = 169$, $r_2 = 176$, $r_3 = 183$, $r_4 = 190$, Δr_1, Δr_2, Δr_3, $\Delta r_4 = 7$. Since the global OAM is also zero (as in the case above), the OAM density exists equally in both the negative and positive quadrants, evident in Figs 6.4.6 (d) and (e). As this is also a non-symmetric superposition, the OAM density is not uniform in all radial directions of the optical field (evident in Fig. 6.4.6 (e)) and so the OAM density plotted in Fig. 6.4.6 (d) is an average over all angular positions.

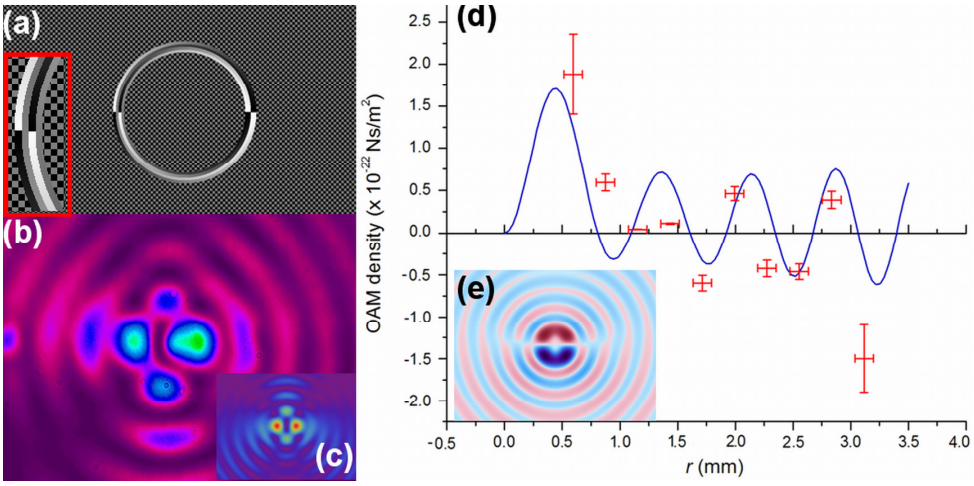

Fig. 6.4.6. (a) The hologram used to generate the experimental field given in (b) of which the theoretical field is represented in (c). A magnification of the ring-slit is given as an insert in (a). (d) The theoretical (blue curve) and experimentally measured (red points) OAM density. (e) A density plot of the OAM density. Red denotes negative OAM and blue denotes positive. Light to dark blue denotes an increase in positive OAM and light to dark red denotes an increase in negative OAM.

For each of the six optical fields, the on-axis intensity recorded at CCD_2 for each of the match-filters (varying in ring-slit radius and azimuthal order) was measured and implemented using Eqs (1.3.8) and (6.2.7). It is evident that in all our tests, there is very good agreement between the experimentally measured OAM density values and those calculated theoretically. By our extremely simple technique, we are able, for the first time, to make quantitative measurements of the OAM density, measured in units of the angular momentum per unit volume, Ns/m^2.

6.5. Conclusion

In this chapter we have we have derived experimental and theoretical expressions for the OAM density for both symmetric and non-symmetric superpositions of Bessel beams and tested the agreement [8, 9]. Our measurement technique can be used on any optical field carrying OAM. Even though the global OAM is zero, the OAM density can be made to oscillate from positive to negative by appropriately adjusting the widths of the ring-slits or the azimuthal orders within the ring-slits, making it an ideal tool in the field of optical trapping and tweezing. Previous studies to obtain the OAM density have involved the rotation of trapped particles, which is not only an indirect measurement, but also a very difficult experiment to execute. The technique we

present, requires only an SLM and a lens, and is therefore easy to implement. Measuring the OAM spectrum of fields has direct relevance in the optical control of flow in micro-fluidic devices and in constructing optically-driven micro-machines. Being able to determine the local OAM is important for imaging [21] and optical funnels [22].

6.6. References

[1]. V. Garces-Chavez, D. McGloin, M. J. Padgett, W. Dultz, H. Schmitzer, and K. Dholakia, "Observation of the transfer of the local angular momentum density of a multiringed light beam to an optically trapped particle," Phys. Rev Lett. **91**(9), 093602 (2003).

[2]. C. H. J. Schmitz, K. Uhrig, J. P. Spatz, and J. E. Curtis, "Tuning the orbital angular momentum in optical vortex beams," Opt. Express **14**(15), 6604-6612 (2006).

[3]. S. H. Tao, X. C. Yuan, J. Lin, and R. E. Burge, "Residue orbital angular momentum in interferenced double vortex beams with unequal topological charges," Opt. Express **14**(2), 535-541 (2006).

[4]. K. Volke-Sepulveda, V. Garces-Chavez, S. Chavez-Cerda, J. Arlt and K. Dholakia "Orbital angular momentum of a high-order Bessel light beam," J. Opt. B Quantum Semiclassical Opt. **4**(2), S82-S89 (2002).

[5]. V. Garces-Chavez, K. Volke-Sepulveda, S. Chavez-Cerda, W. Sibbett, and K. Dholakia, "Transfer of orbital angular momentum to an optically trapped low-index particle," Phys. Rev. A **66**(6), 063402 (2002).

[6]. M. V. Vasnetsov, J. P. Torres, D. V. Petrov, and L. Torner, "Observation of the orbital angular momentum spectrum of a light beam," Opt. Lett. **28**(23), 2285-2287 (2003).

[7]. M. Hautakorpi, J. Lindberg, T. Setälä, and M. Kaivola, "Rotational frequency shifts in partially coherent optical fields," J. Opt. Soc. Am. A **23**(5), 1159-1163 (2006).

[8]. I. Litvin, A. Dudley and A. Forbes, "Poynting vector and orbital angular momentum density of superpositions of Bessel beams," Opt. Express **19**(18), 16760-16771 (2011).

[9]. A. Dudley, I. Litvin, and A. Forbes, "Quantitative measurement of the orbital angular momentum density of light," App. Opt. **51**(7), 823-833 (2012).

[10]. S. Franke-Arnold, J. Leach, M. J. Padgett, V. E. Lembessis, D. Ellinas, A. J. Wright, J. M. Girkin, P. Ohberg, and A. S. Arnold, "Optical ferris wheel for ultracold atoms," Opt. Express **15**(14), 8619-8625 (2007).

[11]. L. Paterson, M. P. MacDonald, J. Arlt, W. Sibbett, P. E. Bryant, and K. Dholakia, "Controlled rotation of optically trapped microscopic particles," Science **292**(5518), 912-914 (2001).

[12]. D. McGloin, V. Garcés-Chávez, and K. Dholakia, "Interfering Bessel beams for optical micromanipulation," Opt. Lett. **28**(8), 657-659 (2003).

[13]. A. Mair, A. Vaziri, G. Weihs, and A. Zeilinger, "Entanglement of the orbital angular momentum states of photons," Nature **412**, 313-316 (2001).

[14]. H. I. Sztul and R. R. Alfano, "The Poynting vector and angular momentum of Airy beams," Opt. Express **16**(13), 9411-9416 (2008).

[15]. M. J. Padgett, and L. Allen, "The Poynting vector in Laguerre-Gaussian laser modes," Opt. Commun. **121**(39141), 36-40 (1995).

[16]. L. Allen and M. J. Padgett, "The Poynting vector in Laguerre-Gaussian beams and the interpretation of their angular momentum density," Opt. Commun. **184**(1), 67-71 (2000).

[17]. R. Zambrini and S. M. Barnett, "Angular momentum of multimode polarization patterns," Opt. Express **15**(23), 15214-15227 (2007).

[18]. A. T. O'Neil, I. MacVicar, L. Allen and M. J. Padgett, "Intrinsic and extrinsic nature of the orbital angular momentum of a light beam," Phys. Rev. Lett. **88**(5), 053601 (2002).

[19]. M. V. Berry, "Paraxial beams of spinning light," Proc. SPIE **3487**, 6-11 (1998). doi: 10.1117/12.317704.

[20]. R. Vasilyeu, A. Dudley, N. Khilo, and A. Forbes, "Generating superpositions of higher-order Bessel beams," Opt. Express **17**(26), 23389-23395 (2009).

[21]. L. Torner, J. P. Torres, and S. Carrasco, "Digital spiral imaging," Opt. Express **13**(3), 873-881 (2005).

[22]. J. A. Rodrigo, A. M. Caravaca-Aguirre, T. Alieva, G. Cristóbal, and M. L. Calvo, "Microparticle movements in optical funnels and pods," Opt. Express **19**(6), 5232-5243 (2011).

CHAPTER SEVEN

Conclusions and future study

7.1. Conclusions

In chapter one a literature review of optical OAM was given and it was shown that beams carrying a phase factor of $\exp(il\theta)$ possess a well-defined OAM. Definitions for some of the solutions to the Helmholtz wave equation, which are utilized in this thesis, such as Gaussian beams, LG beams and Bessel beams were also given.

Experimental techniques for generating or detecting fields carrying OAM were presented and discussed in the second chapter of this thesis. Two types of digital holograms were examined: the spiral and fork holograms, for the production and measurement of OAM. Other OAM tools discussed were spiral phase plates, which could be used to increase or decrease the OAM of a transmitted beam, and cylindrical lenses, which convert HG modes into LG modes. Another device which was used to sort odd and even OAM modes, for which we have developed a robust adaptation [1], is a Dove-prism embedded Mach-Zehnder interferometer [2]. Our interferometer has no degrees of freedom and correct functioning of the device was achieved with two mirrors external to the interferometer. Our device sorted twenty-one OAM states of light with a contrast higher than 85.3%.

In chapter three we extended the Dove prism embedded Mach-Zehnder interferometer to produce an optical system that acted as an amplitude damping channel for a two-level OAM system [3]. We tested the concept of our device using the vortex mode ($l = 1$) and a Gaussian mode and illustrated that it agrees well with the theoretical model. Such an optical system could be used to represent the dynamics of a quantum system that incurs the loss of energy.

The forth chapter contained two techniques which we developed for the generation of superimposed higher-order Bessel beams [4, 5]. In our first approach we illuminated a physical ring-slit aperture with a beam that has an azimuthally varying phase [4]. Later, we simplified our technique with a single hologram [5]. In both cases very good agreement between the

experimentally produced fields and the theoretical predictions was obtained. We also revealed the existence of higher-order vortices in the produced field by interfering it with a plane wave. The rotation rates of the produced superimposed Bessel beams could be controlled by varying the azimuthal order $|l|$ and the difference, Δk, between the two radial wave-vectors [5]. We were able to show very good agreement between the experimentally measured and theoretically predicted rotation rates, illustrating that these fields are an ideal tool for the controlled rotation of trapped particles. We also studied the near-field of the superimposed higher-order Bessel beams and showed that the ring-slit field, which exhibited no rotation in its intensity profile, transformed from an annular structure (embedded with singularities) to a petal structure [6].

Instead of encoding the phase within the ring-slit with an azimuthally varying phase with a random phase modulation, non-diffracting speckle fields were obtained. In chapter five we investigated the generation of non-diffracting speckle fields with a single ring-slit hologram and illustrated good agreement between our experimentally produced non-diffracting speckle fields and theoretical predictions. The phase modulation within the ring-slit hologram was described by either a binary or a continuous phase modulation for two different distributions, namely uniform and normal, and we examined the effect these distributions have on the structure of the speckle field [7]. By adjusting the standard deviation of the distribution one could control the evolution of the non-diffracting chaotic speckle into a non-diffracting zero-order Bessel beam. This allows one to 'tailor-make' a non-diffracting speckle field for specific optical functions, such as non-destructive testing of materials.

In chapter six we derived experimental and theoretical expressions for the OAM density for both symmetric and non-symmetric superpositions of Bessel beams and presented a simple measurement technique to obtain the OAM density [8, 9]. We tested our experimental technique on both symmetric and non-symmetric superpositions of Bessel beams and obtained very good agreement with our theoretical predictions. OAM density measurements are relevant in controlling the flow in micro-fluidic devices and in constructing optically-driven micro-machines.

7.2. Future study

Since our robust interferometer, presented at the end of chapter two, has proved to be very efficient at separating odd and even OAM modes, one could introduce such a device into a quantum entanglement setup for the detection of odd and even OAM states of photon pairs.

Currently OAM states in quantum entanglement experiments are detected with the fork hologram which produces a Gaussian beam in the desired diffraction order that is then coupled into a single mode fibre [10]. The fork hologram can be replaced with the robust 'odd even OAM sorter' so as to simultaneously detect odd and even OAM states as opposed to detecting one OAM state at a time. This device represents the OAM analogy to the polarizing beam-splitter and so this robust device can be incorporated into quantum optic experiments to perform similar tomography measurements on OAM states that are made with polarization (in the case that the OAM state-space is restricted to a two state-space: odd and even). One could also use this device to sort odd and even OAM states before they are further sorted into their individual ports by incorporating a technique which converts the OAM state of light to a specific lateral position [11]. Since the detection spots marking the different lateral positions slightly overlap [11], first separating the odd and even OAM states into separate ports will reduce the overlapping of the detection spots and allow for the detection of an increased OAM state-space.

With the amplitude damping channel that we discussed in chapter three, one could incorporate this device into a quantum entanglement setup so as to mimic a lossy environment for one of the entangled photon pairs. One could then predict analytically the entanglement decay in OAM states when one of the entangled photon pairs is passed through such a channel. Experimentally this will be achieved by introducing the OAM amplitude damping channel into one of the arms of a quantum entanglement system (where a photon in the one arm possesses an entangled photon in the other arm). The concurrence of the entanglement is measured before the OAM amplitude damping channel is introduced and then after the channel has been incorporated which will result in a quantitative comparison of the decoherence of entanglement due to interactions with a noisy environment.

Even though we investigated the dynamics from chaotic non-diffracting speckle to a structured non-diffracting zero-order Bessel beam by varying the standard deviation of different distributions describing the phase modulation, there are other structural attributes of the speckle field that still need to be investigate. Further investigations into how the geometry and the dimensions of the ring-slit have on the clustering (or snake-like patterns) of the speckles could be made.

Finally, with the experimental technique that we developed for the measurement of the OAM density of optical fields, presented in chapter six, a method to extract the entire OAM spectrum of an optical field (at a specific radial position) in a single measurement could be developed.

This could be achieved by combining the hologram used to represent the required match filter with the transforming element implemented in Ref. [11] so that not only can one extract the entire OAM spectrum by measuring the weightings (or intensities) present at the different lateral positions, but one can select the radial position within the optical field.

7.3. References

[1]. M. Lavery, A. Dudley, A. Forbes, J. Courtial and M. Padgett, "Robust interferometer for the routing of light beams carrying orbital angular momentum," New J. of Phys. **13**(9), 093014 (2011).

[2]. J. Leach, M. J. Padgett, S. M. Barnett, S. Franke-Arnold, and J. Courtial, "Measuring the orbital angular momentum of a single photon," Phys. Rev. Lett. **88**(25), 257901 (2002).

[3]. A. Dudley, M. Nock, T. Konrad, F. S. Roux, and A. Forbes, "Amplitude damping of Laguerre-Gaussian modes," Opt. Express **18**(22), 22789-22795 (2010).

[4]. R. Vasilyeu, A. Dudley, N. Khilo, and A. Forbes, "Generating superpositions of higher-order Bessel beams," Opt. Express **17**(26), 23389-23395 (2009).

[5]. R. Rop, A. Dudley, C. López-Mariscal, and A. Forbes, "Measuring the rotation rates of superpositions of higher-order Bessel beams," J. Mod. Opt. **59**(3), 259-267 (2012).

[6]. A. Dudley and A. Forbes, "From stationary annular rings to rotating Bessel beams," J. Opt. Soc. Am. A **29**(4), 567-573 (2012).

[7]. A. Dudley, R. Vasilyeu, V. Belyi , N. Khilo, P. Ropot, and A. Forbes, "Controlling the evolution of nondiffracting speckle by complex amplitude modulation on a phase-only spatial light modulator," Opt. Commun. **285**(1), 5-12 (2012).

[8]. I. Litvin, A. Dudley and A. Forbes, "Poynting vector and orbital angular momentum density of superpositions of Bessel beams," Opt. Express **19**(18), 16760-16771 (2011).

[9]. A. Dudley, I. Litvin, and A. Forbes, "Quantitative measurement of the orbital angular momentum density of light," App. Opt. **51**(7), 823-833 (2012).

[10]. A. Mair, A. Vaziri, G. Weihs, and A. Zeilinger, "Entanglement of the orbital angular momentum states of photons," Nature **412**, 313-316 (2001).

[11]. G. C. G. Berkhout, M. P. J. Lavery, J. Courtial, M. W. Beijersbergen, and M. J. Padgett, "Efficient Sorting of Orbital Angular Momentum States of Light," Phys. Rev. Lett. **105**(15), 153601 (2010).

APPENDIX

A1: Procedure for Calibrating a Spatial Light Modulator

The purpose of performing the calibration is to verify that for your working wavelength a phase shift from 0 to 2π is achieved over all the 256 grey-levels. If the phase shift for the assigned grey-levels does not fall in the range from 0 to 2π then the voltages applied to the electrodes of the pixels need to be adjusted appropriately so as to achieve the correct phase modulation. So the first step in calibrating the SLM, for a particular wavelength, is to measure the phase modulation over the 256 grey-levels. This is achieved by interfering two beams which are reflected off of the SLM (where one of the beams undergoes a phase modulation over all 256 grey-levels) and so causes a shift in the interference pattern. The experimental setup to perform such a measurement can be represented as follows.

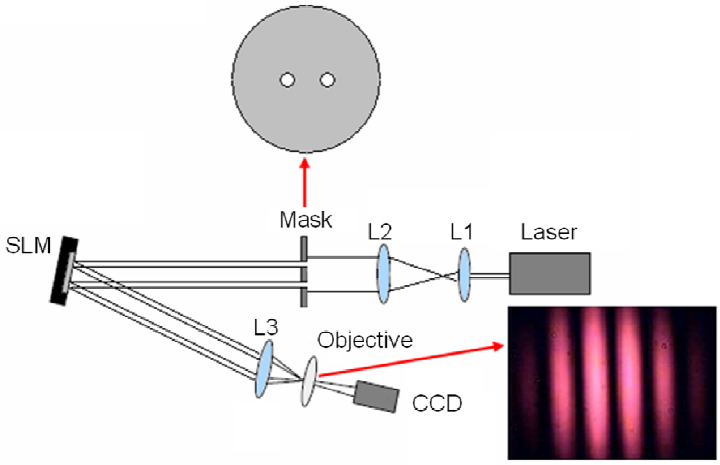

Fig. A1.1. A schematic of the calibration experiment.

An expanded laser beam is passed through a “double hole” mask. Each of the two beams is directed to the display of the SLM. The beams, reflected from the SLM, interfere in the focal plane of a lens and this interference pattern is enlarged and imaged onto a camera.

By considering the interference of two plane waves and introducing a phase shift in one of the waves, a shift in the position of the interference pattern is observed. The complex amplitudes of two identical plane waves can be written as follows:

$$\begin{aligned} u_1 &\approx \exp(i\phi_1) \\ u_2 &\approx \exp(i\phi_2) \end{aligned} \tag{A1.1}$$

In determining the intensity profile of the addition of these two fields the following term gives rise to the interference pattern.

$$I = |u_1 + u_2|^2 \approx (\cos\phi_1)^2 \tag{A1.2}$$

Introducing a phase shift in one of the beams, results in the following term describing the interference pattern:

$$\begin{aligned} u_1 &\approx \exp(i\phi_1) \\ u_2 &\approx \exp(i(\phi_1 + \delta)) \\ I = |u_1 + u_2|^2 &\approx (\cos\phi_1 + \cos(\phi_1 + \delta))^2 \end{aligned} \tag{A1.3}$$

By varying the phase of one of the beams, the position of the interference pattern shifts. It is this principle that is used to measure the phase shift over all 256 grey-levels.

1. Amplitude for two identical plane waves:

$$u_1 \approx e^{i\phi_1}$$

$$u_2 \approx e^{i\phi_1}$$

$$I = |u_1 + u_2|^2 \approx (\cos(\phi_1))^2$$

2. Now introduce a phase shift in one of the beams:

$$u_1 \approx e^{i\phi_1}$$

$$u_2 \approx e^{i(\phi_1+\delta)}$$

$$I = |u_1 + u_2|^2 \approx (\cos(\phi_1) + \cos(\phi_1 + \delta))^2$$

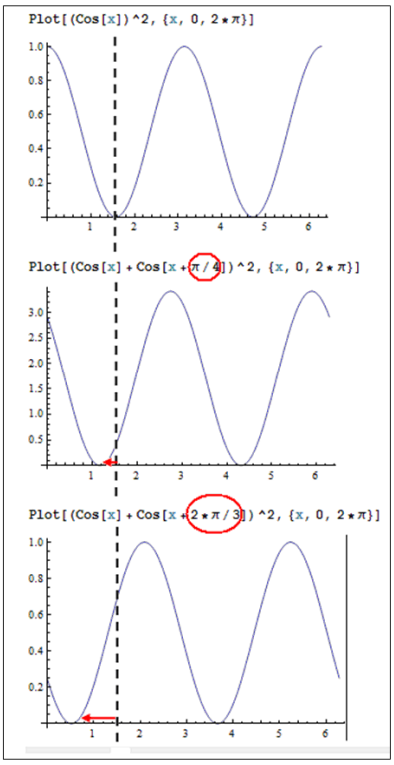

Fig. A1.2. Summary on how a phase shift in one of the beams is directly proportional to a shift in the interference pattern.

In the experimental setup, where the two beams are reflected off of the SLM display, one half of the display is addressed with a constant grey-level while the other half is addressed with a grey-level varying from 0 to 255. As the grey-level of the one half of the screen changes so the interference pattern shifts and this shift in the interference pattern is directly proportional to the phase shift experience by the beam.

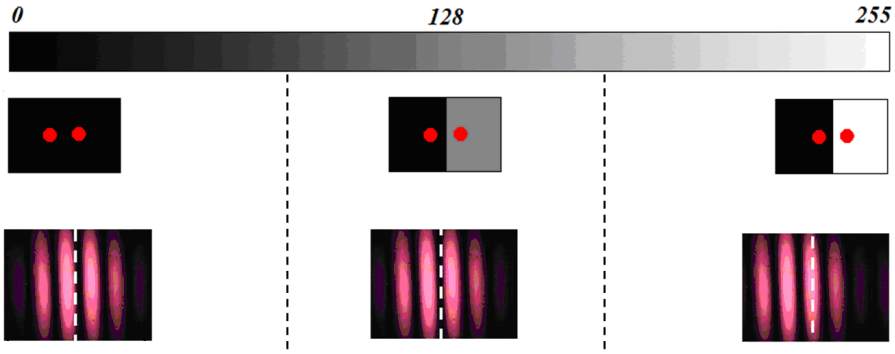

Fig. A1.3. Illustration of how a change in grey-level shifts the interference pattern.

After the one half of the screen has been addressed with all 256 grey-levels, the software that we use in the calibration of the SLM plots the 1D intensity profile of the interference pattern for each grey-level.

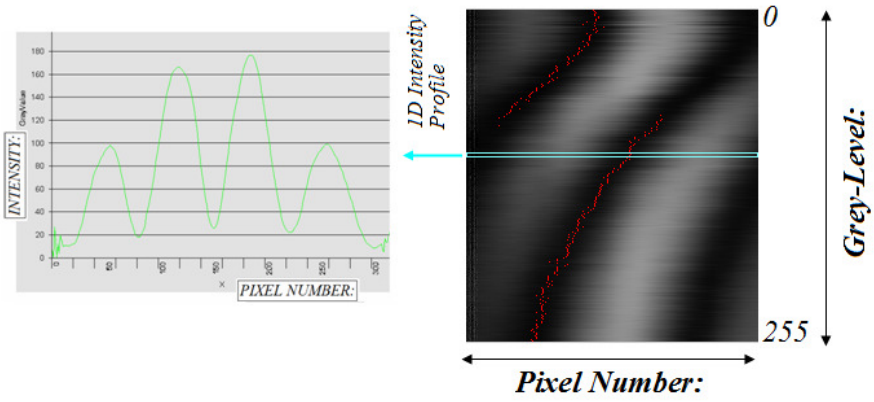

Fig. A1.4. A plot of the 1 D intensity profile of the interference pattern for a particular grey-level.

The above plot consists of 256 rows each containing the 1D intensity profile of the interference pattern for that particular grey-level. The red dots mark the intensity minima of the interference pattern for each grey-level. From these measurement points the pixel position of the intensity minima can be plotted as a function of the grey-level to produce the following plot.

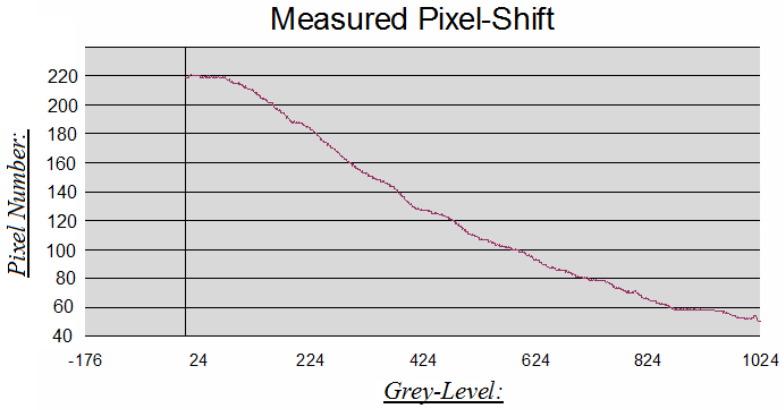

Fig. A1.5. A plot of the intensity minima pixel position as a function of the grey-level.

By comparing the red measurement points (in Fig. A1.4) and the plot of the pixel position as a function of the grey-level (Fig. A1.5) you will notice that the discontinuity in the measurement

points doesn't appear. The program knows the period of the intensity minima, the pixel distance from minimum to minimum, and so adjusts the measurement points to remove the discontinuity in the plot. The reason that the range of the x-axis (in Fig. A1.5) varies from 0 to 1024 (and not 0 to 255) is due to the way in which the device is configured. The device needs to be programmed with 1024 values; so the first of every four values is the measured value.

The shift in the minima of the interference pattern is directly proportional to the phase modulation and the information below illustrates how the phase modulation is determined. The phase shift induced by a particular grey-level can be determined by performing the following calculation.

$$\frac{(pixel \quad \# \quad for \quad grey-level\, X - starting \quad pixel \quad \#)}{\frac{1}{2}\, period \quad pixel \quad dis\tan ce} \qquad \text{(A1.4.)}$$

The difference between the pixel position for a particular grey-level and the pixel position for a grey-level of 0 (for no phase modulation) is determined and divided by half of the period. Below is an example of the calculated phase shift when calibrating the SLM.

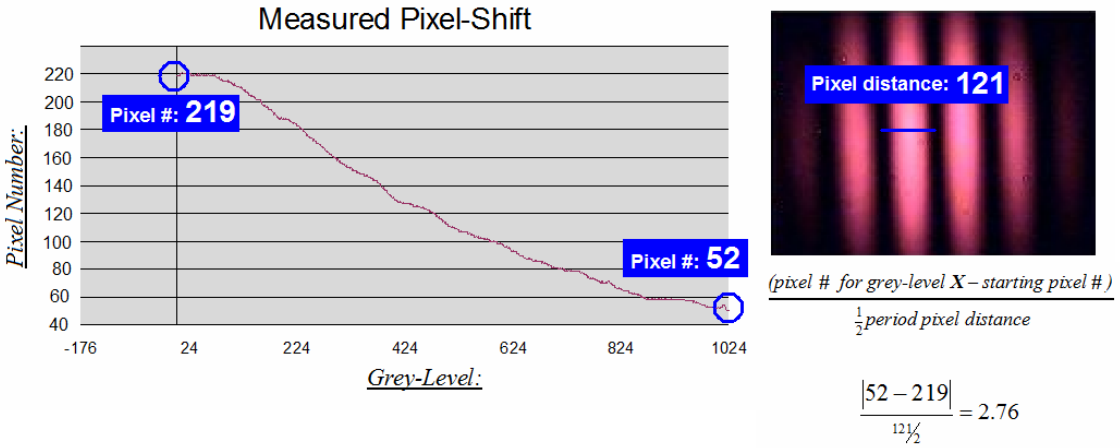

Fig. A1.6. Example of calculating the phase shift.

By substituting in the appropriate values, it is calculated that a grey-level of 255 induces a phase shift of about 2.8π. This illustrates that for this particular wavelength the device is not correctly calibrated. The voltages which address the individual pixels, need to be adjusted appropriately so as to produce the required 2π phase shift over all 256 grey-levels.

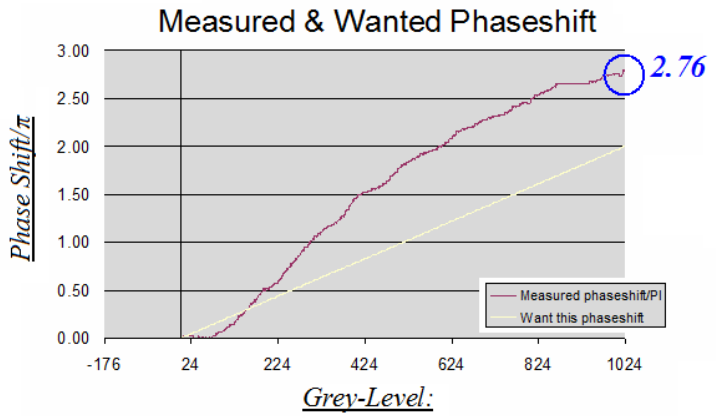

Fig. A1.7. Plot of the measured phase shift (red) and the desired phase shift (yellow).

After the calibration has been performed and the voltages have been adjusted appropriately, repeating the previously described measurements should produce a 2π phase shift over all grey-levels.

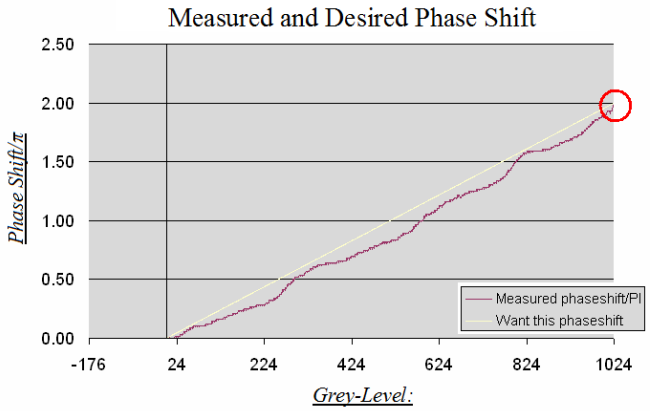

Fig. A1.8. Plot of the measured phase shift (red) after the voltages have been adjusted appropriately.

Some general issues regarding the calibration procedure are listed below:

1.

Since the calibration relies on measuring the phase shift in the interference pattern, a good interference pattern needs to be obtained so as to obtain accurate measurements. It is essential to check that the intensity distribution of the beam on the "2 hole mask" is uniform. In other words, check that equal intensity is passing through the two holes.

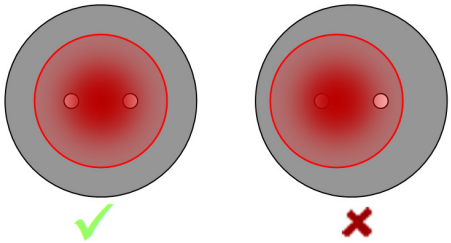

Fig. A1.9. Illustration for how the “2 hole mask” should be illuminated.

2.

Make sure that the two spots are superimposed exactly on top of each other in the focal plane. Below is an image of a good, crisp interference pattern and an interference pattern where the two spots are not perfectly superimposed.

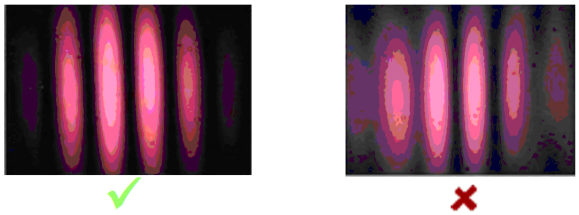

Fig. A1.10. Illustration for a correct and incorrect interference pattern.

3.

Another factor which could lead to incorrect measurements is if the two beams are not positioned on the SLM correctly, resulting in the one beam not experiencing the correct phase modulation.

Fig. A1.11. Illustration of how to position the two spots on the SLM.

4.

When performing the calibration and recording the measurements, do this with the lights off. Any additional light sources (even light emitted from a computer screen) may affect your measurements.

A2: Showing that the operator S_θ is linear

The equation for S_θ, is defined as

$$S_\theta = \frac{\varepsilon_0 \omega c^2 i}{4}\left(u\nabla u^* - u^*\nabla u\right), \tag{A2.1.}$$

where u is the amplitude distribution of the optical field. u^* can then be written in terms of u as follows:

$$\begin{aligned} u + u^* &= A_0\left(J_l \exp(i\Delta kz)\exp(il\theta) + \alpha_0 J_{-l}\exp(-i\Delta kz)\exp(-il\theta)\right) \\ &\quad + A_0\left(J_l \exp(-i\Delta kz)\exp(-il\theta) + \alpha_0 J_{-l}\exp(i\Delta kz)\exp(il\theta)\right) \\ u + u^* &= \left(A_0 J_l + A_0\alpha_0 J_{-l}\right)2\cos(\Delta kz + l\theta) \\ \rightarrow u^* &= \underbrace{2A_0\left(J_l + \alpha_0 J_{-l}\right)\cos(\Delta kz + l\theta)}_{X} - u, \end{aligned} \tag{A2.2.}$$

where for convenience we have marked the terms not involving u as X.

Substituting u^* into Eq. A2.1, results in

$$\begin{aligned} S_\theta &\propto u\nabla u^* - u^*\nabla u \\ &\propto u\nabla(X - u) - (X - u)\nabla u \\ &\propto u\nabla X - u\nabla u - X\nabla u + u\nabla u \\ &\propto u\nabla X - X\nabla u. \end{aligned} \tag{A2.3.}$$

This is a linear operator, i.e., $S_\theta(u_1 + u_2) = S_\theta(u_1) + S_\theta(u_2)$, and the linear momentum (in the azimuthal co-ordinate) from the Poynting vector for a sum of fields is equal to the sum of the linear momentum of each individual field.

B1: Publication 1

Generating superpositions of higher–order Bessel beams

Ruslan Vasilyeu[1], Angela Dudley[2,3], Nikolai Khilo[1], and Andrew Forbes[2,3,*]

[1] *B.I. Stepanov Institute of Physics of NAS of Belarus, Nezalezhnasti Ave., 68, 220072 Minsk, Belarus*
[2] *School of Physics, University of KwaZulu-Natal, Private Bag X54001, Durban 4000, South Africa*
[3] *CSIR National Laser Centre, PO Box 395, Pretoria 0001, South Africa*
*aforbes1@csir.co.za

Abstract: We report the first experimental generation of the superposition of higher-order Bessel beams, by means of a spatial light modulator (SLM) and a ring slit aperture. We present illuminating a ring slit aperture with light which has an azimuthal phase dependence, such that the field produced is a superposition of two or more higher-order Bessel beams. The experimentally produced fields are in good agreement with those calculated theoretically. The significance of these fields is that even though one is able to generate fields which carry zero orbital angular momentum, a rotation in the field's intensity profile as it propagates is observed.

©2009 Optical Society of America

OCIS codes: (140.3300) Laser Beam Shaping; (080.4865) Optical Vortices.

References and links

1. J. Durnin, "Exact solutions for nondiffracting beams. I. The scalar theory," J. Opt. Soc. Am. A **4**(4), 651–654 (1987).
2. J. Durnin, J. J. Miceli, Jr., and J. H. Eberly, "Diffraction-free beams," Phys. Rev. Lett. **58**(15), 1499–1501 (1987).
3. R. M. Herman, and T. A. Wiggins, "Production and uses of diffractionless beams," J. Opt. Soc. Am. A **8**(6), 932–942 (1991).
4. J. Arlt, and K. Dholakia, "Generation of high-order Bessel beams by use of an axicon," Opt. Commun. **177**(1-6), 297–301 (2000).
5. J. Turunen, A. Vasara, and A. T. Friberg, "Holographic generation of diffraction-free beams," Appl. Opt. **27**(19), 3959–3962 (1988).
6. A. Vasara, J. Turunen, and A. T. Friberg, "Realization of general nondiffracting beams with computer-generated holograms," J. Opt. Soc. Am. A **6**(11), 1748–1754 (1989).
7. H. S. Lee, B. W. Stewart, K. Choi, and H. Fenichel, "Holographic nondiverging hollow beam," Phys. Rev. A **49**(6), 4922–4927 (1994).
8. G. Indebetouw, "Nondiffracting optical fields: some remarks on their analysis and synthesis," J. Opt. Soc. Am. A **6**(1), 150–152 (1989).
9. J. A. Davis, E. Carcole, and D. M. Cottrell, "Nondiffracting interference patterns generated with programmable spatial light modulators," Appl. Opt. **35**(4), 599–602 (1996).
10. J. A. Davis, E. Carcole, and D. M. Cottrell, "Intensity and phase measurements of nondiffracting beams generated with a magneto-optic spatial light modulator," Appl. Opt. **35**(4), 593–598 (1996).
11. C. Paterson, and R. Smith, "Higher-order Bessel waves produced by axicon-type computer-generated holograms," Opt. Commun. **124**(1-2), 121–130 (1996).
12. J. H. McLeod, "The axicon: a new type of optical element," J. Opt. Soc. Am. **44**(8), 592–597 (1954).
13. D. McGloin, G. C. Spalding, H. Melville, W. Sibbett, and K. Dholakia, "Three-dimensional arrays of optical bottles," Opt. Commun. **225**(4-6), 215–222 (2003).
14. D. McGloin, V. Garcés-Chávez, and K. Dholakia, "Interfering Bessel beams for optical micromanipulation," Opt. Lett. **28**(8), 657–659 (2003).
15. T. A. King, W. Hogervorst, N. S. Kazak, N. A. Khilo, and A. A. Ryzhevich, "Formation of higher-order Bessel light beams in biaxial crystals," Opt. Commun. **187**(4-6), 407–414 (2001).
16. V. V. Kotlyar, S. N. Khonina, R. V. Skidanov, and V. A. Soifer, "Rotation of laser beams with zero of the orbital angular momentum," Opt. Commun. **274**(1), 8–14 (2007).
17. L. Burger, and A. Forbes, "Kaleidoscope modes in large aperture Porro prism resonators," Opt. Express **16**(17), 12707–12714 (2008).

#117284 - $15.00 USD Received 15 Sep 2009; revised 22 Oct 2009; accepted 4 Dec 2009; published 7 Dec 2009
(C) 2009 OSA

1. Introduction

There is an extensive body of literature on generating zero order and higher-order Bessel beams. Durnin [1] first discovered a set of solutions for the free-space Helmholtz equation which are propagation-invariant and are mathematically described by Bessel functions. Even though it is not possible to experimentally generate an ideal Bessel beam, as it contains an infinite number of rings over an infinite area resulting in the beam carrying infinite energy, an approximation can be realized in the form of Bessel-Gauss beams that propagate diffraction-free over a finite distance [2–11].

Zero-order Bessel beams possess a bright central maximum, while the higher-orders have a dark central vortex, which propagates over an extended distance in a diffraction-free manner. Zero order Bessel beams can be generated by illuminating a ring slit aperture, placed in the back focal plane of a lens, with a plane wave [2]. Refractive optical elements, such as axicons [3,4,12] and diffractive optical elements such as computer generated holograms [5,6,9–11,13], have been used to generate both zero and higher-order Bessel beams. In particular it has been shown that it is possible to create a superposition of high-order Bessel beams by extending the results in ref [4]. to illuminate an axicon with a superposition of Laguerre-Gauss (LG) beams [14]. This overcomes the problem of creating a Bessel beam interferometer, but requires the creation of high order LG beams on demand in the laboratory.

In this paper we extend Durnin's original experiment to create a ring slit aperture in the Fourier plane with multiple azimuthal phase components at varying radial distances, thereby producing a superposition of higher-order Bessel beams as the output. The concept is illustrated graphically in Fig. 1, where two separable azimuthal phase components, namely $\exp(im\varphi)$ and $\exp(in\varphi)$, are combined to produce a superposition of an m^{th} order and n^{th} order Bessel beam.

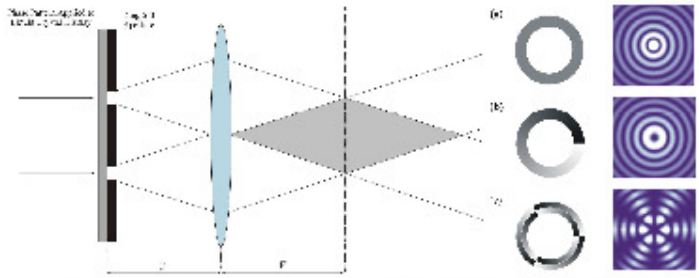

Fig. 1. Extension of Durnin's ring slit experiment [2]. (b) and (c): Illuminating the ring slit aperture with a beam whose angular spectrum carries an azimuthally varying phase generates higher-order and superpositions of higher-order Bessel beams.

2. Theory

An ideal Bessel beam (in cylindrical coordinates, (r,φ,z)) is characterized by a transverse component of the electrical field:

$$E(r,\phi,z) = a_0 J_m(k_r r)\exp\left[i\left(k_z z + m\phi\right)\right], \tag{1}$$

where J_m is the m^{th} order Bessel function, while k_z and k_r are the longitudinal and transverse wave numbers respectively, with $k_r = k_0\sin\alpha$, $k_z = k_0\cos\alpha$, and $k_0 = 2\pi/\lambda$; λ is the wavelength and α is the opening angle of the cone on which the waves traverse. It is seen from Eq. (1) that higher–order Bessel beams ($|m| > 1$) have an azimuthal phase dependence, $\exp(im\varphi)$, on the beam axis and hence have a nondiffracting dark core.

#117284 - $15.00 USD Received 15 Sep 2009; revised 22 Oct 2009; accepted 4 Dec 2009; published 7 Dec 2009
(C) 2009 OSA

Consider the ideal case where an incident Gaussian beam is transformed to a ring field, with radius R and width 2Δ, by a ring slit aperture. If the ring slit aperture is divided equally in the radial direction to yield two azimuthal phase components, denoted by azimuthal mode index m and n in the inner and outer rings respectively, then the resulting superposition is calculated from the Kirchoff–Huygens diffraction integral

$$A_{m,n}(r,\phi,z) = \frac{-i}{\lambda z}\int_0^{2\pi}\int_{R-\Delta}^{R+\Delta} \tau(r,\phi)\exp\left[i\frac{k_0}{2f}\left(1-\frac{z}{f}\right)r_1^2\right]\exp\left[-i\frac{k_0 r r_1}{f}\cos(\phi_1-\phi)\right] r_1 dr_1 d\phi_1 \quad (2)$$

with the transmission function of the ring slit aperture given by:

$$\tau(r,\phi) = \begin{cases} \exp(im\phi), & R \geq r \geq (R-\Delta) \\ \exp(in\phi), & R \leq r \leq (R+\Delta) \end{cases}. \quad (3)$$

The total field may be decomposed into the contribution resulting from the inner ring (azimuthal mode index m) and the outer ring (azimuthal mode index n), given respectively as:

$$A_m(r,\phi,z) = \frac{-ik_0}{f}\int_{R-\Delta}^{R} i^m \exp(im\phi) J_m\left(\frac{k_0 r r_1}{f}\right)\exp\left[-\frac{r_1^2}{w^2}+\frac{ik_0 r_1^2}{2f}\left(1-\frac{z}{f}\right)\right] r_1 dr_1, \quad (4)$$

$$A_n(r,\phi,z) = \frac{-ik_0}{f}\int_{R}^{R+\Delta} i^n \exp(in\phi) J_n\left(\frac{k_0 r r_1}{f}\right)\exp\left[-\frac{r_1^2}{w^2}+\frac{ik_0 r_1^2}{2f}\left(1-\frac{z}{f}\right)\right] r_1 dr_1, \quad (5)$$

so that the resulting field may be expressed as a superposition of the form:

$$A_{m,n}(r,\phi,z) = A_m(r,\phi,z) + A_n(r,\phi,z). \quad (6)$$

Specifically, the superposition of an m^{th} order Bessel beam with its mirror image ($-m^{th}$ order Bessel beam), results in a spatial intensity pattern of $2m$ spots arranged on the circumference of a ring (with an angular offset depending on whether m is even/odd):

$$A_{m,-m}(r,\phi,z) = J_m(k_r r)\sin(m\phi)\exp(ik_z z). \quad (7)$$

Such a field carries no orbital angular momentum (OAM), although we will show later that there is a rotation in the field structure when it is created with a two-component ring structure as described by Eq. (3).

3. Experimental methodology and results

Our experimental setup is shown in Fig. 2. A HeNe laser (λ ~633 nm) was expanded through a 15 × telescope (f_1 = 10 mm, f_2 = 150 mm) before illuminating a suitable ring slit aperture (R = 3 mm and 2Δ = 150 μm). The resulting field was relay imaged to the plane of the liquid crystal display with a 0.75 × telescope (f_3 = 100 mm, f_4 = 75 mm). The liquid crystal on silicon device used for imparting the azimuthal phase variation on the field was a spatial light modulator (SLM) (Holoeye, HEO1080P) with 1920 × 1080 pixels of pitch 8 μm and calibrated for a 2π phase shift at ~633 nm. The angle of incidence on the SLM was kept as low as possible, typically < 10° in the experiment. Larger angles would cause a phase error as a result of the increased path length in the liquid crystal medium. The Fourier transform field (after the f_5 = 200 mm lens) was magnified with a 10 × objective and detected on a CCD camera (Spiricon, USB L130); both the objective and camera were positioned on a translation stage in order to investigate the propagation of the resulting field. An interferometer, denoted by the shaded box, was introduced in the experimental setup as needed to reveal the phase dislocations in the superposition fields [15].

#117284 - $15.00 USD Received 15 Sep 2009; revised 22 Oct 2009; accepted 4 Dec 2009; published 7 Dec 2009
(C) 2009 OSA

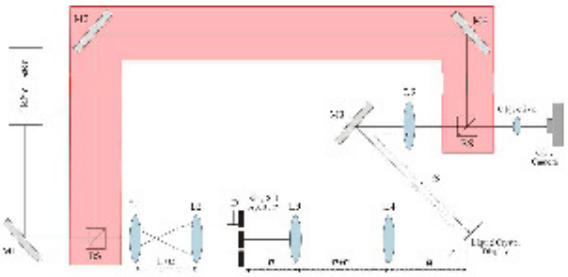

Fig. 2. The experimental design for generating a superposition of two higher-order Bessel beams. The interferometer used to interfere the field produced at the Fourier plane with a plane wave is denoted in the shaded overlay. (M: mirror, BS: beam-splitter, L: lens and D: diaphragm). Note the distances and angles are not to scale.

In such a system alignment of the ring field and the phase pattern is of course important. Careful alignment using standard micrometer adjustable translation stages was done prior to the azimuthally varying patterns loaded onto the SLM. Thereafter the scaling of the image relative to the SLM was sufficient to maintain the alignment for the experiments to follow. Results of our superposition fields, as viewed in the far field, are shown in Fig. 3.

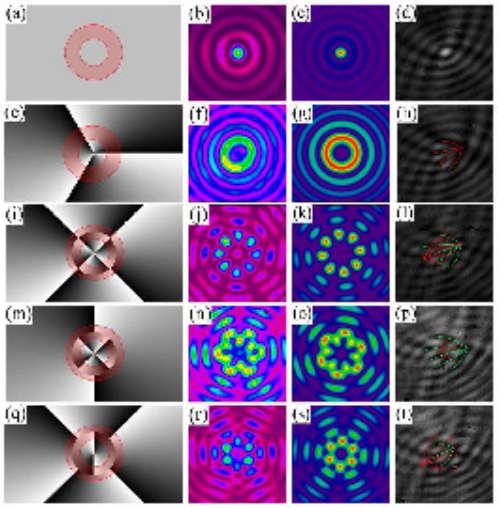

Fig. 3. The columns from left to right represent the phase patterns applied to the liquid crystal display of the SLM, the observed intensity distribution of the superposition, the theoretical prediction, and interference pattern of the superposition field and a plane wave, respectively. Data is shown for (a) – (d): A_0, (e) – (h): A_3, (i) – (l): $A_{4,4}$, (m) – (p): $A_{2,4}$, and (q) – (t): $A_{4,2}$. The illuminated ring slit is shown as a shaded overlay on the phase pattern.

With no azimuthally varying phase (Fig. 3(a)) the resulting pattern (Fig. 3(b)) is the well known zeroth order Bessel beam, while with a single azimuthal component to the phase

#117284 - $15.00 USD Received 15 Sep 2009; revised 22 Oct 2009; accepted 4 Dec 2009; published 7 Dec 2009
(C) 2009 OSA

(Fig. 3(e)) the corresponding higher-order Bessel beam is reproduced (Fig. 3(f)). The vortex nature of this field is confirmed in the interferogram of Fig. 3(h) where three dislocations are noted in the fork-like pattern. When more than one azimuthal component is introduced to the SLM, the resulting pattern becomes more complex. Nevertheless, in all cases the theoretical prediction is in excellent agreement with that measured experimentally, as is easily noted by comparison of columns two and three in Fig. 3 for any given row. As noted earlier in the theory section, when the orders of the two azimuthal phases are equal but opposite in sign, a petal-like pattern is produced. This is evident in Figs. 3(j) and 3(k) for both the measured and calculated fields respectively. Note also that the phase patterns used for a given azimuthal component are not required to extend to the origin. Due to the azimuthally varying phase which is imparted to the angular spectrum of the ring field, the resulting fields possess vortices which can be investigated by interference with the Gaussian source [15]. Since the beam size of the Gaussian beam is large in comparison to the Bessel field in the Fourier plane, the wavefront of the Gaussian field can be assumed to be flat, similar to a plane wave. The interference patterns obtained contain two overlapping forks, illustrating the presence of two higher-order Bessel fields. The number of dislocations or spaces between the 'fork-prongs' conveys the order of the Bessel fields involved in the superposition. The direction of the 'fork-prongs' illustrates that the two higher-order Bessel fields are of opposite handedness.

While we have demonstrated the concept here with the superposition of two Bessel fields, it is possible in principle to extend this to any number of azimuthal components. Figure 4 shows a three-component superposition, with azimuthal mode indices (outer to inner radii) of –3, 0 and 3 respectively. As expected, the theoretical predictions are in excellent agreement with experiment. However, superpositions of more than three higher-order Bessel beams were not attempted due to the restricting dimensions of the ring slit aperture and the resolution of our SLM.

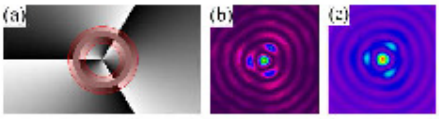

Fig. 4. (a) Phase pattern applied to the liquid crystal display. The shaded overlay denotes the section of the phase pattern which is illuminated by the ring field. (b) The experimental beam cross-section of the field produced at the Fourier plane. (c) It is in good agreement with the calculated field.

Apart from investigating the field produced at the Fourier plane, the propagation of these fields was also considered. Experimental images of the intensity profile of the produced field were captured along its propagation. A schematic of this is illustrated in Fig. 5. In studying these images, some of which are presented as video clips in Fig. 6, it is evident that the intensity profile containing the highest amount of energy occurs half way along the field's propagation. For our experimental setup this occurs at approximately 205 mm after L5. This is in close agreement with the theoretical prediction that the intensity profile containing the highest amount of energy occurs at the focal length of the Fourier transforming lens ($f_5 = 200$ mm).

#117284 - $15.00 USD Received 15 Sep 2009; revised 22 Oct 2009; accepted 4 Dec 2009; published 7 Dec 2009
(C) 2009 OSA

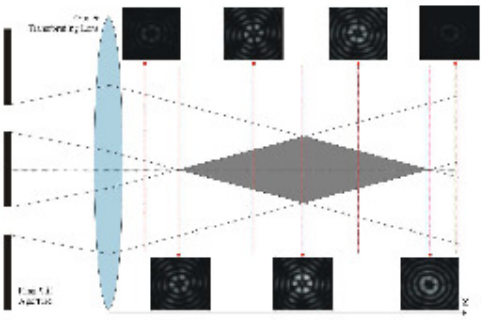

Fig. 5. Images of the intensity profile of the experimentally produced field $A_{3,-3}$ captured at intervals along its propagation. The grey area denotes the region in which the Bessel field exists.

In the video clips in Fig. 6 one also notes a rotation of the field as it propagates. This is a surprising phenomenon as in both cases an m^{th} order Bessel beam is superimposed with a $-m^{th}$ order Bessel beam, resulting in the field carrying no orbital angular momentum (as seen from Eq. (7)). However, one witnesses a rotation in the cross-section intensity distribution of the beam.

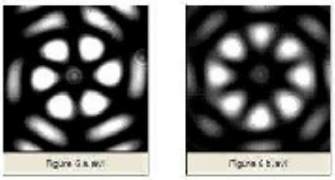

Fig. 6. Video clips containing experimental images for fields (left): $A_{3,-3}$ (media 1) and (right): $A_{4,-4}$ (media 2) which were captured at intervals along the beam's propagation.

In generating a superposition of two higher-order Bessel fields using our set-up, the ring slit aperture is divided equally in the radial direction to yield two ring slits. The Bessel field produced by each ring slit propagates with slightly differing wave vectors, and hence the superposition field is made up of modes with differing phase velocities. In such a situation one would expect the interference pattern of the modes to change during propagation. To see that this interference leads to a rotation of the field, consider the following superposition:

$$A_{m,-m}(r,\phi,z) = J_m(k_{1r}r)\exp(i(k_{1z}z+m\phi)) + J_{-m}(k_{2r}r)\exp(i(k_{2z}z-m\phi)) \qquad (8)$$

where the wavevectors differ by an amount $\Delta k = k_{2z} - k_{1z}$. The expression in Eq. (8) may be written in the form:

$$A_{m,-m}(r,\phi,z) \sim J_m(k_r r)\exp(ik_{1z}z+m\phi)\left(1+\exp[i(\Delta k z-2m\phi)]\right), \qquad (9)$$

from which we note that the intensity of the superposition is given by the following proportionality:

$$I_{m,-m}(r,\phi,z) \propto J_m^2(k_r r)\left(1+\cos(\Delta k z-2m\phi)\right). \qquad (10)$$

#117284 - $15.00 USD Received 15 Sep 2009; revised 22 Oct 2009; accepted 4 Dec 2009; published 7 Dec 2009
(C) 2009 OSA

Such a field experiences a rotation of its intensity pattern during propagation at a constant angular velocity, and at a rate along the propagation axis given by:

$$\frac{d\phi}{dz} = \frac{\Delta k}{2m}. \tag{11}$$

Figure 7 shows animations of rotating fields based on Eq. (10). The experimental observation of the rotation of the field, despite the absence of any OAM in the final field, is in agreement with that predicted theoretically [16].

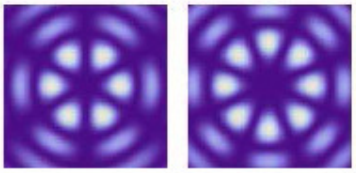

Fig. 7. Video clips containing theoretically calculated images for the rotation of fields (left): $A_{3,3}$ (media 3) and (right): $A_{4,4}$ (media 4).

By analyzing the experimental images recorded after the Fourier transforming lens, we can deduce the experimental propagation distance of the produced fields: 330 mm, 360 mm and 370 mm for the fields $A_{3,-3}$, $A_{4,-4}$, and $A_{2,-4}$ respectively; this is found to be in very good agreement with theory (~375 mm). The non-diffracting nature of the superposition fields can be understood from the fact that they are derived from the annular structure of the ring aperture, with the azimuthal phase only an additional degree of freedom. We report sans results that changing the dimensions of the ring slit aperture, as well as the focal length of the Fourier transforming lens, results in fields of differing non-diffracting propagation distances, as one might reasonably expect.

4. Conclusion

We have presented a technique to experimentally realize the superposition of higher-order Bessel beams, and demonstrated the superposition of both two and three higher-order Bessel beams, with the measured results in good agreement with the calculated fields. The propagation of these superposition fields was investigated, illustrating that these fields are propagation-invariant in accordance with prediction. The wavefront dislocations present in the higher-order Bessel beams were revealed by interferometric means, confirming the existence of higher-order vortices. These fields may aid the understanding of resonant transverse modes observed in certain laser resonators [17], and in optical trapping and tweezing for the control of micro-sized particles. In particular, in the case of generating a superposition of two higher-order Bessel beams which possess equal orders of azimuthal phase but of differing sign, the produced field carries no orbital angular momentum. Despite this, these beams are likely to be able to trap a particle in their intensity distribution and cause it to rotate over a spiral path along the beam's optical axis.

Finally, we would like to point out that the approach outlined here has not been optimized for energy transmission; the loss through the ring slit aperture is very high as may be expected. If this approach is to be followed in an application, then it would require a minor adjustment in set-up, for example, replacing the ring slit with a double axicon system to create the initial ring field.

Acknowledgements

We gratefully acknowledge the support from the National Research Foundation (Grant number 67432).

#117284 - $15.00 USD Received 15 Sep 2009; revised 22 Oct 2009; accepted 4 Dec 2009; published 7 Dec 2009
(C) 2009 OSA

B2: Publication 2

Amplitude damping of Laguerre-Gaussian modes

Angela Dudley,[1,2] Michael Nock,[2] Thomas Konrad,[2] Filippus S. Roux,[1] and Andrew Forbes[1,2,*]

[1] *CSIR National Laser Centre, PO Box 395, Pretoria 0001, South Africa*
[2] *School of Physics, University of KwaZulu-Natal, Private Bag X54001, Durban 4000, South Africa*
*aforbes1@csir.co.za

Abstract: We present an amplitude damping channel for Laguerre-Gaussian modes. Our channel is tested experimentally for a Laguerre-Gaussian mode, having an azimuthal index $l = 1$, illustrating that it decays to a Gaussian mode in good agreement with the theoretical model for amplitude damping. Since we are able to characterize the action of such a channel on orbital angular momentum states, we propose using it to investigate the dynamics of entanglement.

©2010 Optical Society of America

OCIS codes: (050.0050) Diffraction and gratings; (050.4865) Optical vortices; (270.0270) Quantum optics.

References and links

1. M. A. Nielsen and I. L. Chuang, *Quantum computation and quantum information*, Cambridge University Press, 380, Cambridge (2000).
2. M. W. Beijersbergen, L. Allen, H. E. L. O. Van der Veen, and J. P. Woerdman, "Astigmatic laser mode converters and the transfer of orbital angular momentum," Opt. Commun. **96**(1-3), 123–132 (1993).
3. L. Allen, M. W. Beijersbergen, R. J. C. Spreeuw, and J. P. Woerdman, "Orbital angular momentum of light and the transformation of Laguerre-Gaussian laser modes," Phys. Rev. A **45**(11), 8185–8189 (1992).
4. M. W. Beijersbergen, R. P. C. Coerwinkel, M. Kristensen, and J. P. Woerdman, "Helical-wave-front laser-beams produced with a spiral phaseplate," Opt. Commun. **112**(5-6), 321–327 (1994).
5. V. Yu Bazhenov, M. V. Vasnetsov, and M. S. Soskin, "Laser beams with screw dislocations in their wavefronts," JETP Lett. 52, 429–431 (1990).
6. J. E. Curtis, B. A. Koss, and D. G. Grier, "Dynamic holographic optical tweezers," Opt. Commun. **207**(1-6), 169–175 (2002).
7. H. He, M. E. J. Friese, N. R. Heckenberg, and H. Rubinsztein-Dunlop, "Direct observation of transfer of angular momentum to absorptive particles from a laser beam with a phase singularity," Phys. Rev. Lett. 75(5), 826–829 (1995).
8. A. Mair, A. Vaziri, G. Weihs, and A. Zeilinger, "Entanglement of the orbital angular momentum states of photons," Nature **412**(6844), 313–316 (2001).
9. J. Leach, M. J. Padgett, S. M. Barnett, S. Franke-Arnold, and J. Courtial, "Measuring the orbital angular momentum of a single photon," Phys. Rev. Lett. **88**(25), 257901 (2002).
10. T. Konrad, F. de Melo, M. Tiersch, C. Kasztelan, A. Aragão, and A. Buchleitner, "Evolution equation for quantum entanglement," Nat. Phys. **4**(4), 99–102 (2008).
11. B. Perz, C. H. Monken, E. R. Eliel, and J. P. Woerdman, "Transport of orbital-angular-momentum entanglement through a turbulent atmosphere," Quant-ph, 1–5 (2009).
12. C. E. R. Souza and A. Z. Khoury, "A Michelson controlled-not gate with a single-lens astigmatic mode converter," Opt. Express **18**(9), 9207–9212 (2010).
13. R. Zambrini and S. M. Barnett, "Quasi-intrinsic angular momentum and the measurement of its spectrum," Phys. Rev. Lett. **96**(11), 113901 (2006).
14. M. Born and E. Wolf, *Principles of Optics* (Pergamon Press, Oxford, 1980), 6th ed.

1. Introduction

Amplitude damping is a quantum operation which describes the energy dissipation from an excited system, such as an atom or a spin system, to an environment [1]. Under the action of an amplitude damping channel, the ground state, $|0\rangle$, is left invariant, but the excited state, $|1\rangle$, will either remain invariant or it will decay to the ground state, by losing a quantum of energy to the environment. The probability that the excited state remains unchanged or that it decays to the ground state is given by $1-p$ and p, respectively, illustrating that the amplitude of the

#133212 - $15.00 USD Received 10 Aug 2010; revised 4 Oct 2010; accepted 5 Oct 2010; published 13 Oct 2010
(C) 2010 OSA

excited state has been 'damped'. This quantum operation is a fundamental tool in classifying the behaviour of many quantum systems that incur the loss of energy, from describing the evolution of an atom that spontaneously emits a photon to how the state of a photon evolves in an optical system due to scattering and attenuation. The amplitude damping channel is an elementary quantum operation which is used to model quantum noise in understanding the dynamics of open quantum systems [1].

For the case of a two-level system, the state change under the action of amplitude damping is defined by the following transformation

$$|\psi\rangle\langle\psi| - M_0|\psi\rangle\langle\psi|M_0^* + M_1|\psi\rangle\langle\psi|M_1^*, \tag{1}$$

where M_0 and M_1 are the Krauss operators defined as

$$M_0 - \begin{pmatrix} 1 & 0 \\ 0 & \sqrt{1-p} \end{pmatrix} \tag{2}$$

and

$$M_1 - \begin{pmatrix} 1 & 0 \\ 0 & \sqrt{p} \end{pmatrix}, \tag{3}$$

The initial state of the two-level system is written as

$$|\psi\rangle - \alpha|0\rangle + \beta|1\rangle, \tag{4}$$

where $|0\rangle$ and $|1\rangle$ represent the ground state and excited state of the system, respectively and α and β denote complex amplitudes with $|\alpha|^2 + |\beta|^2 = 1$.

By making use of the Kraus operators, M_0 and M_1, and coupling the system appropriately to an environment with two orthogonal states $|K=0\rangle_E$ and $|K=1\rangle_E$, the unitary time evolution operator, U_{SE}, of the system, S, and the environment, E, produces the following transformations

$$|0\rangle_S|K-0\rangle_E \xrightarrow{U_{SE}} |0\rangle_S|K-0\rangle_E, \tag{5}$$

$$|1\rangle_S|K-0\rangle_E \xrightarrow{U_{SE}} \sqrt{p}|0\rangle_S|K-1\rangle_E + \sqrt{1-p}|1\rangle_S|K-0\rangle_E, \tag{6}$$

where K represents an environment observable, such as a path along which a photon propagates.

Equation (5) illustrates that the ground state of the system remains invariant and an excitation of the system is not absorbed by the environment and consequently the environment too remains in the ground state. In the transformation given in Eq. (6), an excitation of the system transforms into an excitation shared in a superposition between the system and the environment. The excitation of the system either decays to the ground state or it remains as an excitation with probabilities p and 1-p, respectively, resulting in the environment either acquiring an excitation or remaining in the ground state with probabilities p and 1-p, respectively.

Combining Eqs. (4), (5) and (6) and adapting them for the case of a two-level OAM system, the overall transformation for such a channel is described as

$$\alpha|l-0\rangle^A + \beta|l-1\rangle^A \rightarrow \alpha|l-0\rangle^A + \beta\left(\sqrt{1-p}|l-1\rangle^A + \sqrt{p}|l-0\rangle^B\right), \tag{7}$$

$|l=0\rangle$ and $|l=1\rangle$ are state vectors representing a single photon in the LG_0 mode (ground state) and LG_1 mode (excited state), respectively, and the upper indices A and B refer to the two

#133212 - $15.00 USD Received 10 Aug 2010; revised 4 Oct 2010; accepted 5 Oct 2010; published 13 Oct 2010
(C) 2010 OSA

states of the environment, the ground and excited states, respectively. Later it will be illustrated that the two environments are represented as two optical paths. Discarding the environment leaves the system in a statistical mixture of being excited with probability p or de-excited with probability 1-p, which is the characteristic trait of amplitude damping.

It is now well known that the Laguerre-Gaussian (LG_{lp}) laser modes carry OAM of $l\hbar$ per photon [2,3]. Since the OAM is determined only by the azimuthal phase dependence, $\exp(il\varphi)$, of these modes, we neglect the radial index p for the rest of the paper. The generation of LG_l beams (a variety of which are depicted in Fig. 1(a) - 1(d)) has advanced from cylindrical lens mode converters [2] to spiral phase plates (SPP) [4] and the most frequently used 'fork' holograms [5]. Recently these 'fork' holograms have been realized with the use of spatial light modulators (SLM) [6]. Since the discovery of light beams carrying OAM many new research areas have emerged in the field of optical angular momentum, from transferring OAM to matter in optical tweezers [7] to investigating the conservation and entanglement of OAM in parametric down conversion [8]. In investigating the dynamics of entangled OAM states one requires components that manipulate and measure OAM states. The 'fork' holograms that can be used to generate OAM in the various diffraction orders [5] were also used by Mair *et al* to sort and infer OAM states [8].

But how to implement amplitude damping for the OAM states of light? Recently it has been shown that LG_l beams of odd and even orders of l could be sorted in a Mach-Zehnder interferometer incorporating Dove prisms in each arm [9]. In this paper we show that by adapting this device it may be used for a new application: an amplitude damping channel for the azimuthal modes of LG_l beams.

Due to the fact that photons with OAM represent multiple-level systems, storing and processing information in OAM states of photons promise high storage and parallel computation capacity per photon. However, many tasks in quantum information processing depend upon entanglement, resulting in the need to investigate the evolution of entanglement due to interactions with an environment [10]. For example, examining how the entanglement of OAM states decoheres through a turbulent medium has already been pursued [11], but there is value in outlining how to execute "text-book" quantum channels for the OAM states of light, in part due to the ability to analytically calculate the expected concurrence of the system after the channel. Recently a controlled-not gate [12] has been realized through the use of suitable optical elements, and here we show for the first time how an amplitude damping channel may be implement, using known optical systems.

2. Concept of the channel

The diagrammatic setup for the amplitude damping channel for LG_l modes, which is depicted in Fig. 1(e), is based on a Mach-Zehnder interferometer with a Dove prism in each arm. Such an optical system has already been shown to be useful for the sorting of modes [9] as well as determining the intrinsic versus extrinsic nature of OAM in arbitrary beams [13]. Here we outline how this versatile device may also be used for a new application (amplitude damping) as yet unreported in the literature. For the benefit of the reader, we outline the principle of the device and highlight its use as an amplitude damping channel.

#133212 - $15.00 USD Received 10 Aug 2010; revised 4 Oct 2010; accepted 5 Oct 2010; published 13 Oct 2010
(C) 2010 OSA

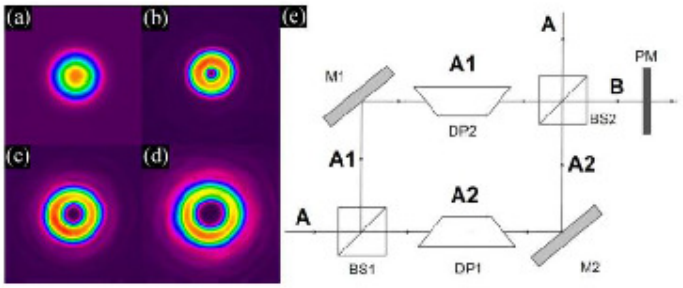

Fig. 1. (a) – (d) Intensity profiles of various LG_l modes for (a) $l = 0$, (b) $l = 1$, (c) $l = 2$, and (d) $l = 3$. (e) Schematic of the amplitude damping channel (BS: beam-splitter, M: mirror, DP: Dove prism, PM: phase mask).

A Mach-Zehnder interferometer can be aligned appropriately so that constructive interference will occur in either output paths A or B, where A and B represent the two states of the environment, the ground and excited states, respectively. By placing a Dove prism, which flips the transverse cross section of a transmitted beam [14], in each arm of the interferometer, a relative phase shift between the two arms is introduced. More specifically, this relative phase shift, $\Delta\phi$, is proportional to both the helicity, l, of the incoming LG_l beam and the relative angle, θ, between the two Dove prisms: $\Delta\phi = 2l\theta$. In varying the relative angle, θ, between the two Dove prisms, the LG_l beam will either exit solely in path A or path B or in a weighted superposition of both paths A and B. One is able to control how much of the initial LG_l mode will exit into the two environments, A (the ground state of the environment) and B (the excited state of the environment). A phase mask, which decreases the azimuthal mode index by 1, is placed in path B resulting in the 'excited' LG_l mode decaying to an 'unexcited' LG_{l-1} mode, thus performing the action of amplitude damping.

In following the LG_l mode through arms $A1$ and $A2$ of the interferometer to output path A, the additional phase picked up by the beam from each of the components is given by

$$\varphi_{A1\to A} = \underset{BS1}{\pi} + \underset{M1}{\pi} + \underset{DP2}{2l\theta} + \underset{BS2}{\frac{2\pi}{\lambda}t} + \frac{2\pi}{\lambda}d_1 \tag{8}$$

and

$$\varphi_{A2\to A} = \underset{BS1}{\frac{2\pi}{\lambda}t} + \underset{M2}{\pi} + \underset{BS2}{\pi} + \frac{2\pi}{\lambda}d_2, \tag{9}$$

respectively. $d1$ and $d2$ are the path lengths of the two arms, $A1$ and $A2$, respectively and t is the optical path length of the beam-splitter. The phase difference in output path A is consequently given by

$$\Delta\varphi_A = 2l\theta, \tag{10}$$

since the interferometer is constructed such that the path lengths of the two arms are equal.

Similarly, it can be shown that the phase difference in output path B is

$$\Delta\varphi_B = \pi + 2l\theta, \tag{11}$$

#133212 - $15.00 USD Received 10 Aug 2010; revised 4 Oct 2010; accepted 5 Oct 2010; published 13 Oct 2010
(C) 2010 OSA

where the additional phase shift of π is due to the reflection in the first beam-splitter. The amplitude of the field for a LG_l mode emerging after the second beam-splitter in path A and path B is described as

$$U^A = \frac{U_0}{2}\left(e^{i(l\theta+2\delta)} + e^{il\theta}\right) = U_0 e^{il\theta} e^{i\delta} \cos l\theta \tag{12}$$

and

$$U^B = \frac{U_0}{2}\left(e^{i(l\theta+2\delta)} - e^{il\theta}\right) = U_0 e^{il\theta} e^{i\delta} i \sin l\theta, \tag{13}$$

respectively. U denotes the amplitude of the field and the negative sign in Eq. (13) for the field emerging in path B from arm $A2$ is due to an additional phase shift of π, evident in Eq. (11).

In the case of propagating a LG_1 mode through the interferometer there is a non-vanishing relative phase difference ($\Delta\phi = 2\theta$) between the two arms of the interferometer, leading to partially constructive and destructive interference of the LG_1 mode in both paths A and B

$$|l=1\rangle^A \rightarrow \cos\theta |l=1\rangle^A + \sin\theta |l=1\rangle^B, \tag{14}$$

As we are only interested in the intensity of the field, as this gives the probability of the single photon state, we have neglected the phase components and will do so for the rest of the paper. The intensity of the LG_1 mode exiting in the two paths, A and B, is proportional to $\cos^2\theta$ and $\sin^2\theta$, respectively and consequently the probabilities of the LG_1 mode existing in the two paths follow the same trend. The incoming LG_1 mode exits in a superposition of paths A and B with probabilities $\cos^2\theta$ and $\sin^2\theta$, respectively and a phase mask, in path B, decreases the azimuthal mode index, l, by 1, converting the 'exited' LG_1 mode to an 'unexcited' Gaussian mode

$$|l=1\rangle^A \rightarrow \cos\theta |l=1\rangle^A + \sin\theta |l=0\rangle^B. \tag{15}$$

When a LG_0 mode enters the device there is no azimuthal phase dependence in such a mode, the field is unaffected by the Dove prisms and no phase difference occurs between the two arms; the result is that the Gaussian mode exits in path A. The transformation of the Gaussian mode through the interferometer is denoted as

$$|l=0\rangle^A \rightarrow |l=0\rangle^A. \tag{16}$$

Combining Eqs. (15) and (16), the general equation for the amplitude damping of OAM, given in Eq. (7), is obtained, where $\sqrt{1-p} = \cos\theta$ and $\sqrt{p} = \sin\theta$

$$\alpha|l=0\rangle^A + \beta|l=1\rangle^A \rightarrow \alpha|l=0\rangle^A + \beta\left(\cos\theta|l=1\rangle^A + \sin\theta|l=0\rangle^B\right). \tag{17}$$

From the definition of amplitude damping which states that the ground state will remain invariant while the excited state decays to the ground state with a probability p, it is sufficient to experimentally investigate each case individually in order to verify the action of our amplitude damping channel.

3. Experimental methodology and results

A HeNe laser (λ = 632.8 nm) was directed onto a phase-only SLM (HoloEye PLUTO VIS SLM with 1920 × 1080 pixels of pitch 8 μm and calibrated for a 2π phase shift at λ = 632.8 nm). The mode of the field was prepared before it entered the channel by programming an appropriate phase pattern. The two exiting paths of the interferometer were monitored for various angles, θ, between the two Dove prisms using a CCD camera (Spiricon LW130).

#133212 - $15.00 USD Received 10 Aug 2010; revised 4 Oct 2010; accepted 5 Oct 2010; published 13 Oct 2010
(C) 2010 OSA

To confirm the correct operation of the interferometer, we first repeated the sorting experiment of Ref [9]. When the relative angle between the Dove prisms was set to $\theta = \pi/2$, the interferometer sorted the incoming field into even LG_l modes (path A) and odd LG_l modes (path B). We can confirm this result for incoming LG_l modes having indices $l = 0$ to 4, as shown in Fig. 2(a). In the special case that $l = 0$ (Gaussian mode) the interferometer only produces an output in path A (Fig. 2(b)). This experiment is instructive when considering the errors in the system due to imperfect alignment and environmental fluctuations. The variance in the data set of Fig. 2(b) for path A (where we should expect 100% transmission) and for path B (where we should expect no transmission) is given as 0.88 ± 0.06 and 0.15 ± 0.08, respectively. In performing the measurements depicted in Fig. 3, for each occurrence for which the Dove prism was rotated, constructive and destructive interference was first achieved in paths A and B, respectively, for the case of an incoming Gaussian beam. This ensured that the interferometer was correctly aligned before the LG_l mode entered the channel.

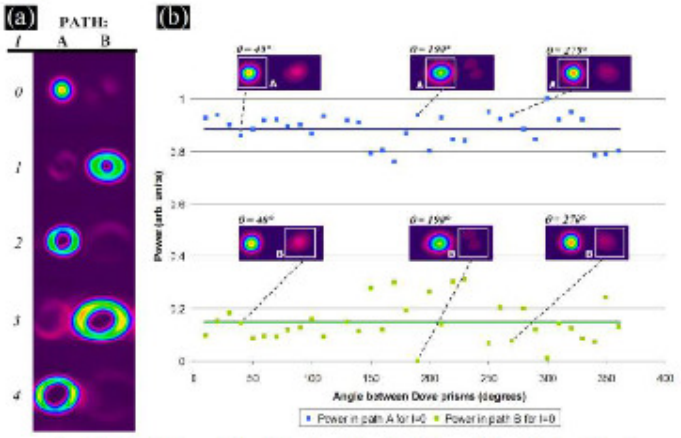

Fig. 2. (a) The interferometer 'sorting' various LG_l modes. The even LG_l modes ($l = 0$, 2 and 4) exit in path A and the odd LG_l modes exit in path B as expected [9]. (b) Plot of the power of the beam in path A (light blue points) and path B (light green points) for various values of θ. The dark blue line (dark green line) is the mean of all the measured powers in path A (path B).

To test the amplitude damping channel concept, the incoming mode was set to LG_1 and the angle between the two Dove prisms varied from 0° through to 360°. The results are shown graphically in Fig. 3. In Fig. 3(a) it is evident that when the relative angle between the two Dove prisms is an even multiple of 90°, maximum transmission of the LG_1 mode occurs, which is in agreement with the 'LG_l sorting' nature of this device. At an angle of an even multiple of 90°, the reverse occurs in path B (shown in Fig. 3(b)), where minimum transmission of the LG_1 mode occurs. When the relative angle between the two Dove prisms is an odd multiple of 90°, minimum transmission of the LG_1 mode occurs in path A and maximum transmission in path B. For angles varying between 0° and 90° (and multiples of these angles) the LG_1 mode exits in both paths A and B. As the angle increases from 0° to 90° the transmission of the LG_1 mode in path A decreases, but consequently increases in path B. In our theoretical model, the probability that the LG_1 mode exits in paths A and B is given by $\cos^2\theta$ and $\sin^2\theta$, respectively (depicted in Eq. (17)) and it is evident from Figs. 3(a) and 3(b) that our measured data are in very good agreement with the predicted model. The errors given

#133212 - $15.00 USD Received 10 Aug 2010; revised 4 Oct 2010; accepted 5 Oct 2010; published 13 Oct 2010
(C) 2010 OSA

in the measurements in Fig. 3 are the standard deviations of the measurements in Fig. 2(b), for paths A (0.06) and B (0.08).

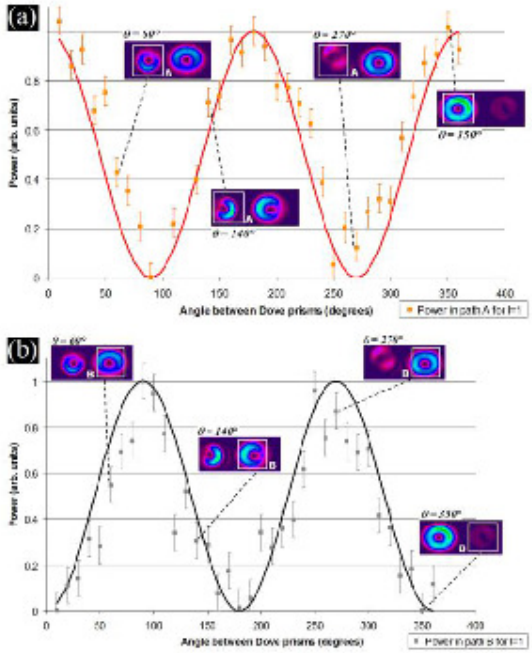

Fig. 3. Plot of the power of the beam in path A ((a); orange points) and path B ((b); grey points) for various values of θ. The measured results follow the theoretical curves: $P_A \sim \cos^2\theta$, ((a); red curve) and $P_B \sim \sin^2\theta$ ((b), black curve).

4. Conclusion

We have outlined how the concept of "amplitude damping" in quantum systems may be implemented for the OAM states of light using a standard optical system comprising an interferometer with Dove prisms in both arms, and have verified this experimentally using the LG_0 and LG_1 laser modes. We have shown excellent agreement between theory and experiment, and believe this is the first time such a concept has been outlined in the literature. With this idea, one is able to mimic the well known quantum operation where an excitation (or in this case OAM) is lost to the environment, a key testing bed for the interaction of entangled states with an environment. The advantage of this particular concept – amplitude damping – is that the entanglement decay can be predicted analytically, while the concurrence of the entanglement may easily be measured both before and after the channel with standard state tomography techniques, thus allowing for a quantitative comparison of theory and experiment in the decoherence of entanglement due to interactions with a noisy environment.

#133212 - $15.00 USD Received 10 Aug 2010; revised 4 Oct 2010; accepted 5 Oct 2010; published 13 Oct 2010
(C) 2010 OSA

B3: Publication

New Journal of Physics
The open-access journal for physics

Robust interferometer for the routing of light beams carrying orbital angular momentum

Martin P J Lavery[1], Angela Dudley[2,3], Andrew Forbes[2,3], Johannes Courtial[1] and Miles J Padgett[1]

[1] Department of Physics and Astronomy, University of Glasgow, Glasgow, UK
[2] CSIR National Laser Centre, Pretoria, South Africa
[3] School of Physics, University of KwaZulu-Natal, Durban, South Africa
E-mail: m.lavery@physics.gla.ac.uk and ADudley@csir.co.za

New Journal of Physics **13** (2011) 093014 (6pp)
Received 21 June 2011
Published 7 September 2011
Online at http://www.njp.org/
doi:10.1088/1367-2630/13/9/093014

Abstract. We have developed an interferometer requiring only minimal angular alignment for the routing of beams carrying orbital angular momentum. The Mach–Zehnder interferometer contains a Dove prism in each arm where each has a mirror plane around which the transverse phase profile is inverted. One consequence of the inversions is that the interferometer needs no alignment. Instead the interferometer defines a unique axis about which the input beam must be coupled. Experimental results are presented for the fringe contrast, reaching a maximum value of $93 \pm 1\%$.

The orbital angular momentum (OAM) carried by light is an extremely useful optical characteristic, with applications in many areas of optics. It was Allen *et al* who recognized that a helically phased light beam with a phase cross section of $\exp(i\ell\phi)$ carries an OAM of $\ell\hbar$ per photon [1, 2]. An example is Laguerre–Gaussian (LG) beams which have a helical phase structure. The integer ℓ is unbounded, giving a large state space in which to encode information [3–5].

The use of diffractive elements containing an ℓ-fold fork dislocation has become commonplace for the generation of helically-phased beams [6, 7]. The fork diffraction grating, when illuminated with a Gaussian beam, for example from a single-mode fibre, produces the helical mode in the first diffraction order. This grating can also be used in reverse to couple light with a helical phase into a single-mode fibre [8]. Sequentially changing the dislocation in the fork allows a range of ℓ values to be measured, but checking for N states requires at least N photons [8]. Recently it has been shown that two diffractive optical elements can

© IOP Publishing Ltd and Deutsche Physikalische Gesellschaft

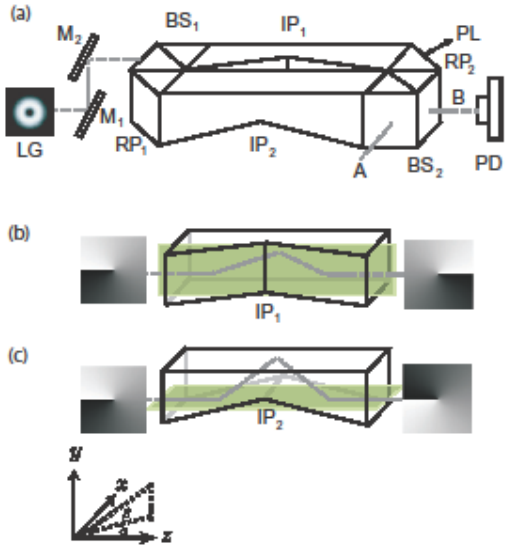

Figure 1. (a) Schematic of the robust odd–even OAM router (M, mirror; BS, beam-splitter; RP, right-angled prism; IP, inverting prism; PL, piezoelectric; A, output port A; B, output port B and PD, photo-diode). (b) and (c) illustrate the effect of the prisms on their own. It can be seen that the beams behind the two prisms are rotated by 180° with respect to each other. An inverting prism, like a Dove prism, has a mirror plane, indicated in green, around which any transmitted beam is flipped.

be used to transform OAM states into transverse momentum states. A lens can then separate the resulting states into a specified lateral position, allowing for the efficient measurement of multiple states simultaneously [9, 10]. In both of the above systems, however, the nature of a mode transformation means that the OAM of the light is changed during the measurement process.

A method to route OAM at the single-photon level was outlined by Leach *et al*. It is based on a Mach–Zehnder interferometer with a Dove prism in each arm [11]. When the two Dove prisms are orientated with respect to each other by an angle of θ, there is a relative phase difference between the two arms in the interferometer of $\Delta\psi = 2\ell\theta$ (figure 1(a)). In the specific case of $\theta = 90°$, constructive interference will occur at one of the two output ports for all even ℓ-valued states and then for odd ℓ-valued states in the other output port. In principle, this routing can be achieved with 100% efficiency and with no loss of the input beam's helical phase structure. Simultaneously maintaining the alignment of many such interferometers has proved technically challenging.

Preserving the structure of the input beam is important for many experiments, for example to demonstrate amplitude damping of Laguerre–Gaussian laser modes [12] and in the

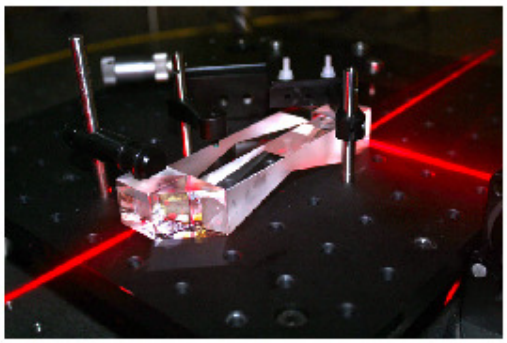

Figure 2. Photo of the robust interferometer sketch in figure 1(a).

development of a linear optical CNOT gate for OAM [13, 14]. In each of these experiments interferometers similar to that outlined by Leach *et al* were used. Attempting to make this interferometric technique more robust, Slussarenko *et al* reconfigure the Mach–Zehnder interferometer as a Sagnac interferometer [15]. This approach reduces the number of degrees of freedom within the interferometer, but requires additional polarization optics.

In this paper we present a compact, robust interferometer, removing many of the previously required degrees of freedom. The technique outlined by Leach *et al* requires that the beams transmitted through the two Dove prisms are co-linear at the output of the interferometer (BS_2 in figure 1(a)). This alignment was previously achieved by the accurate positioning of the Dove prisms, mirrors and beam splitters with the interferometer [11, 12, 14]. A Dove prism has a mirror plane, around which the transverse cross section of any transmitted beam is inverted (figure 1(b)). Considering these mirror planes, a different approach to alignment can be taken. The intersection of the mirror plane in each Dove prism defines the path an input beam is required to take for the two beams to be co-linear at the output ports. Hence, by controlling the direction of the input beam, the interferometer can be aligned without precise alignment of any of the constituent components. The requirement is that the whole beam is always contained within the aperture of the prisms. An additional fine control for the path length is required such that the integer ℓ states completely constructively, or destructively, interfere at the output ports of the interferometer.

In our approach we use specially manufactured inverting prisms, previously discussed by Leach *et al* [16]. The beam enters and exits each inverting prism at an optical face perpendicular to the optical axis. This allows for the introduction of right-angled prisms, as opposed to mirrors, meaning all optical surfaces can be bonded into a single, robust unit, shown in figure 2.

We demonstrate the case of $\alpha = 90°$, for the routing of states with even and odd ℓ values. The intersection of the mirror planes of the prisms IP_1 and IP_2 (see figures 1(b) and (c)) was found through the use of external coupling mirrors, M_1 and M_2 in figure 1(a).

In our experimental implementation of the compact interferometer, we use a linearly polarized Gaussian beam with a complex phase profile $\exp(i\ell\phi)$ as our basis set of OAM. These modes were prepared by expanding a HeNe laser beam to illuminate an ℓ-fold fork diffraction grating, encoded with only phase information on a spatial light modulator (SLM)

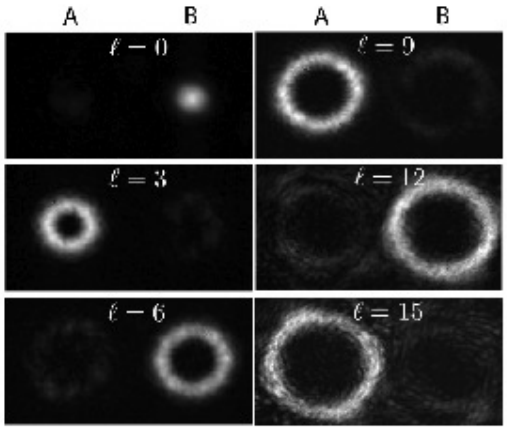

Figure 3. The interferometer routing odd and even helically-phased light beams into ports A and B, respectively. For demonstration purposes we also encode intensity information to the hologram pattern to generate the LG modes shown above.

as this gives a high diffraction efficiency over all $\exp(i\,\ell\phi)$ modes. To allow the precise control of constructive and destructive interference in the interferometer, the second right-angled prism, RP_2, was attached to a piezoelectric mount, giving fine control over the path difference within the interferometer. When the input mode is correctly aligned, the routing of odd and even ℓ-valued LG modes into the output ports A and B, respectively, is achieved. Experimental results are shown in figures 3 and 4. The large number of degrees of freedom previously required has been reduced to five degrees of freedom, position (x, y) and tilt (α, β) of the input beam, and a small adjustment of the path length difference in the interferometer.

To test the performance of the interferometer in separating odd and even ℓ-valued $\exp(i\,\ell\phi)$ modes, the intensity of the interference pattern in one of the output ports was monitored with a photodiode, while the path length of the interferometer was oscillated back and forth between constructive and destructive interference by driving the piezoelectric stage. The ability of the router to separate the input modes can be characterized by the fringe contrast [17]. The contrast is defined as $(v_{max} - v_{min})/(v_{max} + v_{min})$, where v_{max} and v_{min} are the measured maximum and minimum voltages from the photodiode.

In our assessment of the performance of our interferometer we recognize that a potential limitation is imposed by the purity with which $\exp(i\,\ell\phi)$ modes can be produced by the SLM and associated optics. SLMs are themselves a source of aberration in the optical system since their flatness is typically specified at one or two optical wavelengths. In this experiment we use the central region of an optically-addressed SLM, which is typically flatter than the alternative technology, normally liquid crystal on silicon. Despite using the flattest of our SLMs and careful alignment of the associated optics it is likely that residual aberrations will lead to a degradation in the performance of the interferometer, especially at high values of ℓ.

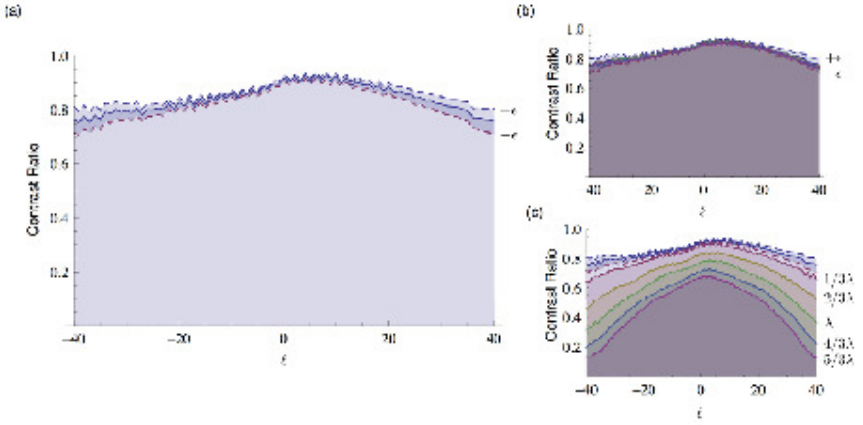

Figure 4. The contrast measured over the OAM mode range of $\ell = -40$ to $\ell = 40$, (a) without and (b) with, additional aberrations. The error in the measured contrast ratio is determined by considering the standard deviation of the voltage received when no light is incident on the photodiode. In (b) and (c) the effect of aberration on the contrast is shown for astigmatism and trefoil, respectively. The magnitude of aberration was determined by the total phase height variation across the diameter of the beam incident on the SLM. The same magnitude of aberration was applied in the form of astigmatism and trefoil, with an approximate value of $1/3\lambda$, $1/3\lambda$, $2/3\lambda$, λ, $5/3\lambda$ and $4/3\lambda$, where λ is the wavelength of the incident light.

To investigate the effect of aberrations we scan the input modes over the range of $\ell = \pm 40$ for various degrees of additional astigmatism and trefoil aberrations which we encode on the SLM. For no additional aberrations, we observe that for low values of ℓ the contrast is in the region of 90%, falling to around 75% at $\ell = \pm 40$ (see figure 4). At these higher values of ℓ we note that trefoil aberration (figure 4(c)) has significantly more impact on the contrast than astigmatism (figure 4(b)). When an aberration is added to a beam carrying OAM, the beam is no longer a single ℓ valued mode and is instead a superposition of different ℓ valued modes, centred about the original value. As astigmatism is two-fold rotationally symmetric, the result in a superposition containing further modes with $\Delta\ell = \pm 2$, resulting in no observable degradation of the contrast obtained from the even/odd separation (see figure 4(b)). In comparison, trefoil aberrations are three-fold rotationally symmetric, resulting in superposition containing further modes with $\Delta\ell = \pm 3$, and hence causing a noticeable degradation in the contrast of the even/odd separation.

In summary, we have developed a robust odd-even OAM router with a reduction in the number of degrees of freedom to simply that of the input light beam. A change in the orientation angle α allows the routing of beams with different ℓ values into the two output ports [11]. Cascading multiple interferometers, with coupling mirrors between each stage, would allow the

routing of a beam into one of many output ports where each corresponds to a different ℓ value of the input beam [11]. The routing of an OAM beam with the preservation of the helical structure is useful for data processes and transfer, as multiple gates can be used sequentially to carry out more complex operations on a input beam.

Acknowledgments

AD would like to thank the University of Glasgow and the CSIR National Laser Centre for their support. MJP thanks the Royal Society for its support. This research was supported by EPSRC, the DARPA InPho program through the US Army Research Office award W911NF-10-1-0395 and part of the European collaboration EC FP7 255914, PHORBITECH.

References

[1] Allen L *et al* 1992 *Phys. Rev.* A **45** 8185
[2] Yao A M and Padgett M J 2011 *Adv. Opt. Photonics* **3** 161–204
[3] Vaziri A, Weihs G and Zeilinger A 2002 *Phys. Rev. Lett.* **89** 240401
[4] Barreiro J T, Wei T C and Kwiat P G 2008 *Nat. Phys.* **4** 282
[5] Leach J *et al* 2010 *Science* **329** 662
[6] Bazhenov V Yu, Soskin M S and Vasnetsov M V 1992 *J. Mod. Opt.* **39** 985
[7] Heckenberg N R 1992 *Opt. Quantum Electron* **24** S951
[8] Mair A *et al* 2001 *Nature* **412** 313
[9] Berkhout G C G *et al* 2010 *Phys. Rev. Lett.* **105** 153601
[10] Lavery M P J, Berkhout G C G, Courtial J and Padgett M J 2011 *J. Opt.* **13** 064006
[11] Leach J *et al* 2002 *Phys. Rev. Lett.* **88** 257901
[12] Dudley A *et al* 2010 *Opt. Express* **18** 22789
[13] O'Brien J L *et al* 2004 *Phys. Rev. Lett.* **93** 080502
[14] Deng L, Wang H and Wang K 2007 *J. Opt. Soc. Am.* B **24** 2517
[15] Slussarenko S *et al* 2010 *Opt. Express* **18** 27205
[16] Leach J *et al* 2004 *Phys. Rev. Lett.* **92** 013601
[17] Michelson A 1927 *Studies in Optics* (Chicago, IL: University of Chicago)

B4: Publication

Author's personal copy

Optics Communications 285 (2012) 5–12

Contents lists available at SciVerse ScienceDirect

Optics Communications

journal homepage: www.elsevier.com/locate/optcom

Controlling the evolution of nondiffracting speckle by complex amplitude modulation on a phase-only spatial light modulator

Angela Dudley [a,b], Ruslan Vasilyeu [c], Vladimir Belyi [c], Nikolai Khilo [c], Piotr Ropot [c], Andrew Forbes [a,b,*]

[a] School of Physics, University of KwaZulu-Natal, Private Bag X54001, Durban 4000, South Africa
[b] CSIR National Laser Centre, P.O. Box 395, Pretoria 0001, South Africa
[c] B.I. Stepanov Institute of Physics of NAS of Belarus, Nezalezhnasti Ave., 68, 220072 Minsk, Belarus

ARTICLE INFO

Article history:
Received 18 April 2011
Received in revised form 31 August 2011
Accepted 5 September 2011
Available online 18 September 2011

Keywords:
Nondiffracting
Speckle field
Bessel beams
Spatial light modulator
Complex amplitude modulation

ABSTRACT

In this work we investigate the structure of nondiffracting speckle fields, both experimentally and theoretically. We are able to produce very good agreement between the experimentally recorded and theoretically calculated fields by using complex amplitude modulation on a phase-only spatial light modulator to implement controlled ring-slit experiments for the generation of nondiffracting speckle fields. The structure of the nondiffracting speckle due to binary and continuous phase modulations for both a uniform and a normal distribution is investigated. We find that we are able to engineer whether the nondiffracting field will appear as speckle or a structured zero-order Bessel beam by adjusting the standard deviation in the distribution. Having the ability to control where in the spectrum, from fully-developed nondiffracting speckle to a symmetric zero-order Bessel beam, the nondiffracting field will exist can prove to be a useful resource in the non-destructive testing of materials.

© 2011 Elsevier B.V. All rights reserved.

1. Introduction

Nondiffracting fields have interested researchers due to the fact that their intensity profile remains unchanged during propagation. Since Durnin [1] first discovered a set of solutions for the free-space Helmholtz equation, which are propagation-invariant and are mathematically described by Bessel functions, there has been extensive research into nondiffracting fields. These nondiffracting Bessel beams, both zero- and higher-orders, can be generated with the use of computer-generated holograms [2–4] and axicons [5–7]. Later, these computer-generated holograms were easily reproduced with the use of spatial light modulators (SLMs) [8]. Zero-order Bessel beams have achieved much interest due to their ability to reconstruct after an obstacle [9,10] and their long nondiffracting propagation region offered in the form of z-dependent Bessel-like beams [11]. A superposition of higher-order Bessel beams has also been achieved by illuminating an axicon with a superposition of Laguerre–Gaussian beams [12] or by illuminating a ring field onto two separable azimuthal phase variations on a SLM [13]. Propagation-invariant spot arrays [14], as well as arbitrary arrays of nondiffracting beams [15] have been generated by inserting a diffractive element into Durnin's ring-slit [16]. Recently, nondiffracting beams with arbitrary intensity profiles have been produced by calculating their corresponding complex spectra and using the constraints of Helmholtz–Gauss beams [17].

In the area of nondiffracting beams, we are particularly interested in nondiffracting speckle fields. One of the first attempts at generating nondiffracting speckle fields was achieved by illuminating a weakly scattering diffuser (produced by spraying finishing mist on a flat glass plate) with a thin ring field [18]. Recently, simpler and more efficient methods of generating nondiffracting speckle fields have been realised with the use of a single SLM [19]. This is a computational approach, equivalent to the experimental setup of Ref. [18], where the computer-generated pattern applied to the SLM is the Fourier transform of a ring-slit with a random binary pattern within the width of the ring-slit.

Even though numerous publications have been dedicated to the generation of nondiffracting speckle fields, to the best of our knowledge none have shown agreement between theoretically calculated and experimentally measured fields. This is because by illuminating a diffuser with a ring field [18] to experimentally produce speckle, it is virtually impossible to define the transmission function mathematically (either in terms of phase or amplitude) within the ring field with the accuracy required for a prediction, as this is extremely sensitive to laser beam alignment. In this report we attempt to resolve this issue. We too make use of a single SLM, similar to that in Ref. [19], however we implement a checkered board phase-mask allowing us to operate our phase-only SLM in both phase and amplitude mode. Having control over both the phase and amplitude when addressing the SLM offers the possibility to define the transmission function of the ring-slit and so a theoretical calculation of the resulting speckle can be made.

Much attention has been paid to the formation of speckle, as an understanding in how speckle is formed is imperative in the

* Corresponding author at: School of Physics, University of KwaZulu-Natal, Private Bag X54001, Durban 4000, South Africa.
E-mail address: aforbes1@csir.co.za (A. Forbes).

0030-4018/$ – see front matter © 2011 Elsevier B.V. All rights reserved.
doi:10.1016/j.optcom.2011.09.004

Author's personal copy

development of tools for the removal of speckle in optical fields [20,21]. Even though the presence of speckle in optical beams may not be desirable, speckle is proving useful for metrological techniques [22–26] and nondiffracting speckle is of particular interest in the non-destructive testing of materials [27], all of which benefit from a knowledge of speckle formation.

Investigations into the formation of speckle have considered the effect the dimensions and the geometry of the ring-slit have on the longitudinal correlation [28] and the clustering (or snake-like patterns) of the speckles [29,30], respectively. The structure of the random phase-mask too has an influence on the formation of speckle clustering [30,31]. If the diffuser is weak, radial speckle chains are produced and as the diffuser becomes stronger so speckle clusters turn into isotropic winding chains [30]. The fractal structure of speckle patterns has also been investigated by illuminating a diffuser with a fractal object [32]. We have attempted to make further investigations into the formation of speckle by studying the effect that binary and continuous phase modulations, within the ring-slit, have on the structure of the speckle.

In this paper we experimentally generate nondiffracting speckle fields by complex amplitude modulation on our phase-only spatial light modulator. We first discuss the principle behind the complex amplitude modulation, which in our case takes the form of a checkered board pattern [33], and illustrate its benefit in the study of nondiffracting beams. Subsequently, we experimentally investigate the effect binary and continuous phase modulations, for both the uniform and normal distribution, have on the structure of the speckle and in particular investigate the standard deviation, σ, as the statistical variable for the distributions. A theoretical explanation, which builds on from the checkered board phase-mask, is given, proving the validity of what we experimentally witness.

2. Checkered board phase-mask

2.1. Theoretical description

In order to encode a SLM with a ring-slit for the generation of nondiffracting fields, one would require a SLM that can control both phase and amplitude. A phase-mask, such as that in Fig. 1(a), would be encoded onto a phase and amplitude SLM, where the region within the ring-slit would modify the phase of the incident light and the black regions, surrounding the ring-slit, would not transmit the incident light. With our phase-only SLM, we encode the sections of the phase-mask, in which we do not want to transmit any light, with a checkered board pattern. An example of such a phase-mask is given in Fig. 1(b).

To explain why a checkered board, consisting of alternating sets of pixels that are assigned phase values that are out of phase by π, can be used to mimic an amplitude mask, one should visualise a complex plane (Fig. 2(a)) to represent such phase values. The checkered board is described by a binary uniform distribution, where the weighting of each phase value, 0 and π, is equal. In the complex plane representation this translates to each vector having the same amplitude, but pointing in opposite directions along the x-axis. The resultant, therefore, has no amplitude and is located at the origin of the complex plane. The fact that the resultant has no amplitude means that the average amplitude of the field at the checkered board phase-mask is zero. The amplitude of the resultant vector in the complex plane is often referred to as the DC-offset [34]. So in this case there is no DC-offset at the checkered board phase-mask. The fact that the average amplitude of the field at the checkered board phase-mask is zero, results in a zero in the intensity on the propagation axis in the Fourier plane, with the light shifted away from the origin due to the high spatial frequency of the checkered board, as illustrated in Fig. 2(c). For the case where a phase-only SLM is addressed with a single uniform grey-level (Fig. 2(d)), the resultant vector in the complex plane does have an amplitude (which lies along the positive x-axis), meaning the average amplitude at this phase-mask is non-zero, giving rise to an on-axis intensity (Fig. 2(e)) in the Fourier plane.

2.2. Experimental methodology and results

The experimental setup is denoted in Fig. 3. A HeNe laser ($\lambda \sim 633$ nm) was expanded through a 6× telescope before illuminating a HoloEye, HEO1080P SLM, having 1920× 1080 pixels of pitch 8 μm and calibrated for a 2π phase shift at ~633 nm. Previously in our work, a physical aperture in the form of a ring-slit would be imaged onto the SLM and the phase modulation within the ring field would be modified [13]. However, with this approach, in the case of nondiffracting speckle fields, one cannot define the transmission function of the ring field. With the checkered board approach on the other hand, a single phase-mask, which generates both the ring field and the phase modulation within the ring field, was encoded onto the SLM. The dynamic addressing of SLMs allows the radius and width of the ring-slit, the frequency of the phase modulation, the number of grey-levels used to represent the phase modulation, and the distribution used to describe the phase modulation to be varied appropriately. Experimentally, through 'trial-and-error', it was found that the checkered board pattern produced the best results when each checker was assigned to an area of 5×5 pixels on the SLM. Phase-masks consisting of a ring-slit surrounded by a checkered

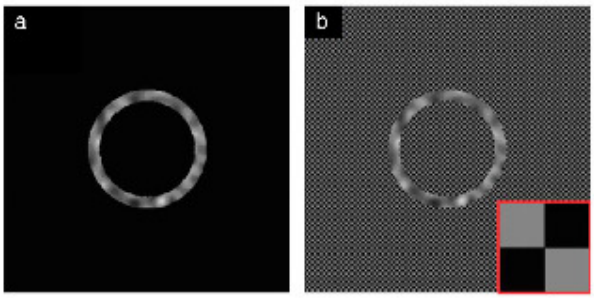

Fig. 1. In order to reproduce Durnin's ring-slit [16] experiment (with the addition of a phase modulation inside the ring), either (a) the light can be suitably apertured by a physical ring and then modulated; or (b) complex amplitude modulation can be used on a phase-only SLM to execute both the "amplitude" and "phase" transformations in one step. The inset in (b) shows the checkered board pattern used to modulate the amplitude.

Author's personal copy

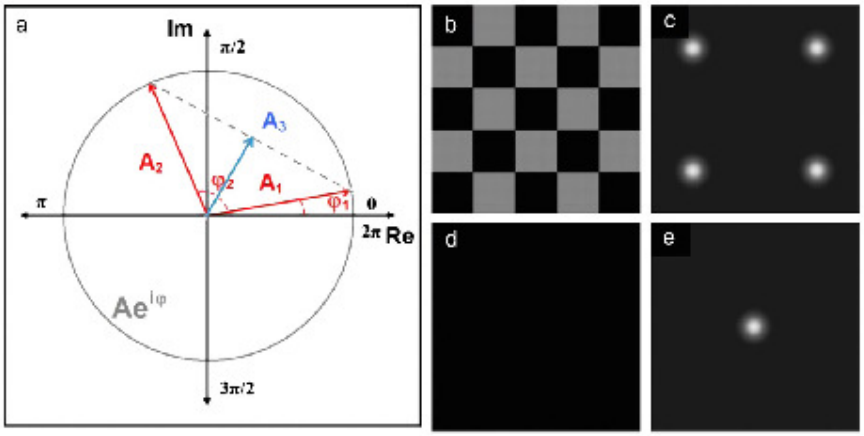

Fig. 2. (a) A generalised example of the complex plane, the angles, φ_1 and φ_2, for each vector, A_1 and A_2, represents a phase value in the phase-mask. The resultant amplitude, A_3, is denoted by the blue vector. (b) The checkered board phase-mask and (c) the corresponding Fourier plane, illustrating that the light is distributed off of its propagation axis. (d) A plain black phase-mask. (e) The Fourier transform of the phase-mask in (d) illustrating an on-axis intensity component.

board of various checker areas (varying from 3×3 to 9×9 pixels) were generated and used to generate a third-order Bessel beam. The phase-mask which diffracted the on-axis intensity away from the vortex in the middle of the third-order Bessel beam the best, consisted of a checker area of 5×5 pixels. The plane at the SLM (P1) was relay imaged with a 1× telescope to plane P2 (denoted in Fig. 3). A physical ring-slit, denoted within the red border, was introduced into the experimental setup at P2 when needed, to allow for comparison between the results obtained with the ring-slit phase-mask and the physical ring-slit in conjunction with the random phase-mask. The field at plane P2 was Fourier transformed, with the use of lens L5, before being magnified by a 10× objective and detected on a CCD camera.

A comparison between the results obtained with the physical ring-slit and a random phase-mask (column 1 Fig. 4) and the phase-mask which incorporates the checkered board pattern (column 3 Fig. 4), was made and is illustrated in Fig. 4. Results were first obtained by illuminating the SLM when it was addressed by the phase-masks given in column 3 of Fig. 4. The SLM was then addressed with the same random phase-masks as those in column 3, but with the checkered board pattern removed (i.e. those in column 1), and the field at the SLM was then imaged onto a physical ring-slit ($R=3$ mm and $2\Delta=150\,\mu$m). The alignment of the physical ring-slit was adjusted until the field in the Fourier plane resembled that which was obtained with the checkered board phase-mask. Both approaches produce identical results, illustrating that the checkered board pattern is extremely effective in mimicking an amplitude mask. The results imply that the physical ring-slit can be replaced by a single phase-mask, offering the possibility of dynamically addressing the parameters which describe the ring-slit, such as radius, width and phase modulation.

By implementing the checkered board approach, we are able to define the phase modulation within the ring-slit with very high resolution, so as to compute theoretical predictions of the resulting speckle fields. An example is shown in Fig. 5, illustrating that the experimentally produced nondiffracting speckle field is in very good agreement with the theoretical prediction. This approach, for the first time, allows for quantitative studies in the dynamics of speckle formation, and requires only a spatial light modulator to execute.

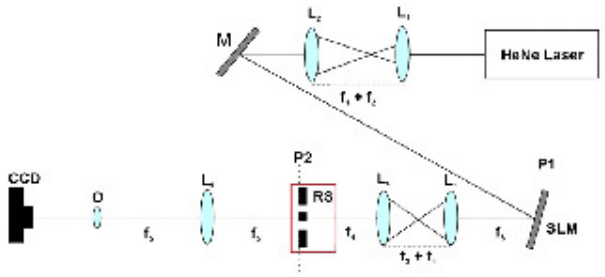

Fig. 3. The experimental design for generating nondiffracting speckle fields. The physical ring-slit (RS) which can be introduced into the optical setup when needed is denoted inside the red border. (L: lens ($f_1=25$ mm; $f_2=150$ mm; $f_3=50$ mm; $f_4=50$ mm; $f_5=200$ mm); M: mirror; SLM: spatial light modulator; O: objective; CCD: CCD camera).

Author's personal copy

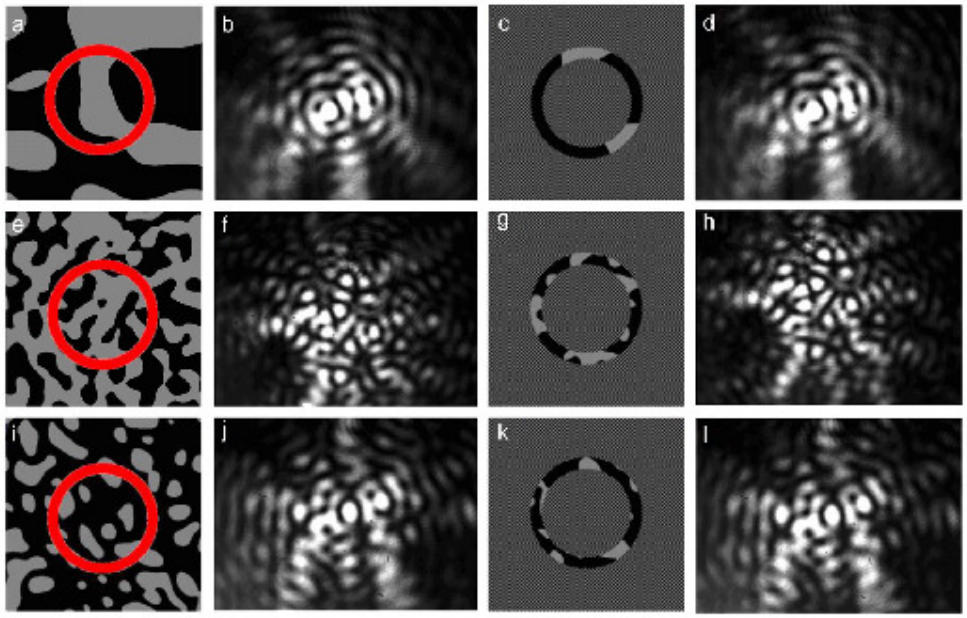

Fig. 4. Column 1: Random phase-masks which were illuminated with a ring field, denoted in red. Column 2: The corresponding experimentally measured Fourier transform. Column 3: The same random phase-masks as those in column 1, but with the checkered board approach implemented. Column 4: The experimentally measured Fourier transform of column 3.

3. Nondiffracting speckle fields

3.1. Experimental results

Within the ring-slit we investigate four different forms of phase modulation, described by the following distributions: (i) continuous uniform, (ii) binary uniform, (iii) continuous normal and (iv) binary normal.

The phase distribution within the ring-slit can be described by a continuous uniform distribution, where the phase values exists in the range $\{0, 2\pi\}$, and is defined as

$$\phi(x,y) = 2\pi \times U(x,y), \tag{1}$$

where $U(x,y)$ is a uniform random number in the range $\{0,1\}$.

In the case that the phase values within the ring-slit are described by a binary uniform distribution, there is an equal probability that the phase values will be assigned either a value of 0 or π,

$$\phi(x,y) = \begin{cases} 0, & U(x,y) \le 0.5 \\ \pi, & U(x,y) > 0.5 \end{cases}. \tag{2}$$

For the continuous normal distribution, phase values within the ring-slit are selected from a normal distribution having a mean of zero and a standard deviation of 1 and are defined as

$$\phi(x,y) = 2\pi \times N(x,y), \tag{3}$$

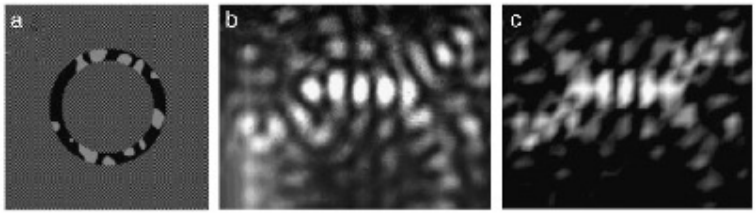

Fig. 5. (a) The phase-mask applied to the SLM. (b) The corresponding experimentally produced field in the Fourier plane and (c) the theoretically calculated field at the Fourier plane.

Author's personal copy

where $N(x,y)$ is a normal random number. The probability density function for our continuous normal distribution is

$$f(x) = \frac{1}{\sqrt{2\pi\sigma^2}} \exp\left(\frac{-(x-\mu)^2}{2\sigma^2}\right), \quad (4)$$

where μ and σ are the mean and standard deviation, respectively. For the final case, the binary normal case, phase values within the ring-slit are assigned a value of either 0 or π, where the probability of selecting either value is bounded by a Gaussian envelop,

$$\phi(x,y) = \begin{cases} 0, & N(x,y) \le 0.5 \\ \pi, & N(x,y) > 0.5 \end{cases}. \quad (5)$$

Fig. 6 contains the phase-masks and corresponding fields in the Fourier plane for the continuous uniform and binary uniform distributions. The phase-masks and the corresponding fields in the Fourier plane for the continuous normal and binary normal distributions are given in Fig. 7. The frequency of the phase modulation within the ring-slit increases for each row in Figs. 6 and 7. For the phase-masks in Figs. 6 and 7, the checkered board patterns have been removed, so as to highlight the phase-modulation within the ring-slit.

It is evident, from column 2 of Fig. 6, that in the case of the continuous uniform distribution (where 256 grey-levels represent the transition from white, 0, to black, 2π) the zero-order Bessel beam starts to reconstruct as the frequency of the phase modulation increases. However, this is not the case with the binary uniform distribution and instead as the frequency of the phase modulation increases, so the speckle becomes more chaotic (evident in column 4 of Fig. 6). For the continuous normal (column 2, Fig. 7) and binary normal (column 4, Fig. 7) distributions, the nondiffracting speckle starts to evolve into a zero-order Bessel beam as the frequency of the phase modulation increases.

3.2. Theoretical description using the complex plane approach

3.2.1. Continuous uniform distribution

The effect that the description of the phase modulation within the ring-slit has on the formation of the resulting field, can also be explained by the complex plane approach. The checkered board pattern is a specific form of phase modulation where the two vectors, A_1 and A_2, are weighted and positioned on the complex plane in such a way that they produce a resultant having zero amplitude, thus completely suppressing the on-axis intensity in the Fourier plane. For the continuous uniform phase modulation, 256 vectors (A_1 to A_{256}), all having the same amplitude and emanating from the origin of the complex plane from 0 to 2π, produce a resultant, having the same amplitude as each of the 256 vectors, and pointing along the negative x-axis (i.e. $\varphi = \pi$). Therefore the average amplitude of the field at the plane of a phase-mask, having a continuous uniform phase modulation, is non-zero and due to the ring-slit geometry restricting this phase modulation, a zero-order Bessel beam manifests in the Fourier plane, evident in the three images in column 2 of Fig. 6.

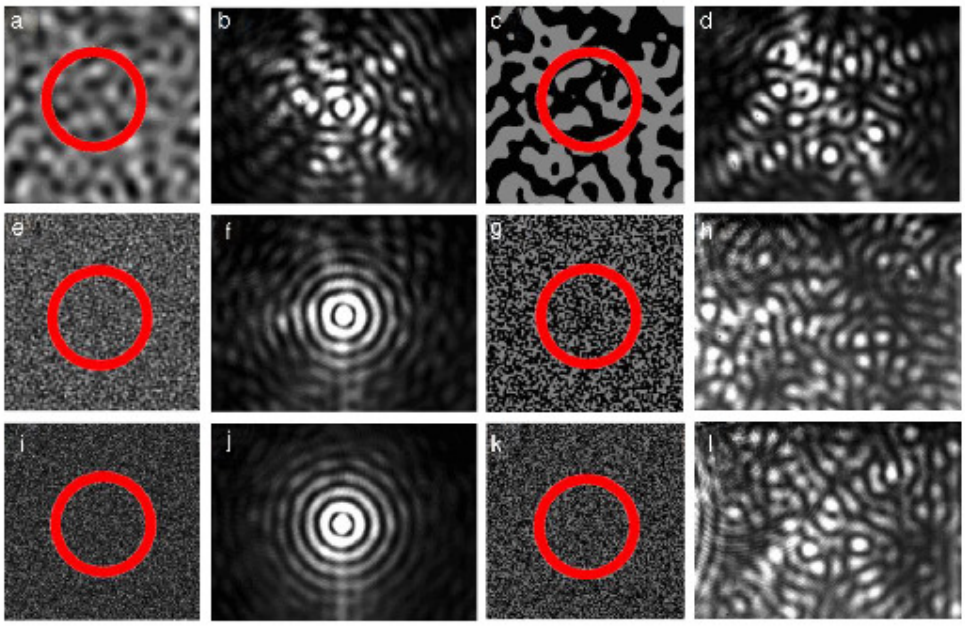

Fig. 6. Column 1: Phase-masks, where the phase modulation within the ring-slit is described by a continuous uniform distribution (the frequency of the phase modulation increases with each row, (a) and (c) 10 pixels; (e) and (g) 50 pixels; (i) and (k) 100 pixels). The red ring denotes the ring-slit. Column 2: The corresponding experimentally recorded Fourier plane. Column 3: Phase-masks, where the phase modulation within the ring-slit is described by a binary uniform distribution (the frequency of the phase modulation increases with each row). The red ring denotes the ring-slit. Column 4: The corresponding experimentally recorded Fourier plane.

Author's personal copy

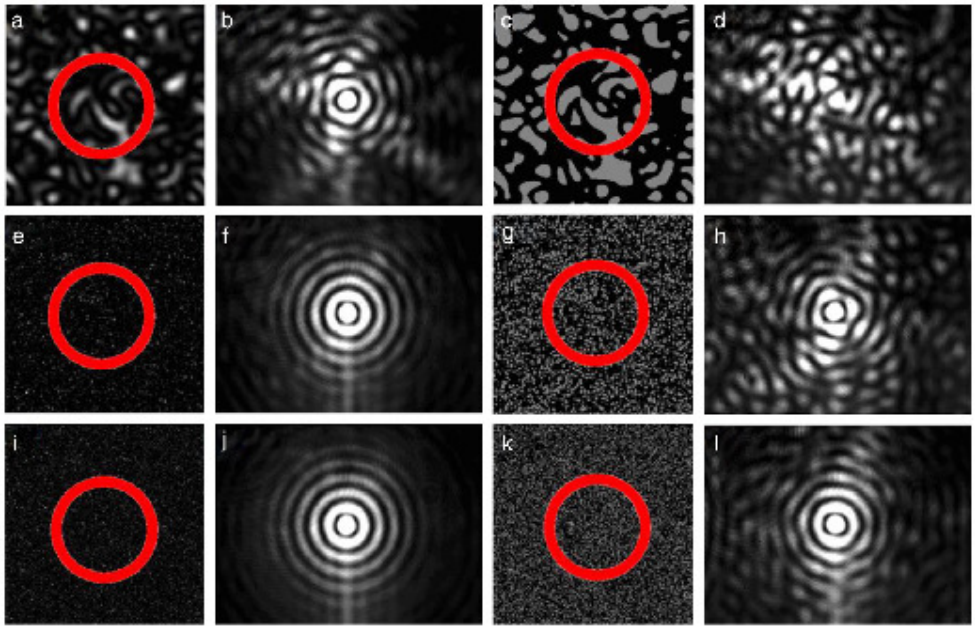

Fig. 7. Column 1: Phase-masks, where the phase modulation within the ring-slit is described by a continuous normal distribution (the frequency of the phase modulation increases with each row, (a) and (c) 10 pixels; (e) and (g) 50 pixels; (i) and (k) 100 pixels). The red ring denotes the ring-slit. Column 2: The corresponding experimentally recorded Fourier plane. Column 3: Phase-masks, where the phase modulation within the ring-slit is described by a binary normal distribution (the frequency of the phase modulation increases with each row). The red ring denotes the ring-slit. Column 4: The corresponding experimentally recorded Fourier plane.

In order to verify if the DC-offset experiences an increase or a decrease with an increase in the frequency of the phase modulation, we analysed the standard deviation within the ring-slit for all four distributions. A graph illustrating how the standard deviation for each distribution varies as a function of the frequency of the phase modulation is given in Fig. 8. The x-axis in Fig. 8 represents an

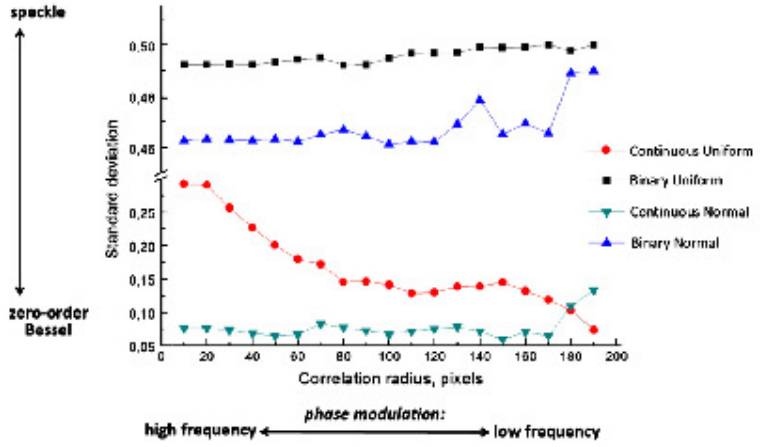

Fig. 8. Graph of the standard deviation for each of the four distributions as a function of the frequency of the phase modulation (or correlation radius).

Author's personal copy

increase in the correlation radius of the phase modulation within the ring-slit. The correlation radius denotes the distance over which a 2π phase shift occurs in the phase modulation. A small correlation radius therefore means the frequency of the phase modulation is high, whilst a large correlation radius means the frequency of the phase modulation is low. The y-axis denotes the standard deviation of the distribution. As the frequency of the phase modulation decreases, the standard deviation for the continuous uniform distribution decreases, meaning that the range in which the 256 vectors exist on the complex plane becomes smaller. If all 256 vectors on the complex plane are restricted to a segment which has a small opening angle, then the amplitude of the resultant vector will increase, resulting in the zero-order Bessel beam becoming more predominant in the Fourier plane.

3.2.2. Binary uniform distribution

In the binary uniform phase modulation there is an equal probability that either a value of 0 or π will be selected and so the two vectors on the complex plane each have the same amplitude, but point in opposite directions ($\varphi_1 = 0, \varphi_2 = \pi$). This is the same scenario as with the checkered board phase-mask. The amplitude of the resultant is zero, so the mean of the amplitude of the field within the ring-slit is zero and so no zero-order Bessel beam develops in the Fourier plane. Instead as the frequency of the phase modulation increases, so the 'noise' around the DC-offset increases and the nondiffracting speckle becomes more chaotic, evident in column 4 of Fig. 6. From Fig. 8, it is evident that the standard deviation for the uniform binary distribution does not vary as the frequency of the phase modulation increases. Therefore the amplitude of the two vectors in the complex plane remain unchanged as the frequency of the phase modulation increases and so no change occurs in the DC-offset and no zero-order Bessel beam forms in the Fourier plane.

3.2.3. Continuous normal distribution

The continuous normal distribution is represented on a complex plane by 256 vectors, whose amplitudes are weighted by a normal distribution, resulting in the resultant vector having a non-zero amplitude. Since the DC-offset (an average amplitude of the field) exists at the ring-slit, a zero-order Bessel beam becomes visible in the Fourier plane. This is evident experimentally in column 2 of Fig. 7. For the continuous normal distribution, as the frequency of the phase modulation increases the standard deviation remains fairly constant (evident in Fig. 8) and so not much change is noted in the average amplitude of the field within the ring-slit. In this case, as the frequency of the phase modulation increases not much change is noted in the intensity of the zero-order Bessel beam in the Fourier plane.

3.2.4. Binary normal distribution

The last case which we considered was a binary normal distribution. Due to the fact that the probability of selecting either a phase value of 0 or a phase value of π, is bounded by a normal distribution, the amplitudes of the two vectors in the complex plane are not equal. This leads to the resultant vector having a non-zero amplitude and so a mean amplitude exists within the ring-slit giving rise to a zero-order Bessel beam in the Fourier plane, evident in column 4 of Fig. 7. As the frequency of the phase modulation increases, the standard deviation decreases ever so slightly, evident in Fig. 8. This means that there is a slight increase in the amplitude of the resultant vector (or the mean amplitude within the ring-slit) and so the zero-order Bessel beam appears as the frequency of the phase modulation increases.

4. Discussion

From Fig. 8, it is evident that by engineering the frequency of the phase modulation we do not see much of a transition from nondiffracting speckle to a zero-order Bessel beam, as only one distribution (the binary normal distribution) shows a transition from chaotic speckle to a zero-order Bessel beam. This is in agreement with what we experimentally witness. In comparing Figs. 6 and 7, the binary normal distribution (column 4, Fig. 7) displays the development from fully-developed speckle to a zero-order Bessel beam. The two continuous cases do not seem to attain the state of chaotic speckle, also evident in the intensity profiles in column 2 of Figs. 6 and 7. Instead of chaotic speckle we see Bessel-like clusters, i.e. the clusterisation of the speckle occurs at the centre of the field, coinciding with the centre of the zero-order Bessel beam. The binary uniform distribution however is the polar opposite, in that increasing the frequency of the phase modulation, does not result in the field attaining a quasi-zero-order Bessel beam state (evident in Fig. 8 and in the intensity profiles in column 4 of Fig. 6).

Even though varying the frequency of the phase modulation does not show much promise for three of the four distributions, we also varied the standard deviation for all four cases. This restricts the two vectors to a smaller area on the complex plane and so the zero-order Bessel beam becomes more predominated in the Fourier plane as the standard deviation decreases. Simulated results are given in Fig. 9 (row 1: continuous uniform, row 2: binary uniform, row 3: continuous normal, and row 4: binary normal). It is evident that by varying the standard deviation, the field can develop from chaotic speckle to a zero-order Bessel beam. Therefore for any distribution, one can select where in the 'speckle to zero-order Bessel beam' spectrum the field can exist by a single parameter — the standard deviation.

Often nondiffracting fields are used in the non-destructive testing of materials. If one has a 'dial' which can be used to select either a zero-order Bessel beam, or fully-developed nondiffracting speckle, or any mixture in-between, one can develop fields that are 'tailor-made' to optimise the assessment of materials and solutions. Nondiffracting fields are also widely used in optical tweezers. By being able to switch between a zero-order Bessel beam and nondiffracting speckle, one can randomly disperse particles, accumulated in the column of the Bessel beam, in a predetermined area of a cell or sample. In studying the phase modulations in solutions, one can image a ring field onto a solution and by taking the Fourier transform; the structure of the resulting field can be studied. As we have investigated the effect of the frequency of the phase modulation, within the ring-slit, has on the structure of the resulting field, one can use this approach to analyse the phase modulations within chemical solutions.

5. Conclusion

In this work we illustrate a technique which allows one to operate a phase-only SLM in both phase and amplitude mode, resulting in the generation of nondiffracting speckle fields with a single SLM. Our results obtained with this technique are in very good agreement with an already known approach using Durnin's ring-slit [16]. This approach allows one to have control over the dimensions of the ring-slit and the phase modulation within the ring-slit. Our experimentally produced speckle fields using the checkered board approach are in good agreement with the theoretical predictions. The effects of binary and continuous phase modulations for two different distributions, (uniform and normal), on the structure of the speckle field were investigated. It was noted that we can control the evolution of the fully-developed nondiffracting speckle into a zero-order Bessel beam by adjusting the standard deviation of the distribution. The effect of both distributions, (continuous and binary), is explained by analysing the DC component of the Fourier series. Having the ability to control the development of nondiffracting speckle into a zero-order Bessel beam is a useful tool in the non-destructive testing of materials and in optical tweezing.

Author's personal copy

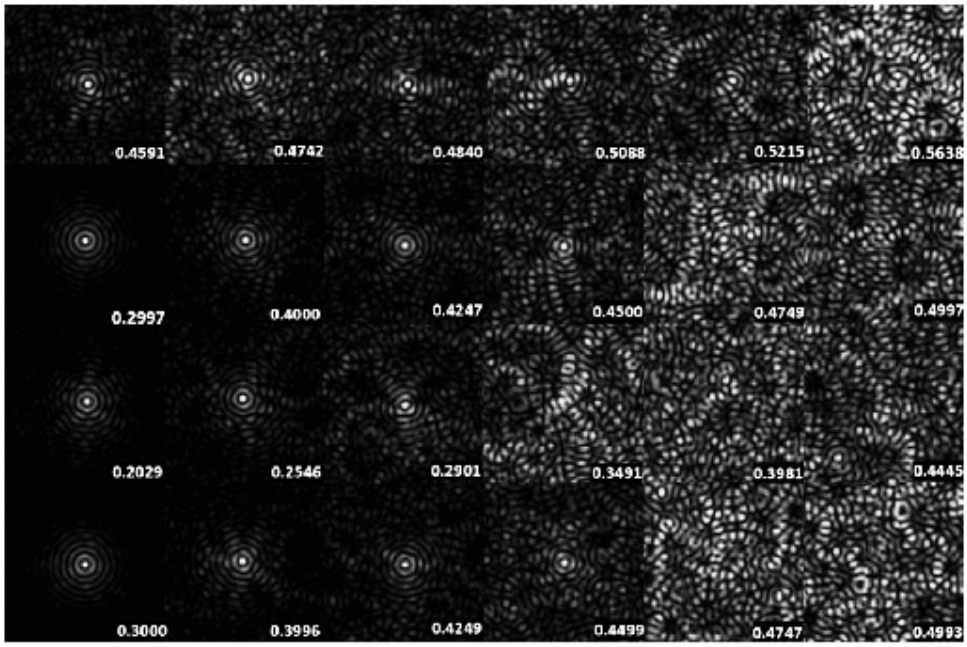

Fig. 9. Simulated images for the field in the Fourier plane, for each of the four corresponding distributions. Row 1: continuous uniform. Row 2: binary uniform. Row 3: continuous normal. Row 4: binary normal. The standard deviation increases from left to right. The values for the standard deviation are given in the bottom right corner of each image.

Acknowledgements

We gratefully acknowledge the support from the National Research Foundation (Grant number 67432). We would like to thank Dr F. S. Roux and Dr Carlos Lopez-Mariscal for their helpful discussions.

References

[1] J. Durnin, Journal of the Optical Society of America. A 4 (1987) 651.
[2] J. Turunen, A. Vasara, A.T. Friberg, Applied Optics 27 (1988) 3959.
[3] A. Vasara, J. Turunen, A.T. Friberg, Journal of the Optical Society of America. A A6 (1989) 1748.
[4] C. Paterson, R. Smith, Optics Communications 124 (1–2) (1996) 121.
[5] G. Scott, N. McArdle, Optical Engineering 31 (1992) 2640.
[6] R.M. Herman, T.A. Wiggins, Journal of the Optical Society of America. A 8 (6) (1991) 932.
[7] J. Arlt, K. Dholakia, Optics Communications 177 (1–6) (2000) 297.
[8] J.A. Davis, J. Guertin, D.M. Cottrell, Applied Optics 32 (1993) 6368.
[9] Z. Bouchal, J. Wagner, M. Chlup, Optics Communications 151 (1998) 207.
[10] I. Litvin, M. McLaren, A. Forbes, Optics Communications 282 (2009) 1078.
[11] V. Belyi, A. Forbes, N. Kazak, N. Khilo, P. Ropot, Optics Express 18 (3) (2010) 1966.
[12] D. McGloin, V. Garcés-Chávez, K. Dholakia, Optics Letters 28 (8) (2003) 657.
[13] R. Vasilyeu, A. Dudley, N. Khilo, A. Forbes, Optics Express 17 (26) (2009) 23389.
[14] V. Kettunen, J. Turunen, Optics Letters 23 (1998) 1247.
[15] J. Lautanen, V. Kettunen, P. Laakkonen, J.Turunen, Journal of the Optical Society of America. A 17 (2000) 2208.
[16] J. Durnin, J.J. Miceli, J.H. Eberly, Physical Review Letters 58 (1987) 1499.
[17] C. Lopez-Mariscal, K. Helmerson, Optics Letters 35 (2010) 1215.
[18] J. Turunen, A. Vasara, A.T. Friberg, Journal of the Optical Society of America. A 8 (1991) 282.
[19] D. Cottrell, J. Craven, J. Davis, Optics Letters 32 (2007) 298.
[20] R.K. Tyson, Principles of Adaptive Optics, Academic Press, London, 1991.
[21] M.C. Roggemann, B. Welsh, Imaging through Turbulence, CRC Press, Boca Raton, FL, 1996.
[22] E. Kolenovic, W. Osten, W. Jueptner, Proc of SPIE 3744 (1999) 0277-786X.
[23] W. Wang, T. Yokozeki, R. Ishijima, M. Takeda, S. Hanson, Optics Express 14 (2006) 10195.
[24] F. Chiang, Optics and Lasers in Engineering 47 (2009) 274.
[25] P. Picart, J. Pascal, J. Brenau, Applied Optics 40 (2001) 2107.
[26] P. Jacquot, Speckle Interferometry: A Review of the Principal Methods in Use for Experimental Mechanics Applications, Blackwell Publishing Ltd Strain, 2008.
[27] P. Jacquot, M. Fournier, Interferometry in Speckle Light, Springer, Berlin, 2000.
[28] M. Ibrahim, J. Uozumi, T. Asakura, Optical Review 5 (1998) 129.
[29] K. Uno, J. Uozumi, T. Asakura, Optics Communications 114 (1995) 203.
[30] M. Ibrahim, J. Uozumi, T. Asakura, Optik 106 (1997) 33.
[31] V. Belyi, N. Kazak, N. Khilo, P. Ropot, Proc of SPIE 6729 (2007) 67290C-1.
[32] J. Uozumi, M. Ibrahim, T. Asakura, Optics Communications 156 (1998) 350.
[33] D.W.K. Wong, G. Chen, Applied Optics 47 (2008) 602.
[34] M.L. Boas, Mathematical Methods in the Physical Sciences, third ed. Wiley, Hoboken, NJ, 2006.

B5: Publication 5

Poynting vector and orbital angular momentum density of superpositions of Bessel beams

Igor A. Litvin,[1,3] Angela Dudley[1,2] and Andrew Forbes[1,2,*]

[1]*CSIR National Laser Centre, PO Box 395, Pretoria 0001, South Africa*
[2]*School of Physics, University of KwaZulu-Natal, Private Bag X54001, Durban 4000, South Africa*
[3]*ilitvin@csir.co.za*
[*]*aforbes1@csir.co.za*

Abstract: We study theoretically the orbital angular momentum (OAM) density in arbitrary scalar optical fields, and outline a simple approach using only a spatial light modulator to measure this density. We demonstrate the theory in the laboratory by creating superpositions of non-diffracting Bessel beams with digital holograms, and find that the OAM distribution in the superposition field matches the predicted values. Knowledge of the OAM distribution has relevance in optical trapping and tweezing, and quantum information processing.

©2011 Optical Society of America

OCIS codes: (050.0050) Diffraction and gratings; (050.4865) Optical vortices; (270.0270) Quantum Optics.

References and links

1. R. A. Beth, "Mechanical detection and measurement of the angular momentum of light," Phys. Rev. **50**(2), 115–125 (1936).
2. M. W. Beijersbergen, L. Allen, H. E. L. O. Van der Veen, and J. P. Woerdman, "Astigmatic laser mode converters and the transfer of orbital angular momentum," Opt. Commun. **96**(1-3), 123–132 (1993).
3. L. Allen, M. W. Beijersbergen, R. J. C. Spreeuw, and J. P. Woerdman, "Orbital angular momentum of light and the transformation of Laguerre-Gaussian laser modes," Phys. Rev. A **45**(11), 8185–8189 (1992).
4. J. Arlt and K. Dholakia, "Generation of high-order Bessel beams by use of an axicon," Opt. Commun. **177**(1-6), 297–301 (2000).
5. H. I. Sztul and R. R. Alfano, "The Poynting vector and angular momentum of Airy beams," Opt. Express **16**(13), 9411–9416 (2008).
6. H. He, M. E. J. Friese, N. R. Heckenberg, and H. Rubinsztein-Dunlop, "Direct observation of transfer of angular momentum to absorptive particles from a laser beam with a phase singularity," Phys. Rev. Lett. **75**(5), 826–829 (1995).
7. A. Mair, A. Vaziri, G. Weihs, and A. Zeilinger, "Entanglement of the orbital angular momentum states of photons," Nature **412**(6844), 313–316 (2001).
8. A. Vaziri, G. Weihs, and A. Zeilinger, "Experimental two-photon, three-dimensional entanglement for quantum communication," Phys. Rev. Lett. **89**(24), 240401 (2002).
9. J. T. Barreiro, T.-C. Wei, and P. G. Kwiat, "Beating the channel capacity limit for linear photonic superdense coding," Nat. Phys. **4**(4), 282–286 (2008).
10. J. Leach, B. Jack, J. Romero, A. K. Jha, A. M. Yao, S. Franke-Arnold, D. G. Ireland, R. W. Boyd, S. M. Barnett, and M. J. Padgett, "Quantum correlations in optical angle-orbital angular momentum variables," Science **329**(5992), 662–665 (2010).
11. G. Gibson, J. Courtial, M. J. Padgett, M. Vasnetsov, V. Pas'ko, S. M. Barnett, and S. Franke-Arnold, "Free-space information transfer using light beams carrying orbital angular momentum," Opt. Express **12**(22), 5448–5456 (2004).
12. S. N. Khonina, V. V. Kotlyar, R. V. Skidanov, V. A. Soifer, P. Laakkonen, and J. Turunen, "Gauss–Laguerre modes with different indices in prescribed diffraction orders of a diffractive phase element," Opt. Commun. **175**(4-6), 301–308 (2000).
13. G. C. G. Berkhout, M. P. J. Lavery, J. Courtial, M. W. Beijersbergen, and M. J. Padgett, "Efficient sorting of orbital angular momentum states of light," Phys. Rev. Lett. **105**(15), 153601 (2010).
14. J. Leach, M. J. Padgett, S. M. Barnett, S. Franke-Arnold, and J. Courtial, "Measuring the orbital angular momentum of a single photon," Phys. Rev. Lett. **88**(25), 257901 (2002).
15. C. Gao, X. Qi, Y. Liu, J. Xin, and L. Wang, "Sorting and detecting orbital angular momentum states by using a Dove prism embedded Mach-Zehnder interferometer and amplitude gratings," Opt. Commun. **284**(1), 48–51 (2011).
16. M. V. Vasnetsov, J. P. Torres, D. V. Petrov, and L. Torner, "Observation of the orbital angular momentum spectrum of a light beam," Opt. Lett. **28**(23), 2285–2287 (2003).

#146350 - $15.00 USD Received 21 Apr 2011; revised 2 Jun 2011; accepted 26 Jul 2011; published 15 Aug 2011
(C) 2011 OSA

17. M. S. Soskin, V. N. Gorshkov, M. V. Vasnetsov, J. T. Malos, and N. R. Heckenberg, "Topological charge and angular momentum of light beams carrying optical vortices," Phys. Rev. A **56**(5), 4064–4075 (1997).
18. S. Franke-Arnold, J. Leach, M. J. Padgett, V. E. Lembessis, D. Ellinas, A. J. Wright, J. M. Girkin, P. Ohberg, and A. S. Arnold, "Optical ferris wheel for ultracold atoms," Opt. Express **15**(14), 8619–8625 (2007).
19. L. Paterson, M. P. MacDonald, J. Arlt, W. Sibbett, P. E. Bryant, and K. Dholakia, "Controlled rotation of optically trapped microscopic particles," Science **292**(5518), 912–914 (2001).
20. D. McGloin, V. Garcés-Chávez, and K. Dholakia, "Interfering Bessel beams for optical micromanipulation," Opt. Lett. **28**(8), 657–659 (2003).
21. K. Volke-Sepulveda, V. Garcés-Chávez, S. Chávez-Cerda, J. Arlt, and K. Dholakia, "Orbital angular momentum of high-order Bessel light beams," J. Opt. B Quantum Semiclassical Opt. **4**(2), S82–S89 (2002).
22. M. J. Padgett and L. Allen, "The Poynting vector in Laguerre-Gaussian laser modes," Opt. Commun. **121**(1-3), 36–40 (1995).
23. L. Allen and M. J. Padgett, "The Poynting vector in Laguerre-Gaussian beams and the interpretation of their angular momentum density," Opt. Commun. **184**(1-4), 67–71 (2000).
24. R. Zambrini and S. M. Barnett, "Angular momentum of multimode and polarization patterns," Opt. Express **15**(23), 15214–15227 (2007).
25. A. T. O'Neil, I. MacVicar, L. Allen, and M. J. Padgett, "Intrinsic and extrinsic nature of the orbital angular momentum of a light beam," Phys. Rev. Lett. **88**(5), 053601 (2002).
26. M. V. Berry, "Paraxial beams of spinning light," SPIE **3487**, 6–11 (1998).
27. L. W. Davis, "Theory of electromagnetic beams," Phys. Rev. A **19**(3), 1177–1179 (2003).
28. S. Orlov and A. Stabinis, "Propagation of superpositions of coaxial optical Bessel beams carrying vortices," J. Opt. A, Pure Appl. Opt. **6**(5), S259–S262 (2004).
29. S. Orlov, K. Regelskis, V. Smilgevicius, and A. Stabinis, "Propagation of Bessel beams carrying optical vortices," Opt. Commun. **209**(1-3), 155–165 (2002).
30. R. Vasilyeu, A. Dudley, N. Khilo, and A. Forbes, "Generating superpositions of higher-order Bessel beams," Opt. Express **17**(26), 23389–23395 (2009).
31. J. Durnin, J. Miceli, Jr., and J. H. Eberly, "Diffraction-free beams," Phys. Rev. Lett. **58**(15), 1499–1501 (1987).
32. J. Lin, X.-C. Yuan, S. H. Tao, and R. E. Burge, "Collinear superposition of multiple helical beams generated by a single azimuthally modulated phase-only element," Opt. Lett. **30**(24), 3266–3268 (2005).
33. M. Dienerowitz, M. Mazilu, and K. Dholakia, "Optical manipulation of nanoparticles: a review," J. Nanophoton. **12**, 1–32 (2008).
34. L. Torner, J. P. Torres, and S. Carrasco, "Digital spiral imaging," Opt. Express **13**(3), 873–881 (2005).
35. J. A. Rodrigo, A. M. Caravaca-Aguirre, T. Alieva, G. Cristóbal, and M. L. Calvo, "Microparticle movements in optical funnels and pods," Opt. Express **19**(6), 5232–5243 (2011).
36. S. H. Tao, X. C. Yuan, J. Lin, and R. E. Burge, "Residue orbital angular momentum in interferenced double vortex beams with unequal topological charges," Opt. Express **14**(2), 535–541 (2006).
37. C. H. J. Schmitz, K. Uhrig, J. P. Spatz, and J. E. Curtis, "Tuning the orbital angular momentum in optical vortex beams," Opt. Express **14**(15), 6604–6612 (2006).

1. Introduction

It has been well known for some time now that photons carry spin angular momentum of $+\hbar$ ($-\hbar$) per photon for left (right) circularly polarised light, and that the transfer of this momentum can be measured in the laboratory when the light passes through a birefringent plate [1]. More recently [2,3] it has been realised that light may also carry an extrinsic component of angular momentum, orbital angular momentum (OAM), when the electric field or mode has an azimuthal angular dependence of $\exp(il\varphi)$, where l is the azimuthal mode index. Such fields carry OAM of $l\hbar$ per photon, and may be found as beams expressed in several basis functions, including Laguerre-Gaussian beams [2], Bessel-Gaussian beams [4] and Airy beams [5] to name but a few. Since the discovery of light beams carrying OAM many new research areas have emerged, from transferring OAM to matter in optical tweezers [6] to investigating the conservation and entanglement of OAM in parametric down conversion for quantum information processing [7–11]. One of the problems has been the measurement of OAM, with various attempts at the efficient sorting of modes carrying OAM using interferometers and computer generated holograms [12–16]. Studies into the angular momentum of combined beams during free space propagation have also been made [17]. In general, one is interested in the superposition of OAM carrying fields, both at the classical [18–20] and quantum levels [7].

In this paper we consider the problem of calculating and then measuring the orbital angular momentum density of a coherent superposition of non-diffracting beams. We derive simple equations for the OAM density from first principles by calculating the Poynting vector of the field, and from this deduce both the linear and angular momentum components. The

#146350 - $15.00 USD Received 21 Apr 2011; revised 2 Jun 2011; accepted 26 Jul 2011; published 15 Aug 2011
(C) 2011 OSA

results indicate that while the intensity pattern of the field is rotating at a fixed angular velocity (dependent on the relative phase velocities of the component fields), the OAM magnitude and direction is dependent on the location within the spatial distribution of the field. That is to say, different parts of the field carry different amounts of OAM, and of various sign. We verify the results by outlining and then executing a new technique for the direct measurement of the OAM density in the laboratory. We show how this approach allows for a quantitative measurement of the OAM spectrum as a function of position within the field.

2. Theory

We wish to consider the OAM density for a general complex scalar field, $u(x,y,z)$, which varies in time (in complex notation) as $\exp(i\omega t)$. This problem has been addressed by others previously [5,21–26], but with some inconsistencies in notation and derivation. For this reason, and for the benefit of the reader, we briefly outline the approach for defining OAM density, starting from the Poynting vector, before applying the result to the specific problem of coherent superpositions of non-diffracting Bessel beams. We start by defining a vector potential in the Lorentz gauge as a representation of our linearly polarized (in the x direction) laser mode as [27]:

$$\vec{A}(x,y,z) = u(x,y,z)\exp(i(kz-\omega t))\bar{x} \tag{1}$$

from which we can easily calculate the electric and magnetic field components of our complex scalar field:

$$\begin{aligned}\vec{B}(x,y,z) &= \nabla\times\vec{A}(x,y,z)\\ \vec{E}(x,y,z) &= \frac{ic^2}{\omega}\nabla\times\vec{B}(x,y,z),\end{aligned} \tag{2}$$

where $\vec{E}$ and $\vec{B}$ are the electric and magnetic fields of the laser mode, respectively, and all other terms have their usual meaning. Equations (2) can readily be solved to find the two fields as functions of the laser mode itself (our complex scalar field):

$$\begin{aligned}\vec{B}(x,y) &= ik\exp(i(kz-\omega t))\left(u(x,y,z)\bar{y}+\frac{i}{k}\frac{\partial u(x,y,z)}{\partial y}\bar{z}\right)\\ \vec{E}(x,y) &= i\omega\exp(i(kz-\omega t))\left(u(x,y,z)\bar{x}+\frac{i}{k}\frac{\partial u(x,y,z)}{\partial x}\bar{z}\right)\end{aligned} \tag{3}$$

Here we have applied the paraxial limit and assumed that the rate of change of the field in the z direction is small compared to the transverse directions to remove derivatives of the field in the z direction. We are now in a position to calculate the time average of the Poynting vector:

$$\vec{S} = \left\langle\vec{S}_{real}\right\rangle = \varepsilon_0 c^2\left\langle\vec{E}_{real}\times\vec{B}_{real}\right\rangle, \tag{4}$$

where for brevity we will drop the arguments of the functions. The subscript *real* indicates that we are required to consider only the real part of the fields ($\cos(kz-\omega t)$), easily found to be:

$$\begin{aligned}\vec{E}_{real} &= \tfrac{1}{2}(\vec{E}+\vec{E}^*)\\ \vec{B}_{real} &= \tfrac{1}{2}(\vec{B}+\vec{B}^*),\end{aligned} \tag{5}$$

By substitution of Eqs. (3) and (5) into (4), and after removing all the oscillating terms since they average to zero (over time), one can show that

#146350 - $15.00 USD Received 21 Apr 2011; revised 2 Jun 2011; accepted 26 Jul 2011; published 15 Aug 2011
(C) 2011 OSA

$$\begin{aligned}\vec{S} &= \varepsilon_0 c^2 \left\langle \vec{E}_{real} \times \vec{B}_{real} \right\rangle \\ &= \frac{\varepsilon_0 c^2}{4}\left(\vec{E}\times\vec{B}^* + \vec{E}^*\times\vec{B}\right) \\ &= \frac{\varepsilon_0 \omega}{4}\left(i\left(u\nabla u^* - u^*\nabla u\right) + 2k|u|^2\,\hat{z}\right),\end{aligned} \tag{6}$$

where it is understood that the gradient applies only in the transverse directions. We now wish to apply Eq. (6) to the problem of a superposition of OAM carrying fields, and we start with the problem of a coherent superposition of two such fields, of opposite handedness (i.e., opposite azimuthal phase), expressed in cylindrical co-ordinates as:

$$u(r,\varphi,z) = u_0(r,z)\exp(i\psi(r,z))\left(\exp(il\varphi) + \alpha_0\exp(-il\varphi)\right), \tag{7}$$

with the parameter α_0 representing the amplitude difference of the two fields (i.e., how the fields are weighted). The amplitude (u_0) and phase (ψ) of the complex scalar field is determined from the characteristics of the mode under study, and will be defined for Bessel and Bessel-Gauss beams a little later in this section. Substitution of Eq. (7) into Eq. (6) and solving for each component of the Poynting vector, we find that:

$$\begin{aligned}S_r &= \frac{\varepsilon_0\omega c^2}{2}\frac{\partial\psi}{\partial r}\left[u_0^2\left(1+\alpha_l^2+2\alpha_l\cos(2l\phi)\right)\right] \\ S_\phi &= \frac{-l\varepsilon_0\omega c^2 u_0^2}{2r}\left(\alpha_l^2-1\right) \\ S_z &= \frac{\varepsilon_0\omega c^2 k u_0^2}{2}\left(1+\alpha_l^2+2\alpha_l\cos(2l\phi)\right)\end{aligned} \tag{8}$$

In the case of a sum of Bessel and Bessel-Gaussian beams, the parameter $\alpha_l = \alpha_0(-1)^l$, whereas for Laguerre-Gaussian beams it takes the form $\alpha_l = \alpha_0$; here α_0 is the constant amplitude weighting of the fields. From these equations we may readily calculate the total angular momentum density of the field, and since by definition our field has a zero spin component, we have the total OAM density (along the direction of propagation, z) as:

$$L_z = \frac{1}{c^2}\left(r\times S\right)_z. \tag{9}$$

In this expression, the units of S are the conventional W/m^2, while the OAM density (L_z) is now expressed as the angular momentum per unit volume, or Ns/m^2. With these fundamentals in place, we are ready to calculate the OAM density for superposition fields.

2.1 Superposition of Bessel beams

Consider the general case of the superposition of two Bessel beams (BBs) of differing cone angles and opposite azimuthal phase; then Eq. (7) becomes

$$u(r,\phi,z) = A_0[J_l(q_1 r)\exp(i\Delta k z)\exp(il\phi) + \alpha_0 J_{-l}(q_2 r)\exp(-i\Delta k z)\exp(-il\phi)], \tag{10}$$

where J_l is the Bessel function of order l. Similar expressions can be found in references [28] and [29]. The cone angles, γ_1 and γ_2, differ as a result of the generation process (see later), but can be set to be equal if so required. As a result of the slightly different cone angles, both the radial and longitudinal wave numbers also differ for the two beams: the radial wave numbers become $q_i = k\sin\gamma_i$, while the longitudinal wave numbers, given by $k_i = k\cos\gamma_i$ differ from the central z-dependent wave number (k) by $\pm\Delta k$ (the subscripts i here refers to the first (second) beam in the superposition). We have maintained a normalization constant A_0 in order to later compare the theoretical results to experiment. Thus the Poynting vector becomes:

#146350 - $15.00 USD Received 21 Apr 2011; revised 2 Jun 2011; accepted 26 Jul 2011; published 15 Aug 2011
(C) 2011 OSA

$$S_r = -\frac{A_0^2 \alpha_0 \varepsilon_0 \omega c^2}{2}\left[\left(q_2 J_{-l-1}(q_2 r) J_l(q_1 r) + q_1 J_{-l}(q_2 r) J_{l+1}(q_1 r)\right)\sin\left(2[l\phi + \Delta k z]\right)\right]$$

$$S_\phi = \frac{A_0^2 l \varepsilon_0 \omega c^2}{2r}\left(J_l^2(q_1 r) - \alpha_0^2 J_{-l}^2(q_2 r)\right) \tag{11}$$

$$S_z = \frac{A_0^2 \varepsilon_0 \omega c^2 k}{2}\left(J_l^2(q_1 r) + \alpha_0^2 J_{-l}^2(q_2 r) + 2\alpha_0 J_l(q_1 r) J_{-l}(q_2 r)\cos\left(2[l\phi + \Delta k z]\right)\right)$$

The time average Poynting vector, in both the r and z directions, has an additional term $\Delta k z$ which is responsible for the slow rotation of the intensity distribution during its propagation. This behavior has been noted previously [30] and we can see that this is a result of the detuning of the radial wave numbers for the superposition of two or more beams. From the equation for S_r, a single non-diffracting beam has no S_r component. However, in the case of a superposition of two non-diffracting beams, the resulting beam has a non-zero S_r component. This results in a small rotation in the z direction, thus changing the intensity distribution of the superposition at a particular radial coordinate. We may easily then compute the OAM density to be:

$$L_z(r) = \frac{l \varepsilon_0 \omega A_0^2}{2}\left(J_l^2(q_1 r) - \alpha_0^2 J_{-l}^2(q_2 r)\right) \tag{12}$$

2.2 Superposition of Bessel-Gauss beams

Following a similar approach to that of section 2.1, we can find the OAM density for a superposition of two Bessel-Gauss beams (BGBs) of differing cone angles and opposite azimuthal phase, defined as

$$u(r, z, \phi) = \left(\frac{1}{\sqrt{1 + (z/z_r)^2}}\right)\exp\left[\left(\frac{ik}{2z\left(1 + (z/z_r)^2\right)} - \frac{1}{w_0^2\left(1 + (z/z_r)^2\right)}\right)\left(r^2 + \gamma^2 z^2\right)\right]$$
$$\times\left(J_l\left(\frac{q_1 r}{1 + i(z/z_r)}\right)\exp(ik_{z1} z)\exp(il\phi) + \alpha_0 J_{-l}\left(\frac{q_2 r}{1 + i(z/z_r)}\right)\exp(ik_{z2} z)\exp(-il\phi)\right)\chi(z), \tag{13}$$

where we assume both fields are modulated by the same Gaussian beam of width w_0, resulting in a Gaussian Rayleigh range of z_r, and for brevity we have collapsed the phase terms related to the piston and Gouy phase shifts into the function $\chi(z)$. We may easily then compute the OAM density to be:

$$L_z(r, z) = \frac{l \varepsilon_0 \omega}{2[1 + (z/z_r)^2]} \times$$
$$\exp\left(-2\frac{r^2 + \gamma^2 z^2}{w_0^2\left(1 + (z/z_r)^2\right)}\right)\left[\left|J_l\left(\frac{q_1 r}{1 + i(z/z_r)}\right)\right|^2 - \alpha_0^2\left|J_{-l}\left(\frac{q_2 r}{1 + i(z/z_r)}\right)\right|^2\right]. \tag{14}$$

These results are consistent with what might be expected using the more general formalism of ref [24], and by extension of the vectorial results in ref [21]. Indeed, our results here are the special case of these two approaches for scalar fields (linear polarized) and where the superposition is due to interference of the two modes. It remains then to define a method of actually measuring this quantity in the laboratory, a subject that has not been adequately addressed to date.

#146350 - $15.00 USD Received 21 Apr 2011; revised 2 Jun 2011; accepted 26 Jul 2011; published 15 Aug 2011
(C) 2011 OSA

2.3 Measuring the OAM density

Much attention has been paid to the measurement of OAM recently [12–16]. It is well known that since the angular harmonics, $\exp(il\varphi)$, are orthogonal over the azimuthal plane, we may express our superposition field in terms of such harmonics:

$$u(r,\phi,z) = \frac{1}{\sqrt{2\pi}}\sum_l a_l(r,z)\exp(il\phi), \tag{15}$$

with

$$a_l(r,z) = \frac{1}{\sqrt{2\pi}}\int_0^{2\pi} u(r,\varphi,z)\exp(-il\varphi)d\varphi. \tag{16}$$

The relative weighting of the power contained in each azimuthal mode can then be defined as [5]:

$$P_l(z) = \frac{\int_0^\infty |a_l(r,z)|^2 r dr}{\sum_l \int_0^\infty |a_l(r,z)|^2 r dr}. \tag{17}$$

From the definition of Eq. (16), one can easily show that the weighting of each harmonic for the case of a superposition of BBs is related to the OAM density through the relation:

$$L_z(r) = \frac{l\varepsilon_0\omega}{4\pi}\left(a_l^2(r) - a_{-l}^2(r)\right). \tag{18}$$

We will show, for the first time, how this quantity may be measured in the laboratory in an easy to implement procedure with a phase-only spatial light modulator (SLM), thus allowing a direct measurement of the OAM density of the light.

3. Experimental methodology

A HeNe laser ($\lambda \sim 633$ nm) was expanded through a 6 × telescope and directed onto the liquid crystal display (LCD) of a SLM (HoloEye, PLUTO-VIS, with 1920 × 1080 pixels of pitch 8 μm and calibrated for a 2π phase shift at ~633 nm) depicted in Fig. 1. The first SLM (denoted as LCD 1) was programmed to produce various superposition fields using the concept of Durnin's ring-slit [31], but implemented digitally [29]. Other techniques to experimentally generate superpositions of helically-phased fields using a single LCD exist and have been implemented by others [32]. By addressing alternating sets of pixels on the SLM with phase values that are out of phase by π, resulting in the light reflected from the LCD being scattered from its initial propagation axis, we are able to make use of our phase-only SLM to represent the ring-slit (which would usually require an amplitude device or mask).

To create a superposition of two non-diffracting beams of opposite handedness, the ring-slit was programmed with two opposite azimuthal phases, and the resulting field Fourier transformed at the focal plane after L3, to produce the field described by Eq. (10). The phase pattern in the annular region was separated into two ring-slits, each possessing an azimuthal phase of equal order but opposite handedness (Fig. 2(a)). When the orders, l/l, of the two azimuthal phases were of equal but of opposite handedness, a 'petal'-structure was produced, where the number of 'petals' is denoted by $2l/l$ (Fig. 2(b) and (c)), as expected from theory [30]. The slight difference in radius of the two rings resulted in cone angles (defined as Rlf with R the ring radius) of $\gamma_1 = 0.0069$ rad and $\gamma_2 = 0.0075$ rad, so that $\Delta k \sim 42.8801$ m^{-1}. Another consequence of the slightly differing ring areas (see Fig. 2(a)) is that the energy contained in the two Bessel beams is not equal. Since the illuminating Gaussian beam was measured to be of radius $w = 13.29$ mm on LCD 1, the energy contained in each ring could be computed, and the weighting coefficients found:

#146350 - $15.00 USD Received 21 Apr 2011; revised 2 Jun 2011; accepted 26 Jul 2011; published 15 Aug 2011
(C) 2011 OSA

$$\alpha_0 = \sqrt{\int_{ring1} \exp(-2(r/w)^2) r dr \Big/ \int_{ring2} \exp(-2(r/w)^2) r dr}. \qquad (19)$$

The resulting images of our non-diffracting superposition field were captured on a CCD camera (Spiricon, LBA-FW-SCOR-7350115), and the objective and camera could be positioned on translation stages with an optical rail in order to investigate the propagation of the resulting field. Once recorded, the resulting superposition field was then magnified with a 10 × objective and directed to the second SLM (LCD 2) for executing the modal decomposition of Eq. (16). This was accomplished by executing an inner product of the incoming field with the match filter set to $\exp(il\varphi)$, for various l values, and for particular radial (r) positions on the field. There are two important aspects of this experiment: firstly, the detection is restricted to the origin of the resulting field after the Fourier transforming lens L4, and secondly, the r dependence of the coefficient a_l is found by implementing the match filter in the form of a narrow (20 pixels) annular ring of radius r.

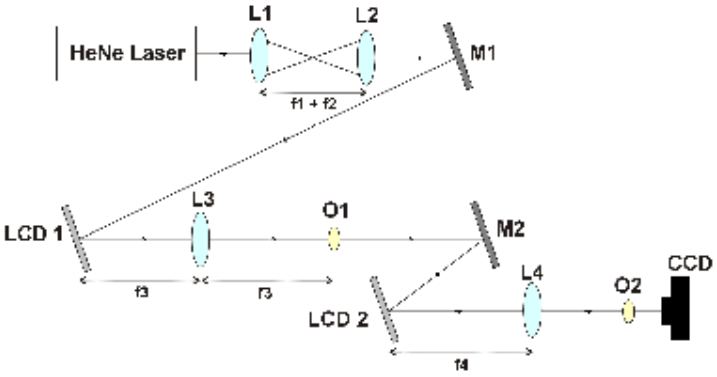

Fig. 1. A schematic of the experimental setup for detecting the OAM density of our superposition modes as a function of r. L: Lens (f1 = 25 mm; f2 = 150 mm; f3 = 200 mm and f4 = 200 mm); M: Mirror; LCD: Liquid Crystal Display; O: Objective; CCD: CCD Camera. The objective, O2, was placed at the focus (or Fourier plane) of lens, L4.

The latter requirement is necessary in order that we find the local OAM density rather than the global OAM density. Figure 3 illustrates the concept: the experimental field (Fig. 3; second and forth row) was subdivided radially into 10 sections, with each section sequentially apertured by an annular ring of width 20 pixels. The phase within the annular ring was varied according to the conjugate of the azimuthal modes in Eq. (15), i.e., the azimuthal integrand of Eq. (16), from –4 to + 4 in l index. Thus the decomposition of our field to find the weighting coefficients could be executed as a function of radial co-ordinate and azimuthal mode. This is the first time such a technique has been demonstrated experimentally, and allows for the OAM density to be measured directly: the OAM spectrum, $a_l(r,z)$ can be found at any radial position across the beam (and of course any z plane). The weighting parameter (α_0) of the superposition field was set by a suitable choice of the width of the two rings in the phase pattern on LCD 1: $\alpha_0 = 0.96$ (nearly equal weighting).

#146350 - $15.00 USD Received 21 Apr 2011; revised 2 Jun 2011; accepted 26 Jul 2011; published 15 Aug 2011
(C) 2011 OSA

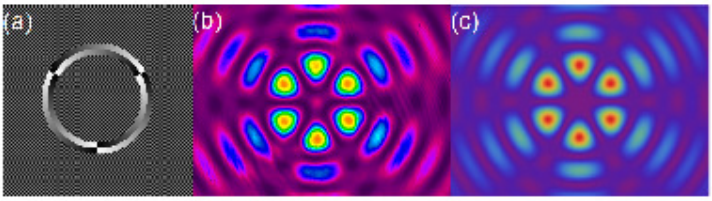

Fig. 2. (a) Annular ring programmed onto the SLM with two azimuthal phase patterns: in this example, + 3 and –3 l values; (b) observed experimental superposition (intensity) with 6 petals, and (c) the theoretically expected intensity pattern. The intensity shown in (b) is an attenuated experimental image with arbitrary false color units so as not to saturate the camera, while that in (c) shows a false color plot normalized to 1 in peak value for visual comparison.

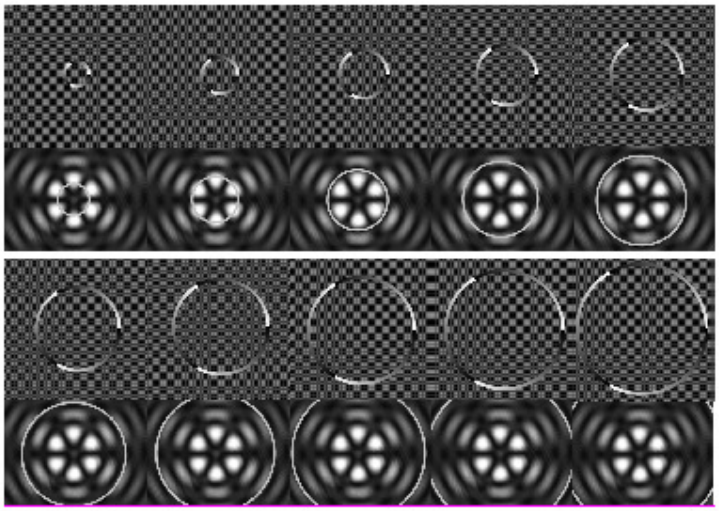

Fig. 3. The superposition field was divided radially, and an annular ring was programmed onto the second SLM in order to execute the inner product at only this radius. The phase within the annular ring was varied in the azimuthal angle for various values of l. The rest of the SLM was programmed with a checkerboard pattern so as to restrict the transmission function to the ring alone. The ten rings applied to LCD 2 have the following radii: $r_1 = 600$ μm, $r_2 = 880$ μm, $r_3 = 1160$ μm, $r_4 = 1440$ μm, $r_5 = 1720$ μm, $r_6 = 2000$ μm, $r_7 = 2280$ μm, $r_8 = 2560$ μm, $r_9 = 2840$ μm and $r_{10} = 3120$ μm. The black and white images in rows 2 and 4 are gray-scale experimental images of the beam, with the attenuation set so as not to saturate the camera. Therefore the intensity units are arbitrary.

Because of the manner in which the experiment was executed, by a Fourier transform evaluated at the origin after the second SLM, the actual measured quantities are related to the OAM density by

$$L_z = \frac{l\omega}{\eta c}\left(\frac{\lambda f}{S_{ring}}\right)^2 \left(I_3(0) - I_{-3}(0)\right), \tag{20}$$

#146350 - $15.00 USD Received 21 Apr 2011; revised 2 Jun 2011; accepted 26 Jul 2011; published 15 Aug 2011
(C) 2011 OSA

where $I_3(0)$ and $I_{-3}(0)$ are the measured signals on the CCD detector (see Fig. 1), f is the focal length of the final Fourier transforming lens, and S_{ring} is the area of the annular ring on the 2nd SLM. The coefficient η is to account for the losses in the optical system, e.g., the efficiency of the SLM and attenuators prior to the camera, which in our experiments was typically 0.0032 (or 0.32%).

4. Results and discussion

Applying Eq. (12), we calculate the dependence of the OAM density of a superposition of BBs, where the two components differ in their radial wave numbers. In Fig. 4(a) we see the results for the case of a 633 nm laser beam in a superposition of + 3 and –3 BBs, where the cone angle of the + 3 beam is fixed at 0.5° (line A on the graph) and that of the –3 BB is varied from 0.4° to 0.6°. Two results are evident: firstly, if the cone angles of the two BBs differ, so that their radial wave numbers differ, then the OAM density changes sign as one moves radially across the field. Secondly, the oscillation in the OAM density can be made to change value (magnitude and sign) by changing the relative difference in the cone angles (see line B of Fig. 4(a)). This is due to the oscillating nature of the Bessel function, where the period of the oscillation depends on the radial wave number, and in this particular case we have a superposition of two oppositely oscillating functions having opposite signs for their angular momentum. This can be seen by considering line B on the graph (varying cone angles), where the OAM density changes from a large positive value to a large negative value as one considers a single ring in the field (single radial position), passing through a zero value in between. In the case that the two cone angles are equal and the amplitude of the two Bessel beams are equal, the resulting superposition carries no angular momentum (see line A of Fig. 4(a)).

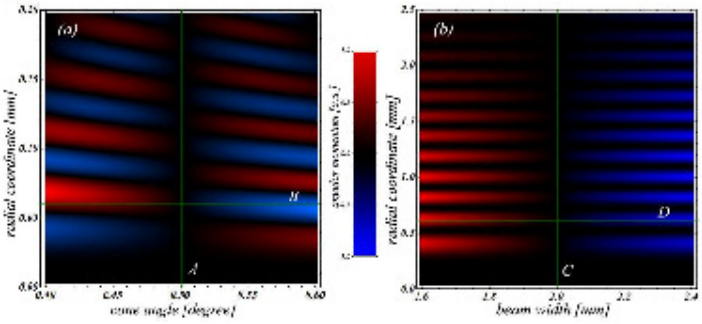

Fig. 4. Calculated change in the local OAM when (a) the cone angle of the two modes differ, and (b) when the weighting of the two modes differ.

Similarly for BGBs, Eq. (14), we calculate the dependence of the OAM density of a superposition of BGBs, where the two components differ in their weighting. In Fig. 4(b) we see the results for the case of a 633 nm laser beam in a superposition of + 5 and –5 BGBs, both having a cone angle of 0.5 °, but with various weightings of the two beams. Clearly even with equal phase velocities ($\Delta k = 0$) the OAM density can be engineered to be non-zero as long as the weighting of the two fields differ: the larger the difference, the greater the OAM density. By considering line D on the graph (varying weighting by varying the input Gaussian beam width), the OAM density changes from a large positive value to a large negative value as one considers a single ring in the field (single radial position), passing through a zero value in between. However for a given weighting of the two fields, as one moves radially across the field, so the OAM density remains either positive or negative (passing through nulls between

#146350 - $15.00 USD Received 21 Apr 2011; revised 2 Jun 2011; accepted 26 Jul 2011; published 15 Aug 2011
(C) 2011 OSA

the rings), but does not oscillate in sign as in the case of Fig. 4(a). The variations in the angular momentum, both in terms of sign and magnitude, results from the variations in the amplitude and cone angles of the superimposed Bessel beams (refer to Fig. 6(a) and (b)). The manipulation of the angular momentum can be implemented efficiently by the method described above and is a useful tool for the controlling of optical forces [33].

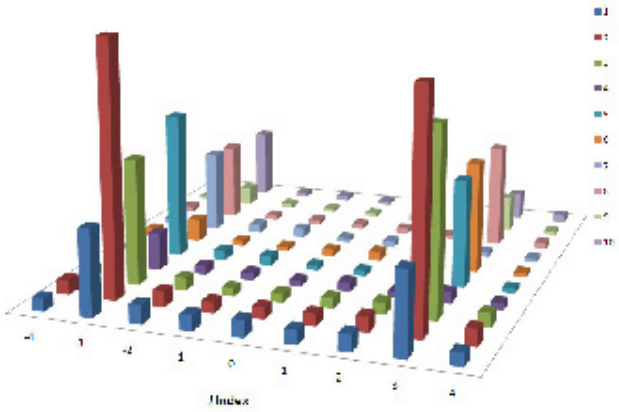

Fig. 5. The measured OAM spectrum (for l values of –4 to + 4) as a function of the radial ring on the beam (equivalent to the radial position on the beam), from 1 to 10, given by: r_1 = 600 μm, r_2 = 880 μm, r_3 = 1160 μm, r_4 = 1440 μm, r_5 = 1720 μm, r_6 = 2000 μm, r_7 = 2280 μm, r_8 = 2560 μm, r_9 = 2840 μm and r_{10} = 3120 μm. The height of each bar represents the measured coefficients $|a_l|^2$.

The predicted OAM density was measured in the laboratory by measuring directly the coefficients given by Eqs. (16) and (17), with the OAM density calculated from Eq. (20). The measured OAM spectrum for the equally weighted superposition beam is shown in Fig. 5

From the spectrum in Fig. 5, the OAM density could be inferred directly and compared to theory, with the results shown in Fig. 6. In Fig. 6 (a) and (b) we see a density plot of the two fields (for + 3 and –3), and the slight shift in rings is evident due to the slightly different radial wave numbers of the two fields. The superposition field is shown in Fig. 6 (c). In all three plots the measured radial positions (r_1 through r_{10}) are overlaid as vertical lines. The core result is Fig. 6 (d), where the analytical OAM density prediction (solid curve) as a function of the radial position on the superposition field is shown with the measured OAM density (red bars). It is very clear that there is excellent quantitative agreement between the two (with the exception of the first measurement radius which appears to have a large error). This agreement can also be noted by considering Fig. 6 (e) and (f), where the theoretical and experimental data are shown for the $|a_3|^2$ and $|a_{-3}|^2$ coefficients as a function of the radial position on the beam.

It should be noted that this is the first direct measurement of the OAM density, or OAM spectrum, to date. The importance of measuring the spectrum has been pointed out by others, where knowledge of the spectrum or local OAM is critical for imaging [34] and optical funnels [35], but the few measurements of the OAM either only consider the global OAM using an optical trapping set-up [36,37], or are unduly complicated by making use of Doppler shifts in due to a rotating detector [16]. In the method proposed here, the same principles (and optical elements) applied in creating the superposition fields can be used to decompose them.

#146350 - $15.00 USD Received 21 Apr 2011; revised 2 Jun 2011; accepted 26 Jul 2011; published 15 Aug 2011
(C) 2011 OSA

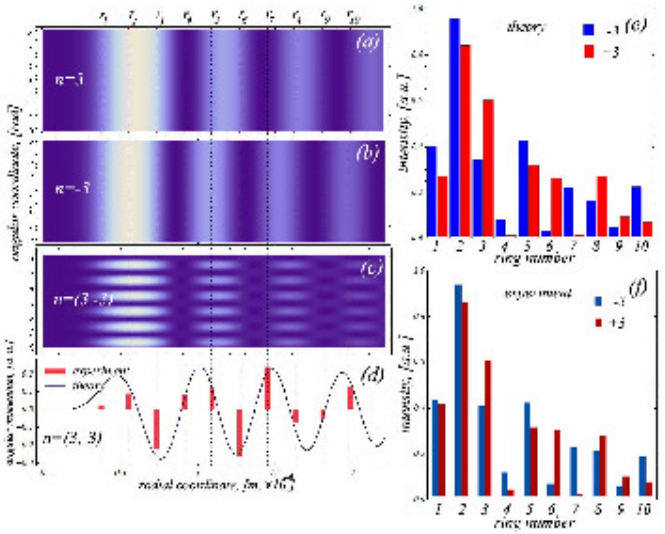

Fig. 6. (a) – (c): Density plots of the three Bessel beams plotted as (r, ϕ) for the + 3 case, the –3 case, and the superposition, respectively; (d) plot of the orbital angular momentum density as a function of radial position on the field – the theory is the solid curve and the experimental data is overlaid as red bars; (e) theoretical prediction of the coefficient $|a_l|^2$ (or the on axis intensity of the inner product) as a function of the radius of the match filter. Rings 1 to 10 denote those given in the first and third rows of Fig. 3; (f) corresponding experimental data.

It is interesting to consider the role of the Gouy phase shift in such measurements, since in general this is a function of the azimuthal order of the field. This is not the case for a superposition of Bessel beams, as reported here, and so may be neglected. However, in the case of Laguerre-Gaussian modes (which are used extensively in quantum information studies) the Gouy phase shift would be identical for fields of opposite handedness, proportional to $2p + |l| + 1$, where p is the radial order. This means that modes of $+l$ and a $-l$ will have the same phase shift, so again it can be considered as a constant phase offset (but dependent on z). However, while the OAM arises from the azimuthal phase variation, the rotation of the Poynting vector is equal to $\arctan(z/z_r)$ when considering the radius of maximum field of $p = 0$, $l \neq 0$ modes (since such modes are a single ring of light), i.e., the rotation looks like the Gouy phase shift of a Gaussian mode. The salient point is that the Poynting vector rotation is proportional to $\arctan(z/z_r)$, and that the maximum rotation is fixed, in the case of a $p = 0$ mode, to $\pi/2$ either side of the beam waist. As the radial order is increased, so the maximum rotation of the field also increases [22,23]. It is however interesting to consider what happens to the OAM density if non-zero radial modes are excited, as will surely be the case for the typical laboratory practices of generating such modes by multiplication of a Gaussian with a purely azimuthal phase function. This case has not yet been treated fully in the literature. The result would, most likely, be a superposition not only in l but also in p, resulting in an OAM spectrum with weighting coefficients different to that of a purely azimuthal superposition, with a larger contribution from the a_0 term in Eq. (16) due to the azimuthal symmetry of the radial orders.

#146350 - $15.00 USD Received 21 Apr 2011; revised 2 Jun 2011; accepted 26 Jul 2011; published 15 Aug 2011
(C) 2011 OSA

5. Conclusion

We have used the Poynting vector approach to study the OAM density within fields that are superpositions of non-diffracting Bessel and Bessel-Gauss beams. We find that while the global OAM is zero, the local OAM spectrum changes radially across the beam, and can be made to oscillate from positive to negative values by a suitable choice of the parameters making up the superposition (e.g., relative phase velocity of the two component beams). The implication is also that in applications such as optical trapping with so-called bottle beams and optical funnels, the rotating intensity distribution may also carry OAM that varies across the beam in a predictable but non-negligible manner. We have demonstrated the theory by creating such superposition beams in the laboratory with a phase-only spatial light modulator, and have implemented a new technique for the direct measurement of the OAM density. Previous studies of such fields either remained purely theoretical, or have attempted to show the OAM component by demonstrating rotation within an optical trapping and tweezing system. Needless to say, the latter is not only an indirect measurement, but also a very difficult experiment to execute. The technique we outline here requires only an SLM and a lens, and is therefore easy to implement in the laboratory (anyone who is able to create the original fields is also now able with the same approach to measure the OAM density). Both the generation of the superposition fields, and the measurement of the OAM spectrum, have direct relevance in quantum studies of OAM entanglement, and classical studies of OAM transfer in optical trapping and tweezing systems.

#146350 - $15.00 USD Received 21 Apr 2011; revised 2 Jun 2011; accepted 26 Jul 2011; published 15 Aug 2011
(C) 2011 OSA

B6: Publication 6

Journal of Modern Optics
2011, 1–9, iFirst

Taylor & Francis

Measuring the rotation rates of superpositions of higher-order Bessel beams

Ronald Rop[a], Angela Dudley[b,c], Carlos López-Mariscal[d] and Andrew Forbes[b,c]*

[a]*Department of Physics, Moi University, P.O. Box 1125, Eldoret 30100, Kenya;* [b]*CSIR National Laser Centre, P.O. Box 395, Pretoria 0001, South Africa;* [c]*School of Physics, University of KwaZulu-Natal, Private Bag X54001, Durban 4000, South Africa;* [d]*US Naval Research Laboratory, 4555 Overlook Ave. SW, Washington, DC 20375, USA*

(*Received 18 August 2011; final version received 15 September 2011*)

Experimental measurements are reported of the rotation rates of superpositions of higher-order Bessel beams. Digitally generated phase masks of two annular rings, were imprinted on a spatial light modulator and used to obtain superpositions of higher-order Bessel beams of the same order but of opposite topological charge. Such a superposition field carries on average zero orbital angular momentum, yet exhibits a rotation in the intensity pattern: the resultant field rotates at a constant rate about the optical axis as it propagates. The rotation rates of the generated fields were measured for different orders and for various values of the difference between the wave-vectors of the superimposing beams, and are shown to be in good agreement with that predicted theoretically.

Keywords: diffraction; holography; grating; rotation; interference; modulation

Downloaded by [CSIR Information Services] at 06:43 01 November 2011

1. Introduction

Bessel beams have received increased attention in recent years owing to their interesting properties (e.g. non-diffracting and self-reconstructing) [1] and potential applications in optical micro-manipulation [2,3]. These beams are a class of propagation-invariant optical beams that are non-singular scalar solutions to the free-space Helmholtz wave equation and are described mathematically by Bessel functions [4,5]. Zero-order Bessel beams have an intensity maximum at the centre while higher-order Bessel beams (HOBBs) have a dark central spot – intensity null – due to a phase singularity at that point, surrounded by alternate bright and dark rings [1]. In addition, HOBBs carry orbital angular momentum (OAM) owing to their azimuthal phase variation. Bessel beams have found a variety of applications, especially in optical trapping. For instance, the ring structure of Bessel beams makes it possible to trap simultaneously both low- and high-index particles [6] while the self-reconstruction property has enabled the simultaneous trapping of particles that are spatially separated [2]. It has also been demonstrated that the OAM and spin angular momentum (SAM) of Bessel beams can be transferred to micro-particles and cold atoms [6–8]. The trapped micro-particles have been shown to rotate, owing to the transferred OAM and SAM, and their rotation rates have been measured [9,10].

Bessel beams, and in general non-diffracting beams (NDBs), can be generated experimentally using refractive or diffractive optical elements. Durnin et al. [5] reported the first experimental realization of a zero-order Bessel beam by illuminating an annular slit placed at the back focal plane of a positive lens. The axicon, also called a conical lens and first constructed and demonstrated by McLeod [11], has been widely used to generate NDBs [12,13] and to convert LGBs into higher-order Bessel beams with high conversion efficiencies of close to 100% [14,15]. Similarly, diffractive axicons implemented with computer-generated holograms (CGHs) [16,17] and axicon-type CGHs programmed on a spatial light modulator (SLM) [18,19] have been used to generate Bessel beams and their superpositions. In [19] it was shown that the intensity of the superposition appeared as a circular pattern with a radius which depended on the order, n, of the Bessel function and that the intensity is azimuthally modulated resulting in $2n$ spots arranged on a circle. Similar intensity patterns were obtained by Vasilyeu et al. [20] by using a SLM and a ring slit aperture. The transverse intensity patterns of the superimposed beams depicted an interesting feature: the pattern rotated about the propagation axis as the beams propagated along the axis [20].

Such rotating optical beams have been theoretically and experimentally realized as superpositions of

*Corresponding author. Email: aforbes1@csir.co.za

ISSN 0950-0340 print/ISSN 1362-3044 online
© 2011 Taylor & Francis
http://dx.doi.org/10.1080/09500340.2011.631714
http://www.tandfonline.com

Downloaded by [CSIR Information Services] at 06:43 01 November 2011

higher-order modes of Bessel beams [20–24], Laguerre–Gauss beams (LGBs) [22,25] and multi-mode hypergeometric beams [22], with the theoretical conditions necessary for the rotation to occur well understood [20,22,23,26,27]. In [21] it was shown that the superposition of HOBBs results in a periodically reconstructing beam with rotating and spiral wave features. Several types of rotating optical beams have been reported. Helicon beams have an intensity pattern which rotates at a constant rate about the optical axis but is otherwise unchanged and consists of superpositions of HOBBs of different orders [23]. Spiralling beams are a special case of Helicon beams and have an intensity pattern that is laterally displaced with respect to the optical axis and rotates as a whole around the axis as the beams propagates along it [21,28–30]. Spiral-type beams have been demonstrated, theoretically [30,31] and experimentally [29], and as modes of a ring resonator with a beam rotator [32] and shown to correspond to the quantum-mechanical ground states of a charged particle in a uniform magnetic field [33]. Optical twisters [34] have both their phase and amplitude describing a helical profile as the beam propagates in free space while optical propellers [35] are optical beams with rotating intensity blades and exhibit self-trapping features. Arlt [36] has also experimentally demonstrated the characteristic rotation of the intensity profile of a partially obstructed optical vortex beam. The intensity cross-section and the geometrical shadow just behind the obstacle rotated in the sense of the beam's handedness.

Despite this extensive body of work on rotating optical fields, a comprehensive experimental study of the observed rotation rates has not yet been done; indeed, no study to date has systematically varied the rotation rate of the beam through control of the parameters predicted by theory. The limited experimental work that does exist has considered only one rotating field, with no parameter control, simply due to the rather complicated manner of generating the rotating beams: fabricated diffractive optical elements with overlapping diffraction orders [23,26]. Such an implementation method makes a full study time consuming and expensive, since each experiment requires a new mask to be fabricated. In this paper we report on the first quantitative, experimental study of the rotation rates of superpositions of HOBBs with rotating intensity profiles. We implement a method that uses a phase-only SLM to modulate the complex amplitude of light to generate rotating Bessel beams by means of digitally generated annular slits. The method has enabled us to measure, quantitatively, the rotation rates of the resultant intensity profiles for any combination of orders and radial wave-vectors – the two parameters predicted by theory to affect the rate of rotation. We show that by digitally varying the dimensions of the ring-slits programmed on the SLM and the order of the superimposing HOBBs, it is possible to control the rotation rates of the intensity profile, thus making such rotating fields an ideal tool for controlled rotation of trapped particles.

2. Theory

The theory of Bessel beams, as scalar and vector fields, has been studied and reported by many investigators since the seminal work of Durnin et al. [4,5]. They showed that Bessel fields are free-space, beam-like, exact solutions of the scalar wave equation that do not experience transverse spreading; although they have finite energy density, they have infinite energy. Chavez-Cerda et al. [21] used a more general formulation to describe these beams by employing linear combinations of Neumann and Bessel functions based on travelling wave solutions of the non paraxial wave equation. They showed that HOBBs, described by higher-order Hankel waves, have a functional dependence on the azimuth coordinate and hence carry OAM. Tervo and Turunen [37] extended the concept of rotating scalar optical fields (Bessel fields in particular) to the case of electromagnetic fields with propagation-invariant states of polarisation and showed that the conditions for rotation are different for scalar and electromagnetic fields. Yu and Dou [38] analysed in detail the vectorial properties of Bessel fields using Hertz potentials, while Hacyan and Jauregui [39] have made a relativistic study of Bessel fields using the same potentials. For a linearly polarised electromagnetic field, a scalar treatment is adequate under certain conditions [40] but detailed electromagnetic behaviour of Bessel fields can only be determined using the vectorial wave equation [41]. In this section we wish to consider the resultant intensity of the coherent superposition of HOBBs. We start by reviewing, for the benefit of the reader, key concepts of the scalar theory of Bessel fields since this is adequate to capture the key aspects of our study.

An ideal Bessel beam is described mathematically by the transverse component of the electric field, in cylindrical coordinates, as

$$E(r,\theta,z) = E_0 J_m(k_r r)\exp[i(k_z z + m\theta)], \qquad (1)$$

where J_m is the mth order Bessel function of the first kind and $k_r = k\sin\alpha$ and $k_z = k\cos\alpha$ are the radial and longitudinal wavenumbers, respectively, k is the magnitude of the wave-vector, and α is the semi-angle of the cone formed by the wave-vectors in frequency space. The angular spectrum of the beam lies on a single ring (thus a single radial wave-vector), the

Downloaded by [CSIR Information Services] at 06:43 01 November 2011

transmission function of which defines the phase of the field: it is understood that the phase within the angular spectrum may be treated as a degree of freedom in creating non-diffracting light fields of arbitrary shapes [42]. Zero-order Bessel beams ($m=0$) are created by encoding a constant phase value within the ring, while HOBBs, $|m|\geq 1$, require an azimuthal phase dependence within the ring and hence have a non-diffracting dark core due to the resulting phase singularity at the origin, its topological charge is given by m. The size (radius) of the dark central spot increases with the order m of the Bessel beam.

The phase of a HOBB varies continuously from 0 to 2π a total of m times in one azimuthal revolution. It is this continuous, periodic variation of the transverse phase with the azimuthal coordinate that makes it possible to generate a rotating Bessel field with propagation-invariant features [43].

2.1. *Superpositions of higher-order Bessel beams*

Bessel beams can be considered as a set of plane waves propagating on a cone, such that each plane wave undergoes the same phase shift $k_z\Delta z$ over a given propagating distance Δz [2]. The angular spectrum of a Bessel field is a ring in k-space and hence a Fourier transform of the ring results in a Bessel beam in configuration space. This is the basis of the first experimental generation of Bessel beams by Durnin et al. [5]. The half-angle α of the cone described by the plane waves is $\alpha=\tan^{-1}(k_r/k_z)$ [2] where k_r and k_z are as defined earlier. The superposition of two Bessel fields can therefore be considered as the interference of two sets of waves, with each traversing a cone of half-angle whose magnitude is determined by the radial and longitudinal wave-vectors of the propagating waves. Figure 1 shows the digitally generated annular rings used to superimpose the Bessel fields and the geometrical illustration of the interaction of the two interfering Bessel beams.

Consider the superposition of two HOBBs of orders equal in magnitude but of opposite topological charge, that is, of orders m and $-m$, respectively. If the two beams propagate with slightly differing wave-vectors, the resultant field may be expressed as

$$E_{m,-m}(r,\theta,z)=J_m(k_{1r}r)\exp[i(k_{1z}z+m\theta)] + J_{-m}(k_{2r}r)\exp[i(k_{2z}z-m\theta)], \quad (2)$$

where k_{1r}, k_{2r} and k_{1z}, k_{2z} are, respectively, the radial and longitudinal wave-vectors of the two beams. The intensity of the superposition is obtained directly from Equation (2) as

$$I_{m,-m}\propto J_m^2(k_{1r}r)+J_{-m}^2(k_{2r}r) + 2J_m(k_{1r}r)J_{-m}(k_{2r}r)\cos(\Delta kz-2m\theta), \quad (3)$$

where

$$\Delta k=k_{2z}-k_{1z}=\frac{2\pi}{\lambda}\left|\cos\left(\frac{r_2}{f}\right)-\cos\left(\frac{r_1}{f}\right)\right|, \quad (4)$$

in which r_1 and r_2 are the radii of the inner and outer annular rings, respectively.

One can simplify Equation (3) by approximating $k_{1r}\sim k_{2r}$ and hence $J_m(k_{1r}r)\sim J_m(k_{2r}r)=J_m(k_rr)$ and applying the Bessel function identity $J_{-m}(k_{2r}r)=(-1)^m J_m(k_{2r}r)$, the intensity of the superposition $I_{m,-m}$ is proportional to

$$J_m^2(k_rr)[1+\cos(\Delta kz-2m\theta)], \quad (5)$$

where k_r is the average radial wave-vector of the two fields. If the longitudinal wave-vectors of the superimposing beams are equal, $\Delta k=0$ and hence

$$I_{m,-m}\propto 2J_m^2(k_rr)\cos^2(m\theta). \quad (6)$$

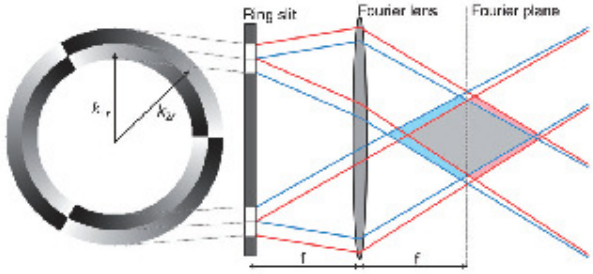

Figure 1. Geometrical illustration of the interaction of two superimposed HOBBs. The grey region depicts where the superposition field exists. The red and blue rays denote the rays from the outer and inner rings, respectively. (The color version of this figure is included in the online version of the journal.)

Downloaded by [CSIR Information Services] at 06:43 01 November 2011

This approximation allows one to more readily note, from Equation (6), that the intensity of the superposition field is modulated in the azimuthal coordinate by the function $\cos^2(m\theta)$. From the properties of the cosine function, we note that the number of intensity maxima is twice the order m of the beams. Thus, the superposition of an mth order Bessel beam with its mirror image ($-m$th order Bessel beam) produces a resultant intensity pattern having $2|m|$ lobes, or 'petals', arranged on the circumference of the set of rings defined by the enveloping Bessel function (radial only).

The intensity profile of the resultant field rotates about the azimuthal coordinate as the beam propagates along the z direction. To see how the rotation arises, consider Equation (5): the term in square brackets determines the angular position of the resultant lobes along the circumference of the circle. Since for any two superimposed beams Δk and order m are constants, the azimuthal coordinate which gives the angular position of the petals changes with the propagation distance of the beam and hence the entire intensity profile rotates about the common centroid, the centre of the dark core. The angle of rotation has been predicted [20,22] to be given by $\theta = \Delta k z/2m$, and the rate of rotation of the intensity profile given by $d\theta/dz = \Delta k/2m$ is constant. The rotation rate, in radians per meter, varies linearly with the difference between the longitudinal wave-vectors of the superimposing beams but inversely with the order $|m|$ of the beams. Thus, by appropriately measuring the angle of rotation of the intensity pattern at various propagation distances, it is possible to determine the rotation rate of the intensity profile and to investigate the effect of changing the values of Δk and order m on the rotation rate. We outline later (see Section 3) a method by which to execute such a study and hence verifying the theory.

2.2. Generation of rotating Bessel beams

Rotating Bessel beams can be realized by superimposing two HOBBs of the same or different orders, or by interfering a HOBB with a reference wavefront (e.g. a plane or a spherical wave). Rotating Bessel beams have been experimentally generated using diffractive optical elements such as an axicon with a phase hologram [23,28,29] or using an annular ring and a phase hologram programmed on an SLM [20]. A Mach–Zehnder type interferometer in which the HOBB is split into two beams has also been applied [43]. The handedness of the beam in one arm of the interferometer is then inverted before recombining it with the other beam to form a superposition of HOBBs. Spiral-type beams have been generated as modes of a ring resonator with a beam rotator [32].

Although the efficiencies of some of these methods are relatively high, the ability to dynamically control the parameters, such as the phase velocity and order of the superimposing HOBBs, which affect the properties of the resultant beam, is limited. This limitation can be overcome by using an SLM onto which digitally generated annular rings are encoded, each ring of equal width but differing radial wave-vectors (see Figure 1). The field emanating from each annular ring propagates with a particular phase velocity determined by the radial wave-vector of the field, which can be controlled by simply altering the average radius of the ring (k_{1r} and k_{2r} in Figure 1). Appropriate modulation of the phase within each ring, thus defining the angular spectrum of the resulting fields, allows one to generate superpositions of two HOBBs. The number of 'petals', the radius of the circular array and rate of rotation of the resultant intensity profile can easily be varied by changing the defining parameters of the phase mask programmed onto the SLM. Figure 1 shows the geometrical evolution of the superposition of the two HOBBs: each field generates its own propagation invariance region (where the conical waves overlap) while the superposition of the HOBBs occurs in the region of overlap between the two propagation invariant regions.

3. Experimental methodology and results

The experimental setup is depicted in Figure 2. A linearly polarised He–Ne laser beam ($\lambda = 632.8$ nm and beam radius of about 0.5 mm) was expanded through a $6\times$ telescope and directed onto the liquid crystal display (LCD) of a SLM (HoloEye, PLUTO-VIS,

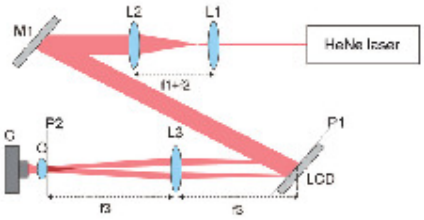

Figure 2. The experimental design for generating rotating petal modes. (L: lens (f1 = 25 mm; f2 = 150 mm; f3 = 200 mm); M1: mirror; LCD: liquid crystal display; O: objective; C: CCD camera; P1: plane of the ring-slit; P2: plane of the Bessel field). The darker red denotes the region in which the Bessel field exists. (The color version of this figure is included in the online version of the journal.)

Downloaded by [CSIR Information Services] at 06:43 01 November 2011

with 1920 × 1080 pixels (each pixel being of width 8 μm) over an active sensor area of approximately 15 × 9 mm^2, with a fill factor of ~90%, and calibrated for a 2π phase shift at 632.8 nm). In a past experiment [20] a physical ring-slit was illuminated by the expanded beam and relay imaged onto the plane of the LCD where the azimuthal phase variation was imparted to the ring field. In this setup we have implemented a technique which allowed us to remove the physical ring-slit from the setup and instead make use of our phase-only SLM to represent the ring-slit. The technique involves addressing alternating sets of pixels on the LCD with phase values that are out of phase by π, resulting in the light reflected from the LCD being scattered from its initial propagation axis [44]. This enabled us to create digital holograms that mimic pure amplitude functions, which we used to encode annular ring transmission functions of full widths 56 μm, 108 μm, 180 μm, 220 μm, 264 μm and 344 μm for each of the experiments, respectively. Each annular ring 'amplitude' transmission function was sub-divided into two ring slits of equal width, with each encoded with an azimuthal 'phase' transmission function, of opposite handedness, from azimuthal order $m=1$ to $m=6$. This approach allowed us to operate our phase-only SLM in both amplitude and phase mode, permitting the reproduction of Durnin's ring-slit [5] but with control over the phase within the annular rings.

Examples of phase patterns addressed to the SLM are given in the top row of Figure 3. Not shown in Figure 3 is a blazed grating of 13 pixels per period, added to the phase patterns to separate the non-diffracted and diffracted components reflected from the SLM (the diffraction efficiency of our SLM is more than 80%). The Fourier transform field, at the focal plane after L3, was magnified with a 10× objective and captured on a CCD camera (Spiricon, LBA-FW-SCOR-7350115). The objective and camera were positioned on translation stages on an optical rail in order to investigate the propagation of the resulting field.

In the phase patterns (top row, Figure 3) the ring-slit is separated into two annular rings each possessing an azimuthal phase of equal order but opposite handedness. The resulting fields for various values of order $|m|$, observed in the Fourier plane, as intensity patterns, are depicted in the middle row of Figure 3. The images were approximately 0.2 mm × 0.2 mm in the Bessel zone. When the orders, $|m|$, of the two azimuthal phases were equal but of opposite handedness, a 'petal' structure was produced, where the number of 'petals' is denoted by $2|m|$. The agreement between experiment (Figures 3(*g*)–(*l*)) and theory (Figures 3(*m*)–(*r*)) is excellent, demonstrating that this simple method is highly accurate for such experiments.

Images of the intensity profiles of these non-diffracting fields were captured at discrete distances, measured from the Fourier lens, along the propagation axis (an example is given in Figure 4) and the angular position of a selected 'petal' was calculated for each frame. The angular position for a particular 'petal' was plotted as a function of the propagation distance of the field (see Figure 5), and the rotation rate of the field was determined from the slope of the straight line which best fits the measured data. Using the example

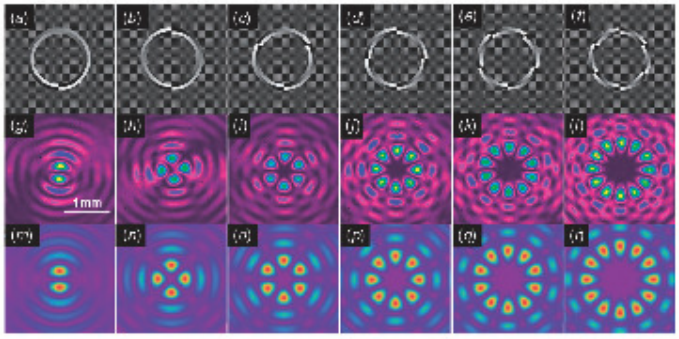

Figure 3. The top row represents the phase patterns applied to the LCD of the SLM for the following values of $|m|$: (*a*) 1, (*b*) 2, (*c*) 3, (*d*) 4, (*e*) 5 and (*f*) 6. The corresponding experimentally observed intensity profiles, for the fields in the Fourier plane, are shown in the middle row and the theoretical predictions in the bottom row. (The color version of this figure is included in the online version of the journal.)

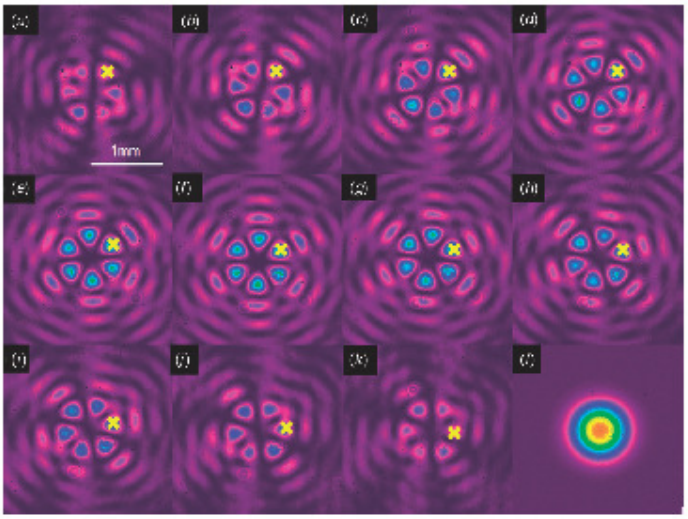

Figure 4. (*a*)–(*k*) Images of the intensity profiles of the experimentally produced field, for $|m|=3$, captured at intervals of 10 mm along the propagation axis. The yellow 'X' denotes a selected 'petal'. Monitoring the change in position of this petal illustrates a rotation in the field as it propagates. (*l*) The initial Gaussian beam which illuminated the SLM. (The color version of this figure is included in the online version of the journal.)

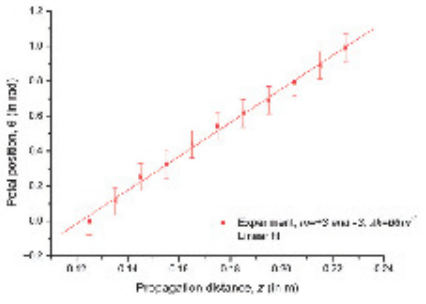

Figure 5. Graph of the angular position of a 'petal', for the field where $|m|=3$ and $\Delta k=66\,\mathrm{m}^{-1}$, as a function of the propagation distance z. (The color version of this figure is included in the online version of the journal.)

in Figure 5, the slope of the linear fit was calculated to be 9.6 rad/m, within 13% of the theoretically calculated result of 11.1 rad/m. The error between the experimentally measured and theoretically calculated rotation rates is attributed to the technique we implemented to calculate the angular position of the 'petal'. The coordinate for the centroid of the petal was obtained by manually selecting the pixel at which the peak value of the 'petal' intensity occurs. In order to determine the standard deviation in the angular position, we assumed that the manually selected coordinate lies within a one-sixth range of the petal's diameter from the true centroid,

$$\theta_\sigma = \arctan\left(\frac{\sigma}{R}\right) = \arctan\left(\frac{D}{18R}\right), \qquad (7)$$

where D is the diameter of the 'petal' and R is the distance from the centre of the field to the centroid of the petal. Since the standard deviation in the 'petal' position is scaled as a function of R and it is evident from Figure 3 that R increases with the order, $|m|$, so the standard deviation also scales as a function of the order, $|m|$. For the example plotted in Figure 5, the standard deviation in the abscissa is 80 mrad. The smallest increment on the optical rail on which the detection system was mounted, and which is equal to the absolute error in the abscissa, was 1 mm. Figure 5 shows the measurement result for the angular position as a function of the propagation distance for the case where the order of the azimuthal phase variation was $|m|=3$ and the difference between the

Downloaded by [CSIR Information Services] at 06:43 01 November 2011

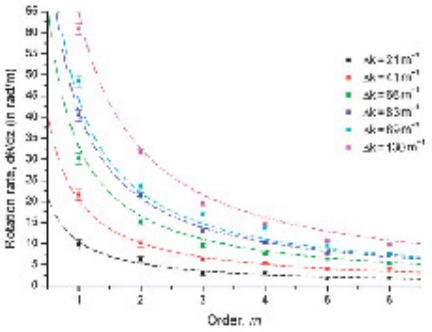

Figure 6. Graphs of the rotation rates, for fields generated for various differences between the longitudinal wave-vectors of the two beams, as a function of the order, $|m|$, of the beams. (The color version of this figure is included in the online version of the journal.)

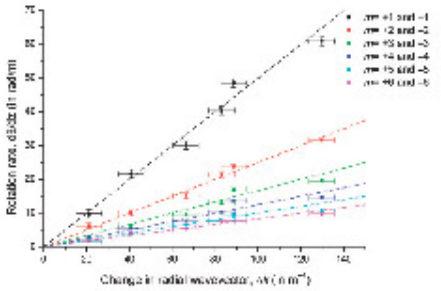

Figure 7. Graphs of the rotation rates for beams of various orders $|m|$ as a function of the difference Δk between the two longitudinal wave-vectors. (The color version of this figure is included in the online version of the journal.)

two wave-vectors was $\Delta k \sim 66\,\mathrm{m}^{-1}$, calculated using Equation (4).

Note in Figure 4 that, as expected, the petal structure appears at the beginning of the propagation invariance region with low intensity, reaches a maximum mid-way through this region, and then decreases again as the conical waves separate out again back to an annular ring structure. However, while the scale of the pattern is invariant, the intensity rotates about the propagation axis. This angular shift as a function of propagation distance can be deduced for the petal structure, with an example of the Figure 4 data shown in Figure 5.

Similar graphs were obtained for various values of $|m|$ and Δk and the corresponding experimental rotation rates were deduced from the slopes of their linear fits (not shown here due to space restrictions). Figures 6 and 7 show the plots of these experimental rotation rates as a function of the order of the azimuthal phase variation, $|m|$, and the difference between the two wave-vectors, Δk, respectively. Overlaid with the experimental data are the theoretical predictions, shown with dashed lines. By increasing the magnitude of $|m|$, there is a hyperbolic decrease in the rotation rate, evident in Figure 6, where measured rotation rates, for six different values of Δk, are plotted as a function of the order $|m|$ of the superimposing beams.

The measured data was also interpreted by plotting the rotation rate as a function of the difference between the two longitudinal wave-vectors as depicted in Figure 7. Increasing the difference between the two wave-vectors, which was achieved by increasing the width of the inner and outer annular rings, increased the rotation rate of the 'petal' structure. Figures 6 and 7 both show good agreement between the measured data (solid points) and the theoretical predictions (dashed curves).

The standard deviation in the rotation rate was determined by the standard deviation in the slope of the graph of the 'petal' position, θ, as a function of the propagation distance, z, by making use of the following relationship;

$$\theta = \text{slope} \times z \rightarrow \text{slope}_\sigma = \frac{\theta_\sigma - nz_\sigma}{z} = \frac{\theta_\sigma}{z}. \quad (8)$$

θ_σ is the standard deviation in the angular position of the petal determined by Equation (6) and z is the median of the propagation intervals at which the field is captured. The standard deviation for the rotation rate, for the case when $|m|=3$, was found to be ~0.5 rad/m. The radius of each ring-slit could be accurately measured to within a single pixel. Taking this absolute error for the radii of the two ring-slits into accounts, the absolute error for the difference between the two wave-vectors (the abscissa of Figure 7) was $\sim 6\,\mathrm{m}^{-1}$. For all the results shown thus far, the azimuthal phase within the outer ring-slit varied from black to white in a clockwise direction and that in the inner ring-slit in an anticlockwise direction. Inverting the handedness of the two ring-slits resulted in the field rotating with the same rate, but in the opposite direction. This is observed in the video slides in Figure 8.

4. Conclusion

We have demonstrated an experimental technique to produce rotating superpositions of Bessel beams using digital implementations of their respective angular

Downloaded by [CSIR Information Services] at 06:43 01 November 2011

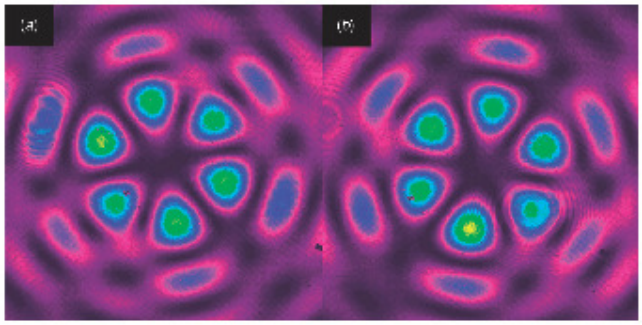

Figure 8. Video clips containing experimental images, captured at intervals along the beam's propagation, for fields generated from phase patterns having the following parameters: $\Delta k = 66\,\mathrm{m}^{-1}$ and (*a*) $m_1 = +3$; $m_2 = -3$ (Video 1) and (*b*) $m_1 = -3$; $m_2 = +3$ (Video 2). (Videos are available in the online version of this journal.) (The color version of this figure is included in the online version of the journal.)

Downloaded by [CSIR Information Services] at 06:43 01 November 2011

spectra on a SLM. We have quantified several physical observables such as the angular displacement of the transverse intensity patterns as a function of the beam propagation distance, beam rotation rates as a function of azimuthal orders for beams with different spatial bandwidths and the dependency of rotation rate with spectral content for superpositions with different azimuthal indexes, all found to be in excellent agreement with theoretical predictions. We have shown that by varying the extent of the annular shaped spectra and the order of the beams imprinted on the SLM, arbitrarily fine control over the rotation rates of the intensity profile can be achieved, thus making these rotating fields an ideal tool for controlled rotation of trapped particles in optical trapping experiments. Finally, it should be noted that overall optical efficiency was not a consideration in this study; however, by illuminating the digital holograms with an annular field from a conical telescope (two inward facing axicons, suitably separated), the efficiency of the system can be made close to the efficiency of the SLM used.

Acknowledgements

We gratefully acknowledge the funding support by the African Laser Centre (Grant LHEAB01) and discussions held with Dr George Amolo and Dr Nicholas Makau of the Department of Physics, Moi University, Kenya.

References

[1] McGloin, D.; Dholakia, K. *Contemp. Phys.* **2005**, *46*, 15–28.
[2] McGloin, D.; Garcés-Chávez, V.; Dholakia, K. *Opt. Express* **2003**, *28*, 657–659.
[3] Arlt, J.; Garces-Chavez, V.; Sibbett, W.; Dholakia, K. *Opt. Commun.* **2001**, *197*, 239–245.
[4] Durnin, J. *J. Opt. Soc. Am. A* **1987**, *4*, 651–654.
[5] Durnin, J.; Miceli Jr, J.J.; Eberly, J.H. *Phys. Rev. Lett.* **1987**, *58*, 1499–1501.
[6] Garces-Chavez, V.; Volke-Sepulveda, K.; Chavez-Cerda, S.; Sibbett, W.; Dholakia, K. *Phys. Rev. A* **2002**, *66*, 063402.
[7] He, H.; Friese, M.E.J.; Heckenberg, N.R.; Rubinsztein-Dunlop, H. *Phys. Rev. Lett.* **1995**, *75*, 826–829.
[8] Tabosa, J.W.R.; Petrov, D.V. *Phys. Rev. Lett.* **1999**, *83*, 4967–4970.
[9] Garces-Chavez, V.; McGloin, D.; Padgett, M.J.; Dultz, W.; Schmitzer, H.; Dholakia, K. *Phys. Rev. Lett.* **2003**, *91*, 1–4.
[10] Volke-Sepulveda, V.; Chavez-Cerda, S.; Garces-Chavez, V.; Dholakia, K. *J. Opt. Soc. Am. B* **2004**, *21*, 1749–1757.
[11] McLeod, J.H. *J. Opt. Soc. Am.* **1954**, *44*, 592–597.
[12] Scott, G.; McArdle, N. *Opt. Eng.* **1992**, *31*, 2640–2643.
[13] Herman, R.M.; Wiggins, T.A. *J. Opt. Soc. Am. A* **1991**, *8*, 932–942.
[14] Arlt, J.; Dholakia, K. *Opt. Commun.* **2000**, *177*, 297–301.
[15] Topuzoski, S; Janicijevic, L. *Opt. Commun.* **2009**, *282*, 3426–3432.
[16] Vasara, A.; Turunen, J.; Friberg, A.T. *J. Opt. Soc. Am. A* **1989**, *6*, 1748–1754.
[17] Paterson, C.; Smith, R. *Opt. Commun.* **1996**, *124*, 121–130.
[18] Davis, J.A.; Guertin, J.; Cottrell, D.M. *Appl. Opt.* **1993**, *32*, 6368–6370.
[19] Davis, J.A.; Carcole, E.; Cottrell, D.M. *Appl. Opt.* **1996**, *35*, 599–602.
[20] Vasilyeu, R.; Dudley, A.; Khilo, N.; Forbes, A. *Opt. Express* **2009**, *17*, 23389–23395.

[21] Chavez-Cerda, S.; McDonald, G.S.; New, G.H.C. *Opt. Commun.* **1996,** *123,* 225–233.
[22] Kotlyar, V.V.; Khonina, S.N.; Skidanov, R.V.; Soifer, V.A. *Opt. Commun.* **2007,** *274,* 8–14.
[23] Paterson, C.; Smith, R. *Opt. Commun.* **1996,** *124,* 131–140.
[24] Pääkkönen, P.; Lautanen, L.; Honkanen, M.; Kuittinen, M.; Turunen, J.; Khonina, S.N.; Kotlyar, V.V.; Soifer, V.A.; Friberg, A.T. *J. Mod. Opt.* **1998,** *45,* 2355–2369.
[25] Khonina, S.N.; Kotlyar, V.V.; Soifer, V.A.; Honkanen, M.; Lautanen, L.; Turunen, J. *J. Mod. Opt.* **1999,** *46,* 227–238.
[26] Schechner, Y.Y.; Piestun, R.; Shamir, J. *Phys. Rev. E* **1996,** *54,* 50–53.
[27] Abramochkin, E.; Volostnikov, V. *Opt. Commun.* **1993,** *102,* 336–350.
[28] Sun, Q.; Zhou, K.; Fang, G.; Liu, Z.; Liu, S. *Appl. Phys. B: Lasers Opt.* **2011,** *11,* 215–221.
[29] Matijosius, A.; Jarutis, V.; Piskarskas, A. *Opt. Express* **2010,** *18,* 8767–8771.
[30] Jarutis, V.; Matijošius, A.; Di Trapani, P.; Piskarskas, A. *Opt. Lett.* **2009,** *34,* 2129–2131.
[31] Alieva, A.; Abramochkin, E.; Asenjo-Garcia, A.; Razueva, E. *Opt. Express* **2010,** *18,* 3568–3573.
[32] Abramochkin, E.; Losevsky, N.; Volostnikov, V. *Opt. Commun.* **1997,** *141,* 59–64.
[33] Abramochkin, E.; Volostnikov, V. *Opt. Commun.* **1995,** *125,* 302–323.
[34] Daria, V.R.; Palima, D.Z.; Glückstad, J. *Opt. Express* **2011,** *19,* 476–481.
[35] Zhang, P.; Huang, S.; Hu, Y.; Hernandez, D.; Chen, Z. *Opt. Lett.* **2010,** *35,* 3129–3131.
[36] Arlt, J. *J. Mod. Opt.* **2003,** *50,* 1573–1580.
[37] Tervo, J.; Turunen, J. *Opt. Express* **2001,** *9,* 9–15.
[38] Yu, Y.Z.; Dou, W.B. *Prog. Electromagn. Res. Lett.* **2008,** *5,* 57–71.
[39] Hacyan, S.; Jauregui, R. *J. Phys. B: At., Mol. Opt. Phys.* **2006,** *39,* 1669–1676.
[40] Lax, M.; Louisell, W.H.; McKnight, W.B. *Phys. Rev. A* **1975,** *11,* 1365–1370.
[41] Volke-Sepulveda, K.; Garces-Chavez, V.; Chavez-Cerda, S.; Arlt, J.; Dholakia, K. *J. Opt. B: Quantum Semicl. Opt.* **2002,** *4,* S82–S89.
[42] López-Mariscal, C.; Helmerson, K. *Opt. Lett.* **2010,** *35,* 1215–1217.
[43] López-Mariscal, C.; Gutiérrez-Vega, J.C.; Chávez-Cerda, S. *Appl. Opt.* **2004,** *43,* 5060–5063.
[44] Wong, D.W.K.; Chen, G. *Appl. Opt.* **2008,** *47,* 602–610.

Downloaded by [CSIR Information Services] at 06:43 01 November 2011

B7: Publication 7

Quantitative measurement of the orbital angular momentum density of light

Angela Dudley,[1,2] Igor A. Litvin,[1] and Andrew Forbes[1,2,*]

[1]Council for Scientific and Industrial Research National Laser Centre, P.O. Box 395, Pretoria 0001, South Africa

[2]School of Physics, University of KwaZulu-Natal, Private Bag X54001, Durban 4000, South Africa

*Corresponding author: aforbes1@csir.co.za

Received 23 September 2011; accepted 15 November 2011;
posted 18 November 2011 (Doc. ID 155256); published 23 February 2012

In this work we derive expressions for the orbital angular momentum (OAM) density of light, for both symmetric and nonsymmetric optical fields, that allow a direct comparison between theory and experiment. We present a simple method for measuring the OAM density in optical fields and test the approach on superimposed nondiffracting higher-order Bessel beams. The measurement technique makes use of a single spatial light modulator and a Fourier transforming lens to measure the OAM spectrum of the optical field. Quantitative values for the OAM density as a function of the radial position in the optical field are obtained for both symmetric and nonsymmetric superpositions, illustrating good agreement with the theoretical prediction. © 2012 Optical Society of America

OCIS codes: 090.1995, 120.4570, 070.6120, 070.3185, 050.4865.

1. Introduction

Since the discovery of optical fields carrying orbital angular momentum (OAM) [1], many new avenues in the field of classical and quantum optics have been initiated, ranging from the transfer of OAM to particles in optical tweezers [2] to the entanglement of OAM in parametric downconversion [3]. Fields that carry OAM of $l\hbar$ per photon, some of which include Laguerre–Gaussian beams [4], Bessel–Gaussian beams [5], and Airy beams [6], have an azimuthal angular dependence of $\exp(il\phi)$ [1,4], where l is the unbounded azimuthal mode index and ϕ is the azimuthal angle. Since these fields possessing OAM offer an unbounded state space, they provide a larger bandwidth for quantum cryptography [7–9], leading to many publications being dedicated to the measurement of OAM in order for higher-dimensional quantum information processing to be a success.

Many techniques exist in the area of measuring OAM, from computer generated holograms [3,10–12] to interferometers [13–15]. Even though the aforementioned techniques are efficient at sorting modes (and even in some cases single photons) carrying OAM, they do not allow one to obtain a quantitative measurement for the OAM density and instead only measure the global OAM—the average value across the entire field. In the last year, more techniques that measure the global OAM have appeared, from demultiplexing free-space OAM-carrying beams [16] to studying the diffraction patterns of helical beams [17]. Many publications demonstrate the transfer of local OAM to trapped particles [18–20] by illustrating that the rotation rates of a particle trapped at different radial positions in a multiringed beam are proportional to r^{-3} [18], or by illustrating that particles trapped at different radial positions in an optical field (produced by interfering two vortex beams with unequal charges) rotate in opposite directions [20]. The only attempts, to the best of our knowledge, to make quantitative measurements of the OAM carried in an optical field have been made by merely measuring these rotation rates [21,22]. Measuring OAM by demonstrating rotation within an optical tweezing system is not only

1559-128X/12/070823-11$15.00/0
© 2012 Optical Society of America

an indirect measurement but also a difficult experiment to conduct. The results of these findings only illustrate that the rotation rates reveal that the transferred angular momentum increases linearly with laser power [21] and that the rotation rates of low-index particles, which locate themselves in the dark regions of optical fields, are not impeded by beam imperfections [22]. Another, even more complicated, technique makes use of Doppler shifts due to a rotating detector [23,24], which allows for the reconstruction of the OAM spectrum of an optical field and has been tested with Laguerre–Gaussian modes of different azimuthal orders [23].

In this paper we present a technique for a simple and direct measurement of the OAM density that requires only a spatial light modulator (SLM) and a lens. Having a tool to perform a quantitative measurement of the OAM density will prove useful not only in quantum information but also in determining the loss in angular momentum as optical vortices breakup during nonlinear propagation [25]. We formulate the theoretical equation for the OAM density for both symmetric and nonsymmetric fields and use the Fresnel diffraction integral to formulate an experimental form for the OAM density, allowing for the first time (to our knowledge) a quantitative measurement of the OAM density of the field. We implement this simple experimental technique to obtain quantitative measurements for the OAM density for both symmetric and nonsymmetric superpositions of nondiffracting higher-order Bessel beams.

2. Concept of the OAM Density Measurement

In this section we investigate how the OAM density of an optical field can be measured. An illustration that will aid the theoretical description, as well as the experimental measurement, of the OAM density is given in Fig. 1(a). Figure 1(a), which denotes a schematic of the experimental setup for the OAM density measurement, is separated into two parts: (1) the generation of the optical field and (2) the measurement of the OAM density, which is achieved by performing a modal decomposition of the optical field.

A. Symmetric Superposition of Two Bessel Beams

In this paper, we use Bessel beams as a basis set for OAM-carrying fields and classify the superpositions of nondiffracting higher-order Bessel beams into symmetric and nonsymmetric. In our derivation of both the theoretical and experimental OAM densities, we will start with the symmetric case and later develop the argument for the nonsymmetric case. Consider the amplitude for a symmetric superposition of two Bessel beams, of opposite azimuthal order, as given by

$$u(r,\theta,z) = A_0(J_l(q_1 r)\exp(i\Delta kz)\exp(il\theta) + a_0 J_{-l}(q_2 r)\exp(-i\Delta kz)\exp(-il\theta)), \quad (1)$$

where J_l and J_{-l} denote the Bessel functions of order l and $-l$, respectively, q_1 and q_2 denote the radial wavenumbers of the two fields, and Δk denotes the difference between the longitudinal wavenumbers. We start with this special case, as the theoretical OAM density is already known [26].

To experimentally create such a field, Durnin's ring slit [27] method is used; however the ring slit is encoded digitally [28] onto an SLM. By dividing the ring slit into two ring slits and encoding the azimuthal phase within the ring slits to vary azimuthally in opposite directions, a superposition of two oppositely handed Bessel beams can be generated. For the example given in Fig. 1(c), the phase within the inner ring slit varies three times in a clockwise

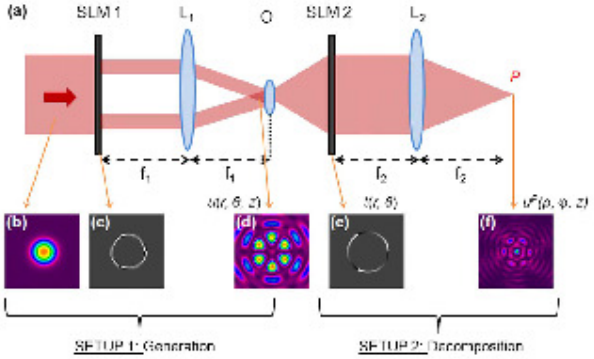

Fig. 1. (Color online) (a) Schematic of the concept for generating the optical field and decomposing its OAM spectrum. (b) The Gaussian beam used to illuminate (c) the digital ring slit hologram for the construction of (d) the optical field, mathematically defined by $u(r,\theta,z)$. (e) The hologram, having a transmission function of $t(r,\theta)$, together with the lens L_2, performs the decomposition, which produces (f) the inner product at plane P, mathematically defined by $u^P(0,\phi,z)$. SLM, spatial light modulator; O, objective—used to magnify the optical field (d).

direction ($l = 3$), and three times in a counterclockwise direction ($l = -3$) in the outer ring slit, thus transforming the initial Gaussian beam [Fig. 1(b)] into a superposition of two Bessel beams, of orders $l = 3$ and -3, denoted by the "petal" structure [Fig. 1(d)].

The widths of the two ring slits can be adjusted, consequently increasing or decreasing the energy present in the two Bessel beams. The energy contained within the first Bessel beam, J_l, is denoted by A_0 in Eq. (1), and the energy contained within the second Bessel beam, J_{-l}, is denoted by $a_0 A_0$, with the constants determined as

$$A_0 = \sqrt{\int_{ring1} \exp(-2(r/\omega)^2) r dr}, \tag{2}$$

$$a_0 = \sqrt{\int_{ring2} \exp(-2(r/\omega)^2) r dr \Big/ \int_{ring1} \exp(-2(r/\omega)^2) r dr}, \tag{3}$$

where ring1 and ring2 denote the bounds of the inner and outer radii for the inner and outer rings, respectively, and ω is the radius of the Gaussian beam illuminating the ring slit.

In determining a theoretical equation for the OAM density, the Poynting vector for the optical field [Eq. (1)] needs to be solved:

$$\vec{S} = \frac{\varepsilon_0 \omega c^2}{4} (i(u \nabla u^* - u^* \nabla u) + 2k|u|^2 \hat{z}), \tag{4}$$

where ε_0 is the permittivity of free space, c is the speed of light, k is the wavenumber, and u is the amplitude of the field described in Eq. (1). The OAM density, L_z, can then be determined from the Poynting vector by the following relationship:

$$L_z = \frac{1}{c^2} (\vec{r} \times \vec{S})_z, \tag{5}$$

resulting in [26]

$$L_z^{\text{THEORY}}(r) = \frac{l \varepsilon_0 \omega A_0^2}{2} (J_l^2(q_1 r) + a_0^2 J_{-l}^2(q_2 r)), \tag{6}$$

the theoretical description of the OAM density for the symmetric superposition described in Eq. (1).

Once the optical field is generated, a quantitative measurement of the OAM density, given theoretically in Eq. (6), can be made by measuring the weighting of each azimuthal mode present in the optical field, which is done by performing the following inner product [depicted in the decomposition section of Fig. 1(a)]:

$$a_n(r, z) = \frac{1}{\sqrt{2\pi}} \int_0^{2\pi} u(r, \theta, z) t(r, \theta) d\theta. \tag{7}$$

a_n is the weighting of the azimuthal mode of order n present in the optical field $u(r, \theta, z)$, described by Eq. (1), and $t(r, \theta)$, which is the transmission function of SLM 2 in Fig. 1(a) and is termed the match filter, is given by the azimuthal mode, $\exp(-in\theta)$, within the bounds $R_1 < r < R_2$. The concept of using a match filter to detect predetermined signals within a noisy background was first demonstrated nearly 50 years ago [29]. This involved implementing complex spatial filters recorded onto film to identify geometric shapes, letters, and signals within random noise. The inner product is executed experimentally by directing the optical field, $u(r, \theta, z)$, onto a match filter [encoded on an SLM and denoted in Fig. 1(e)] and viewing the Fourier transform [depicted in Fig. 1(f)]. The match filter, an example of which is given in Fig. 1(e), consists of a ring slit placed at a particular radial position (R), which allows one to select the radial position within the optical field. The azimuthal phase within the ring slit varies as $\exp(-in\theta)$. For this particular example [Fig. 1(e)], the weighting of the azimuthal mode, $n = 3$ (i.e., a_3), is being measured. By adjusting the azimuthal phase within the ring slit and the radius of the ring slit, various azimuthal weightings at different radial positions in the optical field can be measured. This technique is not restricted to superpositions of Bessel beams but can be used on any OAM-carrying optical field.

To relate the weighting of the azimuthal mode to a quantitative laboratory measurement, we require the inner product of u and t to be determined. The inner product [located at plane P in Fig. 1(a) and defined as $u^P(0, \phi, z)$] is determined by making use of the Fresnel diffraction integral to propagate the field from SLM 2 [the initial field, $u(r, \theta, z)$, multiplied by the transmission function, $t(r, \theta)$, of the match filter] to plane P (the plane of the inner product):

$$u^P(\rho, \phi, z) = \frac{\exp(i2kf)}{i\lambda f} \int_0^{\infty} \int_0^{2\pi} t(r, \theta) u(r, \theta, z) \times \exp(-i\frac{k}{f} r\rho \cos(\theta - \phi)) r dr d\theta, \tag{8}$$

where f is the focal length of the lens used in the decomposition.

If Eq. (8) is evaluated at the origin, $\rho = 0$, then we return the desired inner product between the field $u(r, \theta, z)$ and the match filter $t(r, \theta)$. We also know that when the match filter consists of the complex conjugate of one of the azimuthal modes present in the initial field, the weighting of the azimuthal mode, a_n, [or the on-axis intensity of the inner product, $I(\rho = 0)$] will be nonzero; therefore, we need only consider the cases when the azimuthal mode of the match filter is either l or $-l$ (i.e., $n = l$ and $-l$). By substituting Eq. (1) into Eq. (8), and considering the signal at the origin, $u^P(0, \phi, z)$, for cases when the azimuthal mode index of the match filter is either l or $-l$, we find, respectively,

$$u_l^P(\rho=0,z)=\frac{\exp(i2kf)}{i\lambda f}2\pi A_0\int_{R_1}^{R_2}J_l(q_1r)\times\exp(i\Delta kz)r\mathrm{d}r, \tag{9}$$

$$u_{-l}^P(\rho=0,z)=\frac{\exp(i2kf)}{i\lambda f}2\pi A_0\alpha_0\int_{R_1}^{R_2}J_{-l}(q_2r)\times\exp(-i\Delta kz)r\mathrm{d}r. \tag{10}$$

R_1 and R_2 are the inner and outer radii of the ring slit representing the match filter [Fig. 1(e)]. Since the ring slit in the match filter can be made arbitrarily thin, Eqs. (9) and (10) can be simplified by noting that the ring slit may be assumed to be at a radial position $R\approx R_1\approx R_2$ and of width $2\Delta R$, resulting in

$$u_l^P(\rho=0,z,r=R)=\frac{\exp(i2kf)}{i\lambda f}2\pi A_0 2\Delta R\cdot RJ_l(q_1R)\exp(i\Delta kz), \tag{11}$$

$$u_{-l}^P(\rho=0,z,r=R)=\frac{\exp(i2kf)}{i\lambda f}2\pi A_0\alpha_0 2\Delta R\cdot RJ_{-l}(q_2R)\exp(-i\Delta kz). \tag{12}$$

The Bessel function is evaluated at R, which is the radius of the ring slit, represented in the match filter.

Since the intensity of an optical field is defined as $I_l=\varepsilon_0 c(u_l u_l^*)$, the following relationships between the measured intensity at the origin of the inner product, $I(0)$ (for the two cases where the azimuthal mode index of the match filter is either l or $-l$), and the theoretical Bessel functions can be formed:

$$\frac{I_l(0)}{\varepsilon_0 c}\left(\frac{f\lambda}{4\pi\Delta R\cdot RA_0}\right)^2=J_l^2(q_1R), \tag{13}$$

$$\frac{I_{-l}(0)}{\varepsilon_0 c}\left(\frac{f\lambda}{4\pi\Delta R\cdot RA_0}\right)^2=\alpha_0^2J_{-l}^2(q_2R). \tag{14}$$

Substituting the above two equations, Eqs. (13) and (14), for the Bessel functions, J_l and J_{-l}, into the theoretical result for the OAM density, Eq. (6), results in the following equation:

$$L_z^{\mathrm{EXP}}(R)=\frac{l\omega}{2c\eta}\left(\frac{\lambda f}{S_{\mathrm{Ring}}}\right)^2(I_l(0)-I_{-l}(0)), \tag{15}$$

which is used to calculate quantitative measurements of the OAM density. η is a factor for the optical efficiency of the experimental setup, and S_{Ring} is the area $(4\pi\Delta R\cdot R)$ of the ring slit in the match filter and is a function of its radial position, R.

B. Generalized Symmetric Superposition

The optical field for which we wish to measure the OAM density, as described in Eq. (1), can be extended to a generalized form:

$$u(r,\theta,z)=A_0\sum_{l=-N}^{N}\alpha_l J_l(q_lr)\exp(i\Delta k_l z)\exp(il\theta)+\alpha_{-l}J_{-l}(q_{-l}r)\exp(-i\Delta k_{-l}z)\exp(-il\theta), \tag{16}$$

where α_l and α_{-l} denote the energy contained in each of the ring slits with respect to the energy contained in the innermost ring slit. Because of the fact that the ϕ-component of the Poynting vector, S_ϕ, is a linear operator (the proof is contained in detail in Appendix A), the OAM density for the generalized field described in Eq. (16) can be described both theoretically and experimentally by extending the results given in Eqs. (6) and (15) as, respectively,

$$L_z^{\mathrm{THEORY}}(r)=\frac{\varepsilon_0\omega A_0^2}{2}\sum_{l=-N}^{N}l\alpha_l^2J_l^2(q_lr)-l\alpha_{-l}^2J_{-l}^2(q_{-l}r), \tag{17}$$

$$L_z^{\mathrm{EXP}}(R)=\frac{\omega}{2c\eta}\left(\frac{\lambda f}{S_{\mathrm{Ring}}}\right)^2\sum_{l=-N}^{N}l(I_l(0)-I_{-l}(0)). \tag{18}$$

C. Nonsymmetric Superposition of Two Bessel Beams

The other case that is investigated in this paper is that of nonsymmetric superpositions of Bessel beams, and in the following equations we will outline the theoretical analysis for obtaining the OAM density. The amplitude of a nonsymmetric superposition of two Bessel beams can be described as

$$u(r,\theta,z)=A_0(J_l(q_1r)\exp(i\Delta kz)\exp(il\theta)+\alpha_0J_m(q_2r)\exp(-i\Delta kz)\exp(im\theta)), \tag{19}$$

where the azimuthal indices are of different orders, $l\neq m$. Following the same procedure in determining the Poynting vector and consequently the OAM density previously described for the symmetric case [Eqs. (4) and (5)], the OAM density is determined theoretically by

$$L_z^{\mathrm{THEORY}}(r,\phi,z)=\frac{\varepsilon_0\omega A_0^2}{2}(lJ_l^2(q_1r)+m\alpha_0^2J_m^2(q_2r)+(l+m)\alpha_0\cos((l-m)\phi+2\Delta kz)J_l(q_1r)J_m(q_2r)). \tag{20}$$

Since the above equation is a function of the azimuthal angle, ϕ, in the plane of the inner product, it is evaluated by summing the OAM density values for a range of angles varying from 0 to 2π.

Equation (20), unlike the OAM density for the symmetric case, is a function of Δkz, and given that its effect on the optical field is only a constant phase shift (a rotation in the intensity profile of the optical field), it can be ignored.

To relate a quantifiable measurement to the theoretical OAM density [Eq. (20)], the same procedure as described in Eqs. (8)–(14) is followed, and the final results, which relate the on-axis intensity in the inner product plane P to the theoretical Bessel functions, are

$$\frac{I_l(0)}{\varepsilon_0 c}\left(\frac{f\lambda}{4\pi\Delta R \cdot RA_0}\right)^2 = J_l^2(q_1 R), \tag{21}$$

$$\frac{I_m(0)}{\varepsilon_0 c}\left(\frac{f\lambda}{4\pi\Delta R \cdot RA_0}\right)^2 = \alpha_0^2 J_m^2(q_2 R). \tag{22}$$

Here in the theoretical analysis of the nonsymmetric case, the azimuthal mode index, n, of the match filter is set to both l and m.

Substituting the above two equations, Eqs. (21) and (22), into Eq. (20), the form for obtaining an experimental measurement of the OAM density is

$$L_z^{\mathrm{EXP}}(R,\phi,z) = \frac{\omega}{2c\eta}\left(\frac{\lambda f}{S_{\mathrm{Ring}}}\right)^2\Big(lI_l(0) + mI_m(0) + (l+m)\cos((l-m)\phi + 2\Delta kz)\sqrt{I_l(0)}\sqrt{I_m(0)}\Big). \tag{23}$$

This result is also a function of the angle, ϕ, in the plane of the inner product, and since only a single measurement of the on-axis intensity in the inner product plane can be made, no measurement for the angle ϕ can be obtained. To resolve this issue, the experimental equation for the OAM density is integrated over ϕ, resulting in the average OAM density

$$\overline{L_z^{\mathrm{EXP}}(R)} = \frac{\omega}{2c\eta}\left(\frac{\lambda f}{S_{\mathrm{Ring}}}\right)^2 (lI_l(0) + mI_m(0)), \tag{24}$$

where the term Δkz can be neglected. Since the above experimental measurement, Eq. (24), has no angular dependence on the optical field, the measurement does not pertain to a specific radial direction but is in fact merely an average measurement across the field.

D. Generalized Nonsymmetric Superposition

Similarly, as in the symmetric case, the amplitude of the nonsymmetric superposition can be extended to consist of many Bessel beams, as in the following form:

$$u(r,\theta,z) = A_0\sum_{l=-N}^{N}\sum_{m=-N}^{N}\alpha_l J_l(q_l r)\exp(i\Delta k_l z)\exp(il\theta) + \alpha_m J_m(q_m r)\exp(i\Delta k_m z)\exp(im\theta). \tag{25}$$

Even though the ϕ-component of the Poynting vector, S_ϕ, is a linear operator and the theoretical and experimental OAM densities can be extracted by extending the simple form in Eqs. (20) and (23), the equations become very cumbersome and have thus been neglected in this paper. However, if the reader wishes to calculate the OAM density for such fields, this can be easily achieved by substituting the amplitude of the field into Eq. (4) to determine the Poynting vector for calculating the theoretical OAM density.

In this paper we experimentally test the results given above by measuring the OAM density for six separate optical fields. The first three fields consist of a superposition of two Bessel beams, of orders 3 and −3, where (1) the energy in the two ring slits (used to generate the optical fields) is equal, (2) that in the outer ring slit is heavily weighted, and (3) that in the inner ring slit is heavily weighted. The theoretical and experimental OAM densities are calculated through the use of Eqs. (6) and (15). The fourth optical field is a nonsymmetric superposition of two Bessel beams, where $l = 3$ and $m = -4$, and the required results are obtained through the use of Eqs. (20) and (24). The fifth involves a superposition of three Bessel beams, and even though the OAM density is not explicitly given in the paper, it is easily calculated by substituting the amplitude of the optical field into Eqs. (4) and (5). This is also the case with the last optical field, a nonsymmetric superposition of four Bessel beams.

The experimental setup for measuring the OAM density of the optical fields, discussed above, is given in the following section, accompanied with the theoretical and experimental results.

3. Experimental Methodology and Results

The experimental setup for the measurement of the OAM spectrum at specific radial positions for the coherent superposition of Bessel beams is denoted in Fig. 2. To generate the various superimposed Bessel beams, for which we intend to calculate the OAM density, a HeNe laser ($\lambda \sim 633$ nm) was expanded through a 6× telescope and directed onto the liquid-crystal display (LCD) of an SLM labeled LCD_1. The fields consisting of superpositions of higher-order Bessel beams were generated in a similar approach to Durnin's ring slit [27] method, except the ring slits were implemented digitally [28] onto LCD_1 (HoloEye, PLUTO-VIS, with 1920 × 1080 pixels of pitch 8 μm and calibrated for a 2π phase shift at ~633 nm).

Some of the digital ring slit holograms programmed onto LCD_1 for the creation of superimposed Bessel beams are given in the first column of Fig. 3. To create an amplitude ring slit digitally on a phase-only SLM, the area surrounding the ring

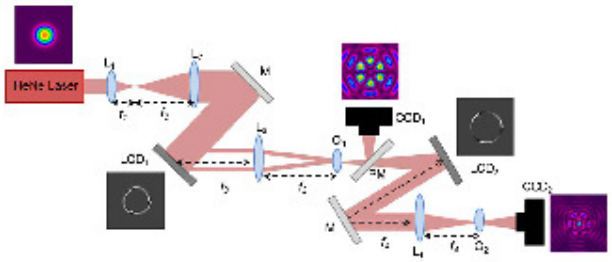

Fig. 2. (Color online) Schematic of the experimental setup for measuring the OAM density of symmetric and nonsymmetric superpositions of Bessel beams as a function of the radial position, R. L, lens ($f_1 = 25$ mm, $f_2 = 150$ mm, $f_3 = 200$ mm, and $f_4 = 200$ mm); M, mirror; LCD, liquid-crystal display; O, objective; PM, pop-up mirror; CCD, CCD camera. The objective, O_2, was placed at the focus (or Fourier plane) of lens L_4. The corresponding optical fields or holograms are represented at the appropriate planes.

slit, which we do not want to transmit any light, is encoded with a "checkerboard" pattern. By assigning alternating sets of pixels on LCD_1 with phase values that are out of phase by π, the light reflected from the LCD is scattered from its initial propagation axis [30–32].

A. Symmetric Superposition of Two Bessel Beams

The first three digital holograms, represented in the first column of Fig. 3, consist of a ring slit separated into two ring slits possessing azimuthal phases of equal order but opposite handedness (i.e., $l_{inner} = 3$ and $l_{outer} = -3$). However, the widths of the two ring slits differ in Figs. 3(d) and 3(g). This allowed us to control the weighting of the two Bessel beams and subsequently set the values of A_0 and α_0 in Eq. (1). The dimensions (in pixels) of the ring slits in Fig. 3 are (a) $r_1 = 173$, $r_2 = 188$, Δr_1, $\Delta r_2 = 15$; (d) $r_1 = 173$, $r_2 = 188$, $\Delta r_1 = 7$, $\Delta r_2 = 23$; (g) $r_1 = 173$, $r_2 = 188$, $\Delta r_1 = 23$, $\Delta r_2 = 7$. In the case that LCD_1 was encoded with two ring slits where the orders of the two azimuthal phases were of equal but opposite handedness, a "petal" structure was produced, where the number of "petals" is denoted by $2|l|$ [Figs. 3(b) and 3(c)], as expected from theory [28]. In the following two cases [Figs. 3(d) and 3(g)], the two ring slits had slightly different areas, resulting in the energy contained in the two Bessel beams being of slightly different weightings. In Figs. 3(e) and 3(f), the $l = -3$ order Bessel beam is heavily weighted by increasing the area of the outer ring slit, giving rise to a "smearing" of the "petals" as the $l = -3$ order Bessel beam dominants the optical field. Similarly, this is also evident in the case of Figs. 3(h) and 3(i), where the $l = 3$ order Bessel beam is heavily weighted by increasing the area of the inner ring slit.

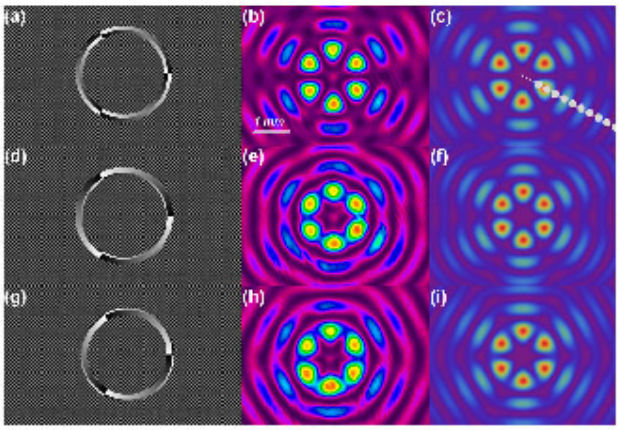

Fig. 3. (Color online) Digital ring slits [first column—(a), (d), (g)] and the corresponding experimentally produced fields in the Fourier plane [second column—(b), (e), (h)] accompanied by theoretically calculated fields [third column—(c), (f), (i)]. The ten white dots in (c) denote the radial positions of each of the ten ring slits used in the match filters.

The resulting superposition field, formed at the focal plane of L_3, was magnified with a 10× objective, O_1, and directed to the LCD of the second SLM, LCD_2. A pop-up mirror, PM_1, was used to direct the field at the plane of LCD_2 so as to be recorded on CCD_1 (Spiricon, LBA-FW-SCOR-7350115), so that the radial positions within the optical field could be quantitatively measured. LCD_2, programmed with a match filter, $\exp(-in\theta)$, together with lens L_4, was used to perform the inner product of the incoming field with the match filter given in Eq. (7). The match filter, also programmed as a digital hologram, consists of a single ring slit which also makes use of the "checkerboard" pattern. Since the match filter is programmed digitally, the radius of the ring slit, as well as the azimuthal phase within the ring slit, can be easily varied. This dynamical aspect of the SLM allows us to radially locate where in the optical field we wish to make a measurement of the OAM density. In this paper, the match filters consist of ring slits having 10 different radii [$r_1 = 75$, $r_2 = 110$, $r_3 = 145$, $r_4 = 180$, $r_5 = 215$, $r_6 = 250$, $r_7 = 285$, $r_8 = 320$, $r_9 = 355$, and $r_{10} = 390$ (given in pixels), each consisting of a width of 20 pixels], where the phase within the rings, n, varied as the complex conjugate of the azimuthal modes present in the incoming optical field. The location of the ten radial positions in the optical field is illustrated in Fig. 3(c). Because LCD_2 was orientated as the mirror image of LCD_1 in our experimental setup, the complex conjugate of the azimuthal mode index, n, on LCD_1 is equivalent to n on LCD_2. If the reader wishes to orientate the experimental setup differently, such that the two SLMs have the same orientation (i.e., are not mirror images of each other), the complex conjugate of the azimuthal mode index, n, on LCD_1 is then equivalent to $-n$ on LCD_2. The OAM density for a particular radial position can then be measured directly from Eqs. (15) and (24) by measuring the on-axis intensity of the inner product.

In determining the OAM density for the first three optical fields, denoted experimentally in the second column of Fig. 3, the intensity at the origin of the resulting field at the Fourier plane of L_4 was measured with a CCD camera, CCD_2, for each of the match filters and substituted into Eq. (15) or (24). The measured OAM densities as a function of the radial position for the first three optical fields are given in Fig. 4.

In Fig. 4(a), since the incoming optical field consists of an equal weighting of $l_{\text{inner}} = 3$ and $l_{\text{outer}} = -3$ order Bessel beams [Fig. 3(b)], the OAM density represented in the x–y plane consists of evenly sized concentric rings of positive and negative OAM. This is also evident in the radial cross-sectional profile of the OAM density in Fig. 4(b). The OAM density oscillates evenly around a value of zero. In the following two cases, where $l_{\text{inner}} = -3(+3)$ is heavily weighted, the OAM is predominantly negative (positive) and is evident in Fig. 4(d) [(f)]. This is also evident in Fig. 4(c) [(e)], where the OAM density exists predominantly in the negative (positive) quadrant of the graph.

A theoretical error band for the OAM density was obtained by determining the minimum and maximum values for the OAM density when the inner and outer radii of the ring slit in the match filters were displaced by half the width of the ring slit (i.e., 10 pixels). The error is so small that the error bands lie on top of one another and are not evident in the graphs. The experimental x error bar is given by a displacement of the ring slit in the match filter by half of its width, and so the absolute x error is 80 um (10 pixels × 8 um). We narrowed the error in experimentally measuring the on-axis intensity of the inner product to three factors: (1) human error in selecting the on-axis intensity of the inner product on CCD_2, (2) the positioning of CCD_2 in the Fourier pane of L_4, and (3) an adjustment of the ring slit (by half of its width) in the match filter on LCD_2. An aperture having a diameter of 10 pixels was positioned around the on-axis intensity on CCD_2, and the percentage error for the total energy within the aperture when it was moved 7 pixels from the center was included in the experimental error for the OAM density. The second error measurement involved measuring the percentage error for the on-axis intensity when CCD_2 was positioned 1 mm before and 1 mm after the Fourier plane of L_4. Finally, the last error measurement in the OAM density involved measuring the percentage error in the measured intensity when the radius of the ring slit on LCD_2 was either decreased or increased by half of the ring slit width. All of these aforementioned errors were measured and included in all the measurements.

B. Nonsymmetric Superposition of Two Bessel Beams

The fourth digital ring slit [Fig. 5(a)] consists of two ring slits having azimuthal phases $l_{\text{inner}} = 3$ and $l_{\text{outer}} = -4$, which is an example of a nonsymmetric superposition [described mathematically in Eq. (19)]. The dimensions (in pixels) of the ring slits in Fig. 5(a) are $r_1 = 173$, $r_2 = 188$, Δr_1, and $\Delta r_2 = 15$. The field produced [Fig. 5(b)] is in good agreement with the theoretically calculated field [Fig. 5(c)] and consists of a "petal" structure, where the number of "petals" is given by $|l_{\text{inner}}| + |l_{\text{outer}}|$, (i.e., 7 petals, for this case). The field has a global OAM of $-1\hbar$ ($3\hbar + -4\hbar$), and therefore the OAM density is mostly negative radially across the field, as is evident in both Figs. 5(d) and 5(e). In a nonsymmetric superposition, the OAM density is not symmetric in the optical field, as is evident in Fig. 5(e). Since the OAM density is not uniform in all radial directions of the optical field, the OAM density plotted in Fig. 5(d) is not for a particular angular point in the optical field, but instead an average over all angular positions.

C. Nonsymmetric Superposition of Three Bessel Beams

The fifth digital hologram [Fig. 6(a)] is divided into three ring slits having the following azimuthal phase variations: $l_{\text{inner}} = -3$, $l_{\text{middle}} = 2$, $l_{\text{outer}} = 1$,

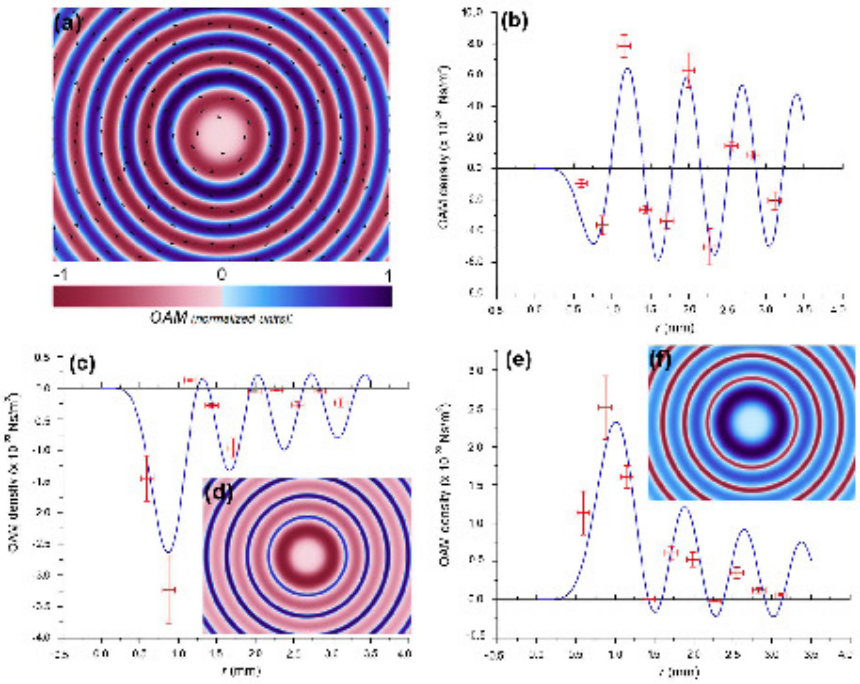

Fig. 4. (Color online) (a) Density plot of the OAM density for the field given in Fig. 3(b). Red denotes negative OAM, and blue denotes positive. Light to dark blue denotes an increase in positive OAM, and light to dark red denotes an increase in negative OAM. (b), (c), (e), The theoretical (blue curve) and experimentally measured (red points) OAM density for the corresponding fields in Figs 3(b), 3(c), and 3(h), respectively. (d), (f), Plots of the OAM density for (c) and (e), respectively, given as insets.

producing a nonsymmetric superposition. The dimensions (in pixels) of the ring slits in Fig. 6(a) are $r_1 = 170$, $r_2 = 180$, $r_3 = 190$, Δr_1, Δr_2, and $\Delta r_3 = 10$. Even though one cannot intuitively predict how the field will manifest in the Fourier plane, our experimental field [Fig. 6(b)] is in very good

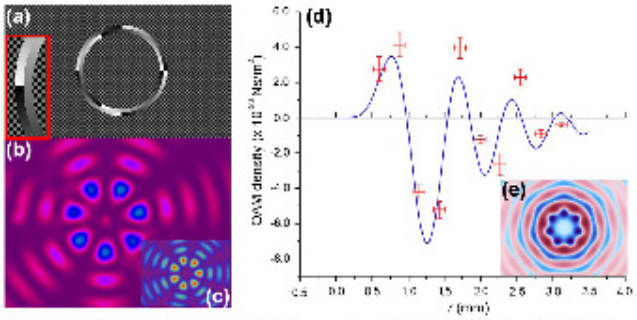

Fig. 5. (Color online) (a) Digital hologram used to generate (b) the experimental field; (c) the theoretical field. A magnification of the ring slit is given as an inset in (a). (d) The theoretical (blue curve) and experimentally measured (red points) OAM density. (e) A plot of the OAM density. Red denotes negative OAM, and blue denotes positive. Light to dark blue denotes an increase in positive OAM, and light to dark red denotes an increase in negative OAM.

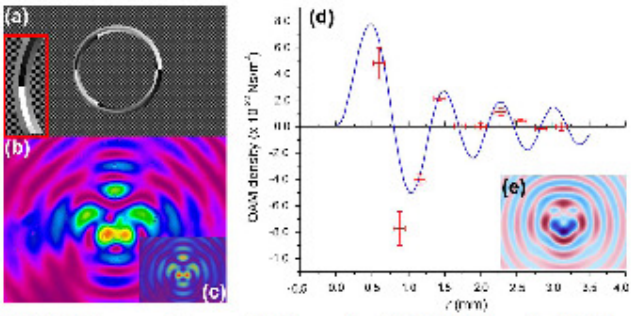

Fig. 6. (Color online) (a) Digital hologram used to generate (b) the experimental field; (c) the theoretical field. A magnification of the ring slit is given as an inset in (a). (d) The theoretical (blue curve) and experimentally measured (red points) OAM density. (e) A plot of the OAM density. Red denotes negative OAM, and blue denotes positive. Light to dark blue denotes an increase in positive OAM, and light to dark red denotes an increase in negative OAM.

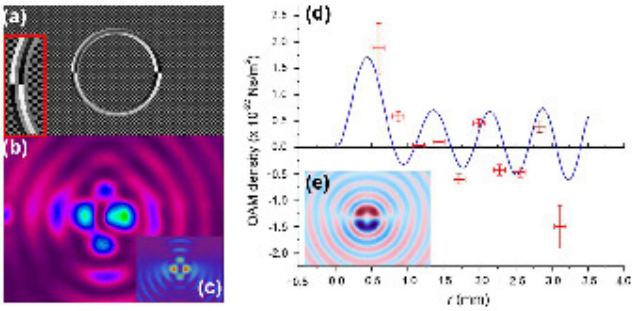

Fig. 7. (Color online) (a) Digital hologram used to generate (b) the experimental field; (c) the theoretical field. A magnification of the ring slit is given as an inset in (a). (d) The theoretical (blue curve) and experimentally measured (red points) OAM density. (e) A plot of the OAM density. Red denotes negative OAM, and blue denotes positive. Light to dark blue denotes an increase in positive OAM, and light to dark red denotes an increase in negative OAM.

agreement with the theoretically calculated field [Fig. 6(c)]. Since the ring slits are equally weighted and the azimuthal mode indices of the ring slits [Fig. 6(a)] sum to zero, the global OAM is zero, giving rise to the OAM density existing equally in both the negative and positive quadrants for the OAM density across the radial direction of the field, as is evident in Figs. 6(d) and 6(e). The OAM density is not uniform in all radial directions of the optical field [evident in Fig. 6(e)], and so the OAM density plotted in Fig. 6(d) is an average over all angular positions.

D. Nonsymmetric Superposition of Four Bessel Beams

A similar behavior is noted in the last optical field, whose digital hologram is depicted in Fig. 7(a). The ring slits have the following azimuthal mode indices: $l_{\text{inner}} = -2$, $l_{\text{middle}} = -1$, $1_{\text{middle2}} = 2$, $l_{\text{outer}} = 1$, which too sum to zero, and the physical dimensions (in pixels) are $r_1 = 169$, $r_2 = 176$, $r_3 = 183$, $r_4 = 190$, Δr_1, Δr_2, Δr_3, and $\Delta r_4 = 7$. Since the global OAM is zero, the OAM density exists equally in both the negative and positive quadrants, as is evident in Figs. 7(d) and 7(e). Once again, the OAM density is not uniform in all radial directions of the optical field [evident in Fig. 7(e)], and so the OAM density plotted in Fig. 7(d) is an average over all angular positions.

For the six cases presented above, the on-axis intensity recorded at CCD_2 for each of the match filters (varying in ring slit radius and azimuthal order) was measured and analyzed using the results obtained from Eqs. (4) and (5). From all six plots, it is evident that there is very good agreement between the experimentally measured OAM density values and those calculated theoretically. For the first time, to the best of our knowledge, the OAM density has been measured as a quantitative value and represented as the angular momentum per unit volume, Ns/m^2, by implementing an extremely simple measurement technique.

4. Conclusion

We have derived expressions for the OAM density for symmetric and nonsymmetric optical fields theoretically and made a direct comparison experimentally.

A simple technique for making such measurements of the OAM density in optical fields is tested on superimposed nondiffracting higher-order Bessel beams. However, the presented measurement technique can be used on any optical field carrying OAM. We obtain quantitative measurements, expressed as the angular momentum per unit volume, Ns/m^2, for the OAM density as a function of the radial position in both symmetric and nonsymmetric optical fields, illustrating good agreement with the theoretical prediction. We find that the OAM density can be made to oscillate from positive to negative by appropriately adjusting the widths of the ring slits or the azimuthal orders within the ring slits, making it an ideal tool in the field of optical trapping and tweezing. Measuring the OAM spectrum of fields has direct relevance in the optical control of flow in microfluidic devices and in constructing optically driven micromachines and parallel molecular or cell assays.

Appendix A

The following proof illustrates that the ϕ-component of the Poynting vector, S_ϕ, is a linear operator. We start with the equation for S_ϕ:

$$S_\phi = \frac{\varepsilon_0 \omega c^2 i}{4}(u\nabla u^* - u^*\nabla u), \tag{A1}$$

where u is the optical field described in Eq. (1).

u^* can be written in terms of u as follows:

$$\begin{aligned} u + u^* &= A_0(J_l \exp(i\Delta kz)\exp(il\theta) \\ &\quad + \alpha_0 J_{-l}\exp(-i\Delta kz)\exp(-il\theta)) \\ &\quad + A_0(J_l \exp(-i\Delta kz)\exp(-il\theta) \\ &\quad + \alpha_0 J_{-l}\exp(i\Delta kz)\exp(il\theta)) \\ u + u^* &= (A_0 J_l + A_0\alpha_0 J_{-l})2\cos(\Delta kz + l\theta) \\ \rightarrow u^* &= \overbrace{\frac{2A_0(J_l + \alpha_0 J_{-l})\cos(\Delta kz + l\theta)}{X}} - u, \end{aligned} \tag{A2}$$

where for convenience we have left the terms not involving u as X.

Substituting u^* into Eq. (A1) results in

$$\begin{aligned} S_\phi &\propto u\nabla u^* - u^*\nabla u \propto u\nabla(X-u) - (X-u)\nabla u \\ &\propto u\nabla X - u\nabla u - X\nabla u + u\nabla u \propto u\nabla X - X\nabla u, \end{aligned} \tag{A3}$$

which is a linear operator, i.e., $S_\phi(u_1+u_2) = S_\phi(u_1) + S_\phi(u_2)$. Thus, the linear momentum (in the azimuthal coordinate) from the Poynting vector of a sum of fields is equal to the sum of the linear momentums of each individual field.

References

1. L. Allen, M. W. Beijersbergen, R. J. C. Spreeuw, and J. P. Woerdman, "Orbital angular momentum of light and the transformation of Laguerre-Gaussian laser modes," Phys. Rev. A **45**, 8185–8189 (1992).
2. H. He, M. E. J. Friese, N. R. Heckenberg, and H. Rubinsztein-Dunlop, "Direct observation of transfer of angular momentum to absorptive particles from a laser beam with a phase singularity," Phys. Rev. Lett. **75**, 826–829 (1995).
3. A. Mair, A. Vaziri, G. Weihs, and A. Zeilinger, "Entanglement of the orbital angular momentum states of photons," Nature **412**, 313–316 (2001).
4. M. W. Beijersbergen, L. Allen, H. E. L. O. Van der Veen, and J. P. Woerdman, "Astigmatic laser mode converters and the transfer of orbital angular momentum," Opt. Commun. **96**, 123–132 (1993).
5. Arlt and K. Dholakia, "Generation of high-order Bessel beams by use of an axicon," Opt. Commun. **177**, 297–301 (2000).
6. H. I. Sztul and R. R. Alfano, "The Poynting vector and angular momentum of Airy beams," Opt. Express **16**, 9411–9416 (2008).
7. A. Vaziri, G. Weihs, and A. Zeilinger, "Experimental two-photon three-dimensional quantum entanglement," Phys. Rev. Lett. **89**, 240401 (2002).
8. J. T. Barreiro, T.-C. Wei, and P. G. Kwiat, "Beating the channel capacity limit for linear photonic superdense coding," Nat. Phys. **4**, 282–286 (2008).
9. J. Leach, B. Jack, J. Romero, A. K. Jha, A. M. Yao, S. Franke-Arnold, D. Ireland, R. W. Boyd, S. M. Barnett, and M. J. Padgett, "Quantum correlations in optical angle-orbital angular momentum variables," Science **329**, 662–665 (2010).
10. G. Gibson, J. Courtial, M. J. Padgett, M. Vasnetsov, V. Pas'ko, S. M. Barnett, and S. Franke-Arnold, "Free-space information transfer using light beams carrying orbital angular momentum," Opt. Express **12**, 5448–5456 (2004).
11. S. N. Khonina, V. V. Kotlyar, R. V. Skidanov, V. A. Soifer, P. Laakkonen, and J. Turunen, "Gauss–Laguerre modes with different indices in prescribed diffraction orders of a diffractive phase element," Opt. Commun. **175**, 301–308 (2000).
12. G. C. G. Berkhout, M. P. J. Lavery, J. Courtial, M. W. Beijersbergen, and M. J. Padgett, "Efficient sorting of orbital angular momentum states of light," Phys. Rev. Lett. **105**, 153601 (2010).
13. J. Leach, M. J. Padgett, S. M. Barnett, S. Franke-Arnold, and J. Courtial, "Measuring the orbital angular momentum of a single photon," Phys. Rev. Lett. **88**, 257901 (2002).
14. M. Lavery, A. Dudley, A. Forbes, J. Courtial, and M. Padgett, "Robust interferometer for the routing of light beams carrying orbital angular momentum," New J. Phys. **13**, 093014 (2011).
15. C. Gao, X. Qi, Y. Liu, J. Xin, and L. Wang, "Sorting and detecting orbital angular momentum states by using a Dove prism embedded Mach–Zehnder interferometer and amplitude gratings," Opt. Commun. **284**, 48–51 (2011).
16. A. Gatto, M. Tacca, P. Martelli, P. Boffi, and M. Martinelli, "Free-space orbital angular momentum division multiplexing with Bessel beams," J. Opt. **13**, 064018 (2011).
17. J. M. Hickmann, E. J. S. Fonseca, W. C. Soares, and S. Chavez-Cerda, "Angular Momentum," Phys. Rev. Lett. **105**, 053904 (2010).
18. V. Garces-Chavez, D. McGloin, M. J. Padgett, W. Dultz, H. Schmitzer, and K. Dholakia, "Observation of the transfer of the local angular momentum density of a multiringed light beam to an optically trapped particle," Phys. Rev. Lett. **91**, 093602 (2003).
19. C. H. J. Schmitz, K. Uhrig, J. P. Spatz, and J. E. Curtis, "Tuning the orbital angular momentum in optical vortex beams," Opt. Express **14**, 6604–6612 (2006).
20. S. H. Tao, X. C. Yuan, J. Lin, and R. E. Burge, "Residue orbital angular momentum in interferenced double vortex beams with unequal topological charges," Opt. Express **14**, 535–541 (2006).
21. K. Volke-Sepulveda, V. Garces-Chavez, S. Chavez-Cerda, J. Arlt, and K. Dholakia, "Orbital angular momentum of a high-order Bessel light beam," J. Opt. B: Quantum Semiclass. Opt. **4**, S82–S89 (2002).
22. V. Garces-Chavez, K. Volke-Sepulveda, S. Chavez-Cerda, W. Sibbett, and K. Dholakia, "Transfer of orbital angular momentum to an optically trapped low-index particle," Phys. Rev. A **66**, 063402 (2002).

23. M. V. Vasnetsov, J. P. Torres, D. V. Petrov, and L. Torner, "Observation of the orbital angular momentum spectrum of a light beam," Opt. Lett. **28**, 2285–2287 (2003).
24. M. Hautakorpi, J. Lindberg, T. Setälä, and M. Kaivola, "Rotational frequency shifts in partially coherent optical fields," J. Opt. Soc. Am. A **23**, 1159–1163 (2006).
25. X. Gan, P. Zhang, S. Liu, Y. Zheng, J. Zhao, and Z. Chen, "Stabilization and breakup of optical vortices in presence of hybrid nonlinearity," Opt. Express **17**, 23130–23136 (2009).
26. I. Litvin, A. Dudley, and A. Forbes, "Poynting vector and orbital angular momentum density of superpositions of Bessel beams," Opt. Express **19**, 16760–16771 (2011).
27. J. Durnin, J. Miceli Jr., and J. H. Eberly, "Diffraction-free beams," Phys. Rev. Lett. **58**, 1499–1501 (1987).
28. R. Vasilyeu, A. Dudley, N. Khilo, and A. Forbes, "Generating superpositions of higher-order Bessel beams," Opt. Express **17**, 23389–23395 (2009).
29. A. V. Lugt, "Signal detection by complex spatial filtering," IEEE Trans. Inf. Theory **10**, 139–145 (1964).
30. D. W. K. Wong and G. Chen, "Redistribution of the zero order by the use of a phase checkerboard pattern in computer generated holograms," Appl. Opt. **47**, 602–610 (2008).
31. C. Lopez-Mariscal and K. Helmerson, "Shaped nondiffracting beams," Opt. Lett. **35**, 1215–1217 (2010).
32. A. Dudley, R. Vasilyeu, V. Belyi, N. Khilo, P. Ropot, and A. Forbes, "Controlling the evolution of nondiffracting speckle by complex amplitude modulation on a phase-only spatial light modulator," Opt. Commun. **285**, 5–12 (2012).

B8: Publication 8

From stationary annular rings to rotating Bessel beams

Angela Dudley[1,2,*] and Andrew Forbes[1,2]

[1]CSIR National Laser Centre, P.O. Box 395, Pretoria 0001, South Africa
[2]School of Physics, University of KwaZulu-Natal, Private Bag X54001, Durban 4000, South Africa
*Corresponding author: adudley@csir.co.za

Received November 28, 2011; revised December 21, 2011; accepted December 21, 2011; posted December 21, 2011 (Doc. ID 159039); published March 22, 2012

In this work we use a phase-only spatial light modulator (SLM) to mimic a ring-slit aperture, containing multiple azimuthally varying phases at different radial positions. The optical Fourier transform of such an aperture is currently known and its intensity profile has been shown to rotate along its propagation axis. Here we investigate the near-field of the ring-slit aperture and show, both experimentally and theoretically, that although the near-field possesses similar attributes to its Fourier transform, its intensity profile exhibits no rotation as it propagates. © 2012 Optical Society of America

OCIS codes: 090.1995, 070.6120, 070.3185, 050.4865.

1. INTRODUCTION

Currently, there is a large amount of literature dedicated to fields carrying orbital angular momentum (OAM). This ranges across Laguerre–Gaussian beams [1], Bessel–Gauss beams [2], and Airy beams [3], all of which carry an OAM of $\hbar$ per photon and have an azimuthal angular dependence of $\exp(il\phi)$ [1,4–6], where l is the unbounded azimuthal mode index and ϕ is the azimuthal angle. Fields carrying OAM offer versatile applications. Some of these applications range from using such fields to transfer OAM for the rotation of trapped particles [5] to the entanglement of OAM in parametric down-conversion [6]. The fact that they offer an unbounded state space provides a larger bandwidth for quantum cryptography [7,8].

We are mainly interested in higher-order non-diffracting Bessel beams as a form of optical field possessing OAM and of particular interest is the generation of superimposed higher-order Bessel beams. One can superimpose higher-order Bessel beams so as to produce a field which either has or does not have a global OAM. In the case of generating a superimposed higher-order Bessel beam, such that there is no global OAM, a rotation in the field's intensity profile as it propagates is evident [9–11]. Such superpositions can be generated by illuminating Durnin's ring-slit aperture [12] with multiple azimuthal phase components at varying radial distances [9], or by encoding a spatial light modulator (SLM) with a single ring-slit hologram [10], or by illuminating an axicon with a superposition of Laguerre–Gaussian beams [13].

In this paper we, theoretically and experimentally, investigate both the near- and far-field intensity profiles of the ring-slit aperture. Since superpositions of Bessel beams are frequently used in optical tweezers, knowledge of the structure of the field at planes, other than its Fourier plane, is imperative. We show that even though the intensity maxima, present in the far-field as $2l$ "petals," arranged on the circumference of a ring [9], are also present in the near-ring-slit field, the angular rotation of the intensity profile, however, does not exist in both the near- and far-field regions. It is well known that the far-field intensity profile rotates as it propagates [9–11] and we show, both theoretically and experimentally, that this is not the case in the near-field, due to the fact that the longitudinal wave vectors all propagate in the same direction (and do not overlap one another) in the near-field, but in differing directions (overlapping one another) in the far-field.

2. THEORY

In this work we implement Durnin's ring-slit aperture experiment [12] and encode a digital ring-slit hologram onto a SLM and illuminate it with an expanded Gaussian beam. We divide the ring-slit aperture into two ring-slits and encode each with an azimuthally varying phase. A schematic of the setup is given in Fig. 1, where the regions of interest, propagating after the ring-slit aperture, are planes P_1 (the near field), the region P_2 (the transition region from near- to far-field) and region P_3 (the far-field).

The ring-slit aperture, has the following transmission function

$$t(r,\phi) = \begin{cases} \exp(il\phi) & R_1 - \frac{\Delta}{2} \le r \le R_1 + \frac{\Delta}{2} \\ \exp(-il\phi) & R_2 - \frac{\Delta}{2} \le r \le R_2 + \frac{\Delta}{2}, \\ 0 & \text{elsewhere} \end{cases} \quad (1)$$

and apart from being illustrated in Fig. 1, is also represented in Fig. 2. R_1 and R_2 are the radii of each of the two ring-slits, respectively, and Δ is the width of each ring-slit (we have chosen the widths of the two ring-slits to be equal). ϕ is the azimuthal angle and l is the azimuthal mode index.

Since the field illuminating the ring-slit aperture is an expanded Gaussian beam and the ring-slits are extremely thin (of the order of micrometers), the optical field within the rings-slit can be described by a plane-wave, $\exp(i(k_z z - \omega t))$. k_z is the longitudinal wavenumber, z is the propagation axis and the time varying component, ωt, can be neglected as the plane-wave field is uniform across the entire $x-y$ plane, at any instant in time. The field produced at the ring-slit aperture (i.e., at the plane P_1 where $z = z_0$), is represented as

 © 2012 Optical Society of America

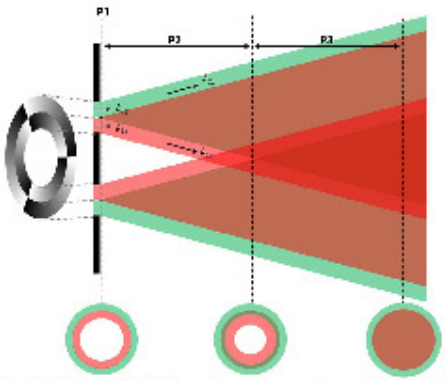

Fig. 1. (Color online) Schematic of the generation of the annular field, propagating from near- (P_1) to far-field (P_3). The green (red) rays denote the rays originating from the outer (inner) ring-slit. The three rings (at the bottom of the schematic) aid the illustration, as to how the annular fields overlap and become completely indistinguishable as the propagation from the aperture increases.

$$A^{P_1}(r,\phi,z_0)=\begin{cases}\exp(il\phi)\exp(ik_{1z}z_0) & R_1-\frac{\Delta}{2}\le r\le R_1+\frac{\Delta}{2}\\ \exp(-il\phi)\exp(ik_{2z}z_0) & R_2-\frac{\Delta}{2}\le r\le R_2+\frac{\Delta}{2}\\ 0 & \text{elsewhere}\end{cases}. \tag{2}$$

k_{1z} and k_{2z} are the longitudinal wavenumbers, defined as $k_{1z}=k\cos\alpha_1$ and $k_{2z}=k\cos\alpha_1$, where $k=2\pi/\lambda$ and α is the opening angle of the cone on which the wave vectors (produced by each of the two ring-slits) propagate.

A simple annular field, containing no azimuthally varying phase factors, is expressed as

$$A^{\mathrm{Ring}i}(r)=\exp\left(\left(\frac{-(r-R_0)}{\Delta/2}\right)^n\right) \tag{3}$$

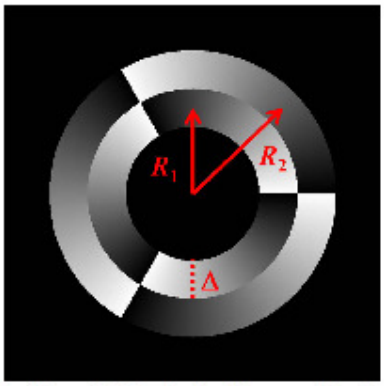

Fig. 2. (Color online) Density plot of the transmission function described in Eq. (1) for an azimuthal mode index of $l=3$.

and is depicted graphically in Fig. 3. R_0 denotes the radius of the ring-slit, Δ is the width of the ring-slit, and n assigns the steepness (or gradient) of the edges of the ring-slit.

The ring-slit aperture that we are considering, consists of two ring-slits of differing radii, and by taking into account that the optical field is a linear system, the two annular fields are additive, resulting in the overall ring-slit field, in the near-field (P_1), been written as

$$\begin{aligned}A^{P_1}(r,\phi,z_0)&=A^{\mathrm{Ring}1}(r)\exp(il\phi)\exp(ik_{1z}z_0)\\&\quad+A^{\mathrm{Ring}2}(r)\exp(-il\phi)\exp(ik_{2z}z_0)\\&=\exp\left(\left(\frac{-(r-R_1)}{\Delta/2}\right)^n\right)\exp(il\phi)\exp(ik_{1z}z_0)\\&\quad+\exp\left(\left(\frac{-(r-R_2)}{\Delta/2}\right)^n\right)\exp(-il\phi)\exp(ik_{2z}z_0).\end{aligned} \tag{4}$$

Since the two ring-slits are arbitrary thin and close to one another, we can assume their radii to be equivalent, i.e., $R_1=R_2=R_0$, resulting in the field simplifying to

$$\begin{aligned}A^{P_1}(r,\phi,z_0)&=\exp\left(\left(\frac{-(r-R_0)}{\Delta/2}\right)^n\right)(\exp(il\phi)\exp(ik_{1z}z_0)\\&\quad+\exp(-il\phi)\exp(ik_{2z}z_0)).\end{aligned} \tag{5}$$

The intensity of the ring-slit field is determined with the following relationship: $I=AA^*$, resulting in

$$\begin{aligned}I^{P_1}\left(r,\phi,z_0\right)&=4\cos^2\left(\frac{k_{1z}z_0-k_{2z}z_0+2l\phi}{2}\right)\\&\quad\times\left(\cosh\left(\frac{2(r-R_0)}{\Delta}\right)-\sinh\left(\frac{2(r-R_0)}{\Delta}\right)\right)^{2n}.\end{aligned} \tag{6}$$

The intensity profile for the ring-slit field, given above in Eq. (6), illustrates that it is modulated in the azimuthal coordinate, ϕ, by the function $\cos^2(2l\phi)$. Therefore, the number of intensity maxima and minima, arranged on the circumference of the ring-slit, is twice the azimuthal mode index, l.

The angular rotation, experienced by the intensity profile, as the ring-slit field propagates in the near-field (P_1) along the z-axis, is then given by

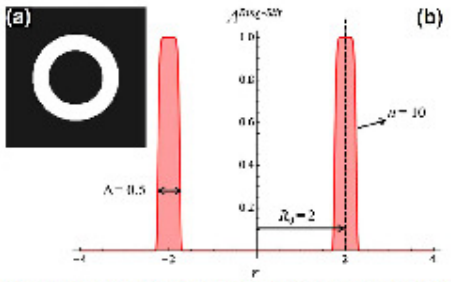

Fig. 3. (Color online) (a) Density plot and (b) cross-sectional plot of the ring-slit aperture described in Eq. (3) for the following parameters: ring-slit radius, $R_0=2$, ring-slit width, $\Delta=0.5$, and gradient, $n=10$ (the units are arbitrary).

$$\frac{d\phi}{dz_0} = \frac{k_{2z} - k_{1z}}{2l}. \tag{7}$$

During the propagation of the ring-slit field, the longitudinal wave vectors, k_{1z} and k_{2z}, both propagate in the same direction, parallel to the z-axis, which is illustrated in Fig. 1. This results in no angular rotation existing, as the ring-slit field propagates,

$$\frac{d\phi}{dz_0} = 0. \tag{8}$$

In determining the field in the region P_2, the region in which the field transitions from near- to far-field, the Fresnel diffraction integral of the field at the ring-slit aperture (Eq. (4)) can be calculated

$$A^{P_2}(r,\phi,z) = \frac{e^{ikz}}{i\lambda z}\int_0^{2\pi}\int_{R_1-\frac{\Delta}{2}}^{R_1+\frac{\Delta}{2}} A^{P1}(r,\phi,z) \times \exp\left(i\frac{k}{2z}(r_1^2 + r^2 - 2rr_1\cos(\phi_1-\phi)\right) r_1\,dr_1\,d\phi_1 \tag{9}$$

and is known to produce the Bessel–Gauss function [14,15]. Each of the two ring-slits (the inner having an azimuthal mode index of l and the outer, $-l$) will contribute to a Bessel–Gauss beam and the resulting superposition of the field in region P_2 can be described as

$$A^{P_2}(r,\phi,z) = A^{BG1}(r,\phi,z) + A^{BG2}(r,\phi,z) = \left(\frac{1}{\sqrt{1+\left(\frac{z}{z_r}\right)^2}}\right)\left(\begin{array}{l}\exp\left[i\left(kz - \frac{k^2r^2}{2R} - \Phi(z)\right) - \left(\frac{1}{\omega^2(z)} - \frac{ik}{2R(z)}\right)\left(r^2 + \left(\frac{k_{2r}z}{k}\right)^2\right) + ik_{1z}z + il\phi\right] J_l\left(\frac{k_{2r}r}{1+i(z/z_r)}\right) + \\ \exp\left[i\left(kz - \frac{k^2r^2}{2R} - \Phi(z)\right) - \left(\frac{1}{\omega^2(z)} - \frac{ik}{2R(z)}\right)\left(r^2 + \left(\frac{k_{2r}z}{k}\right)^2\right) + ik_{2z}z - il\phi\right] J_{-l}\left(\frac{k_{2r}r}{1+i(z/z_r)}\right)\end{array}\right). \tag{10}$$

The functions $\omega(z)$, $R(z)$ and $\Phi(z)$ denote the beam size, radius of curvature and Gouy phase, respectively, and take on the standard Gaussian beam propagation form. J_l is the lth order Bessel function and k_r denotes the transverse wavenumber, associated with each of the two Bessel beams, namely 1 and 2, and is determined as follows: $k_r = k\sin\alpha$.

Similarly the intensity in the region of P_2 can be determined by the following relationship: $I = AA^*$ (which has been neglected here, as the equation is very cumbersome) and the angular rotation results in

$$\frac{d\phi}{dz} = \frac{k_{2z} - k_{1z}}{2l}. \tag{11}$$

The wave vectors in this region all point in opposite directions resulting in a non-zero rotation rate. However the only section of the field which experiences this angular rotation is the section which consists of the contributions from both ring-slits, which visually means: the sections which consist of both green and red rays. As the field propagates further towards the far-field (P_3), the overlap in the field, which consists of both ring-slit contributions, increases, resulting in the angular rotation becoming more evident.

To determine the far-field of the ring-slit aperture (P_3), whose transmission function $t(r,\phi)$ is given in Eq. (1), the Kirchoff–Huygens diffraction integral is used

$$A^{P_3}(r,\phi,z) = \frac{-i}{\lambda z}\int_0^{2\pi}\int_{R_1-\frac{\Delta}{2}}^{R_1+\frac{\Delta}{2}} t(r,\phi_1)\exp\left[i\frac{k}{2f}\left(1-\frac{z}{f}\right)r_1^2\right] \times \exp\left[-i\frac{krr_1}{f}\cos(\phi_1-\phi)\right] r_1\,dr_1\,d\phi_1. \tag{12}$$

The contribution resulting from the inner and the outer ring-slits produces the following superposition, which describes the far-field of the ring-slit aperture [9]

$$A^{P_3}(r,\phi,z) = J_l(k_{1r}r)\exp(il\phi)\exp(ik_{1z}z) + J_{-l}(k_{2r}r)\exp(-il\phi)\exp(ik_{2z}z). \tag{13}$$

The intensity of the superimposed Bessel field is determined with the following relationship: $I = AA^*$, resulting in

$$I^{P_3}(r,\phi,z) \propto J_l^2(k_{1r}r) + J_{-l}^2(k_{2r}r) + 2J_l(k_{1r}r)J_{-l}(k_{2r}r)\cos(k_{1z}z - k_{2z}z + 2l\phi). \tag{14}$$

Since the annular rings generating the superimposed Bessel beams are arbitrarily thin and close to one another, we can assume the transverse wavenumbers to be equivalent (i.e., $k_{1r} \sim k_{2r} = k_r$), resulting in $J_l(k_{1r}r) \sim J_l(k_{2r}r) = J_l(k_r r)$. By implementing the Bessel function identity, $J_{-l}(k_{2r}r) = (-1)^l J_l(k_{2r}r)$, the intensity in Eq. (14) can be simplified to produce

$$I^{P_3}(r,\phi,z) \propto 2J_l^2(k_r r)((-1)^l + 1 + 2(-1)^l\cos(k_{1z}z - k_{2z}z + 2l\phi)). \tag{15}$$

The intensity profile for the superimposed Bessel beams, given above in Eq. (15), illustrates that it is modulated in the azimuthal coordinate, ϕ, by the function $\cos(2l\phi)$. Therefore, the number of intensity maxima is twice the order l of the two Bessel beams, resulting in a superposition of a lth order Bessel beam, with its mirror image, producing an intensity pattern having $2|l|$ intensity maxima, or "petals", arranged on the

circumference of the set of Bessel rings. This intensity profile experiences an angular rotation, as the field propagates along the z-axis, given by

$$\frac{d\phi}{dz} = \frac{k_{2z} - k_{1z}}{2l}. \tag{16}$$

Since the longitudinal wave vectors all propagate in different directions in the far-field and that the field contributions from the two ring-slits completely overlap (evident in Fig. 1), the angular rotation is non-zero and the entire field at P_3 experiences the rotation.

3. EXPERIMENTAL METHODOLOGY

The experimental setup used to generate superpositions of higher-order non-diffracting Bessel beams, for the investigation of the near-field ring-slit aperture, is denoted in Fig. 4. Superimposed Bessel beams were generated by illuminating a ring-slit hologram (an example is given next to LCD_1 in Fig. 4) with an expanded Gaussian laser beam ($\lambda \sim 532$ nm). The Gaussian beam was expanded through a $3\times$ telescope and directed onto the liquid crystal display (LCD) of a SLM (HoloEye, PLUTO-VIS, with 1920×1080 pixels of pitch 8 μm and calibrated for a 2π phase shift at ~532 nm) labeled LCD_1.

The LCD was addressed with a hologram, similar to Durnin's ring-slit aperture [12], however since a phase-only SLM was used, an amplitude ring-slit was created digitally by encoding the area surrounding the ring-slit (the area which must not transmit any light) with a "checkerboard" pattern. By assigning alternating sets of pixels in the ring-slit hologram with phase values that are out of phase by π, the light reflected from LCD_1 is scattered from its initial propagation axis [16,17].

Since the "checkerboard" allows one to mimic an amplitude mask with a phase-only SLM, the azimuthal phase within the ring-slit can be addressed simultaneously in a single hologram. Assigning a single ring-slit with an azimuthal phase that varies from zero to $2\pi n$ times, a nth order Bessel beam will form in the far-field. If the ring-slit is divided into two ring-slits, where the azimuthal phase in each ring-slit varies in opposite directions (similar to that in Figs. 1 and 4) a superposition of two oppositely-handed Bessel beams will be generated. This is illustrated at the Fourier plane, P_3, of the ring-slit hologram given in Fig. 4. Here, the phase within the inner ring-slit varies three times in a clockwise direction ($l_{inner} = 3$) and three times in a counterclockwise direction ($l_{outer} = -3$) in the outer ring-slit, thus transforming the initial Gaussian beam into a superposition of two Bessel beams, of orders $l = 3$ and -3, denoted by the "petal" structure (P_3 in Fig. 4).

More examples of ring-slit holograms are given in the top row of Fig. 5. It is not shown in the holograms, presented in Figs. 4 and 5, but in conducting the experiment, a blazed grating was added to the holograms to separate the undiffracted and diffracted components reflected from LCD_1. A diaphragm, D, was placed at the focal plane after lens L_3 to select only the first diffraction order and neglect all the other unwanted diffraction orders.

Apart from positioning a $10\times$ objective and a CCD camera at the Fourier plane, P_3, of lens L_3, to record the non-diffracting superimposed Bessel beam, a second lens, L_4, was placed a focal length away from the Fourier plane of lens, L_3, to relay the field at LCD_1 to plane P_1. This allowed us to investigate the structure of the ring-slit field (evident at P_1) which produces a "petal" structure in the far-field (illustrated at P_3). The propagation of the ring-slit field, relayed to plane, P_1, was investigated by positioning a CCD camera on a rail and recording the field from plane P_1 to plane P_2 (a distance of two focal lengths from lens, L_4).

In the 'results' section of this paper, we will investigate the fields produced at the three different planes (P_1, P_2, and P_3) for various ring-slit holograms, as well as study the evolution of the field from plane P_1 to plane P_2, for a particular ring-slit hologram. For convenience we will refer to the Fourier transform of the ring-slit hologram (i.e., the field formed at plane P_3) as a "petal"-field. The field at the ring-slit hologram (i.e., the field at plane P_1), we will term the "singularity"-field and that formed at plane P_2 (a distance of $2f$ from lens L_4) will be termed as the "spiral"-field.

4. RESULTS AND DISCUSSION

All the digital ring-slit holograms, used in the experiment (depicted in Fig. 4), are given in the first row of Fig. 5. The first ring-slit hologram, Fig. 5(1a), consists of a single ring-slit containing an azimuthal phase of $l = +3$ and has the following dimensions (in pixels): $R_1 = 180$, $\Delta = 20$. The next five ring-slit holograms, Fig. 5(1b)–5(1f), all consist of two ring-slits, having oppositely varying azimuthal phases, varying in azimuthal order from $l_{inner} = -1$ to -5 ($l_{inner} = +1$ to $+5$), respectively. The ring-slit holograms in Figs. 5(1b)–5(1f) each have the following dimensions (in pixels): $R_1 = 180$, $R_2 = 190$, $\Delta = 10$. The last two ring-slit holograms [Fig. 5(1g) and 5(1h)] are divided into three and four ring-slits, respectively, having the following azimuthal orders $l_{inner} = -3$, $l_{middle} = 2$, $l_{outer} = 1$, and $l_{inner} = -2$, $l_{middle1} = -1$, $l_{middle2} = 2$, $l_{outer} = 1$.

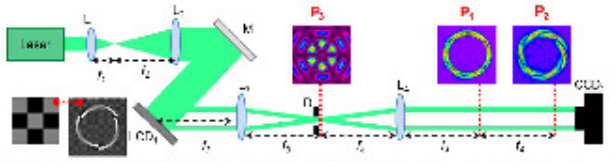

Fig. 4. (Color online) Schematic of the experimental setup for investigating the field formed by a ring-slit hologram, as well as the propagation and Fourier transform of such a field. L: lens ($f_1 = 25$ mm; $f_2 = 75$ mm; $f_3 = 100$ mm; and $f_4 = 100$ mm); M: mirror; LCD: liquid crystal display; D: diaphragm; CCD: CCD camera. The planes of interest are marked P_1, P_2, and P_3. P_3 is the Fourier plane of the ring-slit hologram; P_1 is the relayed-field (in both phase and amplitude) at the ring-slit hologram; and P_2 occurs a distance of $2f$ after L_4.

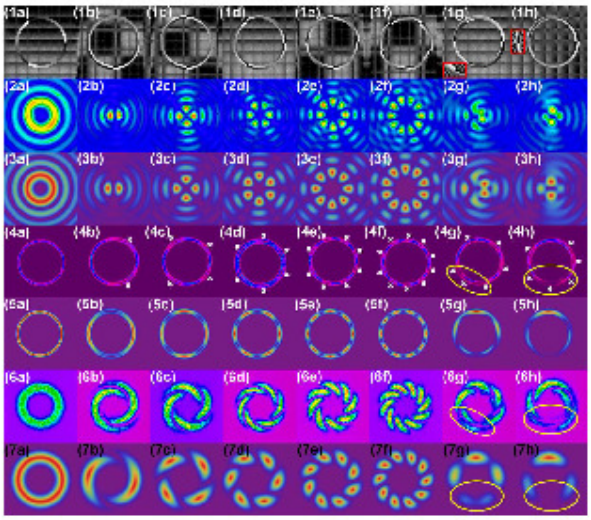

Fig. 5. (Color online) First row: ring-slit holograms addressed to LCD_1. A zoomed-in section of three and four ring-slits are depicted as inserts (1g) and (1h). Second and third rows: experimentally produced and theoretically calculated fields produced in the Fourier plane (i.e., plane P_3), respectively. Fourth and fifth rows: experimental and theoretical fields, respectively, produced at plane P_1 (i.e., the "singularity"-fields). The white "X" marks the singularities. Sixth and seventh rows: experimental and theoretical fields, respectively, produced at plane P_2 (the "spiral"-fields).

The dimensions (in pixels) of the ring-slits in Fig. 5(1g) and 5(1h) are: $R_1 = 180$, $R_2 = 190$, $R_3 = 200$, $\Delta = 10$, and $R_1 = 168$, $R_2 = 176$, $R_3 = 184$, $R_4 = 192$, $\Delta = 8$.

The far-fields of the ring-slit holograms, presented in the first row of Fig. 5, are shown in the second row of Fig. 5, accompanied with their theoretical predictions in the third row [calculated with the use of Eq. (13)]. For a single ring-slit, containing an azimuthal index of $l = +3$, the field produced in the Fourier plane, P_3, is a third-order Bessel beam. In the case that the ring-slit hologram consists of two ring-slits, where the orders of the two azimuthal phases are of equal but opposite handedness, a "petal"-structure is produced, where the number of "petals" is denoted by $2|l|$, as expected from theory [9]. It is interesting, to note from previous investigations [9,11], that even though these fields have a global OAM of zero, their cross-sectional intensity distribution rotates as the "petal"-field propagates, due to the differing radial wave vectors. Their rotation rate, which is dependent on the differing radial wave vectors and the azimuthal index, l, is given in Eq. (16). The fields produced in the Fourier plane, P_3, for the ring-slit holograms, contained in Figs. 5(1g) and (1h) are given in Figs. 5(2g) and (2h), respectively. These two ring-slit holograms consist of three and four ring-slits, respectively, and produce a non-symmetric superposition of higher-order Bessel beams. Even though it is difficult to intuitively predict how the field will manifest in the Fourier plane for these two cases, our experimentally recorded fields (Figs. 5(2g) and 5(2h)) are in very good agreement with the theoretically calculated fields (Figs. 5(3g) and 5(3h)). These two fields are calculated by extending the amplitude distribution, given in Eq. (13), to represent a superposition of three and four Bessel beams, respectively.

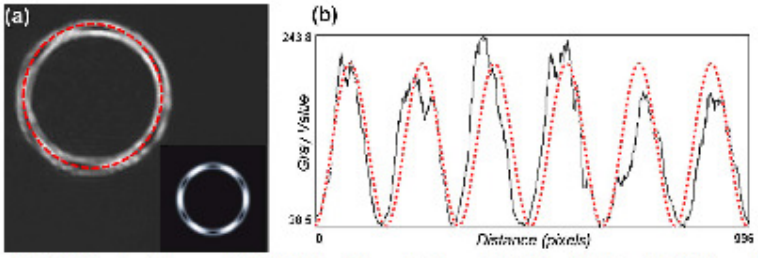

Fig. 6. (Color online) (a) Experimentally recorded field at plane P_1 for a ring-slit consisting of the following azimuthal phases: $l_{inner} = +3$ and $l_{outer} = -3$. Theoretical prediction is given as an insert. The red, dashed ring marks the line for which the intensity profile is plotted. (b) The solid black curve is the experimental intensity profile and the red dashed curve is the theoretical intensity profile, $\cos(2l\phi)$.

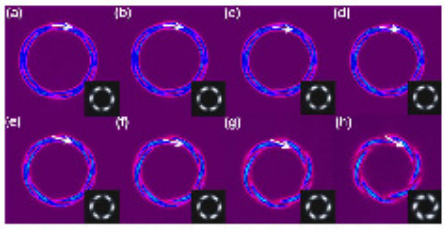

Fig. 7. (Color online) Experimental intensity profiles of the field captured at evenly spaced intervals from plane P_1 to plane P_2. The distances from plane P_1 are given as (a) 0 mm, (b) 10 mm, (c) 20 mm, (d) 30 mm, (e) 40 mm, (f) 50 mm, (g) 60 mm, and (h) 70 mm. The white arrows illustrate the movement of a selected singularity. Inserts are given for the theoretical predictions.

The optical field produced at the plane of the ring-slit hologram (i.e., at the plane of LCD_1) was relayed to plane P_2, where all the other diffraction orders had been removed through the use of the diaphragm, D, and experimental images are shown in the fourth row of Fig. 5. It is interesting to note that when the ring-slit is addressed with a single azimuthally varying phase, no singularities appear in the ring-slit field. However, by introducing a second ring-slit (having a different radial wave-vector) singularities appear in the ring-slit field, where the number of singularities is denoted by $2|l|$ (the same for the number of "petals"). The experimental "singularity"-fields (Figs. 5(4a)–5(4f)), produced at plane P_1, are in good agreement with those predicted theoretically, using Eq. (4) (with $n = 2$) and depicted in the fifth row of Fig. 5 [Figs. 5(5a)–5(5f)]. By increasing the number of ring-slits to either three or four, it becomes very difficult to individually locate each of the singularities in the "singularity"-field as some of them start to overlap. This is evident, experimentally, within the yellow rings in Figs. 5(4g) and 5(4h) and theoretically in Figs. 5(5g) and 5(5h). Since it is difficult to locate the singularities in the "singularity"-field, when the number of ring-slits is increased, we suggest using interferometric techniques to aid the categorizing of the singularities [18].

It is well-known that the intensity of the "petal"-field is dependent on the function $\cos(2l\phi)$, evident in Eq. (15). This cosine behaviour, as a function of the azimuthal angle, of the intensity profile is also present in the "singularity"-field. This is evident in Fig. 6 where the intensity profile, as a function of the angular position in the field, is plotted for the "singularity"-field, for the case of $l_{\text{inner}} = +3$ and $l_{\text{outer}} = -3$. It agrees well with the intensity profile plotted for the theoretically predicted "singularity"-field, given in Eq. (6), illustrating that the intensity maxima of the near- and far-field both depend on the function $\cos(2l\phi)$.

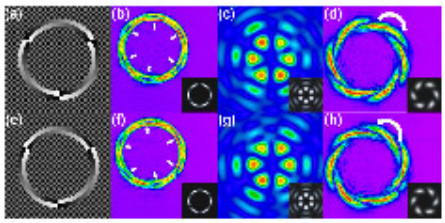

Fig. 8. (Color online) First column: ring-slit hologram applied to LCD_1. Second column: corresponding optical fields for the ring-slits. The white arrows mark the locations of the singularities. Third column: Fourier transform of the ring-slit hologram. Fourth column: corresponding "spiral"-field, produced at plane P_2. white arrow marks the handedness of the "spokes." Theoretical predictions are accompanied as inserts.

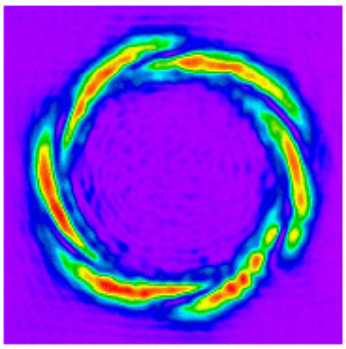

Fig. 9. (Color online) Video clip containing experimental images for the field occurring before and after the Fourier plane for an incoming "spiral"-field produced at plane P_2 (Media 1).

Propagating the field a distance of one focal length from plane P_1 to plane P_2, we see that the annular structure containing singularities transforms into "spirals". The experimental fields produced at plane P_2 for each of the eight ring-slit holograms are given in the sixth row of Fig. 5 and accompanied with theoretical predictions in the seventh row. In the case of a single ring-slit, having a non-zero azimuthal mode index, the "spiral"-field appears as a diverging version of the "singularity"-field. For the five holograms, each consisting of two ring-slits, having opposite azimuthal orders, there are $2|l|$ "spokes" in the "spiral"-field, evident in Figs. 5(6b)–5(6f). Introducing more ring-slits into the hologram results in the "spokes" in the "spiral"-field to merge, making it difficult to resolve individual "spokes" (evident within the yellow rings in Figs. 5(6g), 5(6h), 5(7g), and 5(7h)).

The propagation of the "singularity"-field at plane P_1 to the "spiral"-field (at plane P_2) was recorded and selected experimental images of the field at intervals along its propagation are given in Fig. 7. It is interesting to note that even though a rotation in the intensity profile for the "petal"-field (in the vicinity of plane P_3, i.e., the far-field) exists as the "petal"-field propagates, no rotation in the "singularity"-field or "spiral"-field (i.e., near-field) exists as the field propagates. This is in accordance with the theoretical prediction given in Eq. (8), where the rotation rate for such a field is determined to be non-existent, but becomes more evident the closer the field propagates to the far-field.

Switching the handedness of the azimuthal phases in the two ring-slits, is known to cause the "petal"-field, produced in the Fourier plane, P_3, to rotate in the opposite direction [10]. Even though the "spiral"-field, produced at plane P_2, does not rotate as it propagates, swapping the handedness of the azimuthal phases (within the two ring-slits), results in the

direction of the "spokes" to switch from clockwise to counterclockwise (and vice versa). This is evident in the last column of Fig. 8 and is in good agreement with the theoretical prediction.

Apart from investigating the appearance of the field produced by the ring-slit hologram at different propagation planes, the far-fields of the "spiral"-field (plane P_2) was also investigated and is presented as a media clip in Fig. 9. No rotation in the intensity distribution of the field before and after the existence of the non-diffracting "petal"-field is evident. The "spokes" compresses towards the propagation axis, overlapping and forming a non-diffracting "petal"-field, which exhibits a rotation in its intensity distribution as it propagates, but then the "spokes" expand outwards reconstructing the "singularity"-field.

5. CONCLUSION

In this work we have presented a class of beams which exhibit a rotation in their intensity profile in the far-field, but exhibit no rotation in the near-field. These beams are superimposed higher-order Bessel beams which are produced by encoding multiple azimuthally varying phases at different radial positions within a ring-slit aperture. We studied the field produced at the plane of the ring-slit aperture, as well as at various planes propagating from the ring-slit aperture and witnessed that the field transforms from an annular structure (embedded with singularities) to a "spiral" structure, consisting of "spokes" situated around a ring. The fields produced at the plane of the ring-slit aperture and at a distance of f from the ring-slit aperture are in good agreement with those calculated theoretically. Since Bessel beams, and especially superpositions of Bessel beams, are widely used in optical tweezing, understanding the structure of the field at planes other than the Fourier plane is necessary. The ring-slit field, embedded with singularities, can be used to trap low-index particles at set distances on the circumference of a circle. By adjusting the order, l, of the superimposed Bessel beams, one can control how many singularities are present in the ring-slit field, used to trap low-index particles. The ring-slit aperture dimensions can also be adjusted so as to control the size of the ring-slit and the distance between the singularities.

REFERENCES

1. M. W. Beijersbergen, L. Allen, H. E. L. O. Van der Veen, and J. P. Woerdman, "Astigmatic laser mode converters and the transfer of orbital angular momentum," Opt. Commun. **96**, 123–132 (1993).
2. J. Arlt and K. Dholakia, "Generation of high-order Bessel beams by use of an axicon," Opt. Commun. **177**, 297–301 (2000).
3. H. I. Sztul and R. R. Alfano, "The Poynting vector and angular momentum of Airy beams," Opt. Express **16**, 9411–9416 (2008).
4. L. Allen, M. W. Beijersbergen, R. J. C. Spreeuw, and J. P. Woerdman, "Orbital angular momentum of light and the transformation of Laguerre–Gaussian laser modes," Phys. Rev. A **45**, 8185–8189 (1992).
5. H. He, M. E. J. Friese, N. R. Heckenberg, and H. Rubinsztein-Dunlop, "Direct observation of transfer of angular momentum to absorptive particles from a laser beam with a phase singularity," Phys. Rev. Lett. **75**, 826–829 (1995).
6. A. Mair, A. Vaziri, G. Weihs, and A. Zeilinger, "Entanglement of the orbital angular momentum states of photons," Nature **412**, 313–316 (2001).
7. A. Vaziri, G. Weihs, and A. Zeilinger, "Experimental Two-Photon Three-Dimensional Quantum Entanglement," Phys. Rev. Lett. **89**, 240401–4 (2002).
8. J. T. Barreiro, T.-C. Wei, and P. G. Kwiat, "Beating the channel capacity limit for linear photonic superdense coding," Nat. Phys. **4**, 282–286 (2008).
9. R. Vasilyeu, A. Dudley, N. Khilo, and A. Forbes, "Generating superpositions of higher-order Bessel beams," Opt. Express **17**, 23389–23395 (2009).
10. R. Rop, A. Dudley, C. López-Mariscal, and A. Forbes, "Measuring the rotation rates of superpositions of higher-order Bessel beams," J. Mod. Opt. **59**, 259–267 (2011) http://dx.doi.org/10.1080/09500340.2011.631714.
11. V. V. Kotlyar, S. N. Khonina, R. V. Skidanov, and V. A. Soifer, "Rotation of laser beams with zero of the orbital angular momentum," Opt. Commun. **274**, 8–14 (2007).
12. J. Durnin, J. Miceli Jr., and J. H. Eberly, "Diffraction-free beams," Phys. Rev. Lett. **58**, 1499–1501 (1987).
13. D. McGloin, V. Garcés-Chávez, and K. Dholakia, "Interfering Bessel beams for optical micromanipulation," Opt. Lett. **28**, 657–659 (2003).
14. R. H. Jordan and D. G. Hall, "Free-space azimuthal paraxial wave equation: the azimuthal Bessel-Gauss beam solution," Opt. Lett. **19**, 427–429 (1994).
15. F. Gori, G. Guattari, and C. Padovani, "Bessel-Gauss beams," Opt. Commun. **64**, 491–495 (1987).
16. D. W. K. Wong and G. Chen, "Redistribution of the zero order by the use of a phase checkerboard pattern in computer generated holograms," Appl. Opt. **47**, 602–610 (2008).
17. A. Dudley, R. Vasilyeu, V. Belyi, N. Khilo, P. Ropot, and A. Forbes, "Controlling the evolution of nondiffracting speckle by complex amplitude modulation on a phase-only spatial light modulator," Opt. Commun. **285**, 5–12 (2012).
18. T. A. King, W. Hogervorst, N. S. Kazak, N. A. Khilo, and A. A. Ryzhevich, "Formation of higher-order Bessel light beams in biaxial crystals," Opt. Commun. **187**, 407–414 (2001).

B9: Publication 9

Azimuthal decomposition with digital holograms

Igor A. Litvin,[1] Angela Dudley,[1,2] Filippus S. Roux,[1] and Andrew Forbes[1,2,*]

[1]*CSIR National Laser Centre, PO Box 395, Pretoria 0001, South Africa*
[2]*School of Physics, University of KwaZulu-Natal, Private Bag X54001, Durban 4000, South Africa*
*aforbes1@csir.co.za

Abstract: We demonstrate a simple approach, using digital holograms, to perform a complete azimuthal decomposition of an optical field. Importantly, we use a set of basis functions that are not scale dependent so that unlike other methods, no knowledge of the initial field is required for the decomposition. We illustrate the power of the method by decomposing two examples: superpositions of Bessel beams and Hermite-Gaussian beams (off-axis vortex). From the measured decomposition we show reconstruction of the amplitude, phase and orbital angular momentum density of the field with a high degree of accuracy.

©2012 Optical Society of America

OCIS codes: (070.6120) Spatial light modulators; (120.3940) Metrology; (090.1995) Digital holography; (120.5060) Phase modulation.

References and links

1. J. W. Goodman, *Introduction to Fourier Optics* (McGraw-Hill Publishing Company, 1968).
2. E. Tervonen, J. Turunen, and A. Friberg, "Transverse laser mode structure determination from spatial coherence measurements: experimental results," Appl. Phys. B **49**(5), 409–414 (1989).
3. A. Cutolo, T. Isernia, I. Izzo, R. Pierri, and L. Zeni, "Transverse mode analysis of a laser beam by near- and far-field intensity measurements," Appl. Opt. **34**(34), 7974–7978 (1995).
4. M. Santarsiero, F. Gori, R. Borghi, and G. Guattari, "Evaluation of the modal structure of light beams composed of incoherent mixtures of Hermite-Gaussian modes," Appl. Opt. **38**(25), 5272–5281 (1999).
5. X. Xue, H. Wei, and A. G. Kirk, "Intensity-based modal decomposition of optical beams in terms of Hermite-Gaussian functions," J. Opt. Soc. Am. A **17**(6), 1086–1091 (2000).
6. D. Flamm, O. A. Schmidt, C. Schulze, J. Borchardt, T. Kaiser, S. Schröter, and M. Duparré, "Measuring the spatial polarization distribution of multimode beams emerging from passive step-index large-mode-area fibers," Opt. Lett. **35**(20), 3429–3431 (2010).
7. T. Kaiser, D. Flamm, S. Schröter, and M. Duparré, "Complete modal decomposition for optical fibers using CGH-based correlation filters," Opt. Express **17**(11), 9347–9356 (2009).
8. J. W. Nicholson, A. D. Yablon, S. Ramachandran, and S. Ghalmi, "Spatially and spectrally resolved imaging of modal content in large-mode-area fibers," Opt. Express **16**(10), 7233–7243 (2008).
9. D. B. S. Soh, J. Nilsson, S. Baek, C. Codemard, Y. Jeong, and V. Philippov, "Modal power decomposition of beam intensity profiles into linearly polarized modes of multimode optical fibers," J. Opt. Soc. Am. A **21**(7), 1241–1250 (2004).
10. M. Paurisse, L. Lévêque, M. Hanna, F. Druon, and P. Georges, "Complete measurement of fiber modal content by wavefront analysis," Opt. Express **20**(4), 4074–4084 (2012).
11. O. A. Schmidt, C. Schulze, D. Flamm, R. Brüning, T. Kaiser, S. Schröter, and M. Duparré, "Real-time determination of laser beam quality by modal decomposition," Opt. Express **19**(7), 6741–6748 (2011).
12. I. A. Litvin, A. Dudley, and A. Forbes, "Poynting vector and orbital angular momentum density of superpositions of Bessel beams," Opt. Express **19**(18), 16760–16771 (2011).
13. A. Dudley, I. A. Litvin, and A. Forbes, "Quantitative measurement of the orbital angular momentum density of light," Appl. Opt. **51**(7), 823–833 (2012).
14. R. Vasilyeu, A. Dudley, N. Khilo, and A. Forbes, "Generating superpositions of higher-order Bessel beams," Opt. Express **17**(26), 23389–23395 (2009).
15. R. Rop, A. Dudley, C. Lopez-Mariscal, and A. Forbes, "Measuring the rotation rates of superpositions of higher-order Bessel beams," J. Mod. Opt. **59**(3), 259–267 (2012).
16. R. Rop, I. A. Litvin, and A. Forbes, "Generation and propagation dynamics of obstructed and unobstructed rotating orbital angular momentum-carrying Helicon beams," J. Opt. **14**(3), 035702 (2012).
17. A. M. Yao and M. J. Padgett, "Orbital angular momentum: origins, behaviour and applications," Adv. Opt. Photon. **3**(2), 161–204 (2011).
18. G. Li and X. Liu, "Focus Issue: Space multiplexed optical transmission," Opt. Express **19**(17), 16574–16575 (2011).

#164079 - $15.00 USD Received 5 Mar 2012; revised 23 Apr 2012; accepted 24 Apr 2012; published 26 Apr 2012
(C) 2012 OSA

1. Introduction

Techniques to decompose light by use of Fourier optics have been known for a long time, and have been extensively reviewed to date [1]. Historically, these techniques have been applied to pattern recognition problems, and subsequently to the problem of studying the structure and propagation characteristics of laser beams [2–5]. Despite the appropriateness of the techniques, the experiments were nevertheless rather complex. Recently this subject has been revisited by employing computer generated holograms in a mode multiplexing scheme for the modal decomposition of laser beams from fibres [6–10], and for the real-time measurement of the beam quality factor of a laser beam [11]. While these techniques have significant merit, they require a prefabricated diffractive optical element. This implies that information on the modal basis to be used, and the scale parameters of this basis, are known. To date this has been achieved by first modelling the source under study.

In this paper we consider the problem of the azimuthal decomposition of an arbitrary laser source, without any knowledge of the mode structure, the mode phases, or the scale of the amplitude distribution. We make use of a basis comprising the angular harmonics, which are independent of spatial scale, and express the spatial distribution in terms of spatially dependent coefficients in this basis. The result, as we will show, is that the complete decomposition can be achieved without any scale information. We use this to infer directly from measurements of the intensity of the superposition field, its phase, and its orbital angular momentum (OAM) density distribution. In fact, it is clear that since the entire field is known, all physical quantities associated with the field can be inferred. We illustrate the concept by executing a full azimuthal decomposition of: (i) a superposition of two OAM carrying Bessel beams, with relative phase differences and (ii) an off-axis vortex mode. A comparison of our experimental measurements to the predicted theory shows excellent agreement.

2. Concept and theory

The core idea is to expand our unknown field, $u(r,\phi)$, into a basis that is not dependent on scale. Such a basis is the angular harmonics, $\exp(il\varphi)$, that are orthogonal over the azimuthal plane. To illustrate that the azimuthal decomposition that we employ in this work is completely general, we consider, for example, the Laguerre-Gaussian (LG) basis as our OAM basis. An expansion of an arbitrary optical field in terms of this LG basis is given by

$$u(r,\phi) = \sum_{p,l} c'_{p,l} R_{p,l}(r) \exp(il\phi), \tag{1}$$

where $c'_{p,l}$ denotes the complex coefficients and $R_{p,l}(r)$ is the radial part of the LG mode, which only depends on r. One can now combine, and sum over the part of the expression that contains a p-index

$$u(r,\phi) = \sum_{l} \left[\sum_{p} c'_{p,l} R_{p,l}(r) \right] \exp(il\phi) = \sum_{l} c_l(r) \exp(il\phi), \tag{2}$$

where

$$c_l(r) = \sum_{p} c_{p,l} R_{p,l}(r) = a_l(r) \exp\left[i\Delta\theta_l(r) \right]. \tag{3}$$

If the original expansion in terms of the LG modes is completely general, then by implication, so is the azimuthal expansion with the r-dependent coefficients. The coefficients are given by

$$c_l(r) = \frac{1}{2\pi} \int_0^{2\pi} u(r,\phi) \exp(-il\phi) d\phi. \tag{4}$$

#164079 - $15.00 USD Received 5 Mar 2012; revised 23 Apr 2012; accepted 24 Apr 2012; published 26 Apr 2012
(C) 2012 OSA

The coefficient of the azimuthal modes contains information on the spatial distribution of the field. Each coefficient contains an arbitrary phase, $\Delta\theta_l$, relative to some reference, which we may take to be an external source or for convenience the first mode in the series, $l = 0$ at a specific value of r. To describe $u(r,\phi)$ completely, we are required to determine the phase shift between modes and the magnitude of the coefficients. The coefficients may be found by an inner product calculation and a suitable match filter, as shown in Eq. (4). To implement this calculation in a physically realizable manner, consider the signal at the origin of the Fourier plane after a lens (for wavenumber k and focal length f) after the field has been modulated by a transmission function given by $t_l(r,\phi)$

$$U_l(0) = \frac{\exp(i2kf)}{i\lambda f}\int_0^\infty\int_0^{2\pi} t_l(r,\phi)u(r,\phi)rdrd\phi. \tag{5}$$

Since we wish to implement Eq. (4), it is clear that the transmission function has two requirements: (i) it should have an azimuthal phase variation opposite to the mode being analyzed, (ii) to select the information as a function of r it should consist of an annular slit centered at $r = R$ and of negligible thickness, ΔR. These conditions are satisfied if the transmission function is defined as

$$t_l(r,\phi) = \begin{cases} \exp(-il\phi) & R-\Delta R/2 < r < R+\Delta R/2 \\ 0 & otherwise \end{cases}. \tag{6}$$

The subscript l in t_l and U_l refer to selecting the l^{th} mode in the expansion of Eq. (2). So that

$$\begin{aligned} \tilde{U}_l(R,0) &= \frac{\exp(i2kf)}{i\lambda f}\int_0^\infty\int_0^{2\pi} t_l(r,\phi)u(r,\phi)rdrd\phi \\ &\approx \frac{k\exp(i2kf)}{if}c_l(R)R\Delta R. \end{aligned} \tag{7}$$

By re-arranging the final result in Eq. (7), we find that

$$c_l(R) = \frac{if}{R\Delta Rk\exp(i2kf)}\tilde{U}_l(R,0). \tag{8}$$

Firstly, we note that a measurement of the intensity of the signal, $I_l(R,0)$, at the origin in the Fourier plane returns exactly our desired magnitude of the coefficients, since

$$a_l(R) = |c_l(R)| = \frac{f}{R\Delta Rk}\sqrt{I_l(R,0)}. \tag{9}$$

Secondly, we note that if we interfere our selected l mode with a reference wave and consider the inner product signal, then the unknown phase of the coefficient, $\Delta\theta_l$, can be found. If $|g|\exp(i\alpha)$ represents the complex amplitude of the reference wave of the origin then the intensity, at the origin, as a function of the phase delay is given by

$$\begin{aligned} \tilde{I}_l(\Delta\theta_l) &= |c_l(R)+g|^2 \\ &= a_l^2(R)+|g|^2+2a_l(R)|g|\cos[\Delta\theta_l(R)-\alpha]. \end{aligned} \tag{10}$$

It is a simple task to invert Eq. (10) to find the unknown phase delay between the modes. With the complete azimuthal decomposition of the field achieved, as in Eq. (2), it is possible to calculate the intensity of the field, $|u(r,\phi)|^2$, the phase of the field, $\arg[u(r,\phi)]$, the Poynting vector [12],

#164079 - $15.00 USD Received 5 Mar 2012; revised 23 Apr 2012; accepted 24 Apr 2012; published 26 Apr 2012
(C) 2012 OSA

$$\mathbf{S} = \frac{\varepsilon_0 \omega c^2}{4}\left[i\left(u\nabla u^* - u^*\nabla u\right) + 2k\left|u\right|^2 \bar{z}\right], \tag{11}$$

and finally the OAM density [13]:

$$L_z = \frac{1}{c^2}\left[\mathbf{r}\times\mathbf{S}\right]_z. \tag{12}$$

The pertinent point here is that at no stage has any assumption been made on the scale of the basis functions. This is because we have elected to scan the field with an annular slit, thereby storing the scale information in the coefficient of a scale invariant basis. The scale of any OAM basis function is set by the radial coordinate. Since the radial coordinate becomes a part of the coefficient functions, the scale parameter is removed from the basis functions, resulting in the remaining azimuthal component becoming independent of scale. We will now show how to implement the technique with a phase-only spatial light modulator (SLM), thus allowing a full azimuthal decomposition of the field with digital holograms.

3. Experimental methodology

The experimental realization of the technique comprises two parts: the generation and then decomposition of the field, and is shown schematically in Fig. 1(a). The first SLM (denoted as SLM_1) was programmed to produce various fields. The two cases that we considered were (i) a superposition of two OAM carrying Bessel beams [14] and (ii) an off-axis vortex mode. A Gaussian beam from a HeNe laser [Fig. 1(b)] was expanded through a 5 × telescope and directed onto the liquid crystal display of SLM_1 (HoloEye, PLUTO-VIS, with 1920 × 1080 pixels of pitch 8 μm and calibrated for a 2π phase shift at λ~633 nm) where the hologram used to generate the field of interest was programmed. For the case where a superposition of two OAM carrying Bessel beams were studied, two annular rings modulated in their azimuthal phase [see Fig. 1(c)] were encoded onto SLM_1. The amplitude transmission of 0 everywhere outside the annular ring and 1 inside the ring was programmed using complex amplitude modulation for amplitude only effects on a phase-only device. The hologram takes the form of a high frequency grating that oscillates between phase values of 0 and π, and it has been shown that this results in the required amplitude transmission of Eq. (6) [15]. We shall refer to this as the checkerboard pattern: see zoomed in section of Fig. 1(c). The result is non-diffracting petal-like modes [Fig. 1(d)] that rotate as they propagate, and have been studied in detail elsewhere [15,16].

These fields were then magnified with a 10 × objective and directed to the second SLM (SLM_2) for executing the azimuthal decomposition. This was accomplished by executing an inner product of the incoming field with the match filter set to $\exp(il\phi)$, for various l values, and for particular radial (r) positions on the field, as given by Eq. (6) and illustrated in Fig. 1(e). The typical width of the ring in the experiments was $\Delta R = 80$ μm. The width of the ring, as well as the azimuthal index (l) encoded within the ring, are limited by the resolution of the SLM. The field at the Fourier plane is shown in Fig. 1(f) – note that we only require the intensity at the origin of this plane.

#164079 - $15.00 USD Received 5 Mar 2012; revised 23 Apr 2012; accepted 24 Apr 2012; published 26 Apr 2012
(C) 2012 OSA

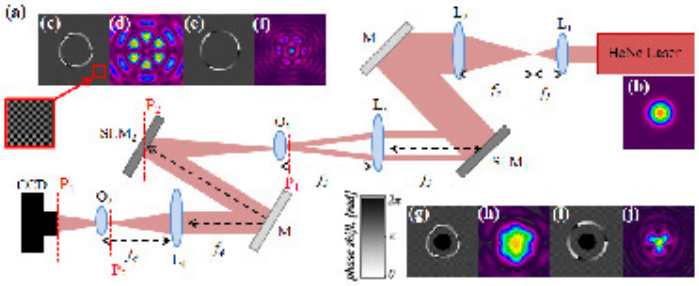

Fig. 1. (a) A schematic of the experimental setup for performing the modal decomposition. L: Lens (f_1 = 15 mm; f_2 = 75 mm; f_3 = 200 mm and f_4 = 200 mm); M: Mirror; SLM: Spatial Light Modulator; O: Objective; CCD: CCD Camera. The objective, O_2, was placed at the focus (or Fourier plane) of lens, L_4. Lens L_3 and L_4 perform a Fourier transform of SLM_1 and SLM_3, respectively, in a 2-*f* system. Objectives O_1 and O_2 are telescopes which image and magnify both the phase and amplitude of the fields at planes P_1 and P_3 to planes P_2 and P_4 respectively. (b) The Gaussian beam used to illuminate SLM_1. (c) The digital hologram used to generate the optical field of interest (d) and the digital hologram (e) used to extract the weightings of the modes from the inner product (f). The digital holograms for generating (g) and decomposing (i) the field, to extract the intermodal phase. The intensity profile of the field at the plane of SLM_2 (h) and CCD (j). Each hologram has a checkerboard pattern, shown as an inset to (c).

In order to measure the phase delay between the modes, we switch off the checkerboard pattern in the centre of both SLMs. This results in a portion of the initial Gaussian beam passing through the entire optical system, without "seeing" the phase holograms. Because it follows the same path as the modes that we wish to study, we can use the central peak of the beam as our reference beam, $|g|\exp(i\alpha)$. Figure 1(g) shows the initial generating step but with a constant phase in the centre of the hologram (black disk), the resulting mixing with the non-diffracting petals [Fig. 1(h)] and after passing through the second SLM [Fig. 1(i)] the resulting interference of the waves [Fig. 1(j)]. The constant phase of the reference could be changed across several values to provide information on the quadrant of the cosine function in Eq. (10). Note that switching between the intensity measurement [Figs. 1(c)–1(f)] and the phase measurement [Figs. 1(g)–1(j)], we require only a change in the holograms loaded onto SLMs 1 and 2. This switching between holograms can be done at 60 Hz, i.e., practically real-time acquisition of the necessary data.

4. Results and discussion

4.1. Superposition of two OAM carrying Bessel beams

To test the accuracy of the method, we first created a superposition of two Bessel beams with opposite handedness, i.e., $m = 3$ and $n = -3$ and defined generally as

$$u(r,\phi) = A_m J_m(kr)\exp(im\phi) + A_n J_n(kr)\exp(in\phi)\exp(i\Delta\theta). \qquad (13)$$

The phase delay, $\Delta\theta$, in Eq. (13) was then varied between 0 and 2π, resulting in a rotation of the intensity pattern, which can easily be measured by observing the angular displacement of any one of the petals. This measured rotation is directly related to $\Delta\theta$, thus allowing the measured phase shift to be compared to the programmed value. The programmed phase shift and resulting petal rotation are shown in Fig. 2(a), and compared to the theoretical rotation. The results of this calibration test are shown in Fig. 2(b), where it is clear that the agreement between measured and actual is very good (slope difference of 0.1%). The error bars were determined through a range of intensity values in the finite region (few pixels) around the

#164079 - $15.00 USD Received 5 Mar 2012; revised 23 Apr 2012; accepted 24 Apr 2012; published 26 Apr 2012
(C) 2012 OSA

origin of the Fourier plane. These results confirm that the setup was working correctly without spurious effects.

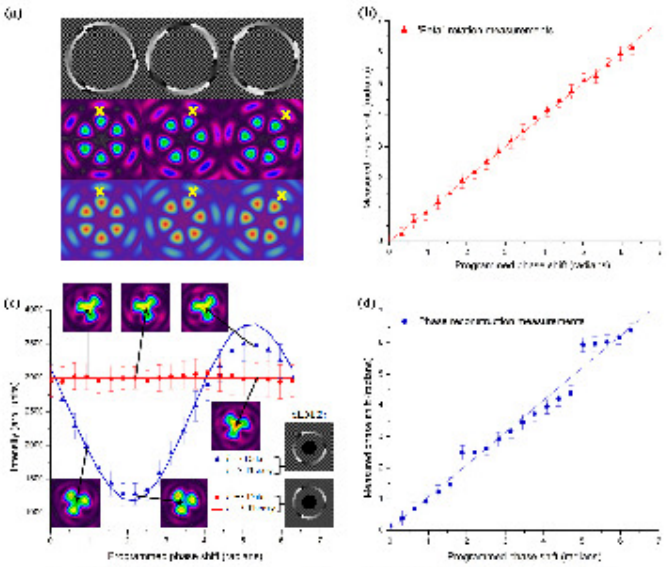

Fig. 2. (a) If the phase is shifted in one of the modes in the initial field (top row), then the measured petal structure of the superposition field (middle row) is seen to rotate, as predicted by theory (bottom row); (b) comparison of the measured phase shift to the actual phase shift; (c) interference of the modes with a reference wave results in changing intensity at the origin of the Fourier plane, which can be used to infer the phase shift per mode; (d) comparison of the measured phase shift to the actual phase shift (see Media 1 and Media 2).

Next, the programmed phase shift $\Delta\theta$ was measured using the interference technique and analyzed using Eq. (10). The phase shift in the $n=-3$ beam was scanned through 0 to 2π and the interference monitored, as shown in Fig. 2(c). By removing the offset phase of the reference beam (corresponding to the maximum in the interference signal), the measured phase could be compared to the programmed phase. The results are also shown in Fig. 2(d), and again the agreement is good (slope difference of 3%), but with some uncertainty near a programmed phase shift of 0.60π and 1.60π; these discontinuities occur at maxima and minima in the interference intensity [Fig. 2(c)], and are due to the flatness of the change in the measured intensity for a change in phase value (three values were used to uniquely determine the phase). To illustrate further that the technique works, we constructed a superposition field with $m=+3$ and $n=-2$, to deliberately break the symmetry of the field. The annular ring on SLM_2, of width 80 μm, was scanned through 28 radial positions (maximum number to scan our field) and the azimuthal phase varied across $l\in[-10,10]$. The only non-zero components (>0.5% of the modal power) were those corresponding to $l=+3$ and $l=-2$, which contained ~95% of the modal power. With all the unknown terms in Eq. (4) measured experimentally, we were able to reconstruct the intensity and phase of the initial field, and compare it to the theoretical prediction (based on our own hologram function on SLM_1). The results for the intensity of the field are shown in Figs. 3(a) and 3(d) while that

#164079 - $15.00 USD Received 5 Mar 2012; revised 23 Apr 2012; accepted 24 Apr 2012; published 26 Apr 2012
(C) 2012 OSA

of the phase of the field is given in Figs. 3(b) and 3(e). There is very good agreement between the theoretically predicted field and the field reconstructed from the azimuthal decomposition.

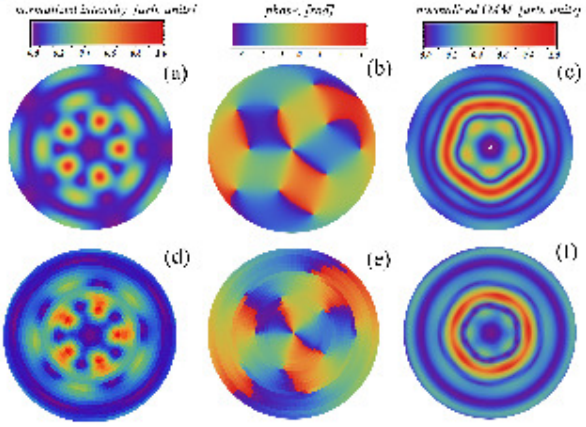

Fig. 3. A comparison of the theoretical (top row) and the experimentally reconstructed (bottom row) images of the (a, d) intensity, (b, e) phase, and (c, f) OAM density of the light.

An interesting application of this technique is the determination of the complete OAM density of the field. It has been known for some time now that photons carry orbital angular momentum ([17] and references therein), yet it remains a challenge to measure the local and global OAM of a field in a manner that is quantitative. Previously we have attempted such measurements without the phase information, and found success for particular structures of optical fields [12,13]. With a full azimuthal decomposition of the field, including the phase delays, we can infer the OAM density of *any* field directly from our measurement. The theoretical and experimental results of this are shown in Figs. 3(c) and 3(f), respectively, and are in agreement.

4.2. Off-axis vortex mode

Next we apply our decomposition technique to the example of a Gaussian beam with an off-axis vortex. The results are presented in Fig. 4.

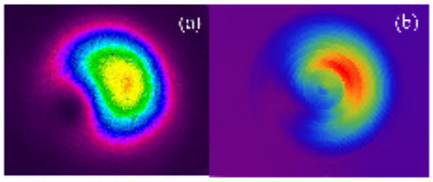

Fig. 4. A comparison of the experimentally recorded intensity (a) and the reconstructed intensity (b), for the off-axis vortex case, created from a superposition of Hermite-Gaussian modes.

#164079 - $15.00 USD Received 5 Mar 2012; revised 23 Apr 2012; accepted 24 Apr 2012; published 26 Apr 2012
(C) 2012 OSA

The same measurement procedure, as that discussed above, was implemented on the field, whose experimentally recorded intensity profile is given in Fig. 4(a). The reconstructed field is shown in Fig. 4(b) illustrating that this technique is successful in the reconstruction of optical fields which possess an on-axis intensity. The problem in this case is that there is no dark core in the centre of the field under investigation where we could pass a Gaussian reference beam through, for the implementation of the phase measurements. In this case we use a section of the field under investigation as our reference (assuming no singularities, a single pixel size region will have a uniform phase).

4.3. Alignment sensitivity

Although one can represent the beam in terms of expansions with respect to any beam-axis, the coefficients in the expansions are sensitive to a shift of the beam-axis. Here, our concern is the fidelity of the reproduced beam rather than the fidelity of the expansion coefficients. Naturally we do not want the beam-axis to be too far off, because that would increase the higher-order coefficients and reduce the fidelity of the reconstructed beam, but small shifts in the beam axis does not pose a serious problem and this is illustrated in Fig. 5(a). The hologram on SLM_2 was displaced with respects to the propagation axis of the field under investigation for step sizes of a single pixel (i.e. 8 μm) and the fluctuation in the on-axis intensity of the inner product, from which the unknown field is reconstructed, shows very little variation (the percentage error is roughly 0.5% per pixel shift). It is fairly easy to get the alignment of our system within such distances from the actual beam axis. If the displacement is much greater (10 times greater) then the alignment does pose a problem and the on-axis intensity of the inner product varies significantly, evident in Fig. 5(b).

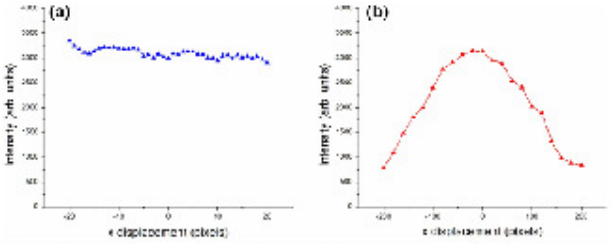

Fig. 5. Graph of the measured on-axis intensity of the inner product as a function of a lateral displacement of the hologram on SLM_2 for a displacement range of (a) −20 to 20 pixels (−160 μm to 160 μm) and (b) −200 to 200 pixels (−1600 μm to 1600 μm).

For the experimental measurements presented here we aligned each SLM to a common propagation axis by initially centering each SLM on a Gaussian mode that propagated through the system. More general alignment techniques, as used by other decomposition methods, could also be employed [6,7].

5. Conclusion

We have outlined an improved method for the azimuthal decomposition of an arbitrary field that requires no scale information of the basis functions, and allows for the phases to be easily measured. It is significant to note that using only minor changes to the digital holograms, we can switch the setup between measuring azimuthal weights to azimuthal phase delays – no optical re-alignment is necessary, and no path length adjustment is required for the phase measurements. Moreover, even though our system is not automated and a scan of all measurements would take 4 hours, in an automated system the holograms can be displayed at fast refresh rates (60 Hz), so that the measurement per radial position takes about 1 s. Using superpositions of OAM carrying Bessel beams as an example, we have

#164079 - $15.00 USD Received 5 Mar 2012; revised 23 Apr 2012; accepted 24 Apr 2012; published 26 Apr 2012
(C) 2012 OSA

shown excellent reconstruction of both the intensity and phase of the field, as well as the OAM density everywhere in the field. We have also shown accurate reconstruction of an off-axis vortex beam, illustrating the versatility of the method. This technique will surely be of relevance to those working in OAM, both at the classical and quantum level, as well as to the emerging field of mode multiplexing for future telecommunications ([18], and references therein), where mode generation and decomposition are necessary tools.

#164079 - $15.00 USD Received 5 Mar 2012; revised 23 Apr 2012; accepted 24 Apr 2012; published 26 Apr 2012
(C) 2012 OSA